PREBUCKLING AND POSTBUCKLING BEHAVIOR OF STIFFENED COMPOSITE PANELS WITH AXIAL-SHEAR STIFFNESS COUPLING

by
Richard Douglas Young

Dissertation submitted to the Faculty of the
Virginia Polytechnic Institute and State University
in partial fulfillment of the requirements for the degree of
DOCTOR OF PHILOSOPHY
in
Engineering Mechanics

APPROVED:

M. W. Hyer, Chair

O. H. Griffin

Z. Gürdal

E. R. Johnson

K. L. Reifsnider

July 12, 1996
Blacksburg, Virginia

Key words: Composite, Anisotropic, Stiffened, Postbuckling, Tailored

PREBUCKLING AND POSTBUCKLING BEHAVIOR OF STIFFENED COMPOSITE PANELS WITH AXIAL-SHEAR STIFFNESS COUPLING

by

Richard Douglas Young

Committee Chair: Michael W. Hyer
Engineering Mechanics

(ABSTRACT)

To advance structural tailoring methods in composite structures, an experimental and numerical investigation of the prebuckling and postbuckling responses of flat rectangular graphite-epoxy composite panels with a centrally located I-shaped stiffener subjected to a uniform end shortening is presented. Axial-shear stiffness coupling is introduced by rotating the stiffener and/or prescribing skin laminates with membrane and bending stiffness coupling. A panel's axial-shear coupling response is defined as the ratio of the panel's shear load to its compression load when a simple end shortening is applied.

Experimental results are reported for five panels. The baseline test panel has an unrotated stiffener and a $[\pm 45/\mp 45/0_3/90]_s$ skin laminate. Two panels have either the stiffener or the entire skin laminate rotated 20°, and the remaining two panels have both the stiffener and the skin laminate rotated by 20°, either in the same direction, or in opposite directions. Extensive experimental data are obtained electronically during quasi-static tests. Finite element models are defined which accurately represent the conditions in the experiment, and geometrically nonlinear analyses are conducted. Measured and predicted responses are compared to verify the numerical models. The panels' stiffness, buckling parameters, load vs. end shortening relations, out-of-plane deformations, and axial-shear coupling responses are reported. The finite element analyses, based on two-dimensional

plate elements, are utilized to address failure due to skin-stiffener separation by estimating the skin-stiffener attachment forces and moments at failure.

The results of a parametric study which isolates the mechanisms which contribute to axial-shear stiffness coupling are reported. It is found that rotating the stiffener or introducing skin anisotropy typically reduces the axial stiffness and buckling loads. The axial-shear coupling response due to rotating the stiffener is constant in prebuckling and increases after skin buckling, and the magnitude of the response can be adjusted by varying the stiffener rotation and rigidity. Skin membrane stiffness coupling creates axial-shear coupling responses that are constant in prebuckling and decrease in magnitude after skin buckling. Skin bending stiffness coupling creates axial-shear coupling responses that are zero in prebuckling and increase in magnitude after skin buckling. Examples are presented which demonstrate how different mechanisms can be tailored independently and then superimposed to effectively tailor a stiffened panel's axial-shear coupling response in the prebuckling and postbuckling load ranges.

Acknowledgments

The financial support of this work by the NASA Graduate Student Researchers Program, the Structural Mechanics Branch of the NASA Langley Research Center, and the Lockheed Martin Engineering & Science Services Langley Program Office, is gratefully acknowledged.

I would like to thank my advisor and mentor, Professor M. W. Hyer, for his technical and professional guidance, encouragement, and unwavering support during the past eight years of study and research. Special thanks are also given to Professors O. H. Griffin, Z. Gürdal, E. R. Johnson, and K. L. Reifsnider for serving on the Ph.D. dissertation and advisory committee and for providing technical guidance during the course of the research.

I am extremely grateful to Dr. J. H. Starnes, Jr. for his continuous support and expert technical guidance throughout my residency and subsequent employment in support of the Structural Mechanics Branch. I am also thankful for the use of the excellent laboratory and computational facilities and I also appreciate the valuable discussions, technical assistance, and advice provided by the researchers of the Structural Mechanics Branch. Special thanks are given to Dr. M. P. Nemeth and the late Dr. M. Stein for insightful discussions on the buckling and postbuckling behavior of plates and the influence of anisotropy.

I am grateful to my supervisors and colleagues at Lockheed Martin for supporting my research over the past six years. I would like to thank B. Cornell, R. F. Vause, M. Swain, A. Stockwell, and E. Fasanella for their encouragement.

Many individuals working for, or under contract to, the Langley Research Center contributed to success of this effort and I would like to acknowledge their support. In particular, I would like to recognize the following individuals for their outstanding technical efforts: W. A. Waters, Jr. (general technical support), K. A. Warnaar and C. W. Huling (computational support), J. J. Kiss and M. A. Cole (testing and data acquisition), J. Y. Smith (specimen lay-up), F. Walters (specimen machining, tabbing, and potting), and D. Croom (specimen surface shape measurement).

I would like to thank all of my friends and colleagues at the Langley Research Center for their valuable support and encouragement. Special thanks are given to my colleagues Dr.

D. S. Norwood, Dr. R. P. Ley, Dr. E. Moas, Jr., Dr. J. P. Fuchs, Dr. C. A. Rose, Dr. P. A. Robinson, and B. F. Tatting for their professional and personal comradeship that made my time at Langley enjoyable and memorable.

I graciously acknowledge my mentor during my formative years at the State University College at Fredonia, M. Grasso, for his dedication to teaching fundamental mechanics and for providing inspiration to pursue academic excellence. I am also thankful to Dr. Charles C. Rankin of the Lockheed Palo Alto Research Laboratory for his friendship and enthusiastic support of the STAGS software.

I will always be indebted to my family and friends. I am especially grateful to my brothers Tom, Dennis, and Tim, and my longtime friends R. Muscato and M. Gregory for their steadfast support. Their confidence in my abilities always gave me a solid foundation from which I could launch any endeavor and find strength in knowing that they believed in me.

I am most grateful to my wife, Lisa Rose Young, for her love and support. I would like to thank her for her patience during the final months of dissertation preparation which also coincided with the initial months of our marriage. We share something special and I look forward to our life together.

Finally, I would like to dedicate this dissertation to my parents, William T. Young, Sr., and Doris L. Young, and thank them for their love, support, and encouragement throughout my life.

Table of Contents

List Of Figures

List Of Tables

1. Introduction

Stiffened laminated composite panels are finding an increased number of applications in structural design. Stiffened panels, generally consisting of beam-like members adhesively bonded or mechanically fastened to a thin laminate, or skin, are typically utilized because of their structural efficiency and their ability to carry additional load after the skin has buckled. The use of laminated fiber-reinforced composites has grown due to their high strength-to-weight and stiffness-to-weight ratios, and the ability to tailor laminate properties for specific applications.

Most early applications of composite materials were developed using conventional metal design practices. As more is learned about tailoring laminate properties, conventional design practices are being rethought and modified to exploit the potential of structural tailoring. In aircraft design, for example, structural tailoring has been employed to build stiffness coupling into the wing structure in order to control aeroelastic deformations. Wing structures have been designed to exhibit bend-twist stiffness coupling to suppress flutter of rear-swept wings and suppress divergence of forward-swept wings. In most applications, bend-twist stiffness coupling of the wing structure was generated by incorporating axial-shear stiffness coupling in the stiffened skins of the wing.

There are two techniques that have been applied for structural tailoring of stiffened panels. Axial-shear stiffness coupling has been incorporated in metallic stiffened panels by utilizing skewed stiffeners, i.e., stiffeners not aligned with the primary direction of loading. In stiffened panels with laminated composite skins, axial-shear stiffness coupling has been generated by rotating the principal direction of orthotropy of the laminated skin relative to the principal direction of loading. To realize fully the potential of structural tailoring of composite stiffened panels, designs should be considered which exaggerate the use of anisotropy in the laminated skins, and possible apply both anisotropic skins and skewed

stiffeners. The axial-shear stiffness coupling available with each tailoring method, and the effects of combining the tailoring methods, will need to be quantified.

Since stiffened panels have been shown to exhibit substantial postbuckling strength, some design practices allow the skin of certain stiffened components to buckle at load levels below design ultimate load conditions. If axial-shear stiffness coupling is to be used in structures with postbuckled skins, it will be necessary to determine if axial-shear stiffness coupling is altered when the skin is allowed to buckle. If buckling changes the coupling, then it may be possible to tailor the structural stiffness to vary as a function of load.

With the above issues in mind, the problem of the prebuckling and postbuckling behavior of composite plates with anisotropic skins and skewed stiffeners was studied in depth in the present investigation. The goal of the present investigation is to demonstrate the nature of the axial-shear stiffness coupling that can exist in a simple stiffened panel. The results of the investigation are primarily intended to promote the use of structurally tailored composite stiffened panels for applications where a specific coupled load-displacement response is desired. There may be direct applications for structures with combined loads, particularly if the ratio of the combined loads varies as a function of the load. In addition to promoting the application of structural tailoring, the results of this study may also be helpful in explaining the response of stiffened panels that have laminated composite skins which have some degree of anisotropy, or stiffeners that are not exactly aligned with the principal direction of loading.

In most generic structural applications designers try to minimize the amount of stiffness coupling. Stiffness coupling in laminated composite plates typically reduces the buckling load and induces a more complicated response, which makes the structure more difficult to analyze. The concept of inducing substantial stiffness coupling to create a tailored structural response is not globally accepted, nor is the concept appreciated. The current investigation is meant to provide insight into the nontraditional structural responses that are possible with structural tailoring and to inspire innovative applications that can only be achieved by using the tailorability of composite materials.

Since stiffness coupling concepts are not widely understood and used, this chapter will start with a brief introduction to stiffness coupling in laminated composites plates. Examples are then presented to demonstrate the variation in membrane and flexural stiffnesses created by rotating the principal direction of orthotropy of several composite laminates.

Also to follow in this chapter is a survey of some of the literature felt to be relevant to the prebuckling and postbuckling response of stiffened composite panels with anisotropic skins and skewed stiffeners. This is followed by an overview of the specific problem addressed in this study and the approach that was used.

1.1 Stiffness Coupling in Laminated Composite Plates

The term composite, as used in the context of materials for structural applications, generally describes a matrix material reinforced with continuous filaments. A tutorial which outlines the mechanics of composite plates is included in this document as Appendix A. This tutorial includes a description of the principles of classical lamination theory, the formulation of the nonlinear strain-displacement relations, laminate constitutive relations, and definitions for membrane and flexural equivalent engineering constants for laminated composite plates. The terminology and nomenclature used in the field of composites varies from one reference to another. The current work contains equations taken primarily from the two textbooks, Mechanics of Composite Materials[1] by R. M. Jones, and Nonlinear Analysis of Plates[2] by C. Y. Chia.

In Section A.4 the constitutive relations for a symmetrically laminated composite plate are given as

$$\begin{Bmatrix} N_x \\ N_y \\ N_{xy} \end{Bmatrix} = \begin{bmatrix} A_{11} & A_{12} & A_{16} \\ A_{12} & A_{22} & A_{26} \\ A_{16} & A_{26} & A_{66} \end{bmatrix} \begin{Bmatrix} \varepsilon_x^o \\ \varepsilon_y^o \\ \gamma_{xy}^o \end{Bmatrix} \qquad \begin{Bmatrix} M_x \\ M_y \\ M_{xy} \end{Bmatrix} = \begin{bmatrix} D_{11} & D_{12} & D_{16} \\ D_{12} & D_{22} & D_{26} \\ D_{16} & D_{26} & D_{66} \end{bmatrix} \begin{Bmatrix} \kappa_x \\ \kappa_y \\ \kappa_{xy} \end{Bmatrix} , \qquad (1.1)$$

where N_i and M_i are the membrane and bending stress resultants, respectively, ε_x^o, ε_y^o, and γ_{xy}^o are the reference surface strains, κ_x, κ_y, and κ_{xy} are the curvatures at the reference surface, and A_{ij} and D_{ij} are the membrane and bending stiffnesses, respectively. Equation (1.1) can be expressed in inverted form as

$$\begin{Bmatrix} \varepsilon_x^o \\ \varepsilon_y^o \\ \gamma_{xy}^o \end{Bmatrix} = \begin{bmatrix} a_{11} & a_{12} & a_{16} \\ a_{12} & a_{22} & a_{26} \\ a_{16} & a_{26} & a_{66} \end{bmatrix} \begin{Bmatrix} N_x \\ N_y \\ N_{xy} \end{Bmatrix} \qquad \begin{Bmatrix} \kappa_x \\ \kappa_y \\ \kappa_{xy} \end{Bmatrix} = \begin{bmatrix} d_{11} & d_{12} & d_{16} \\ d_{12} & d_{22} & d_{26} \\ d_{16} & d_{26} & d_{66} \end{bmatrix} \begin{Bmatrix} M_x \\ M_y \\ M_{xy} \end{Bmatrix} , \qquad (1.2)$$

where $[a] = [A]^{-1}$ and $[d] = [D]^{-1}$, and a_{ij} and d_{ij} are the laminate membrane and bending compliances, respectively. The A_{16}, A_{26}, a_{16}, and a_{26} terms represent coupling between the inplane extensional and shear strains. For a balanced laminate, these coupling terms are equal to zero. The D_{16}, D_{26}, d_{16}, and d_{26} terms represent coupling between the out-of-plane bending and twisting curvatures. For orthotropic laminates (lamina oriented at 0° and 90° only), these terms are equal to zero.

Stiffness coupling can cause a structure to display unusual displacements when deformed. If these unusual displacements are constrained, then unusual restraining forces are generated. First consider coupling of the membrane stiffnesses, then consider coupling of the bending stiffnesses.

1.1.1 Membrane Stiffness Coupling

Consider a laminated composite rectangular plate with no membrane stiffness coupling, i.e., $A_{16} = A_{26} = a_{16} = a_{26} = 0$, loaded by a tensile load in the x-direction only, as shown in Fig. 1-1(a). In the absence of membrane stiffness coupling, the membrane stress-strain relations are given by

$$\begin{Bmatrix} \varepsilon_x^o \\ \varepsilon_y^o \\ \gamma_{xy}^o \end{Bmatrix} = \begin{bmatrix} a_{11} & a_{12} & 0 \\ a_{12} & a_{22} & 0 \\ 0 & 0 & a_{66} \end{bmatrix} \begin{Bmatrix} N_x \\ N_y \\ N_{xy} \end{Bmatrix} \quad . \tag{1.3}$$

If $N_x = (N_x)_{applied}$, and N_y and $N_{xy} = 0$, then Eq. (1.3) reduces to

$$\begin{Bmatrix} \varepsilon_x^o \\ \varepsilon_y^o \\ \gamma_{xy}^o \end{Bmatrix} = \begin{bmatrix} a_{11} & a_{12} & 0 \\ a_{12} & a_{22} & 0 \\ 0 & 0 & a_{66} \end{bmatrix} \begin{Bmatrix} (N_x)_{applied} \\ 0 \\ 0 \end{Bmatrix} \quad , \tag{1.4}$$

or

$$\varepsilon_x^o = a_{11}(N_x)_{applied} \qquad \varepsilon_y^o = a_{12}(N_x)_{applied} \qquad \gamma_{xy}^o = 0 \quad . \tag{1.5}$$

The equivalent membrane Poisson's ratio ν_{xy}^o for the laminate is defined as

$$\nu_{xy}^o = \frac{-\varepsilon_y^o}{\varepsilon_x^o} = \frac{-a_{12}}{a_{11}} \quad . \tag{1.6}$$

That $\gamma_{xy}^{o} = 0$ is a direct result of the coupling term a_{16} being identically equal to zero. The undeformed and deformed configurations for this case are shown in Fig. 1-1(a).

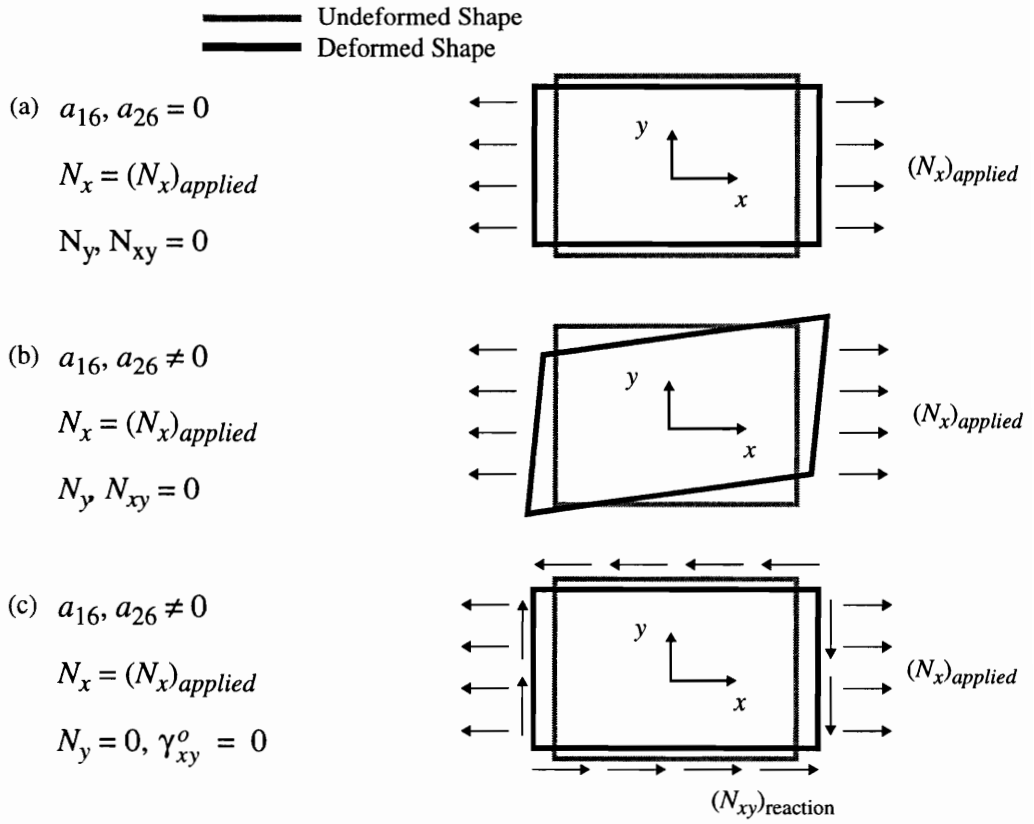

Fig. 1-1 Rectangular plate with membrane stiffness coupling, $N_x = (N_x)_{applied}$

If membrane stiffness coupling is introduced, a_{16} and a_{26} are nonzero and the membrane stress-strain relations are given by

$$\begin{Bmatrix} \varepsilon_x^o \\ \varepsilon_y^o \\ \gamma_{xy}^o \end{Bmatrix} = \begin{bmatrix} a_{11} & a_{12} & a_{16} \\ a_{12} & a_{22} & a_{26} \\ a_{16} & a_{26} & a_{66} \end{bmatrix} \begin{Bmatrix} N_x \\ N_y \\ N_{xy} \end{Bmatrix} \quad . \tag{1.7}$$

If $N_x = (N_x)_{applied}$, and N_y and $N_{xy} = 0$, then Eq. (1.7) reduces to

$$\begin{Bmatrix} \varepsilon_x^o \\ \varepsilon_y^o \\ \gamma_{xy}^o \end{Bmatrix} = \begin{bmatrix} a_{11} & a_{12} & a_{16} \\ a_{12} & a_{22} & a_{26} \\ a_{16} & a_{26} & a_{66} \end{bmatrix} \begin{Bmatrix} (N_x)_{applied} \\ 0 \\ 0 \end{Bmatrix} , \tag{1.8}$$

or

$$\varepsilon_x^o = a_{11}(N_x)_{applied} \qquad \varepsilon_y^o = a_{12}(N_x)_{applied} \qquad \gamma_{xy}^o = a_{16}(N_x)_{applied} . \tag{1.9}$$

The equivalent membrane Poisson's ratio ν_{xy}^o for the laminate is defined as

$$\nu_{xy}^o = \frac{-\varepsilon_y^o}{\varepsilon_x^o} = \frac{-a_{12}}{a_{11}} . \tag{1.10}$$

A nonzero shear strain is created when only an axial stress resultant is applied. The equivalent membrane coefficient of mutual influence $\eta_{xy,x}^o$ is defined as the ratio of the shear strain to the axial strain, or

$$\eta_{xy,x}^o = \frac{\gamma_{xy}^o}{\varepsilon_x^o} = \frac{a_{16}}{a_{11}} . \tag{1.11}$$

The undeformed and deformed configurations for this case are shown in Fig. 1-1(b).

If the same laminate has $N_x = (N_x)_{applied}$ and $N_y = 0$ and the shear deformation is restrained, i.e., $\gamma_{xy}^o = 0$, then a shear stress resultant reaction $(N_{xy})_{reaction}$ is created. For this case Eq. (1.7) reduces to

$$\begin{Bmatrix} \varepsilon_x^o \\ \varepsilon_y^o \\ 0 \end{Bmatrix} = \begin{bmatrix} a_{11} & a_{12} & a_{16} \\ a_{12} & a_{22} & a_{26} \\ a_{16} & a_{26} & a_{66} \end{bmatrix} \begin{Bmatrix} (N_x)_{applied} \\ 0 \\ (N_{xy})_{reaction} \end{Bmatrix} . \tag{1.12}$$

Specifically,

$$(N_{xy})_{reaction} = \frac{-a_{16}}{a_{66}}(N_x)_{applied} = -\eta_{xy,x}^o (N_x)_{applied} . \tag{1.13}$$

The undeformed and deformed configurations for this case are shown in Fig. 1-1(c).

1.1.2 Bending Stiffness Coupling

Consider a laminated composite rectangular plate with no bending stiffness coupling, i.e., $D_{16} = D_{26} = d_{16} = d_{26} = 0$, loaded only by the bending moment resultant M_x as shown in Fig. 1-2(a). In the absence of bending stiffness coupling, the moment-curvature relations are given by

$$\begin{Bmatrix} \kappa_x \\ \kappa_y \\ \kappa_{xy} \end{Bmatrix} = \begin{bmatrix} d_{11} & d_{12} & 0 \\ d_{12} & d_{22} & 0 \\ 0 & 0 & d_{66} \end{bmatrix} \begin{Bmatrix} M_x \\ M_y \\ M_{xy} \end{Bmatrix} \quad . \tag{1.14}$$

If $M_x = (M_x)_{applied}$, and M_y and $M_{xy} = 0$, then Eq. (1.14) reduces to

$$\begin{Bmatrix} \kappa_x \\ \kappa_y \\ \kappa_{xy} \end{Bmatrix} = \begin{bmatrix} d_{11} & d_{12} & 0 \\ d_{12} & d_{22} & 0 \\ 0 & 0 & d_{66} \end{bmatrix} \begin{Bmatrix} (M_x)_{applied} \\ 0 \\ 0 \end{Bmatrix} \quad , \tag{1.15}$$

or

$$\kappa_x = d_{11}(M_x)_{applied} \qquad \kappa_y = d_{12}(M_x)_{applied} \qquad \kappa_{xy} = 0 \quad . \tag{1.16}$$

As indicated in Eqs. (1.16), simple bending of a flat plate causes curvature in two directions. The top surface of the plate is in tension in the x-direction and has Poisson contraction in the y-direction. The bottom surface of the plate is in compression in the x-direction and has Poisson expansion in the y-direction. The through-the-thickness variation of ε_y translates into a nonzero value of κ_y and results in a saddle-shaped deformation. This is sometimes referred to as the anticlastic effect. The undeformed and deformed configurations for this case are shown in Fig. 1-2(a). That $\kappa_{xy} = 0$ is a direct result of the coupling term d_{16} being identically equal to zero. The equivalent flexural Poisson's ratio ν_{xy}^f for the laminate is defined as

$$\nu_{xy}^f = \frac{-\kappa_y}{\kappa_x} = \frac{-d_{12}}{d_{11}} \quad . \tag{1.17}$$

If bending stiffness coupling is introduced, d_{16} and d_{26} are nonzero and the bending moment-curvature relations are given by

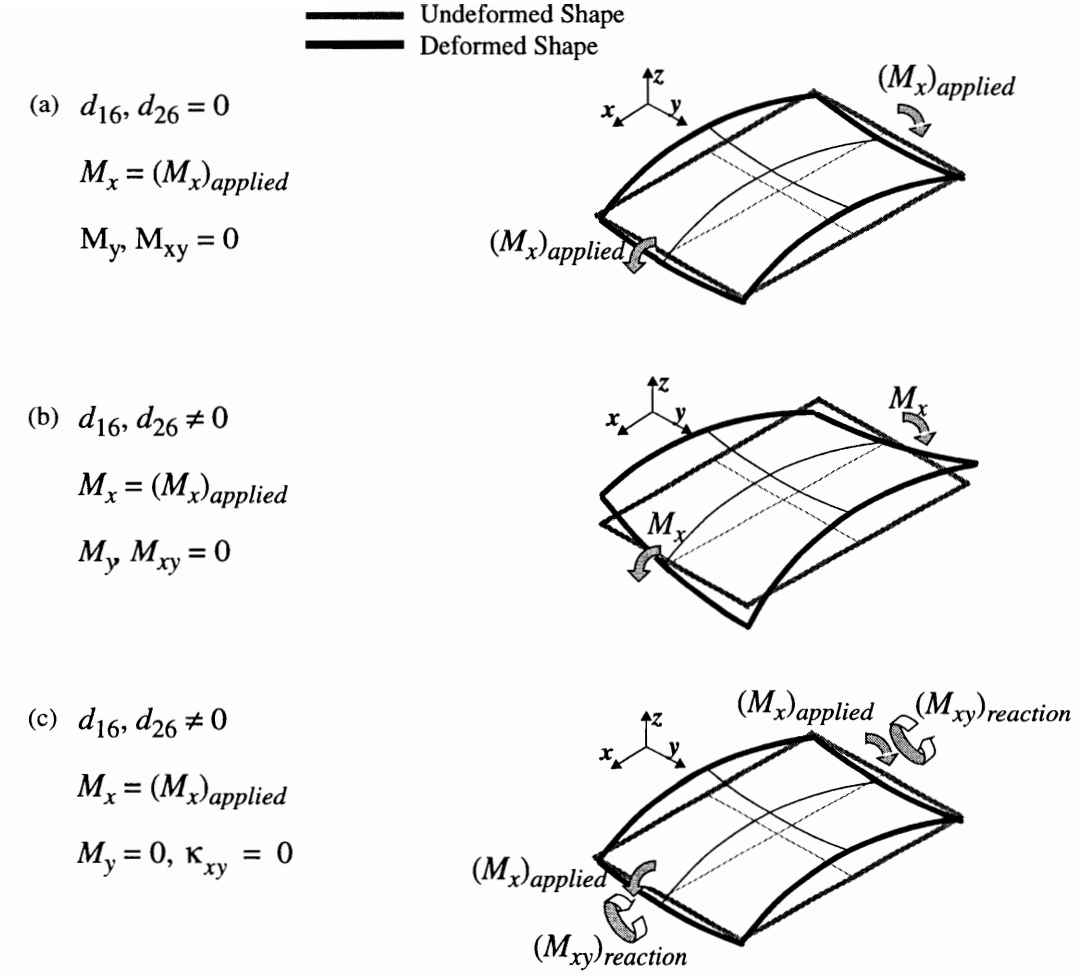

Fig. 1-2 Rectangular plate with bending stiffness coupling, $M_x = (M_x)_{applied}$

$$\begin{Bmatrix} \kappa_x \\ \kappa_y \\ \kappa_{xy} \end{Bmatrix} = \begin{bmatrix} d_{11} & d_{12} & d_{16} \\ d_{12} & d_{22} & d_{26} \\ d_{16} & d_{26} & d_{66} \end{bmatrix} \begin{Bmatrix} M_x \\ M_y \\ M_{xy} \end{Bmatrix} \quad . \tag{1.18}$$

If $M_x = (M_x)_{applied}$, and M_y and $M_{xy} = 0$, then Eq. (1.18) reduces to

$$\begin{Bmatrix} \kappa_x \\ \kappa_y \\ \kappa_{xy} \end{Bmatrix} = \begin{bmatrix} d_{11} & d_{12} & d_{16} \\ d_{12} & d_{22} & d_{26} \\ d_{16} & d_{26} & d_{66} \end{bmatrix} \begin{Bmatrix} (M_x)_{applied} \\ 0 \\ 0 \end{Bmatrix} \quad . \tag{1.19}$$

or

$$\kappa_x = d_{11}(M_x)_{applied} \qquad \kappa_y = d_{12}(M_x)_{applied} \qquad \kappa_{xy} = d_{16}(M_x)_{applied} \quad .(1.20)$$

The equivalent flexural Poisson's ratio ν_{xy}^f for the laminate is defined as

$$\nu_{xy}^f = \frac{-\kappa_y}{\kappa_x} = \frac{-d_{12}}{d_{11}} \quad . \tag{1.21}$$

A nonzero twisting curvature is created when only an M_x bending stress resultant is applied. The equivalent flexural coefficient of mutual influence $\eta_{xy,\,x}^f$ is defined as the ratio of the twisting curvature to the axial bending curvature, or

$$\eta_{xy,\,x}^f = \frac{\kappa_{xy}}{\kappa_x} = \frac{d_{16}}{d_{11}} \quad . \tag{1.22}$$

The undeformed and deformed configurations for this case are shown in Fig. 1-2(b).

If the same laminate has $M_x = (M_x)_{applied}$ and $M_y = 0$ and the twisting rotation is restrained, i.e., $\kappa_{xy} = 0$, then a twisting moment stress resultant reaction $(M_{xy})_{reaction}$ is created. For this case Eq. (1.18) reduces to

$$\begin{Bmatrix} \kappa_x \\ \kappa_y \\ \kappa_{xy} \end{Bmatrix} = \begin{bmatrix} d_{11} & d_{12} & d_{16} \\ d_{12} & d_{22} & d_{26} \\ d_{16} & d_{26} & d_{66} \end{bmatrix} \begin{Bmatrix} (M_x)_{applied} \\ 0 \\ (M_{xy})_{reaction} \end{Bmatrix} \quad , \tag{1.23}$$

and solution leads to

$$(M_{xy})_{reaction} = \frac{-d_{16}}{d_{66}}(M_x)_{applied} = -\eta_{xy,\,x}^f (M_x)_{applied} \quad . \tag{1.24}$$

The undeformed and deformed configurations for this case are shown in Fig. 1-2(c).

Bending stiffness coupling can cause skewing of out-of-plane deformations. To demonstrate this skewing, consider the buckling deformations of two rectangular plates that are loaded in compression, with clamped boundary conditions on the loaded top and bottom edges and simple supports on the sides. A contour plot of the out-of-plane buckling deformation for a plate that does not have any bending stiffness coupling is shown in Fig. 1-3(a).

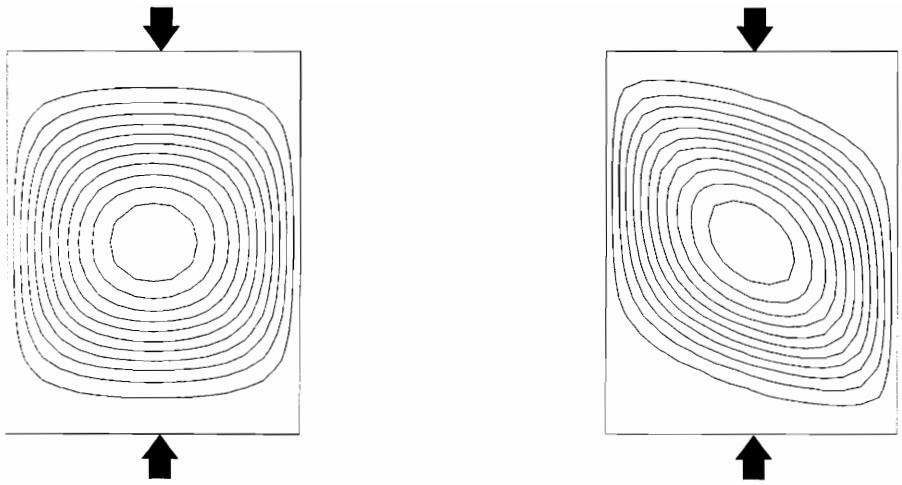

(a) $d_{16}, d_{26} = 0$ (b) $d_{16}, d_{26} \neq 0$

Fig. 1-3 Skewing of buckling deformations caused by bending stiffness coupling

The contour plot shows that the out-of-plane deformation for this plate is symmetric with respect to the vertical and horizontal center lines. A contour plot of the out-of-plane buckling deformation for a plate that has substantial bending stiffness coupling is shown in Fig. 1-3(b). The bending stiffness coupling causes bending and twisting curvatures in the buckling deformation, and the out-of-plane deformation of the plate is skewed.

1.1.3 Stiffness Coupling of Built-Up Structures

The previous discussion has addressed stiffness coupling of thin plates. Section A.6 demonstrates that the stiffness of a structure that is formed by joining thin plates is most easily influenced by tailoring the membrane stiffness of the subcomponents. To study this, consider a box beam with bending load applied as shown in Fig. 1-4. Assume that the upper and lower face sheets have membrane stiffness coupling such that $a_{16} > 0$. The bending load on the box beam causes the upper face sheet, Skin(2), to be loaded in tension, i.e., $(N_x)^{\text{Skin(2)}} > 0$. Applying these conditions to Eq. (1.9), the shear strain in the Skin(2) is positive and Skin(2) deforms as shown in the top portion of Fig. 1-4(b). This deformation is consistent with the behavior previously displayed in Fig. 1-1(b). Conversely, the bending load on the box beam causes the lower face sheet, Skin(1), to be loaded in compression, i.e., $(N_x)^{\text{Skin(1)}} < 0$. The shear strain in the Skin(1) is negative and Skin(1) deforms as shown in the lower portion of Fig. 1-4(b). With the upper and lower face sheets shearing in opposite directions, the net result is that the box beam twists when subjected to a simple bending load, $(M_x)^{\text{box}}$, as shown in Fig. 1-4(c).

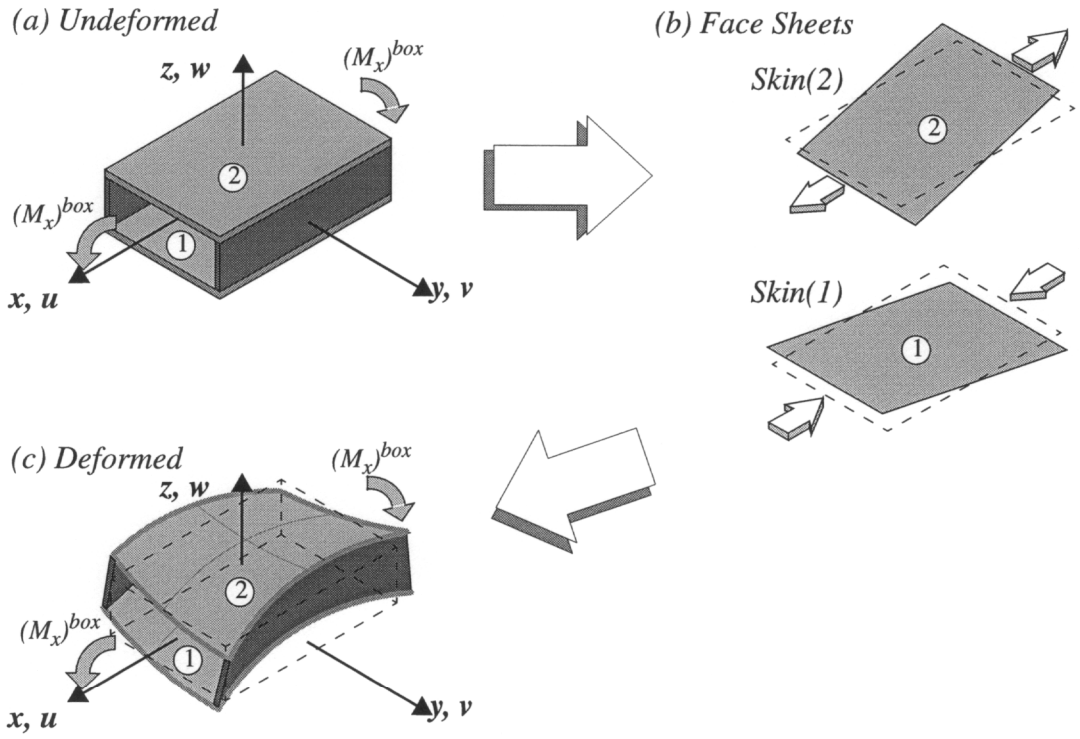

Fig. 1-4 Deformation of box beam with tailored face sheets under simple bending

1.1.4 Tailoring of Laminate Membrane and Bending Stiffnesses

The membrane and bending stiffnesses of a laminate are functions of the material properties and orientation of each lamina forming the laminate. To demonstrate how the membrane and bending stiffnesses can vary for different laminates, several examples are considered below. The laminates considered are assumed to be constructed from Hercules, Inc. AS4-3502 graphite-epoxy unidirectional preimpregnated tape. Nominal lamina elastic properties for this graphite-epoxy system are given in Table 1-1. In each example a baseline laminate stacking sequence is defined. The baseline laminate is then rotated by an angle β about the laminate's normal, such that the principal direction of inplane orthotropy of the laminate is no longer aligned with the *x*-*y* coordinate axes, as shown in Fig. 1-5. For instance, a baseline $[\pm 45/0/90]_s$ laminate with $\beta = 20°$ is equivalent to a $[65/-25/20/-70]_s$ laminate. For each baseline laminate, membrane and bending stiffnesses are presented by plotting equivalent engineering constants as β is varied from 0° to

Table 1-1 Typical Material Properties: Hercules AS4-3502 Graphite-Epoxy[3]

E_1	19.40 Msi
E_2	1.48 Msi
G_{12}	0.82 Msi
ν_{12}	0.30
V_f	0.62 (Ref. 4)
t_{ply}	0.0055 in.

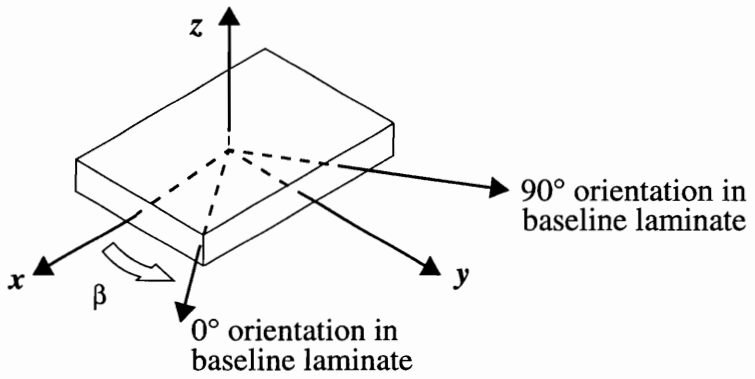

Fig. 1-5 Entire baseline laminate rotated β from *x*-*y*-*z* geometric coordinate axes

90°. In each plot, the equivalent engineering moduli defined in Section A.5 are normalized by the moduli for 2024-T3 aluminum alloy (E_{Al} = 10.50 Msi, G_{Al} = 3.95 Msi). The moduli E_x^o and E_x^f, where o and f indicate inplane and bending, respectively, are divided by E_{Al}, and G_{xy}^o and G_{xy}^f are divided by G_{Al}. This normalization is done to permit comparison of the extensional and shear moduli on a single figure, while scaling the results relative to an aluminum plate of the same thickness. Note that comparing the stiffness of composite and aluminum plates of equal thickness does not reflect the difference in weight density between the materials. Also, structural stability is difficult to quantify by considering the equivalent engineering constants only. The following examples are included to demonstrate stiffness tailoring, and should not be extended to quantify structural efficiency.

Unidirectional Laminate $[0]_{16}$ Rotated by β

For a laminate composed of 16 layers, all having the same orientation, A_{ij} and D_{ij} vary exactly as $\overline{Q}_{ij}$. Figure 1-6 shows how the equivalent engineering constants for a $[0]_{16}$ laminate vary when the laminate is rotated from β = 0° to β = 90°. Since this laminate is

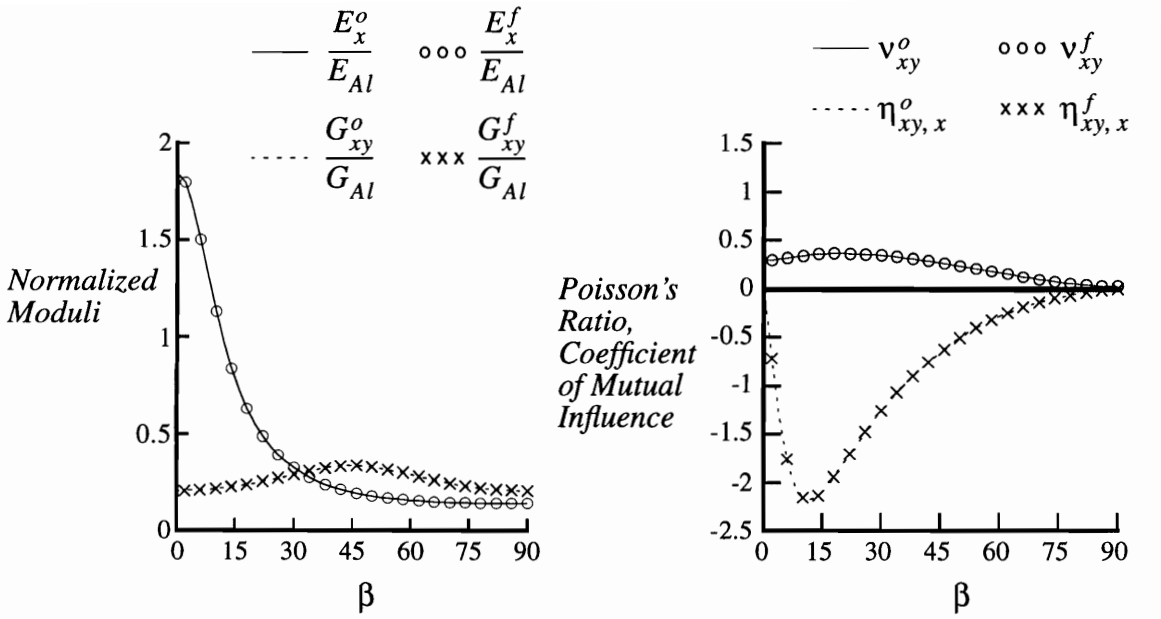

Fig. 1-6 Equivalent engineering constants for unidirectional laminate $[0]_{16}$ rotated by β

uniform through the thickness, the membrane and flexural equivalent engineering constants are equal. The moduli E_x^o and E_x^f have a large value for β near zero, but decrease quickly when β increases from zero. The moduli G_{xy}^o and G_{xy}^f have a small value for all values of β and are largest at β = 45°. The coefficients of mutual influence $\eta_{xy,x}^o$ and $\eta_{xy,x}^f$ are equal to zero for β = 0° and 90°, but are large compared to Poisson's ratios ν_{xy}^o and ν_{xy}^f for intermediate angles, reaching maximum magnitudes when β = 12°.

Orthotropic Laminate, with Alternating Lamina Orientations, Rotated by β

Figure 1-7 shows how the equivalent engineering constants for a $[0/90]_{4s}$ laminate vary when the laminate is rotated from β = 0° to β = 90°. The stacking sequence prescribes that the baseline laminate is assembled with alternating 0° and 90° lamina, with minimal clustering of lamina of the same orientation. Alternating the lamina orientations causes the equivalent membrane and flexural engineering constants to be nearly equal. The baseline laminate has an equal number of lamina in the 0° and 90° directions, giving $E_x^o(0°) = E_x^o(90°)$ and an E_x^o that is a minimum when β = 45°. The moduli G_{xy}^o and G_{xy}^f are a minimum for β = 0° and 90°, and are large when β = 45°. Poisson's ratios ν_{xy}^o and ν_{xy}^f are almost equal to zero for β = 0° and 90°, but are quite substantial for intermediate values of β. The coefficient of mutual influence $\eta_{xy,x}^o$ is equal to zero for β = 0°, 45°, and 90°. The

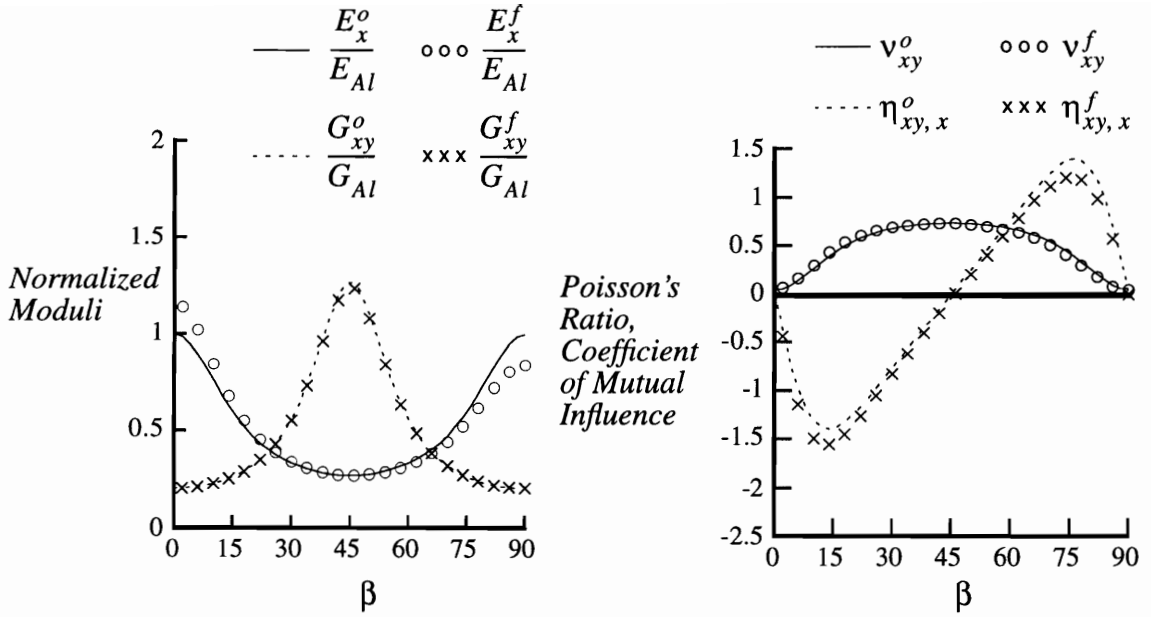

Fig. 1-7 Equivalent engineering constants for orthotropic laminate $[0/90]_{4s}$ rotated by β

coefficient of mutual influence $\eta^f_{xy,x}$ is equal to zero for β = 0° and 90°, and has a small nonzero value at β = 45°. For intermediate values of β, both coefficients of mutual influence $\eta^o_{xy,x}$ and $\eta^f_{xy,x}$ can become quite large, obtaining maximum negative and positive values when β = 12° and 78°, respectively.

Orthotropic Laminate, with Lamina of the Same Orientation in Groups of Four, Rotated by β

Figure 1-8 shows how the equivalent engineering constants for a $[0_4/90_4]_s$ laminate vary when the laminate is rotated from β = 0° to β = 90°. This baseline laminate is similar to the $[0/90]_{4s}$ laminate of the previous example, except that the stacking sequence prescribes that lamina of the same orientation are grouped together. In Eq. (A.31) the expression for A_{ij} is expressed as a summation of the product of $\bar{Q}_{ij}$ times the thickness for each lamina. This simple summation indicates that A_{ij} is not sensitive to the stacking sequence, i.e., the order in which the laminae are assembled. Thus, the membrane equivalent engineering constants E^o_x, G^o_{xy}, ν^o_{xy}, and $\eta^o_{xy,x}$ are unchanged from the previous example.

In Eq. (A.31) D_{ij} is defined as the through-the-thickness integral of the product $\bar{Q}_{ij}z^2$. Unlike the simple summation in A_{ij}, the contribution of each lamina to D_{ij} for the laminate is weighted by the square of the z-location of the lamina. This weighting makes D_{ij} sensi-

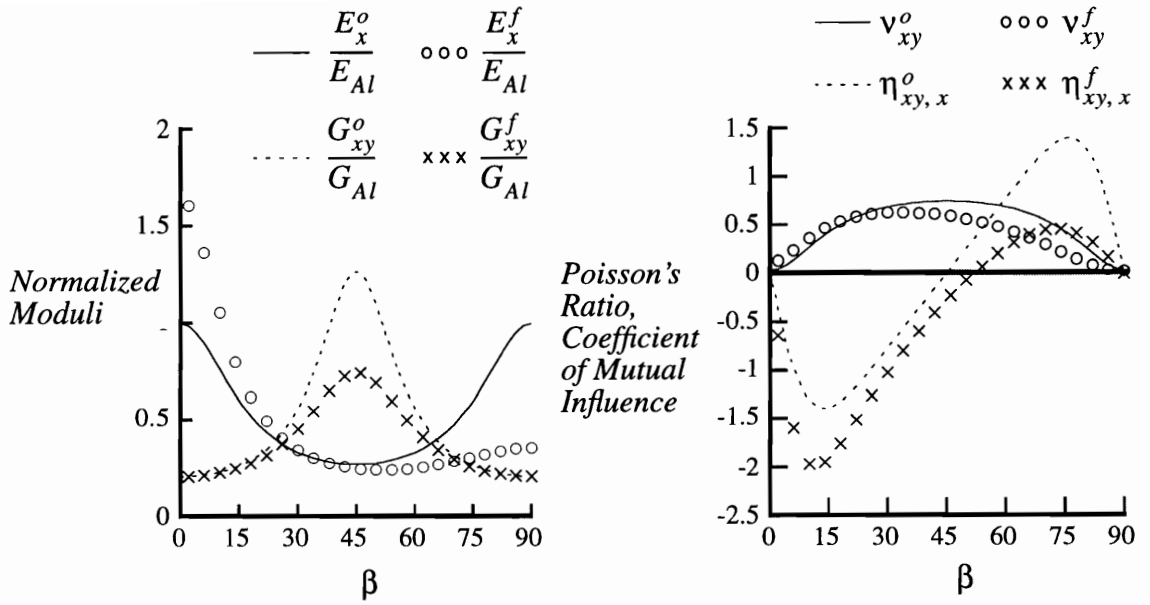

Fig. 1-8 Equivalent engineering constants for orthotropic laminate $[0_4/90_4]_s$ rotated by β

tive to the stacking sequence. In this baseline laminate grouping the four 0° laminae and locating them further from the reference surface gives the 0° laminae greater weight than the 90° laminae when contributing to D_{ij}. The equivalent engineering constants for flexure differ from those obtained for the $[0/90]_{4s}$ laminate. As a result of grouping $E_x^f(0°)$ is much larger than $E_x^f(90°)$, and G_{xy}^f is substantially reduced when β = 45°. Grouping of layers also causes the relationship for the flexural coefficient of mutual influence $\eta_{xy,x}^f$ to be shifted in the negative direction relative to the relationship for $\eta_{xy,x}^f$ for the $[0/90]_{4s}$ laminate.

Practical Structural Laminate Rotated by β

Figure 1-9 shows how the equivalent engineering constants for a $[\pm 45/\mp 45/0_3/90]_s$ laminate vary for values of β from 0° to 90°. This laminate satisfies the rule-of-thumb guideline established by some aircraft manufacturers which requires that laminates have a minimum of four fiber orientations with at least 10% of the laminae in each direction. This rule-of-thumb was created to minimize the presence of structural response and failure mechanisms that are difficult to understand and predict. Unfortunately, this rule-of-thumb also restricts the amount of structural tailoring available to a designer. Several observations can be made by comparing the equivalent engineering constants for a

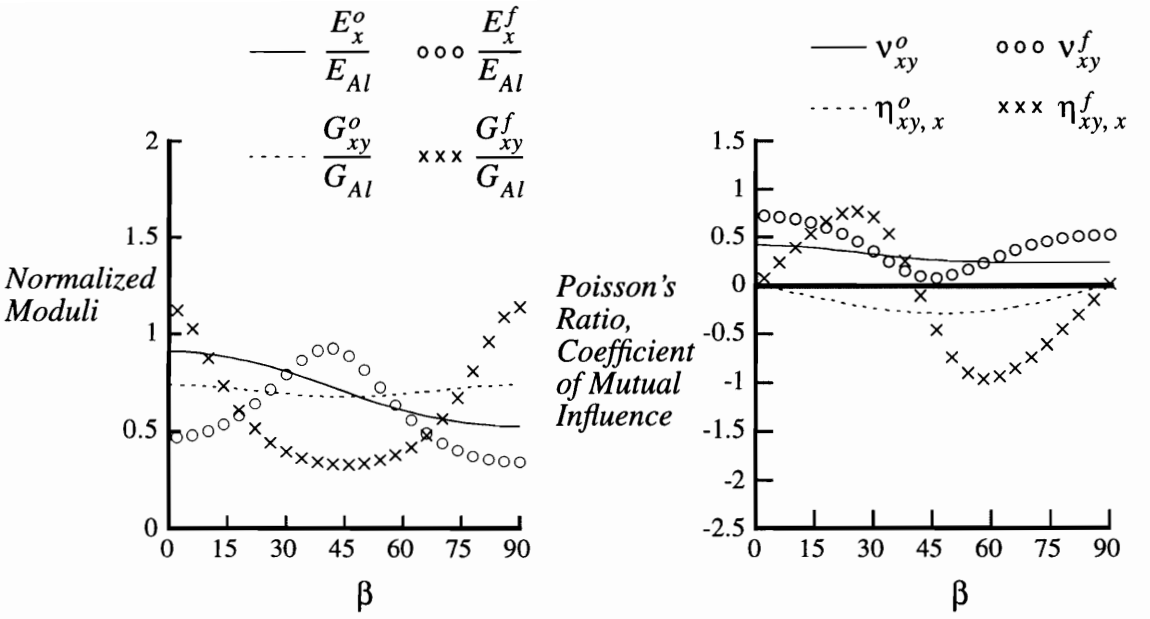

Fig. 1-9 Equivalent engineering constants for laminate $[\pm 45/\mp 45/0_3/90]_s$ rotated by β

$[\pm 45/\mp 45/0_3/90]_s$ laminate shown in Fig. 1-9 with those for the other laminates shown in Figs. 1-6 to 1-8. In general, the equivalent engineering constants for a $[\pm 45/\mp 45/0_3/90]_s$ laminate are less sensitive to the laminate orientation, β. Since this laminate has layers in more directions, it is more likely that a laminate orientation which reduces the stiffness of one layer also increases the stiffness of another layer, thus causing a smoothing effect. Compared to other laminates, the equivalent moduli vary less dramatically with changes in β, and the stiffness couplings as reflected by the coefficients of mutual influence are much smaller. The $[\pm 45/\mp 45/0_3/90]_s$ laminate also differs from the other laminates in that the membrane equivalent engineering constants of this laminate show no correlation with the flexural equivalent engineering constants. In the $[\pm 45/\mp 45/0_3/90]_s$ laminate the membrane stiffness is dominated by the 0° layers, while the flexural stiffness is dominated by the ±45° layers because they are further from the laminate midplane.

With some of the basic principles of elastic coupling and structural tailoring addressed, attention is turned to a review of literature that is relevant to the prebuckling and postbuckling response of stiffened composite panels with anisotropic skins and skewed stiffeners.

1.2 Literature Review

Structural tailoring of stiffened panels has been used for over 40 years to address practical aircraft design issues. The predominant application of structural tailoring to date has been in the area of aeroelastic tailoring. This literature review opens by first describing the development of structural tailoring of stiffened panels, beginning with metallic structures, and then showing how the introduction of composite materials affected design practices. Previous studies are cited which describe stiffened panel designs which employed skewed stiffeners or anisotropic skins to create membrane stiffness coupling in wing cover panels to induce bending stiffness coupling in wing structures. The literature review then presents studies which considered nonorthogonal stiffeners, outside the context of structural tailoring. Up to this point in the review, all of the literature is limited to buckling-resistant designs. The remainder of the review presents material to support extension of stiffness tailoring in the postbuckling response range. This material addresses analytical and experimental work in the area of postbuckling of unstiffened and stiffened laminated composite shells.

1.2.1 Structural Tailoring of Stiffened Panels

Previous studies in structural tailoring which utilize stiffness coupling in stiffened panels have been limited exclusively to aeroelastic tailoring applications. It is important to note that aeroelastic tailoring is only one possible application of structural tailoring, and that the current study is not intended to solely address aeroelastic tailoring. With this in mind, the following discussion is presented to describe the development and current state of structural tailoring design practices.

A survey article[5] published in 1986 presents the historical background of aeroelastic tailoring, the theory underlying the technology, a summary of trend studies that have been performed, and a list of 89 references on the topic. In this reference aeroelastic tailoring is defined as "the embodiment of directional stiffness into an aircraft structural design to control aeroelastic deformation, static or dynamic, in such a fashion as to affect the aerodynamic and structural performance of that aircraft in a beneficial way." Some of the papers reviewed as a result of the above survey article, plus papers found independent of the survey article, are discussed below.

The earliest documented use of stiffness tailoring was in 1949 when Munk patented a

wooden propeller design which utilized the directional properties of fibrous wood to cause the propeller blades to twist favorably as the thrust increased. In the same time period, emphasis on the use of rear-swept or forward-swept wings for high-speed flight created increased interest in the aeroelastic behavior of swept wings. Simple flexure of a swept wing induces twisting curvature about an axis normal to the direction of flight. In rear-swept wings, this twisting curvature produces a forward rotation of the wing cross section parallel to the direction of flight, thus reducing the local angle of attack. This effect, known as "wash out", reduces the aerodynamic lift. Conversely, in forward-swept wings this twisting curvature produces an increase in the local angle of attack, "wash in", which increases the aerodynamic lift. Greater lift causes greater flexure, which causes more "wash in", causing greater lift. Above a critical speed, termed the divergence speed, an instability phenomenon results as the aerodynamic forces predominate over the restraining structural forces, causing deformations to increase until structural failure occurs. In 1948 Diederick and Budiansky[6] examined "bending-torsion" divergence of swept wings and identified a drastic drop in divergence speed with forward sweep.

In 1949 Mansfield[7] recognized that swept wings will likely have ribs that are not at right angles to the stringers, thereby causing skewness in the structural geometry that would induce bend-twist stiffness coupling. A general theory was developed to depict the elastic behavior of a conventional single-cell wing stiffened with swept ribs (or stringers). In 1952 Mansfield[8] extended his earlier work to show that a conventional two-spar single-cell structure with swept stringers could be designed to maintain a constant angle of attack along the span despite flexural distortion.

The research activity of the 1950's was followed by nearly a 20 year lapse of interest in structural tailoring. Around 1970 the birth of modern composite materials spurred a renewed interest in structural tailoring. The directional properties of composite materials could be applied to provide a significant level of anisotropy to induce coupling between bending and twisting deformations. As discussed in Ref. 5, General Dynamics released the TSO computer program in 1972. This program applied the unique properties of composite materials in the aeroelastic and strength optimization of aircraft lifting surfaces.

Early research applications for composites in structural tailoring involved flutter suppression. In 1972 Soong[9] considered a built-up NACA delta-wing modeled with beam-type members, and layered anisotropic plates. Soong concluded that "flutter speed is increased when spars, stiffeners, and major stiffness direction of plates are made to be par-

allel to, or more swept back than, the leading edge of the wing." Also in 1972, Cooper and Stroud[10] investigated selective reinforcement of wing structure for flutter prevention by bonding patches of composite material to the skin of a metallic delta-wing. In 1974, Housner and Stein[11] reported flutter analysis of rear-swept wings with balanced composite skins. Varying only the ply orientation of symmetrical cross-ply laminates, bend-twist coupling stiffness was not introduced.

In 1975 Rockwell International was selected to design a highly maneuverable advanced technology (HiMAT) remotely piloted research aircraft. The design employed composite materials to tailor the stiffness of the canard and wing skins in order to modify twist, providing additional performance in transonic maneuverability. The design methodology employed is documented in Ref. 12.

In 1977 Gratke and Williams[13] showed that the twist due to flexure of a rear-swept metallic wing could be influenced through substructure orientation. Gratke and Williams investigated four substructure arrangements for a 35 degree rear-swept wing and showed that selected rearrangement of the wing substructure could advantageously influence the wing twist due to flexure, and increase performance without increasing weight or cost.

In 1979 Gimmestad[14] presented a computer code for aeroelastic optimization of a composite high-aspect-ratio wing. The wing structure was modeled as a composite box beam with anisotropic beam bend-twist stiffness coupling effects included, and aeroelastic loads, jig shape, stability, and flutter were considered. To demonstrate the computer code, Gimmestad presented the results of an aeroelastic design study of a high-aspect-ratio wing which was rear-swept 35°. Two materials were considered. The first was a graphite-epoxy composite material with the wing covers made of a $[0_2/\pm 45/90]$ laminate. Bend-twist stiffness coupling was obtained by rotating the entire lay-up of the cover panels -20°, -10°, 0°, and 10° relative to the wing elastic axis. The second material considered was 7075-T6 aluminum alloy. The wing cover panels were stiffened with stringers and were modeled using smeared stringer theory. A baseline configuration had the stringers parallel to the elastic axis. Anisotropy was obtained by rotating the stringers -45°, -20°, -5°, and 20° relative to the elastic axis. For each configuration aeroelastic and flutter analyses were conducted, with results showing some of the effects of anisotropy on the aeroelasticity of a high-aspect-ratio wing. Gimmestad concluded that anisotropic effects created by rotating stringers in a metallic structure are similar to those in composite structures, although the benefits were not as pronounced. Gimmestad's conclusion that the benefits are not as pro-

nounced does not seem to be supported by the results presented in the reference.

In 1975 Krone[15] presented landmark results demonstrating the use of materially tailored wing skins to eliminate divergence of swept-forward airfoils, overcoming the severe weight penalty encountered in the conventional metallic designs. These results renewed interest in the swept-forward wing concept. Weishaar[16] extended Krone's work in 1979, again tailoring laminated composite wing skins to induce bend-twist stiffness coupling, thereby precluding divergence of swept-forward wings. In this work more attention is given to identifying the mechanisms of bend-twist stiffness coupling and divergence suppression. In 1981 Sherrer, et al.[17] conducted low-speed wind tunnel tests to provide experimental data illustrating the above findings. In 1984 aeroelastic tailoring was posed as a multivariable optimization problem by Oyibo.[18]

Reviewing the above references, it is noted that structural tailoring of metallic structures was achieved by modifying the location and orientation of internal beam-like components. With the introduction of composite materials, this concept was abandoned in favor of tailoring the laminated cover skin. It is important to note that the above references have imposed common assumptions when developing analytical models. The following assumptions were made regarding the structure:

1. stress-strain relations were linear;
2. there was no buckling of the skin;
3. in most cases, stringers were smeared into equivalent stringer-sheets which carried only end loads.

1.2.2 Arbitrarily Oriented Stiffeners (Not Skewed to Obtain Stiffness Coupling)

In the review of structural tailoring of stiffened panels, it was noted that Mansfield[7,8], Soong[9], and Gimmestad[14] examined skewing the stringers and ribs at particular orientations in order to obtain stiffness coupling. The current section of the review presents work in which stiffeners had arbitrary orientations, and stiffness coupling was not considered.

In 1976 Shastry and Rao[19] presented a finite element vibration analysis of isotropic plates with arbitrarily oriented stiffeners. The purpose of this work was to measure the reliability and precision of the beam and triangular plate elements used in the stiffened plate analysis.

In 1986 Al-Shareedah and Seireg[20] studied isotropic plates with arbitrarily oriented stiff-

eners loaded by transverse pressure. Their analysis followed a generic energy formulation, and applied the undetermined multipliers method to attach the stiffeners to the plate at discrete points. This method was applied by Phillips and Gürdal[21] in 1990 to analyze and optimize geodesically stiffened composite panels. Phillips considered inplane loading of orthotropic plates with rotated balanced stiffeners. Balanced stiffener configurations have equal numbers of stiffeners at $+\theta$ and $-\theta$ orientations. Thus, no axial-shear stiffness coupling is generated.

In 1990 Won[22] presented an analysis for an isotropic plate stiffened with arbitrarily oblique and equally spaced eccentric stiffeners, loaded by transverse pressure. Won followed an energy formulation, smearing the effect of the stiffeners over the plate. Won's contribution was to include the joint stiffness of intersecting stiffeners in the smeared stiffness.

All of the references found used only linear strain displacement relations.

1.2.3 Buckling and Postbuckling

Reference 23, by Becker, is an example of an early design handbook for isotropic stiffened panels. Becker addressed local buckling of stiffener sections, and buckling of plates with sturdy stiffeners (no local buckling). Results are presented in numerous charts and tables.

References 24 - 26 are recent reviews of theoretical and experimental work with laminated composite plates and shells. Kedward, et al.[24] reviewed the classical expressions for predicting initial buckling of flat plate elements (18 references), while Arnold and Kedward[25] reviewed initial buckling, postbuckling, and failure characteristics of composite stiffened panels (82 references). Leissa[26] presented a comprehensive summary of buckling and postbuckling behavior of laminated composite plates and shell panels. Most of the 392 included references dealt with symmetric, balanced composite plates, with approximately 20% of the references on stiffened plates.

Nemeth[27] provided valuable insight into the importance of anisotropic bending stiffnesses on the buckling of composite plates.

1.2.4 Postbuckling of Unstiffened Panels

References 28 - 42 examine postbuckling of unstiffened panels. An even distribution of analysis and experiments is represented. All analyses are based on von Kármán nonlinear

strain-displacement relations, and Kirchoff-Love assumptions. The works of Stein[31], Sharmon and Humpherson[32], Chan[34], and Feng[35] are primarily analytical with only supplemental experimental results included. Jensen and Lagace[41] and Jeffrey[42] provided two-part studies, relying equally on analysis and experiments, while Rouse[40] presented experimental results only. In each reference it was shown that plates supported on the edges can demonstrate considerable reserve load carrying capacity beyond their initial buckling load.

Early references considered only isotropic material, with later work including the effect of varying degrees of anisotropy. Jensen and Lagace[41] and Jeffrey[42] considered the most highly anisotropic laminates, including unbalanced and unsymmetric laminates. The objective of Jensen and Lagace[41] was to isolate the different elastic couplings inherent in unbalanced and unsymmetric laminates, and determine their effects on panel buckling and postbuckling behavior. The elastic couplings considered were bending-stretching, the stretching-shearing and bending-twisting combination, and stretching-twisting coupling.

Feng[35] used an unstiffened plate analysis with edge constraints to provide forces at the edge of a stiffener as input into a separate program for bondline strength analysis. For shear panel tests Feng claims predicting a failure load due to stiffener disbonding which was within 2% of the average of the experiments. The details of the bondline analysis are not included in the reference.

While all of the references considered axial compressive loading, Feng[35], Stein[36], Zhang and Mathews[38], and Chia[39] also considered combined compression and shear loading. Stein[36] observed a larger reduction in postbuckling stiffness under pure shear loading than under pure axial loading. Stein also noted that a plate buckled in shear retains 90% of its axial stiffness. In contrast, a plate buckled in compression retains only 20% of its shear stiffness. Stein quantified these findings by stating that the shear results depend to a great extent on inplane boundary conditions.

Levy, et al.[29] and Stein[30,31,37] addressed the issue of mode changing in postbuckled plates.

1.2.5 Postbuckling of Stiffened Panels

References 43 - 49 examined postbuckling of stiffened composite panels. All of the references dealt with flat laminated composite skins reinforced with composite open-section stiffeners. There was no work in the literature with rotated stiffeners and postbuckled

skins. Even though all these references considered laminated skins, the attention given to the presence and influence of anisotropy was minimal. Below is a summary of the configurations each reference considered.

Dickson, et al.[43] described an analysis procedure for design of stiffened plates loaded in biaxial compression or tension, and shear. The primary thrust of this work was in addressing stringer instability after advanced postbuckling of the skin. Skin buckling lowered the skin's inplane stiffness, forcing the stiffeners to carry a proportionately greater share of the applied load. Also, skin buckling induced secondary forces and deformations on the stiffeners. The increase in stiffener load and induced stiffener deformations combined to make the stiffeners more susceptible to local, column, and torsional instability. Dickson examined torsional or torsional-flexural buckling of the stiffeners while incorporating the effect of the attached postbuckled skin. Dickson considered only balanced symmetric skins but did retain bending stiffness coupling terms D_{16} and D_{26} in the analysis. Experiments consisted of compression loading of three panels, each with four I-shaped longitudinal stiffeners.

Starnes, et al.[46] presented the results of on experimental study of postbuckled compression loaded panels with four I-shaped longitudinal stiffeners. Starnes considered quasi-isotropic skins only. Nonlinear structural analyses were conducted using a general nonlinear finite element analysis computer code, STructural Analysis of General Shells[50-52] (STAGS). The results from the STAGS code correlated well with the test results up to failure. A strong argument for modeling stiffeners as branched shells rather than discrete beams was made by comparing the buckling solutions of STAGS models applying various levels of modeling detail and the buckling solutions obtained using the PASCO[53] computer code. In the experiments some panels supported as much as three times their initial buckling loads before failing. Failure of all panels appeared to initiate in a skin-stiffener interface region. No analysis of this local skin-stiffener separation failure was included.

The skin-stiffener failure observed by Starnes, et al.[46] prompted Dickson, et al.[44] to investigate stiffener attachment concepts for stiffened graphite-epoxy panels. These concepts included adhesive bonding, adhesive bonding reinforced with mechanical fasteners, and cocuring the stiffener and skin after stitching the stiffener attachment flange to the skin. Also considered was the effect of a graphite-epoxy pad or insert in the skin under the stiffener attachment flange. This investigation was primarily an experimental study. To compliment the experiments, an analytical procedure described in Wang and Biggers[45]

was used to examine the effect of the padded-skin concept and relative stiffnesses of the skin and stiffener attachment flange on the skin-stiffener interface stresses.

Rouse[47] presented results of an experimental study of the postbuckling response and failure of inplane shear-loaded graphite-epoxy panels stiffened with two I-shaped longitudinal stringers. Finite element analysis with STAGS was used to estimate buckling loads. Rouse observed failure due to skin-stiffener separation.

Stein[48] presented a numerical study of postbuckled compression-loaded panels with open-section stiffeners. Stein noted combinations of large twisting strains and bending strains in postbuckled panels which would lead to delamination of the stringers. Stein observed that anisotropic attachment flanges could increase the twisting strains, thus promoting skin-stiffener separation.

General purpose finite element codes such as STAGS have been useful in verifying and correlating experimental results, but were considered inappropriate for preliminary design or parametric studies. Attempts were made to develop procedures which were computationally efficient and convenient, yet retained the level of modeling detail required to represent local response phenomena. One such attempt was presented by Sheinman and Frostig.[49] Arbitrary stiffened laminated panels were modeled by plate elements. A variational principle in terms of out-of-plane deflection and the Airy stress function was used to obtain nonlinear equilibrium equations, boundary conditions, and continuity conditions between elements. In this analysis, all anisotropic terms were retained, and examples in the reference included laminates with extensive anisotropic coupling.

It is important to note that in the literature nearly all postbuckled stiffened panels studied experimentally failed due to premature skin-stiffener separation along the bondline, while most analyses do not address this mode of failure. Several papers that address the interlaminar normal and shear stresses at the skin-stiffener interface are listed in Refs. 54 - 61. In general, the references include local detailed analyses of varying complexity, and consider only specific loading conditions. This area of research is under development, with current capabilities falling short of reliable prediction of failure due to skin-stiffener debonding for stiffened panels under general loading.

1.2.6 Summary of the Literature Review

The literature review presented above spans several research topics. To define the objective of the current study, the findings from different areas of research are related and shortcomings in the current understanding of structural tailoring are identified.

The primary thrust of work in structural tailoring of stiffened panels was to develop wing configurations with directional stiffness properties, or stiffness coupling. Early references in this area examined metallic constructions and suggested rotating the orientation of underlying ribs and stringers to induce directional stiffness properties. Twenty years later the introduction of composite materials spurred research in tailoring the wing skins to induce directional stiffness properties. Only two references, Ref. 13 and Ref. 14, pursued the earlier suggestions of rotating the stiffening members of the structure. Reference 14 was the only source which included results for metallic structures with rotated stringers and composite structures with tailored wing skins, and compared the effectiveness of these two tailoring techniques. Little has been written on how the methods differ in their contribution to the directional stiffness of the structure. A common limitation to all references on aeroelastic tailoring was the assumption that the structures were buckling resistant. Thus, in the aeroelastic tailoring work stiffness coupling was examined, but the effect of the coupling on buckling loads, and any postbuckling phenomena were not considered. The remainder of the references in the literature review do not have a primary objective of inducing a tailored structural response. The references on arbitrarily oriented stiffeners were mostly concerned with demonstrating analytical techniques, and there was no mention of orienting the stiffeners to create stiffness coupling. Based on the available literature, it does not seem that the full potential for stiffness tailoring of stiffened panels has been realized.

Jensen and Lagace[41] examined the effect of certain couplings on buckling and postbuckling behavior of anisotropic plates, noting that these couplings tend to reduce buckling loads. Even though this reference considers several types of coupling, no previous investigation of the postbuckling of unstiffened panels focused on obtaining a specific coupled structural response and quantifying how this response was affected by panel buckling. Jensen and Lagace[41] briefly mentioned aeroelastic tailoring through stiffness coupling of wing skins, and went on to state that conventional aircraft wing panels are often designed to operate in the postbuckled region. Lagace[62] quantified this statement by noting that postbuckling is often allowed in upper wing skin panels for loads between limit load and

ultimate load. Thus, a study examining tailoring for stiffness coupling should consider the effect of these couplings on the buckling load and postbuckling response, as well as how postbuckling changes the desired coupling.

Several references reported that stiffened panels could carry loads considerably higher than their initial buckling load, thus supporting the extension of structural tailoring into the postbuckling load range. It is expected that geometrically nonlinear deflections in the postbuckling load range will alter the response of a tailored panel. If buckling does change the coupling response, then these changes should be quantified, and possibilities for load-dependent directional stiffness tailoring should be examined.

Finally, it was noted that nearly all postbuckled stiffened panels observed in experiments failed due to skin-stiffener separation. If stiffened panels are to be tailored for application in the postbuckling load range, it would follow that the issue of skin-stiffener separation should be considered. Predicting failure of tailored stiffened panels may be difficult, or impossible, since there is no general solution for skin-stiffener separation under arbitrary loading.

Preliminary results from the current study were reported by Young et al.[63] in 1993. Young reported on the combined effects of tailoring both the skin anisotropy and the stiffener orientation on the buckling and postbuckling response of composite stiffened panels. The structural configurations considered by Young were adopted by Noor et al.[64] in 1996. Noor included the effect of uniform thermal loads and developed hierarchical sensitivity coefficients of the buckling and postbuckling responses, namely addressing the sensitivity of the buckling load and strain energy density to variations in material properties, laminate stiffnesses, and laminate orientation. Although Noor considered the same structural configurations as Young, Noor did not expand on the topic of structural tailoring through stiffness coupling and did not contribute to the results of Young in regards to any of the issues listed above.

1.3 Objective of the Current Study

Previous work in structural tailoring has shown how unique couplings introduced by rotating stiffener orientations, or rotating the principal axis of orthotropy of a wing skin could provide design advantages, yet it is clear there is much still to be done in the way of

exploiting the influence of material anisotropy and stiffener orientation. The objective of the present work is to provide experimental and numerical results which describe the prebuckling, buckling, and postbuckling response of composite stiffened panels which exhibit axial-shear stiffness coupling. The stiffened panels are tailored by employing anisotropic skins with membrane and bending stiffness coupling, and skewed stiffeners. The influence of each tailoring method on the structural response is quantified and explained. Understanding of the mechanisms which control the structural response can then be applied to gain insight into exploiting the response, and inspiring innovative design practices for future applications.

1.4 Approach

The present study consists of an experimental and numerical investigation of the prebuckling, buckling, and postbuckling responses of stiffened panels tailored to exhibit axial-shear stiffness coupling. While considering both the prebuckling and postbuckling responses, the approach used in the present work was:

1. To conduct an exploratory experimental program to examine the axial-shear stiffness coupling in a flat rectangular laminated composite panel with a single stiffener, quantifying the differences in structural response obtained by rotating the stiffener orientation and/or the orientation of the principal direction of orthotropy of the laminated skin.
2. To develop finite element models which accurately represent the physical model.
3. To verify the finite element models by comparing numerically-predicted results with experimental results.
4. To address failure of the panels due to skin-stiffener separation
5. To use the verified models to conduct a parametric study to isolate the mechanisms which contribute to the observed responses.
6. To apply lessons learned to present particular examples which exploit the observed behavior.

Throughout the investigation, efforts were made to explain the mechanisms of the observed responses. The investigation was kept straightforward by considering a simple structural configuration and a simple loading, while using a relatively familiar problem as a baseline.

1.4.1 Structural Configuration

The structural configuration that was selected for the present study consists of a rectangular graphite-epoxy laminated composite panel with a single centrally located I-shaped graphite-epoxy stiffener. Axial-shear stiffness coupling is introduced by rotating the orientation of the stiffener or the principal direction of orthotropy of the skin, or both. The structural parameters varied in the study are shown in Fig. 1-10. The stiffener orientation is represented by the angle α, and the orientation of the principal direction of orthotropy of the skin laminate is represented by the angle β, both measured relative to the axial, or x, direction. A uniform end shortening displacement u is applied to the upper end of the panel in the axial direction, and the axial displacement of the lower end is restrained. The upper and lower ends are clamped and the unloaded sides are simply supported. The axial compressive force corresponding to the applied end shortening is represented by P_x, and the shear force reaction generated by the axial-shear stiffness coupling is represented by P_{xy}. If the upper end of the panel is free to shear in the lateral, or y, direction, then the lateral displacement associated with shear is represented by v. The amount of axial-shear stiffness coupling in the panel is represented by the ratios of P_{xy} to P_x and v to u.

This configuration allows several questions raised in the literature review to be addressed. By including both the stiffener orientation and laminate orientation as vari-

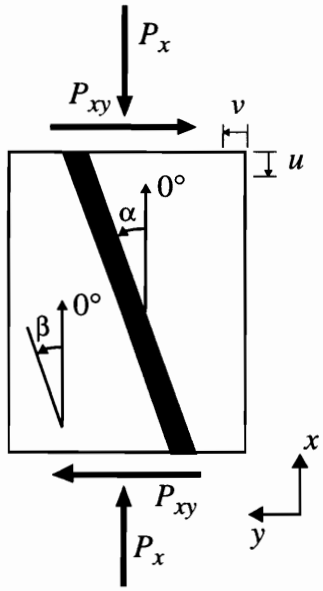

Fig. 1-10 Structural parameters studied

ables, the two tailoring techniques can be assessed independently, or in conjunction with each other. The use of a single discrete stringer, rather than smeared stringer properties, provides information concerning the internal load distribution, component interaction, and stringer deformation. The values of the geometric and material parameters for the panel skin and stiffener have been selected as representative of a lightly loaded stiffened panel with postbuckling strength. Thus, the present study considers the prebuckling and postbuckling load ranges. In each load range the effectiveness of the stiffness tailoring techniques are quantified by assessing the effect on the structures' overall response. Attention is given to understanding the prebuckling response, the onset of buckling, and the postbuckling response.

1.4.2 Chapter Outline

An exploratory experimental program consisting of five test panels with two stiffener orientations and three skin orientations was conducted. The experimental program is discussed in Chapter 2. The test specimens, fabrication, preparation, instrumentation, and experimental procedures are described in detail. A portion of the experimental results are provided in Chapter 2.

Results from the numerical portion of the current study are divided into four chapters. Chapter 3 describes the development of detailed numerical models that were specifically designed to simulate the prebuckling and postbuckling responses of each test panel. Modeling techniques are defined by individually assessing the effects of several modeling details on the predicted buckling and postbuckling response.

In Chapter 4 the results of nonlinear analyses conducted using the detailed numerical models are compared to the measured structural responses from the experiments. The load vs. end shortening responses, prebuckling and initial postbuckling stiffnesses, buckling loads, postbuckling deflections, and axial-shear coupling responses are reported and compared. The numerically-predicted and measured results are compared to verify the accuracy of the numerical models. The axial-shear coupling responses reported in Chapter 4 demonstrate unique structural behavior that has not been identified in other studies on structural tailoring.

The issue of failure of stiffened panels due to skin-stiffener separation is addressed in Chapter 5. The numerically-predicted skin-stiffener attachment forces and moments at loads corresponding to experimental failure are presented and discussed.

In Chapter 6 the unique axial-shear coupling responses reported in Chapter 4 are examined in greater depth. The observed responses are studied and the mechanisms which control the nature of the observed responses are identified. Additional configurations are prescribed to further examine and exploit the controlling mechanisms. The results of a parametric study which isolates and combines the controlling mechanisms are presented.

Finally, in Chapter 7 conclusions are drawn based on the experimental and numerical findings. Suggestions are made as to the implications of the findings on current and future design practices. Also, recommendations are made for further research to extend the current study, and to address some important issues that were not addressed in the current study.

2. Description of the Experiments

To initiate the research, an exploratory experimental program was developed. The primary aim of the experiments was to observe the axial-shear coupling response of stiffened panels in prebuckling and postbuckling. Since there were no similar experiments identified in the open literature, a few examples demonstrating structural behavior which exhibited axial-shear stiffness coupling in panels were needed in order to guide analytical modeling, benchmark analytical results, and assist in identification of any unexpected physical phenomena.

2.1 Test Panels

The five panels tested in this study were fabricated by the author at the NASA Langley Research Center. The panels were fabricated from Hercules, Inc. AS4-3502 graphite-epoxy unidirectional preimpregnated tape (pre-preg). Nominal lamina elastic properties for this graphite-epoxy system were given in Table 1-1 on page 12. All components were constructed from 16-ply laminates.

The baseline stacking sequence for the skin laminate was $[\pm 45/\mp 45/0_3/90]_s$. Each panel used this stacking sequence, with the entire laminate rotated an angle β equal to $-20°$, $0°$, or $20°$ relative to the axial direction. This laminate, although not overly biased, was stiffest in the $0°$ direction, and provided axial-shear stiffness coupling when the laminate was rotated off axis.

The stiffener was an open-section I-stiffener with all sections made with a $[\pm 45/0/90]_{2s}$ laminate. The stiffener sizing was selected such that the stiffener would not dominate the stiffness of the panel, yet would be rigid enough to maintain a node line along the length of the stiffener after skin buckling. The stiffener geometry is shown sche-

matically in Fig. 2-1(a). Each panel used this stiffener geometry, with the stiffener rotated an angle α equal to 0° or 20° relative to the axial direction. A value of 20° was selected in order to introduce maximum shear coupling without sacrificing axial stiffness, and was based in part on information presented in Refs. 7 and 17. There was also a practical limitation on stiffener orientation in order for the stiffener to be potted on the loaded ends.

Photographs of typical test panels are shown in Figs. 2-1(b) and 2-1(c).The panels were sized so that the unsupported panel would be 21.0 in. long and 16.0 in. wide. The configurations selected are shown in Fig. 2-2. Each configuration is represented by a schematic which indicates the stiffener and skin orientations. These schematics are used to specify the configurations when presenting graphical experimental and numerical results in the chapters to follow. Below each schematic is the configuration's identifying name. Configuration B0,0 has an unrotated skin and an unrotated stiffener, and represents the baseline configuration. Configuration B0,2 has the skin laminate rotated 20° relative to the axial direction. Configuration B2,0 has the stiffener rotated 20° relative to the axial direction. Configuration B2,2 has the skin and stiffener rotated 20°, in the same direction. Configuration B2,n2 has the skin and stiffener rotated 20°, but in opposite directions.

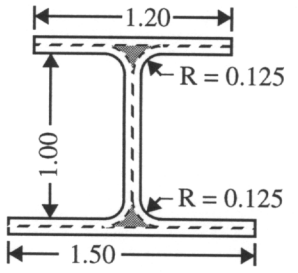

(a) Stiffener geometry, dimensions in inches.

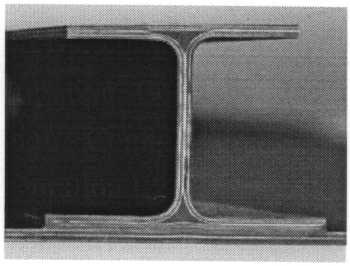

(b) Stiffener-skin cross section.

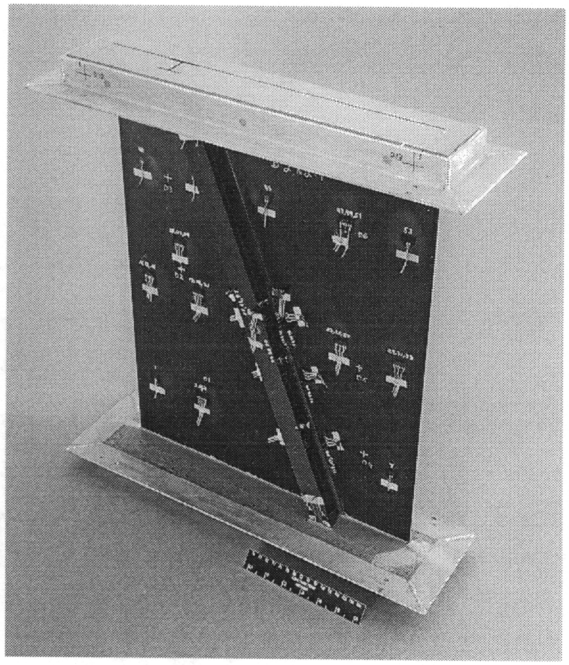

(c) Potted panel: stiffener rotated, $\alpha = 20°$.

Fig. 2-1 Typical test panels

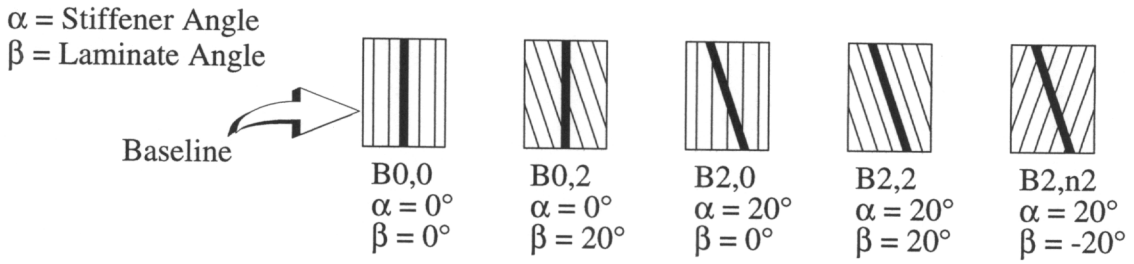

Fig. 2-2 Test panel configurations

To fabricate the panels, the skins and stiffeners were laid up independently, then co-cured in an autoclave. To allow the same tooling to be used for all panels, and to provide for trimming the panel edges, the panels were made oversized. The fabrication process is outlined below.

2.1.1 Tooling

The panels were fabricated by hand lay-up of pre-preg and cured in an autoclave. Before panel assembly was initiated, tooling was designed and fabricated. The tooling is identified in Fig. 2-3 in a cross section schematic of a typical panel just prior to autoclave curing.

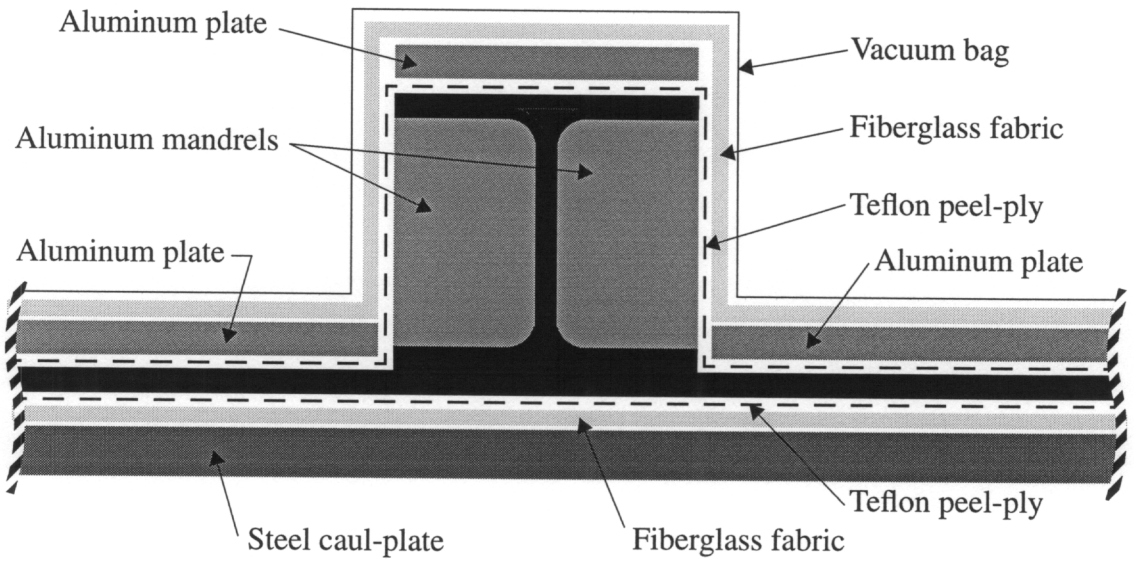

Fig. 2-3 Fabrication cross section prior to autoclave cure

The steel caul-plate under the panel was 0.25 in. thick, 21 in. wide, and 36 in. long. The aluminum plates were 6061 aluminum alloy and were 0.090 in. thick. The aluminum plate above the stiffener was 1.5 in. wide and 32.5 in. long. The aluminum plates on each side of the stiffener were fabricated in pairs. The pair used to make panels with a stiffener orientation of $\alpha = 0°$ were formed by first cutting a plate that was 16.5 in. wide and 32.5 in. long, and then cutting this plate along the axial center-line. The pair used to make panels with a $\alpha = 20°$ stiffener orientation were formed by first cutting a plate that was 16.4 in. wide and 32.5 in. long, and then cutting this plate along a diagonal at 20° from the axial center-line. A sketch of each pair of plates is shown in Fig. 2-4(a) and Fig. 2-4(b).

The aluminum mandrels shown in Fig. 2-3 were machined from 2024 aluminum stock. The mandrels were 32.5 in. long and the cross section dimensions are given in Fig. 2-4(c). Referring to the view sketched in Fig. 2-4(c), the top and bottom sides were machined flat and parallel, and the left side was machined flat and perpendicular to the top side. These three sides were polished because they were mold surfaces.

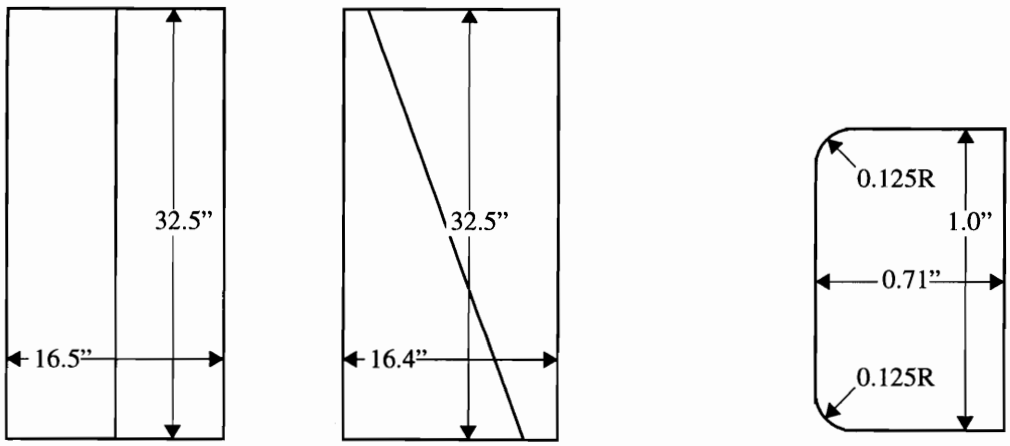

(a) Aluminum plates, $\alpha = 0°$

(b) Aluminum plates, $\alpha = 20°$

(c) Aluminum mandrels

Fig. 2-4 Tooling dimensions

2.1.2 Pre-preg Cutting

The pre-preg from which the panels were fabricated came in rolls of 12 in. width and had to be kept frozen prior to use. To assist in handling, the pre-preg for all laminates was cut at one time, then resealed in individual bags and stored in the freezer. The pre-preg was

paper backed and was cut with razor blades or a paper cutter equipped with templates for different layer angles.

2.1.3 Laying-up the Skin Laminate

Three skin configurations were used for the five panels. The baseline $[\pm 45/\mp 45/0_3/90]_s$ laminate was rotated at orientations of β = [-20°, 0°, 20°] resulting in $[25/-65_2/25/-20_3/70]_s$, $[\pm 45/\mp 45/0_3/90]_s$ and $[65/-25_2/65/20_3/-70]_s$ laminates, respectively. Each skin laminate was assembled to form a rectangular plate that was 32.5 in. long and 18.0 in. wide. The procedure for each panel was identical.

Each skin laminate was laid up one layer at a time. Each layer required several strips of pre-preg to be pieced together. The pieces were placed with fibers running parallel to the joining edges, so the layer had no seams or cut fibers on the interior of the plate. See Fig. 2-5 for an example of this procedure. After piecing together each layer, an iron was used to tack the layer to the layer under it, the edges were trimmed with a razor blade, and then the paper backing was removed. Debulking was performed as needed to remove air trapped between the layers. Debulking was performed at least once for every four layers placed.

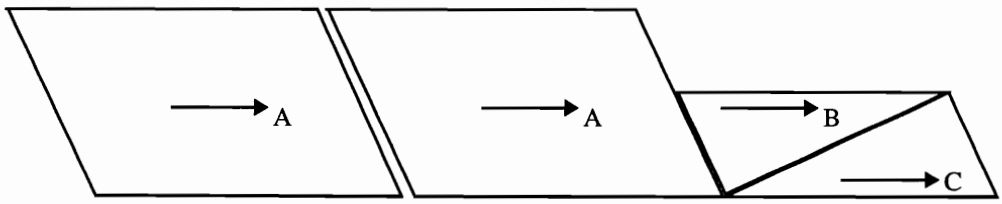

(a) Strips as cut from 12 in. wide roll of pre-preg

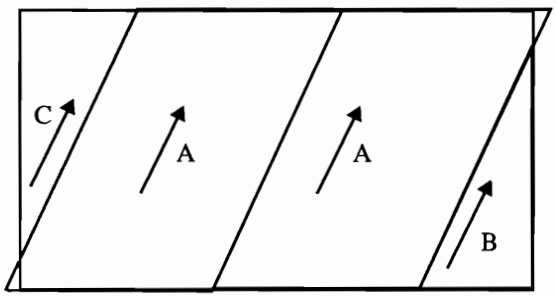

(b) Strips assembled in 32.5 in. by 18.0 in. lamina

Fig. 2-5 Strips of pre-preg joined into seamless 65° layer

Debulking was accomplished by placing the partially constructed laminate on a table, between an assembly of layers of Teflon peel-ply material and fiberglass fabric, covering the assembly with a vacuum bag, and drawing a vacuum on the assembly for 15 minutes. Care was taken not to contaminate the panel during this process. Leaving a piece of Teflon peel-ply or backing paper from the pre-preg in between the laminates layers would produce a delamination.

2.1.4 Laying-up the Stiffener

The stiffeners for all five panels were identical. Once assembled, the stiffener was centrally located on the laminated rectangular skin at an orientation of $\alpha = 0°$ or 20° relative to the skin centerline and co-cured with the skin. The stiffeners were fabricated with a length of 32.5 in.

The stiffener assembly was composed of four laminates and two strips of unidirectional tape. As shown in Fig. 2-6, laminates (a) and (b) formed half of the cap and attachment

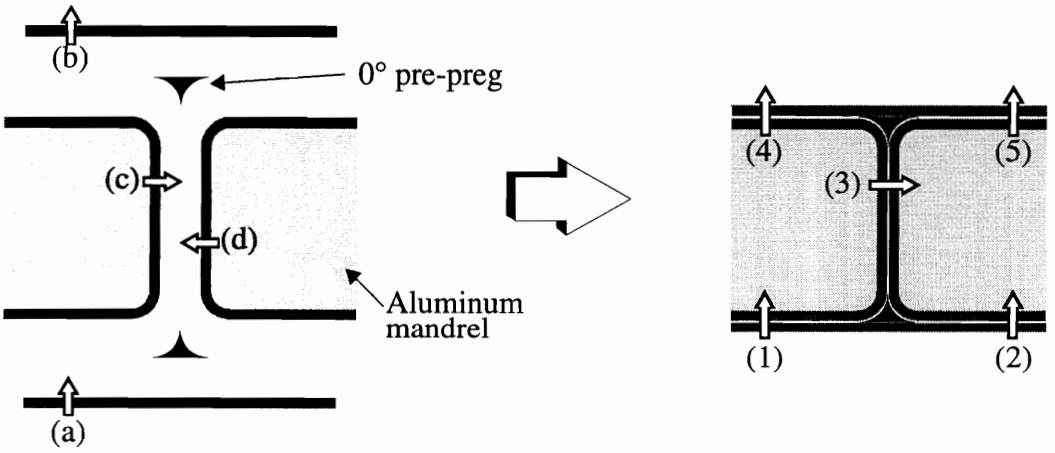

Sub-laminates before assembly
(a) $[\pm45/0/90/\mp45/0/90]$
(b) $[90/0/\pm45/90/0/\mp45]$
(c) $[\pm45/0/90]_2$ (from mandrel)
(d) $[\mp45/0/90]_2$ (from mandrel)

Assembled laminates
(1) $[\pm45/0/90/\mp45/0/90/(90/0/\pm45)_2]$
(2) $[\pm45/0/90/\mp45/0/90/(90/0/\mp45)_2]$
(3) $[\pm45/0/90]_{2s}$
(4) $[(\pm45/0/90)_2/90/0/\pm45/90/0/\mp45]$
(5) $[(\mp45/0/90)_2/90/0/\pm45/90/0/\mp45]$

Fig. 2-6 Stiffener assembly

flanges. These components were laid up as flat 8-ply laminates, trimmed to 1.5 in. width, and debulked. The other two laminates, (c) and (d), formed the web as well as the other half of the cap and attachment flanges. These laminates were channel shaped, and were formed by wrapping 8 layers around a polished aluminum mandrel, debulking them against the mandrel, and trimming their edges. To assemble the stiffener, the left and right halves of the web were clamped together. The radii in the aluminum mandrels created a triangular-shaped void at the top and bottom of the stiffener web. The triangular-shaped void was filled with 0° pre-preg, and then the cap and attachment flange laminates were placed to complete the assembly. The aluminum mandrels were left in place until after curing. The stacking sequences for components (a) - (d) and the resulting laminates after assembling the stiffener components are shown in Fig. 2-6. The stacking sequences were selected to provide nearly quasi-isotropic laminates while minimizing the degree of asymmetry inevitable when constructing an I-stiffener in this fashion.

The panel was now ready for final assembly and preparation for curing. A cross section schematic of an assembled panel just prior to autoclave curing was shown in Fig. 2-3. The steel caul-plate was used as a base and it was cleaned and waxed. The plate was covered with fiberglass fabric and Teflon peel-ply material. The skin laminate was then placed on the peel-ply layer, and the stiffener placed on the skin laminate at the desired orientation. The entire panel was covered with a layer of peel-ply material. Aluminum plates were placed over the stiffener cap and the exposed skin. The entire assembly was then covered with fiberglass fabric and a vacuum bag. The vacuum bag was sealed to the caul-plate with a pliable sealant. A vacuum port and thermo-couple were inserted into the vacuum bag. The fiberglass fabric was used as a bleeder cloth to absorb excess resin during curing. The aluminum plates served two purposes. They gave a better surface finish on the skin by reducing the significance of wrinkles in the vacuum bagging. They also butted up against the edge of the attachment flange to provide a well-formed corner at the stiffener-skin interface.

The entire assembly was then inserted into an autoclave for curing under vacuum, external pressure and heat according to the resin manufacturer's specifications. The cured panel was removed from the vacuum bagging. Mandrels were removed by first cooling the panel in a freezer, and then tapping on the end of the each mandrel with a brass rod and hammer. The panel was then sent to a machine shop to be cut to the final dimensions. The final panels were 24.0 in. long and 16.5 in. wide, with the stiffener cap trimmed to a width of 1.2 in.

(Note: Panel B2,2 was damaged during panel preparation. To remove the damage, the stiffener cap was trimmed to a final width of 1.0 in., rather than the 1.2 in. dimension shown in Fig. 2-1(a).)

2.1.5 Potting the Panels

To protect the loaded edges of the panels during testing, the top and bottom ends of each panel were potted in 1.5 in. of casting compound encased in a aluminum frame. A photograph of a potted panel was shown in Fig. 2-1(c). The aluminum frames were constructed of 1.5 in. by 1.5 in. by 0.1875 in. 6061-T6 aluminum structural angle. Four pieces of angle were welded to form a frame that was 1.5 in. deep and had inside dimensions of 3.375 in. by 18.5 in.

To pot a panel the following sequence was followed:

1. A fixture for supporting the panel in a plane perpendicular to a table was devised.
2. One of the aluminum frames was placed on the table beneath this supporting fixture, with the flanged side of the frame away from the table.
3. A bead of sealant, 0.125 in. thick, was placed between the lower edge of the frame and the table surface.
4. The panel was placed with the end centered in the frame. The panel was clamped to the supporting fixture, holding the panel flat against the supporting fixture and perpendicular to the table.
5. The frame was filled with a casting compound. HYSOL TE5467 aluminum filled epoxy and HD3615 hardener were used.
6. After the casting hardened the panel was inverted and the other end was potted.

2.1.6 Grinding Loaded Ends Flat and Parallel

The bead of sealant used in step 3 above caused the panel and casting compound to extend 0.125 in. beyond the aluminum frame. This allowed the loaded ends of the panel to be ground flat and parallel without machining the aluminum frames. When the panels were ground, they were supported such that the weight of the potted ends did not warp the panel.

2.1.7 Surface Shape Measurement

The potted panels were sent to the Quality Assurance and Inspection Office, NASA Langley Research Center, to be measured for initial geometric imperfections. The panels were

measured after potting because the potted configuration represented the as-tested initial shape. To measure the panel shape, the panels were placed on an optical bench standing upright on the lower potted end. A robotic arm with a contacting probe was used to measure the x-y-z coordinates of the exposed portion of the unstiffened side of the panel. The location of six points on the panel, three points across the width of the panel near each potted end, defined the reference plane in a least squares sense. The robotic arm was then programmed to transverse the unstiffened side of the panel making measurements at 0.25 in. intervals, and reporting the x-y-z coordinates of each surface point relative to the reference plane. Measurements were taken starting 0.25 in. inside the potted ends and the side edges.

The original test plans did not call for measuring initial geometric imperfections, since the buckling of flat panels is not imperfection sensitive. The first panel tested, B2,0, was not measured for initial geometric imperfections. Poor correlation between experimental and analytical predictions for this panel prompted the measuring of the initial geometric imperfections for the remaining panels.

2.1.8 Strain Gaging

Electrical resistance strain gages were used to measure strains. Strain gage patterns were specified for each panel to meet three objectives:

1. Monitor load introduction: Gages were located at several locations across the panel width close to the potted ends.
2. Provide strain data to be used to compute resultant axial and shear loads, P_x and P_{xy}: The panels were loaded with an applied end shortening in a uniaxial load frame. The resultant axial load P_x was recorded by a load cell, but the resultant shear load P_{xy} could not be measured directly. Gages were located at several locations across the width at panel midlength for this purpose.
3. Monitor local deformations associated with panel buckling: Gages were located on the panel skin away from the stiffener where bending due to skin buckling was predicted to be a maximum. Gages were also placed at several locations on the stiffener to monitor the stiffener load and cross section deformation.

Finite element models were developed for each configuration. Linear bifurcation buckling modes obtained using the STAGS analysis code were used to define strain gage patterns. The lowest eigenvalues were closely spaced, so the first and second mode deformations were considered. Drawings were created that specified strain gage locations

and numbering, and the strain gages were mounted by Modern Machine and Tool, Hampton, VA. The strain gages that were used consisted of three-arm rosettes and unidirectional gages (Micro Measurement CEA-06-125UR-350 and CEA-06-125UW-350). Leads that were 10 ft. long were attached to the gages and labeled with the respective gage number. In the prescribed gage pattern nearly all of the gages were "backed-up", i.e., gages were located on the front and back of a laminate in pairs. When strain gages are "backed-up" or "back-to-back," the average of the surface strains is the midplane strain, while the difference in surface strains is twice the bending strain.

The strain gage pattern specified for panels B2,2 and B2,n2 is shown in Figs. 2-7 to 2-9. A total of 130 gages were used for each panel to address the objectives listed above. The strain gage pattern for the panel skin is shown in Fig. 2-7. Gages located along lines 4 in. from each potted end were used to monitor load introduction, while gages located across the panel midlength were used to compute resultant loads. Gages in the center of the unsupported skin were used to indicate skin buckling. In Fig. 2-7 three locations along the stiffener, Locations A, B, and C, indicate stiffener cross sections that were gaged. The gage patterns at Locations A and B are shown in Fig. 2-8. Location A was heavily gaged to predict accurately the load carried in the stiffener at panel midlength. The gages on the stiffener web indicated warping of the stiffener cross section. The gage pattern at Location C is shown in Fig. 2-9(a). The gage patterns for Locations B and C were similar. Finally, a few gages were placed on the stiffener cap near the potted ends to monitor load introduction into the stiffener and to indicate bending in the plane of the stiffener cap. The location of these gages is shown in Fig. 2-9(b).

(Note: As mentioned earlier, panel B2,2 was damaged during panel preparation. To remove the damage, the stiffener cap was trimmed to a final width of 1.0 in., rather than the 1.2 in. dimension shown in Fig. 2-1(a). The change in cap width is reflected in the location of strain gages on the stiffener cap for panel B2,2 in Figs. 2-8(a) and 2-9(b).)

2.1.9 Final Panel Preparation

The shadow moiré interferometry technique was used during testing to monitor visually the out-of-plane displacement of the panel's skin. To prepare the panel, the strain gage leads on the unstiffened side of the panel were grouped and taped down, and this side was painted white. A description of the shadow moiré interferometry method is given in Ref. 65.

All dimensions are in inches.
The small numbers represent the strain gage numbers.

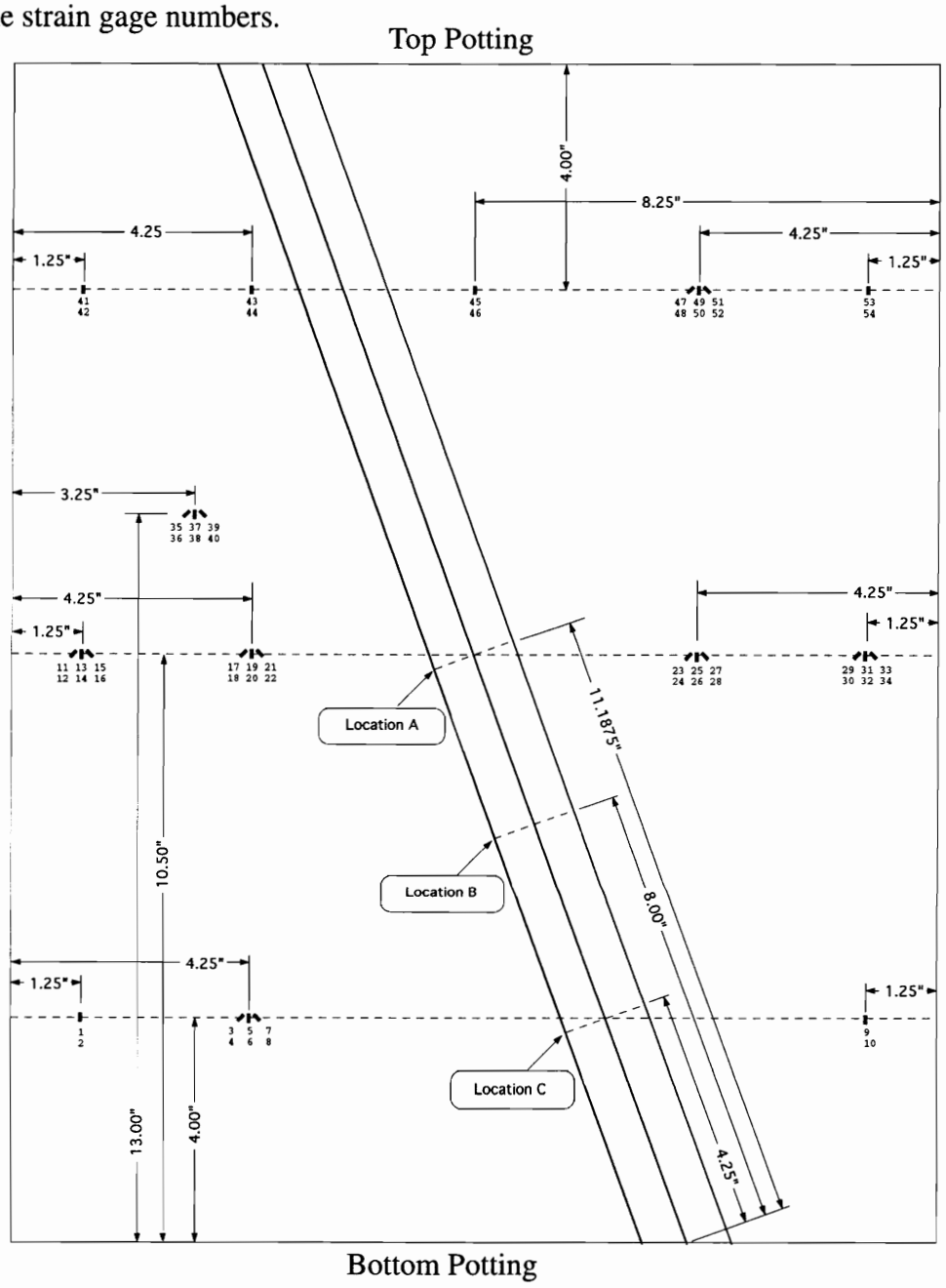

Fig. 2-7 Strain gage pattern B2,2 and B2,n2; skin gages

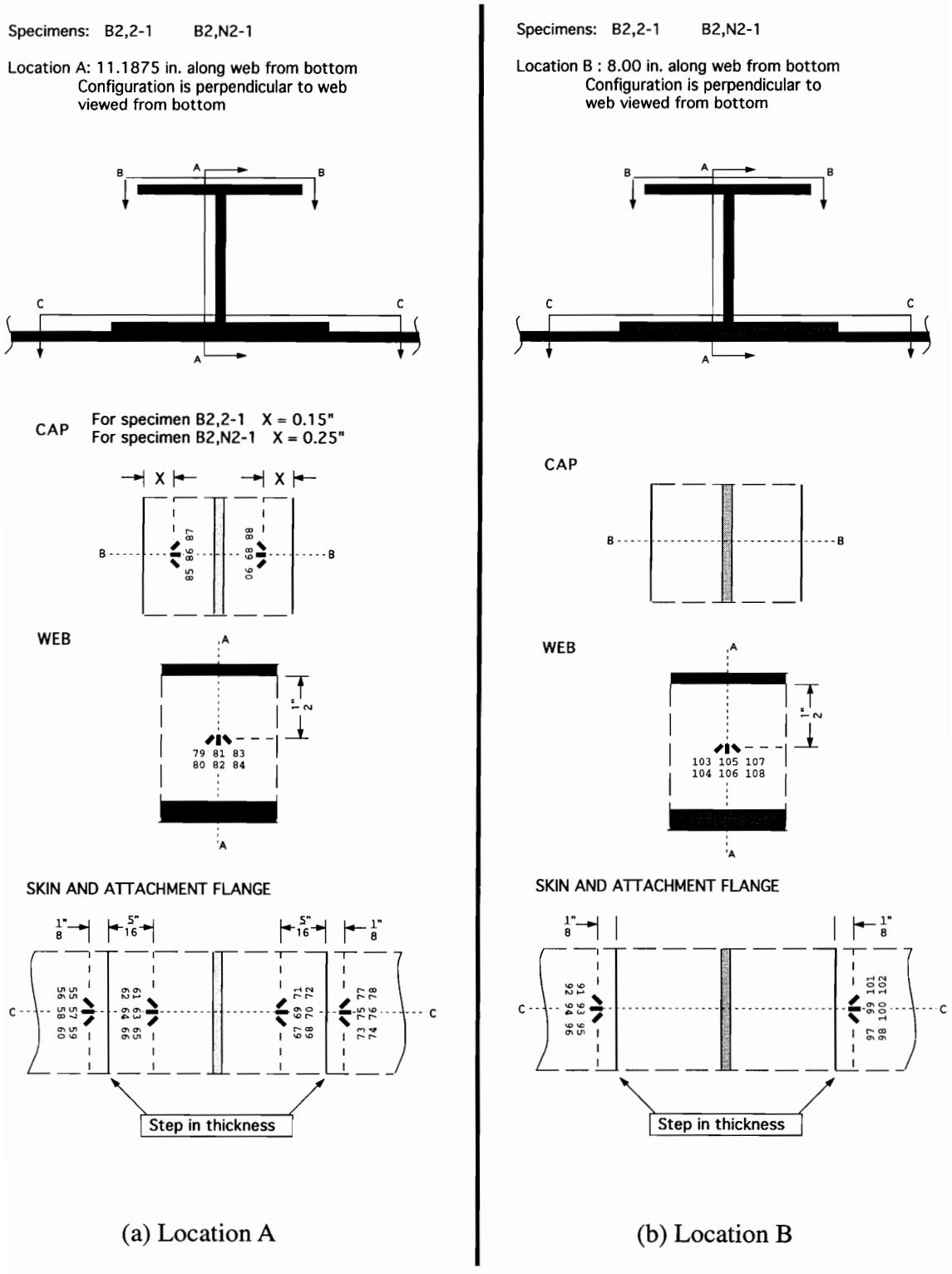

Fig. 2-8 Strain gage pattern B2,2 and B2,n2; stiffener locations A and B

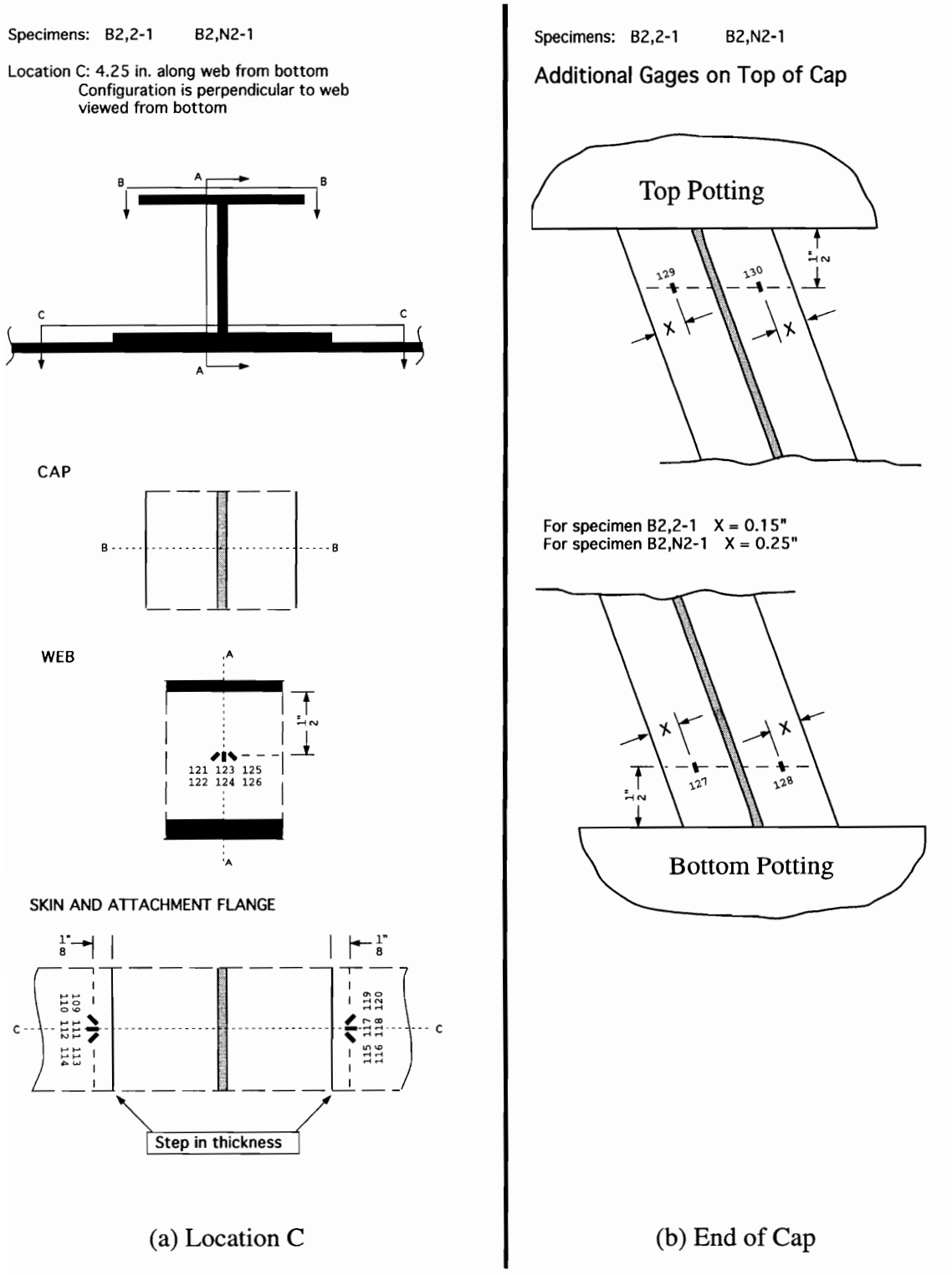

Fig. 2-9 Strain gage pattern B2,2 and B2,n2; stiffener location C and end of cap

During testing, the unloaded edges of the panel were supported by steel knife edges. The knife edges were loosely clamped to the vertical edges of the panel, supporting the panel's skin along a line 0.25 in. from the panel's edge.

2.1.10 Direct-Current Differential Transducers

Direct-current differential transducers (DCDT's) were used to measure longitudinal and lateral displacements of the testing machine platens, and out-of-plane displacements of the panel at selected locations. All DCDT's were mounted to the bottom platen of the test machine using magnetic mounts and supporting hardware.

Seven DCDT's were used to measure displacements on the stiffened side of the panel. The locations of these DCDT's on panels B2,2 and B2,n2 are shown in Fig. 2-10. DCDT's 1 through 6 measured the out-of-plane displacement of the skin, and DCDT 8 measured the inplane displacement in the stiffener cap.

During testing a uniform end shortening was applied to the panels under displacement control. The stiffness coupling in the panels caused substantial lateral displacements of the load frame platens. Five DCDT's were positioned to measure the displacement of the top platen relative to the bottom platen. The locations of these DCDT's are shown in Fig. 2-11. DCDT 9 measured the lateral platen displacement in the plane of the panel, DCDT's 10 and 11 measured the axial displacement, or stroke, between the platens, and DCDT's 12 and 13 monitored the platen displacements normal to the plane of the panel. As indicated in Fig. 2-11, the panels were rotated relative to the platens so that the entire width of the panel could be loaded.

2.1.11 Loads

The axial load P_x^{exp} was measured by the test machine's load cell. The shear load P_{xy}^{exp} could not be measured directly. The shear load P_{xy}^{exp} was estimated using strain data from three-arm strain-gage rosettes located across a horizontal cross section of the panel. The strain gages used to estimate the shear load for panel B2,2 are shown in Fig. 2-7 at the panel midlength (10.5 in. from the bottom potting material) and in Fig. 2-8(a) at the stiffener cross section "Location A." The strain readings from back-to-back strain gage pairs were averaged to obtain the reference surface strains ε_x^o, ε_y^o, and γ_{xy}^o, and then multiplied by the membrane stiffnesses A_{ij} (see Eq. (1.1)) to compute the membrane stress resultant N_{xy} at each strain gage location. The N_{xy} stress resultants at each location were multi-

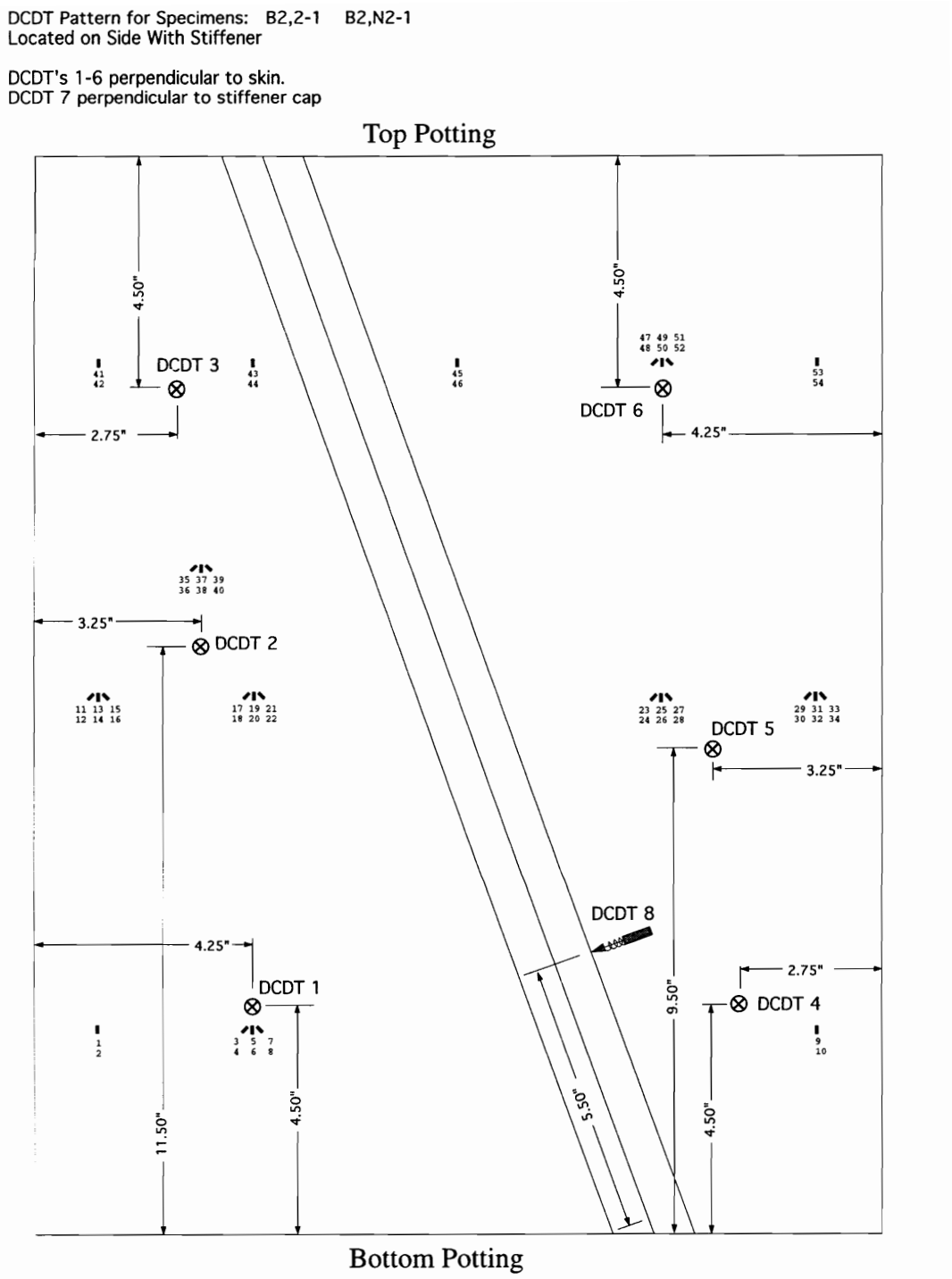

Fig. 2-10 DCDT pattern for panels B2,2 and B2,n2; stiffened side of panel

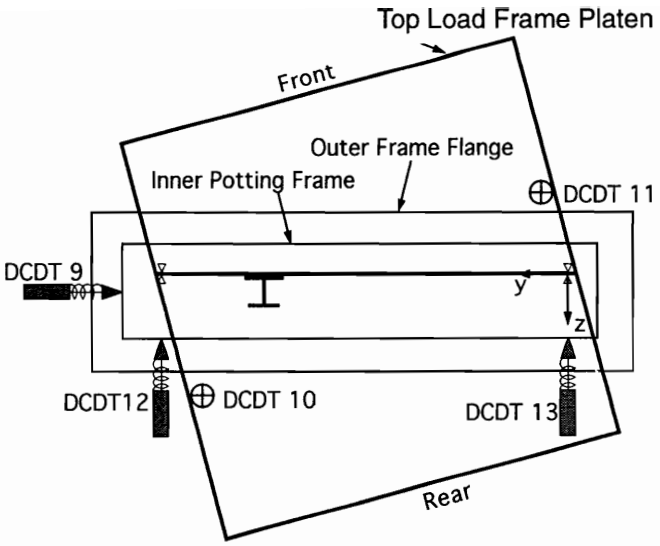

Fig. 2-11 DCDT pattern for panels B2,2 and B2,n2; top load frame platen

plied by the width of the panel adjacent to each strain gage and summed to obtain the integrated panel shear load, P_{xy}^{exp}.

2.2 Testing Procedure

The panels were loaded in compression in a 300-kip-capacity hydraulic test machine located in the Aircraft Structures Laboratory at the Langley Research Center. Readings from the load cell, strain gages, and DCDT's (142 channels) were acquired electronically and were recorded at the rate of one reading of all channels per second. Moiré-fringe patterns were recorded on UCA video tape and with still photographs.

Prior to conducting each test, a procedure was executed to level the platens of the test machine. A load of 2.0 kips was applied to the panel. Readings from back-to-back strain gage pairs located near the corners of the panel were used to detect bending or uneven load introduction. Because of the asymmetry of the panels, strains from diagonally opposed gages were compared. The load was removed and the orientation of the top platen was adjusted to correct for uneven loading. The above sequence was then repeated until the load introduction was satisfactory.

For the actual test, an end shortening was applied under displacement control at approximately 0.010 in. per minute. The panels were loaded until they failed.

2.3 Experimental Results

During loading each panel initially remained flat, and then deformed smoothly from the flat prebuckled state to a stable postbuckling equilibrium state. Each panel exhibited substantial postbuckling strength. Failure occurred due to skin-stiffener separation. As the u and v displacements of the top platen, and the net axial and shear loads, P_x^{exp} and P_{xy}^{exp}, reflect the panel's global response, these quantities are presented for each panel as a guide to the overall observed behavior.

2.3.1 Measured Panel Axial Load vs. End Shortening

The axial load vs. end shortening response of each panel is shown in Fig. 2-12. Buckling is indicated by the change in slope of this response curve. Tangents to the axial load vs. end shortening response on each side of the slope change were used to define two lines for each panel. The slopes of these lines define the prebuckling and initial postbuckling axial stiffness, commonly referred to as EA, while the intersection of these lines defines the buckling load. The procedure for computing panel stiffnesses and the buckling parameters will be described in greater detail in Section 4.2, where the procedure is applied to the experimental and numerically-predicted results. Failure of each panel is indicated in Fig. 2-12 by the open circles at the ends of the curves.

Experimental prebuckling and initial postbuckling axial stiffnesses, buckling loads and end shortening at buckling, and failure loads and displacements are given in Table 2-1. Compared to the baseline configuration, panel B0,0, the configurations with rotated skins and/or rotated stiffeners had lower buckling loads, and lower axial stiffnesses in the prebuckling and initial postbuckling equilibrium states. All of the panels displayed a reduction in stiffness when the skin's buckled. This reduction in axial stiffness is typical of the postbuckling response of stiffened panels. In Table 2-1, the initial postbuckling stiffness of each panel is between 57% and 68% of the prebuckling stiffness of the same panel.

2.3.2 Integrating Stress Resultants

As mentioned in section 2.1.11, the shear load P_{xy}^{exp} was estimated using strain data. The strain distribution across the width of a panel varied with load level. Reference surface membrane strains ε_x^o and γ_{xy}^o in the skin at the midlength of panel B2,2 are shown for two load levels in Fig. 2-13. From Table 2-1, $(P_x)_{cr}^{exp} = 5.12$ kips for this panel. At a prebuckling load of 4.2 kips, the membrane strains are nearly uniform across the panel width. For

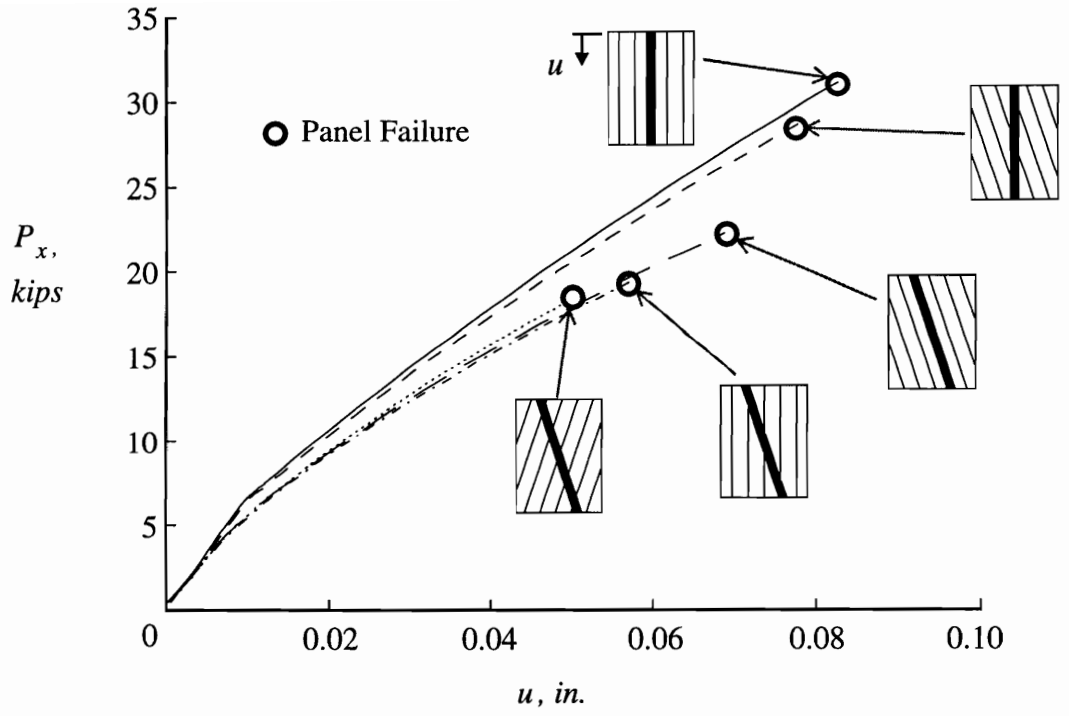

Fig. 2-12 Axial load vs. end shortening response

Table 2-1 Experimental Stiffness, Buckling Loads, and Failure Loads

Configuration	EA (kip)		Buckling		Failure		
	Pre-buckled	Post-buckled	$(P_x)_{cr}^{exp}$ (kip)	u_{cr}^{exp} (mil)	$(P_x)_{ult}^{exp}$ (kip)	u_{ult}^{exp} (mil)	v_{ult}^{exp} (mil)
B0,0	16,380	9,350	6.65	9.74	31.2	82.6	0.710
B0,2	16,020	9,230	6.46	9.82	29.0	78.7	3.86
B2,0	13,180	8,520	5.55	9.57	19.43	56.9	29.4
B2,2	14,430	8,790	5.12	8.38	22.3	68.8	46.8
B2,n2	13,840	9,300	5.16	8.62	18.44	49.8	23.4

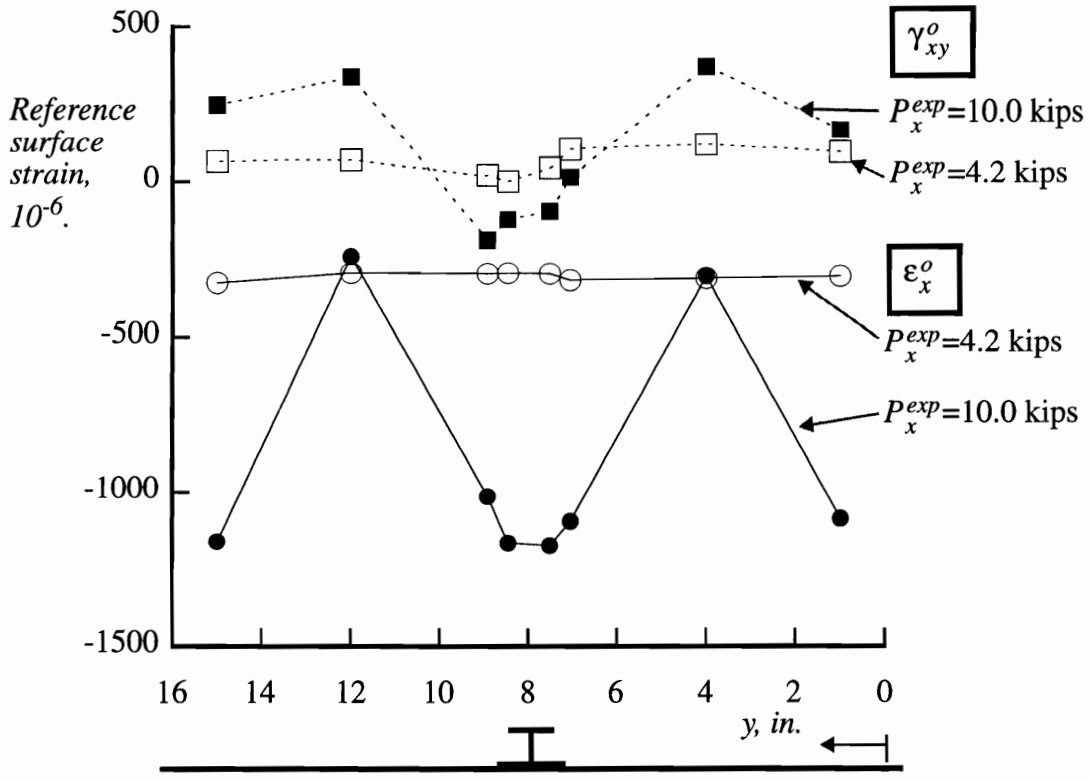

Fig. 2-13 Variation across the width of the reference surface strains ε^o_x and γ^o_{xy}

the postbuckling load of 10.0 kips, the membrane strains show substantial variation across the width. To estimate the shear load P^{exp}_{xy} from strain gage data, accurate material properties must be used to compute stress resultants from strain data, and the method for integrating the stress resultant across the width of the panel must be accurate. In the following sections, the nominal material properties are adjusted to define the material properties of the as-fabricated test panels, and the accuracy of the method used to integrate the stress resultants is accessed. These tasks are achieved by integrating the axial stress resultant N_x across the width of a panel to compute the integrated axial load $P^{exp\,(int)}_x$. The integrated axial load $P^{exp\,(int)}_x$ is compared to the axial load P^{exp}_x that was measured by the load cell.

Adjusting Material Properties for Test Panels

Nominal material properties for AS4-3502 graphite-epoxy tape material were shown in Table 1-1. Rather than use the nominal properties, thickness measurements and the prebuckling response of the baseline configuration, panel B0,0, were used to define the material properties of the as-fabricated test panels.

Thickness measurements were made along the centerline of the unsupported panel skins of all the panels. The average thickness for the 16-layer skins was 0.0784 in., or t_{ply}= 0.00490 in.

The nominal material properties in Table 1-1 are compression properties from Ref. 3, p.116. If these properties were used to estimate the membrane stiffnesses A_{ij} of panel B0,0, then the prebuckling panel stiffness defined by the slope of the integrated axial load $P_x^{exp\,(int)}$ vs. end shortening response was 4.7% lower than the prebuckling panel stiffness defined by the slope of the load cell data P_x^{exp} vs. end shortening response. To achieve better correlation, the nominal material properties were modified by using the rule-of-mixtures procedure described in Ref. 66 to change the fiber volume fraction, V_f, from the assumed value of 0.62 given by Ref. 4 to a value of 0.660. The modified material properties are summarized in Table 2-2.

Table 2-2 Modified Material Properties: Hercules AS4-3502 Graphite-Epoxy

E_1	20.9 Msi
E_2	1.578 Msi
G_{12}	0.886 Msi
ν_{12}	0.297
V_f	0.660
t_{ply}	0.00490 in.

Accuracy of the Integration Method

The method for estimating resultant loads by integrating stress resultants could be checked by comparing the integrated axial load $P_x^{exp\,(int)}$ and the load cell data P_x^{exp}. Using the modified material properties from Table 2-2, this comparison is shown in Fig. 2-14 for each panel. The good correlation of these two quantities in the prebuckling and initial postbuckling load ranges indicates that the modified material properties and the method for integrating the stress resultants are reasonable. Far into the postbuckling load range, the strain distribution becomes less uniform, as shown in Fig. 2-13, and the integration method over-predicts the axial load.

2.3.3 Axial-Shear Force and Displacement Coupling

When a panel with axial-shear stiffness coupling is subjected to a uniform axial end

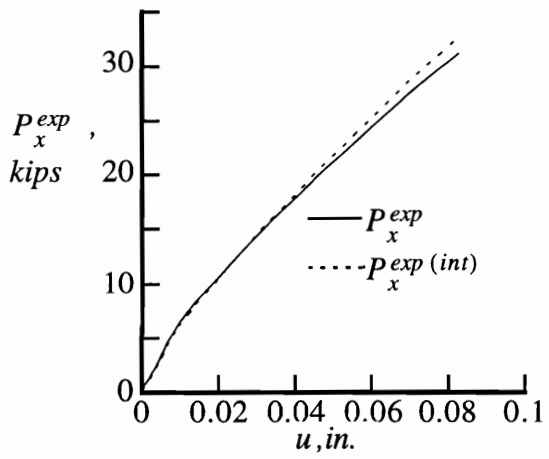

(a) Panel B0,0

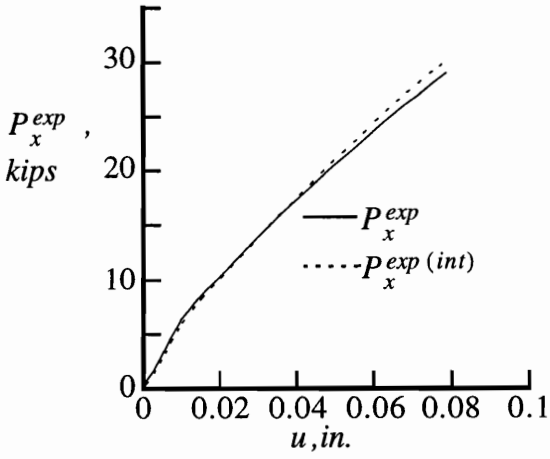

(b) Panel B0,2

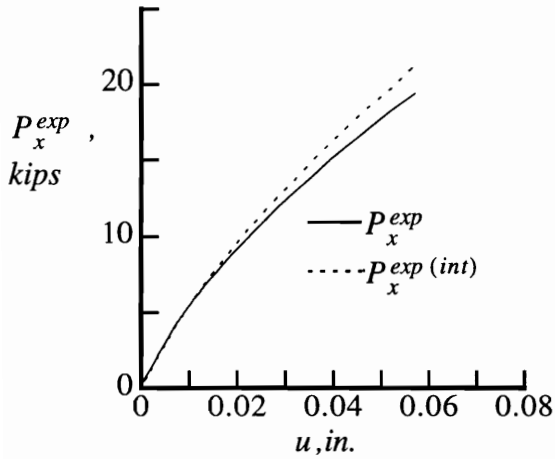

(c) Panel B2,0

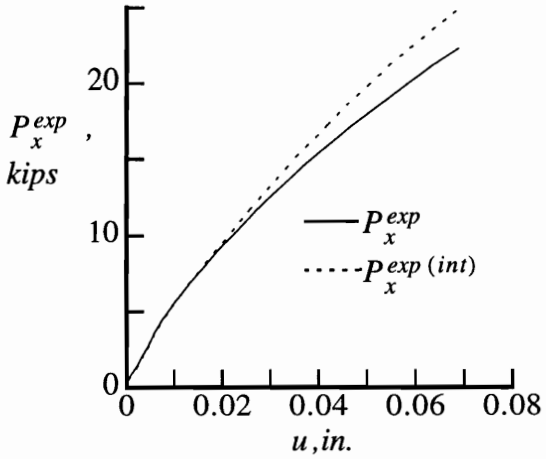

(d) Panel B2,2

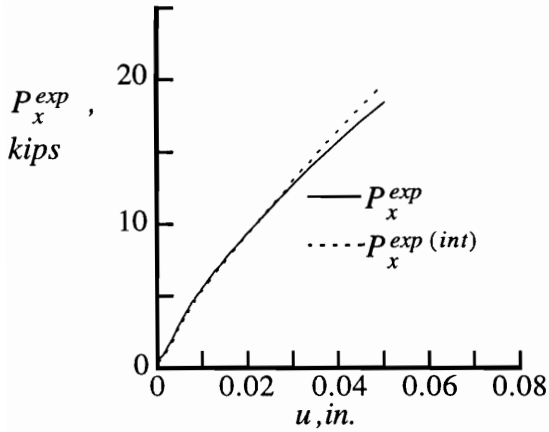

(e) Panel B2,n2

Fig. 2-14 Experimental axial loads: comparison of load cell and integrated stress resultants

shortening, the type of coupling exhibited depends on the boundary condition on the transverse displacement v. Two ideal boundary conditions are considered in Fig. 2-15. The first case assumes that $v = 0$ and is represented in Fig. 2-15(a). In this situation an axial end shortening induces both axial and shear force reactions. This case represents pure force coupling with the amount of force coupling defined by the ratio P_{xy} to P_x. The second case considered assumes that v is uniform, but is unspecified, and the net shear force is equal to zero. As shown in Fig. 2-15(b), instead of a shear force reaction, an axial end shortening induces a shear displacement. This case represents pure displacement coupling with the amount of displacement coupling defined by the ratio v to u. The experimental response was bounded by these two cases. The test machine provided a constraint on the v displacement that was neither rigid nor free. As a result, the panels exhibited a mixture of force and displacement coupling, i.e., a mixed coupling response, as shown in Fig. 2-15(c).

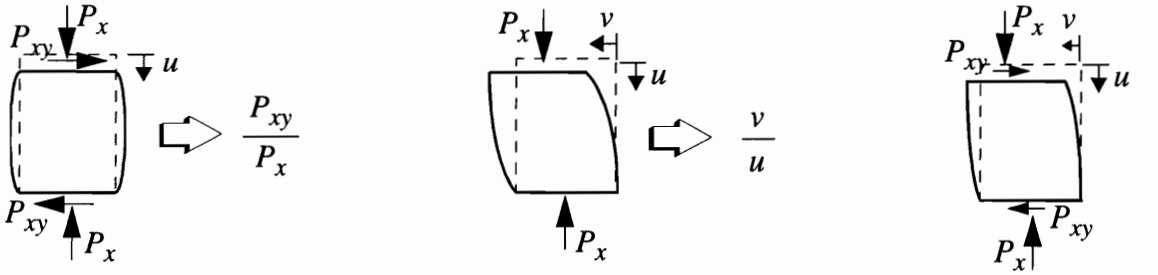

(a) Pure force coupling ($v = 0$, $P_{xy} \neq 0$)

(b) Pure displacement coupling ($v \neq 0$, $P_{xy} = 0$)

(c) Mixed coupling ($v \neq 0$, $P_{xy} \neq 0$)

Fig. 2-15 Axial-shear force and displacement coupling: boundary condition on v

Measured Panel Force Coupling vs. End Shortening

The amount of force coupling in the experiment is defined as the ratio of the panel shear load to the panel axial load, P_{xy}^{exp}/P_x^{exp}. Recall that P_{xy}^{exp} was estimated using strain data while P_x^{exp} was measured by the test machines's load cell. The experimental force coupling vs. end shortening response of each panel is shown in Fig. 2-16. Skin buckling of each panel is indicated in this figure by the open circles. During initial loading the force coupling varied rapidly with increasing load. This rapid variation in coupling probably corresponded to nonuniform load introduction and seating of the test machine and panels. The force coupling in the panels with the unrotated stiffener was small for the entire loading spectrum. The panels which had the stiffener rotated displayed an increase in force coupling after skin buckling.

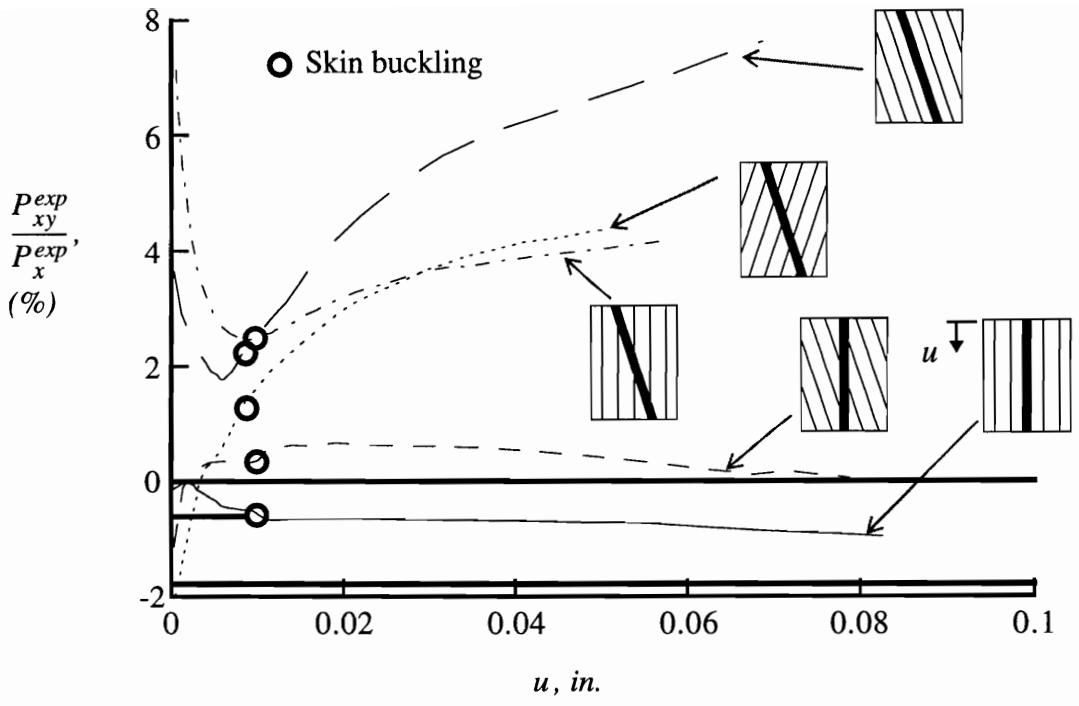

Fig. 2-16 Experimental force coupling vs. end shortening response

Measured Panel Displacement Coupling vs. End Shortening

The amount of displacement coupling in this experiment is defined as the ratio of the panel shear displacement to the panel end shortening, v/u. The experimental displacement coupling vs. end shortening response of each panel is shown in Fig. 2-17. Skin buckling of each panel is indicated in this figure by the open circles. The behavior resembles that of the force coupling shown in Fig. 2-16. During initial loading the displacement coupling varied rapidly. The initial variations in displacement coupling occurred when the u and v displacements were less than 0.005 in. and the aforementioned seating of the test machine and panels translated into substantial displacement coupling. As the end shortening increased, the panel behavior stabilized. The displacement coupling in the baseline configuration B0,0 was near zero for all loads. For the panel with the unrotated stiffener and the skin rotated 20°, panel B0,2, the displacement coupling was about 10% before the skin buckled and reduced to less than 10% after the skin buckled. The panels which had the stiffener rotated displayed an increase in displacement coupling after the skin buckled. The panel with the skin and stiffener both rotated in the same direction displayed the maximum displacement coupling, reaching 68% just prior to failure.

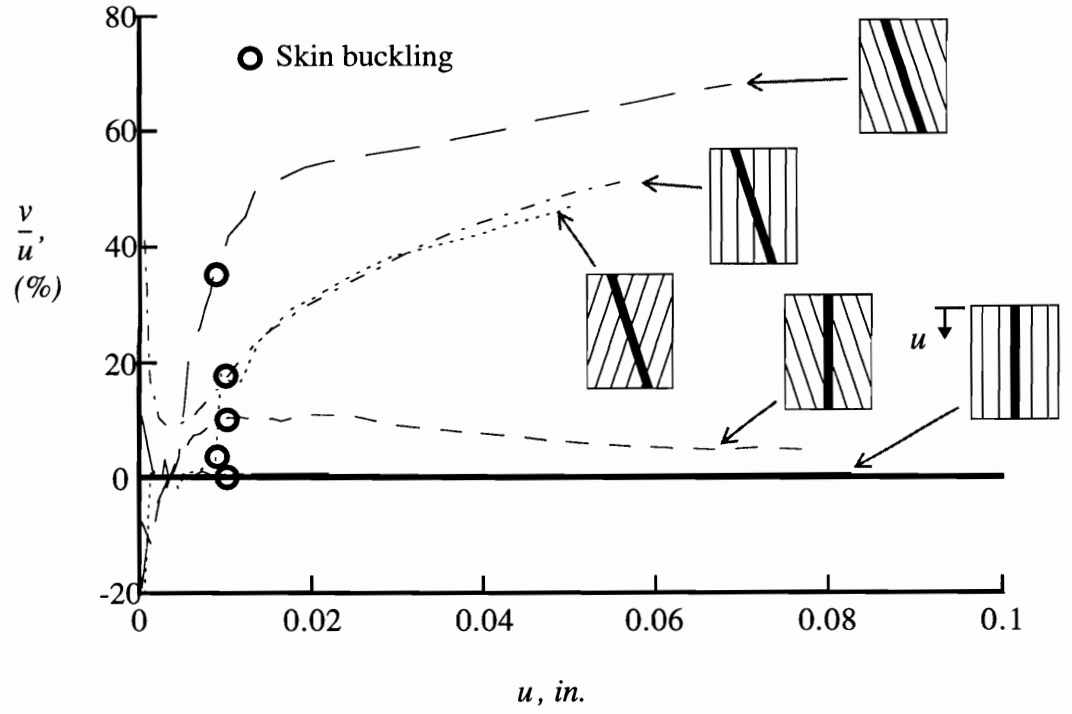

Fig. 2-17 Experimental displacement coupling vs. end shortening response

2.3.4 Out-of-Plane Skin Displacements

Moiré-fringe patterns representing the out-of-plane displacement of the skin were used to identify the buckling mode of each panel and to monitor the postbuckling out-of-plane deformations. All panels had a buckling mode with two lateral half waves.

The panels with the unrotated stiffener had buckling modes with three axial half waves. The development of the out-of-plane skin displacement in the postbuckling response for panel B0,0 is illustrated by the sequence of moiré-fringe patterns, as viewed from the unstiffened side of the panel, shown in Fig. 2-18. Panel B0,0 had the skin and the stiffener unrotated, and the postbuckling skin displacement was typical of a traditional postbuckled stiffened panel.The development of the out-of-plane skin displacement in panel B0,2 was very similar to that shown for panel B0,0.

When the stiffener was rotated, the skin panel was divided into sections that were tapered in width. The buckling modes for panels with the stiffener rotated were initially dominated by single axial half waves located where the skin sections were the widest. With additional loading, additional axial half waves developed in the narrower skin sec-

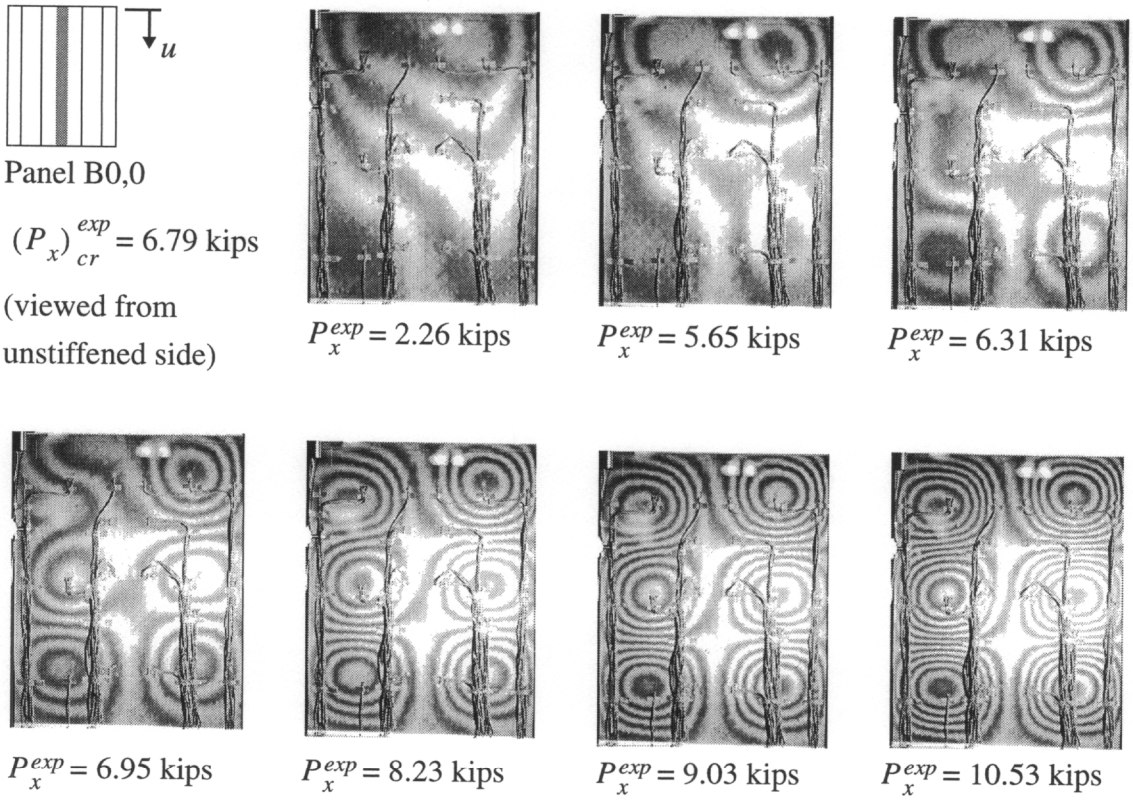

Fig. 2-18 Panel B0,0: moiré-fringe patterns of developing out-of-plane skin displacement during buckling

tions. The development of the out-of-plane skin displacement in the postbuckling response for panel B2,2 is illustrated by the sequence of moiré-fringe patterns, as viewed from the unstiffened side of the panel, shown in Fig. 2-19. Panel B2,2 had the skin and stiffener rotated in the same direction. The rotated stiffener created a node line along the stiffener and caused the postbuckling deflections to be skewed. The development of the out-of-plane skin displacement in panels B2,0 and B2,n2 was very similar to that shown for panel B2,2.

2.3.5 Failure

All of the panels failed when the skin of the panel separated from the stiffener. In each case this separation was a dynamic event, causing damage and greatly reducing the load carrying capacity of the panel. Photographs of the stiffened side of the panels which illustrate that the skin and stiffener separated are shown in Fig. 2-20. In Fig. 2-20(a) a photograph shows the skin of panel B0,0 separated from the stiffener along the entire length of

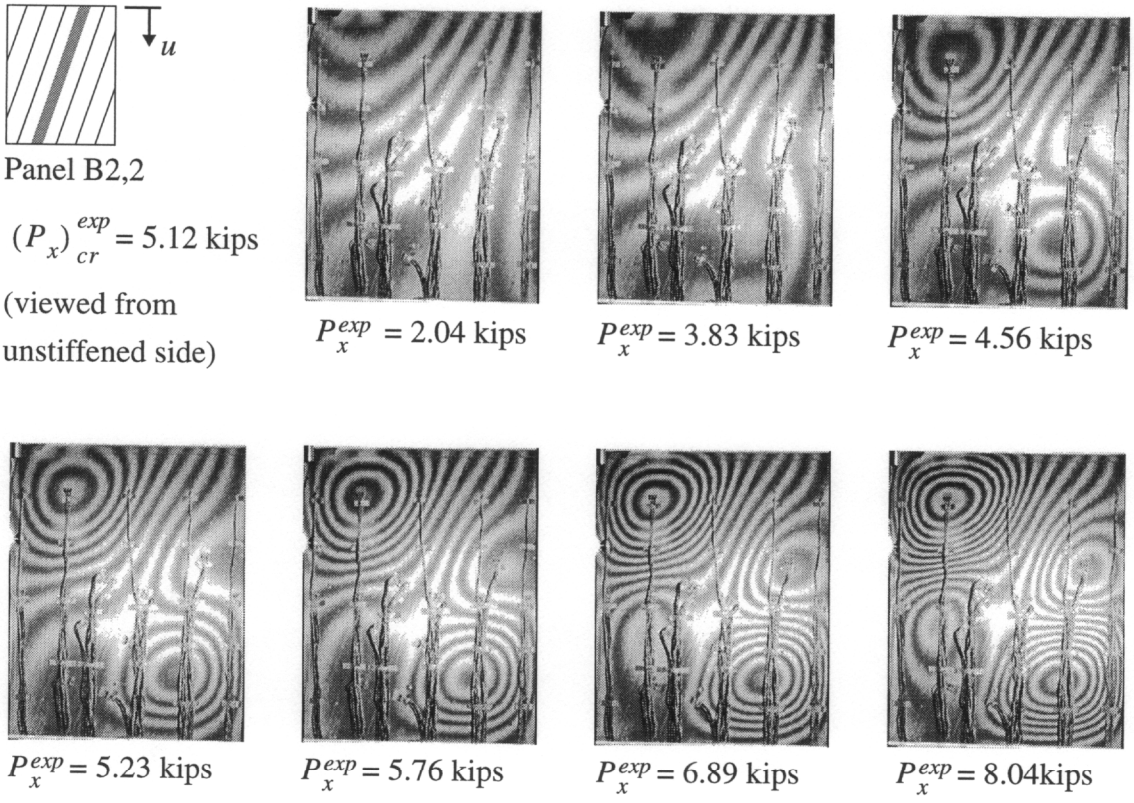

Fig. 2-19 Panel B2,2: moiré-fringe patterns of developing out-of-plane skin displacement during buckling

the stiffener. In Fig. 2-20(b) a photograph shows the skin of panel B2,0 separated from the stiffener in the upper half of the panel. As illustrated in this photograph, a portion of the first layer of the panel skin stayed attached to the stiffener when the skin and stiffener separated.

Moiré-fringe patterns of the out-of-plane skin displacements of each panel just prior to failure, and just after failure, are shown in Fig. 2-21(a) and Fig. 2-21(b), respectively. The photographs in Fig. 2-21(a) show the last moiré-fringe patterns that were recorded prior to skin-stiffener separation. The ultimate load for each panel is shown to the left of the moiré-fringe patterns in Fig. 2-21(a). The photographs in Fig. 2-21(b) show the moiré-fringe patterns that were recorded after skin-stiffener separation. Separation of the skin and stiffener results in large out-of-plane deformations in the skin, and a reduction in the panel axial load, $(P_x)^{exp}$. The residual load in each panel after skin-stiffener separation is shown to the left of the moiré-fringe patterns in Fig. 2-21(b). The moiré-fringe patterns indicate that

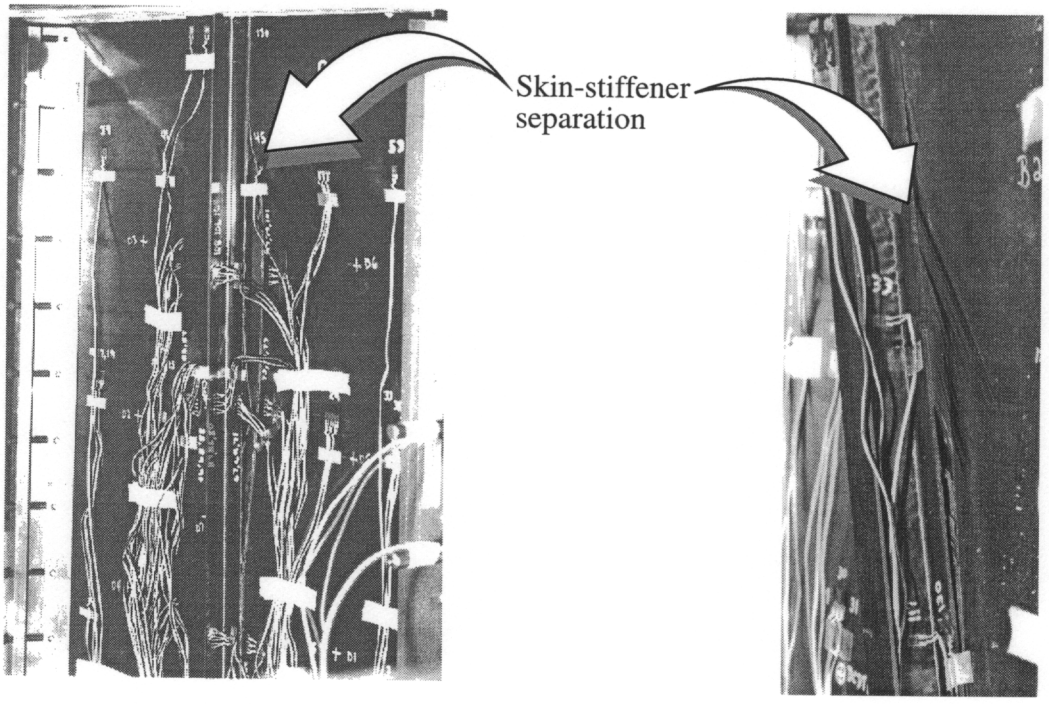

(a) Panel B0,0

(b) Panel B2,0

Fig. 2-20 Photos of failed panels illustrating skin-stiffener separation

panels B0,0 and B0,2 had skin-stiffener separation over the entire length of the stiffener, panel B2,0 had skin-stiffener separation over the top half of the stiffener length, and panels B2,2 and B2,n2 had skin-stiffener separation over the bottom half of the stiffener length.

The ultimate axial loads and corresponding load frame platen displacements at failure for each panel were reported previously in Table 2-1. It is important to note that the panels with the stiffener rotated 20° had significantly lower failure loads and residual load carrying capacity than the panels with the unrotated stiffener.

2.3.6 Additional Experimental Results to be Shown in Chapter 4

The primary objectives of the exploratory experimental program were to demonstrate the structural behavior of these tailored panels in order to guide analytical modeling, benchmark analytical results, and assist in identification of any unexpected physical phenomenon. General experimental procedures and results which reflect the global response of the test panels have been presented. The focus now shifts to development of finite element models which accurately represent the physical conditions. In Chapter 3 modeling procedures are defined which were used to create numerical models for each panel. The

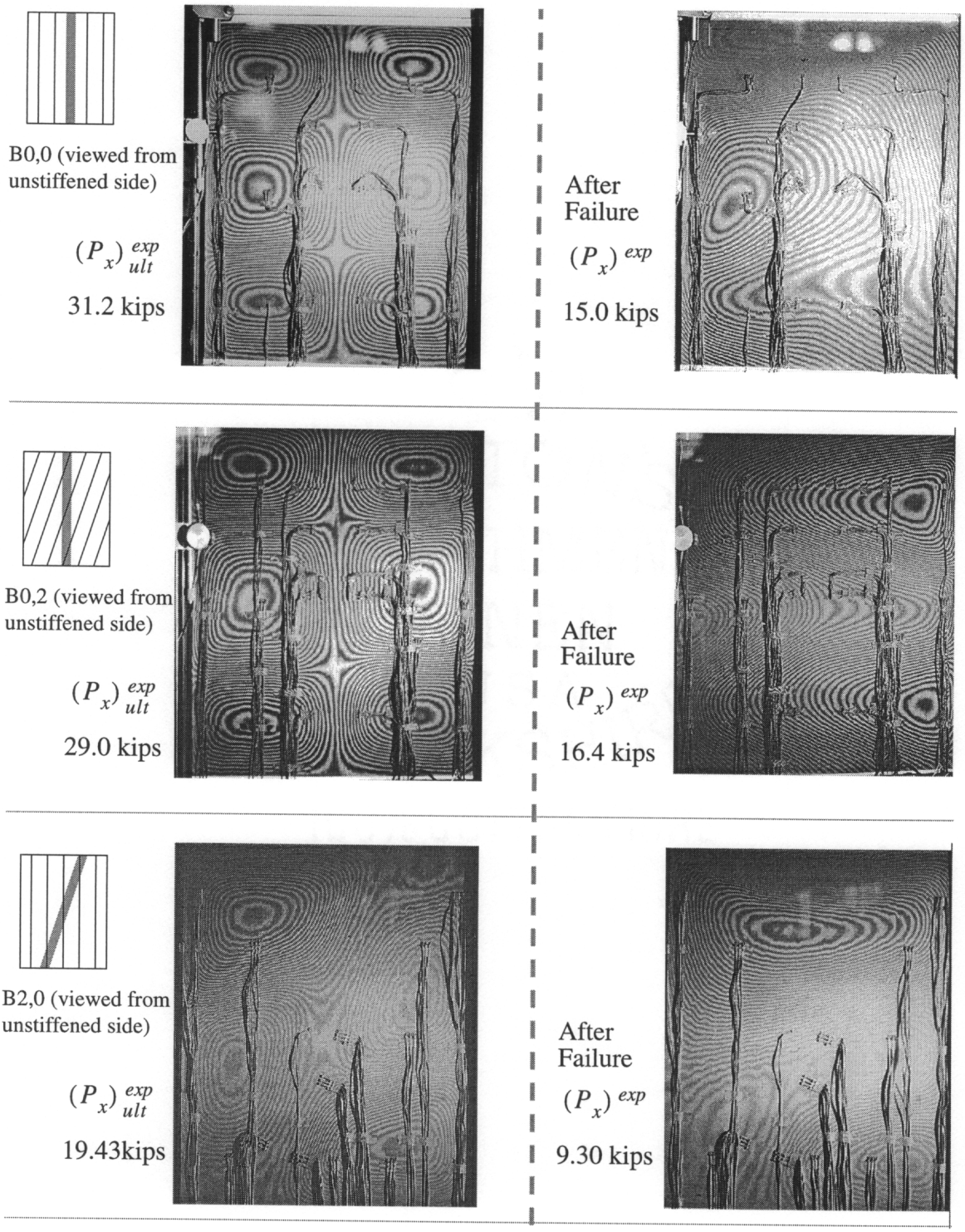

Fig. 2-21 Moiré-fringe patterns prior to and after skin-stiffener separation

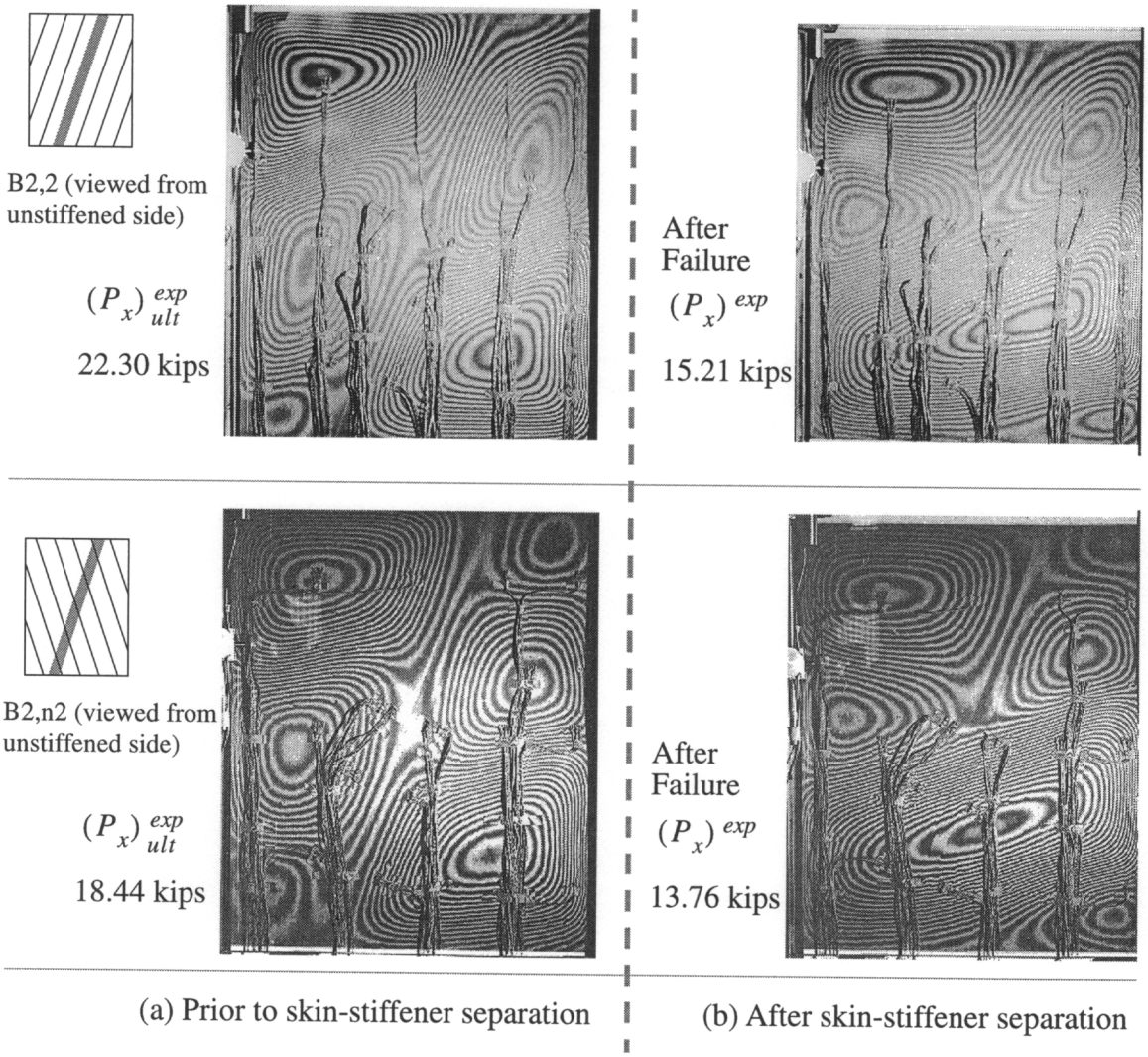

Fig. 2-21 Continued

numerical models created to simulate the response of each panel are verified in Chapter 4 by correlating numerically-predicted results with experimental results. The experimental results presented in Chapter 4 include:

- load versus end shortening relations
- out-of-plane displacement contours of the panel skin as indicated by moiré-fringe patterns
- out-of-plane displacements of the panel skin at discrete points measured using DCDT's

- axial-shear force coupling: axial force readings from the load cell, and shear force computed by integrating measured shear strains from electrical resistance strain gages
- axial-shear displacement coupling: end shortening and transverse displacements of the load frame platens measured using DCDT's.

3. Development of Numerical Models

All numerical results were computed using the STAGS finite element code (Ref. 50). This code was used with success in Refs. 46 and 47 to analyze the postbuckling response of stiffened panels, and was selected for the current effort because of its nonlinear solution capabilities, and its algorithms to resolve singularities at the buckling load.

Prior to conducting the experiments, preliminary analyses using crude models were conducted in order to obtain estimated buckling loads and buckling modes for each specimen. These results were used to prescribe the location of instrumentation for data acquisition during testing.

After completing the experiments, great efforts were made in interpreting experimental data and developing a finite element model which could accurately represent the conditions in the experiments. The ultimate goal of the model development was to understand the response seen in the experiments. To define the level of detail required in the model, a study was conducted to quantify the effect of several modeling details on the predicted response of a composite plate with skewed material axes and skewed stiffeners. The panel with the stiffener and skin both rotated in the same direction, panel B2,2, was selected for this study. The lessons learned from the study were then applied to develop the numerical models for the other panels.

The procedure for the study was as follows. First, a simple baseline finite element model was defined. Because the panel response predicted by this model did not correlate with the experimental results, a list of possible modeling refinements was developed that could possibly make the model more closely resemble the test panel. The effect of each modeling refinement was assessed by creating additional models, each model introducing only one refinement to the baseline model, and comparing the response of each new model to the baseline model. After each modeling refinement was assessed independently, a model

was assembled that incorporated all of the refinements. The predicted response of this model was then compared to the baseline model and the experimental data for panel B2,2. The following sections in this chapter discuss the development and refinement of the model.

Because the panels shown in Fig. 2-1(c) had the top and bottom edges potted, the bottom edge of the model was fully constrained while the top edge was loaded by specifying uniform u- and v-displacements. The net axial and shear loads, P_x and P_{xy}, are determined by summing the reactions in the model. The plate element used in the finite element models was the STAGS 410 displacement-based 4-node quadrilateral shell element with 3 translational and 3 rotational degrees of freedom per node, as shown in Fig. 3-1. The translational degrees of freedom u, v, and w are the translations expressed in the fixed element-local x-y-z coordinate system. The rotational degrees of freedom Ru, Rv, and Rw are the rotations about the x-, y-, and z-axes, respectively. The rotation about the shell element normal, Rw, is called the drilling degree of freedom.

Linear buckling and nonlinear postbuckling analyses were conducted for each model. The panel's global response was reflected in the predicted linear buckling load and nonlinear load vs. end shortening response. These results are presented for each model as a guide to the overall predicted behavior. Recall from Table 2-1, $(P_x)_{cr}^{exp} = 5.12$ kips for panel B2,2. In this chapter, load vs. end shortening results for loads up to 15 kips are considered.

(Note: The finite element model for panel B2,2 modeled the stiffener cap with a 1.0 in. width to account for the modification to the panel that was made during the fabrication and reported in Section 2.1.4.)

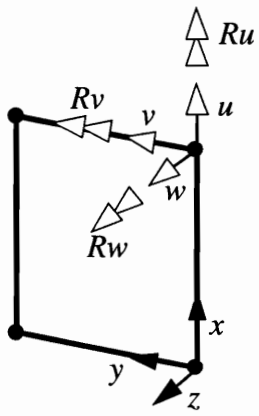

Fig. 3-1 Directions of translational and rotational degrees of freedom

3.1 The Baseline Model

The baseline model, which was the starting point for model development and is shown in Fig. 3-2(a), represented only the unsupported section of the panel, i.e., the 21.0 in. length between the potted ends and the 16.0 in width between the knife edge supports. The panel was assumed to be perfectly flat. The boundary conditions were typical of a clamped-clamped—simply-supported–simply-supported panel with a uniform end shortening:

- Top edge: u = constant, (v, w, Ru, Rv, Rw) = 0.
- Bottom edge: (u, v, w, Ru, Rv, Rw) = 0.
- Sides: (w, Rv) = 0.

The stiffener was modeled as a discrete beam stiffener, rotated 20° from the x-axis, and located with an eccentricity relative to the reference plane of the skin. Nominal material properties from Table 1-1 on page 12 were used in the baseline model.

A linear buckling analysis using the baseline model predicted $(P_x)_{cr}$ = 6.52 kips, as compared to $(P_x)_{cr}^{exp}$ = 5.12 kips for panel B2,2. The axial load vs. end shortening response for the baseline model and the experiment are compared in Fig. 3-2(b). The results from the baseline model do not correlate well with the experimental response. The baseline model over-predicted the stiffness and the buckling load of the panel. Below is a list of modeling refinements that were employed to make the baseline model more closely simulate the response of the panel:

1. The discrete beam stiffener was replaced with a branched shell model.
2. The length of the panel in the potted sections on each end was included in the model.
3. The width of the panel outside the knife edge supports was included in the model.
4. The modified material properties shown in Table 2-2 were used.
5. The top edge of the model was allowed to translate uniformly in the y-direction.
6. Initial geometric imperfections were introduced.

The next section discusses the degree to which each of these refinements influenced the predicted response of the finite element model.

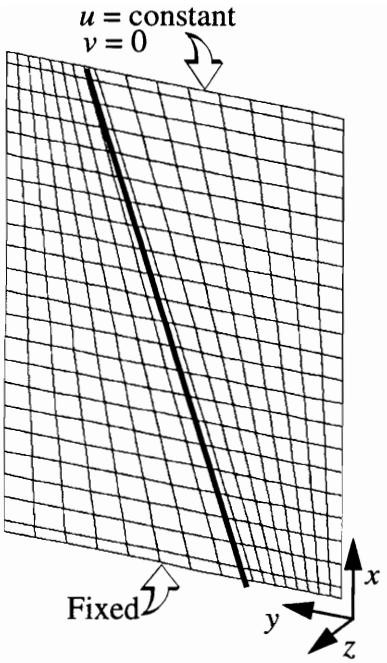

(a) Baseline model

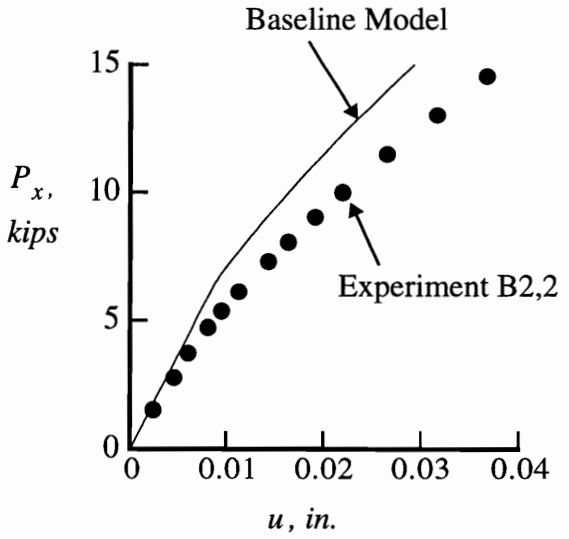

(b) Axial load vs. end shortening response

Fig. 3-2 Baseline model and experiment B2,2

3.2 Incremental Modifications to the Baseline Model

Each of the model refinements just mentioned was independently introduced into the baseline model to show how each model refinement altered the predicted response.

3.2.1 Branched Shell Stiffener Model

The discrete beam stiffener in the baseline model was replaced with a branched shell model as shown in Fig. 3-3. The cap, web, and attachment flanges of the stiffener geometry shown in Fig. 2-1(a) were modeled with plate elements. The strips of 0° fibers that filled the void at the top and bottom of the web (Fig. 2-1(b) and 2-6) were modeled as discrete beams located at each side of the web. The stiffener model was attached to the skin model by imposing full displacement compatibility of coincident nodes. To provide coincident nodes, the reference surface of the stiffener attachment flange was located at the midplane of the panel skin, and the attachment flange laminate was assigned an eccentricity of +0.080 in. based on its physical dimensions.

A linear buckling analysis of the model with the branched shell stiffener predicted $(P_x)_{cr}$ = 7.06 kips. The axial load vs. end shortening response for this model and the baseline model are compared in Fig. 3-3(b). As can be seen in the figure, the prebuckling response of the two models were the same, but the model with the branched-shell stiffener had a higher buckling load and higher postbuckling stiffness. The buckling load and post-buckling stiffness were higher because the attachment flange of the branched shell stiffener provided out-of-plane and inplane stiffness to the panel skin over a finite width, rather than along a line.

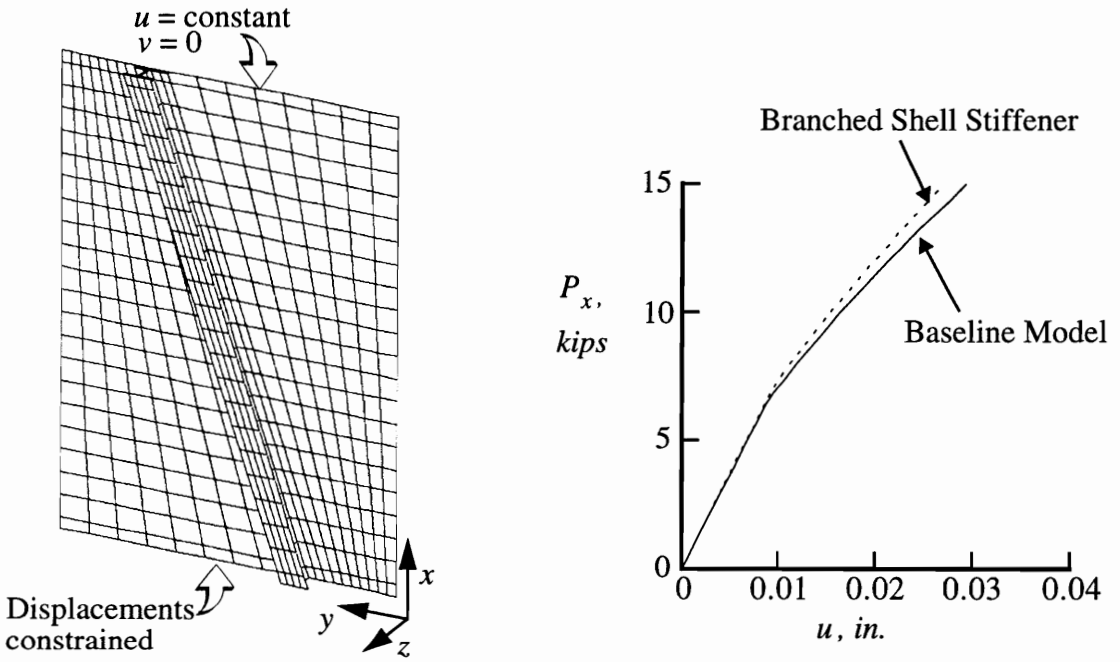

(a) Model with branched shell stiffener (b) Axial load vs. end shortening response

Fig. 3-3 Branched shell stiffener

3.2.2 Extended Length in Potting

The panels had a total length of 24.0 in. The top and bottom edges were potted in 1.5 in. of casting compound, as described in Section 2.1.5. While the baseline model included only the 21.0 in. length of unsupported panel between the potted ends, the model shown in Fig. 3-4(a) used an extended length to represent the potted portion of the panel. The uniform end shortening was still applied at the top edge of the model. The dashed lines on the model indicate the sections of the model located within the potting. It was assumed that

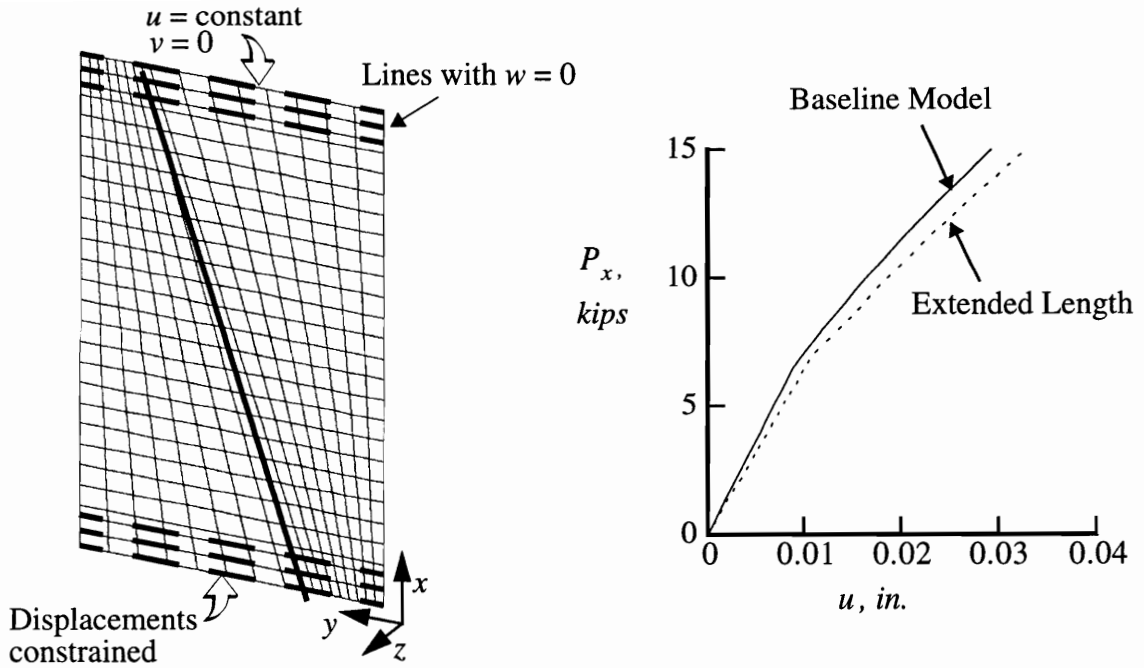

(a) Model with extended length in potting

(b) Axial load vs. end shortening response

Fig. 3-4 Extended length in potting

the potting provided support perpendicular to the panel components. This support was modeled by setting $w = 0$ for nodes within the potting and constraining the u- and v-displacements such that the beam stiffener exited the potted regions at a constant 20°. A linear buckling analysis of the model with the extended length predicted $(P_x)_{cr} = 6.47$ kips. The axial load vs. end shortening response for this model and the baseline model are compared in Fig. 3-4(b). The buckling loads from the two models were similar, but the extended length model was less stiff for all loads. This was the case because axial strain was allowed to occur within the potted ends of the extended length model. For a given amount of end shortening, the longer model had a lower strain, and therefore, a lower axial load.

3.2.3 Extended Width Outside Knife-Edge Supports

The panels had a total width of 16.5 in. The unloaded edges had knife-edge supports located 0.25 in. from the panel edges. While the baseline model included only the 16.0 in. width of panel between the knife-edge supports, the model shown in Fig. 3-5(a) represents an extension to include the entire width. The dashed lines on the model indicate where the

$w = 0$ constraint was imposed. A linear buckling analysis of the model with the extended width predicted $(P_x)_{cr} = 6.74$ kips. The axial load vs. end shortening response for this model and the baseline model are compared in Fig. 3-5(b). The buckling loads from the

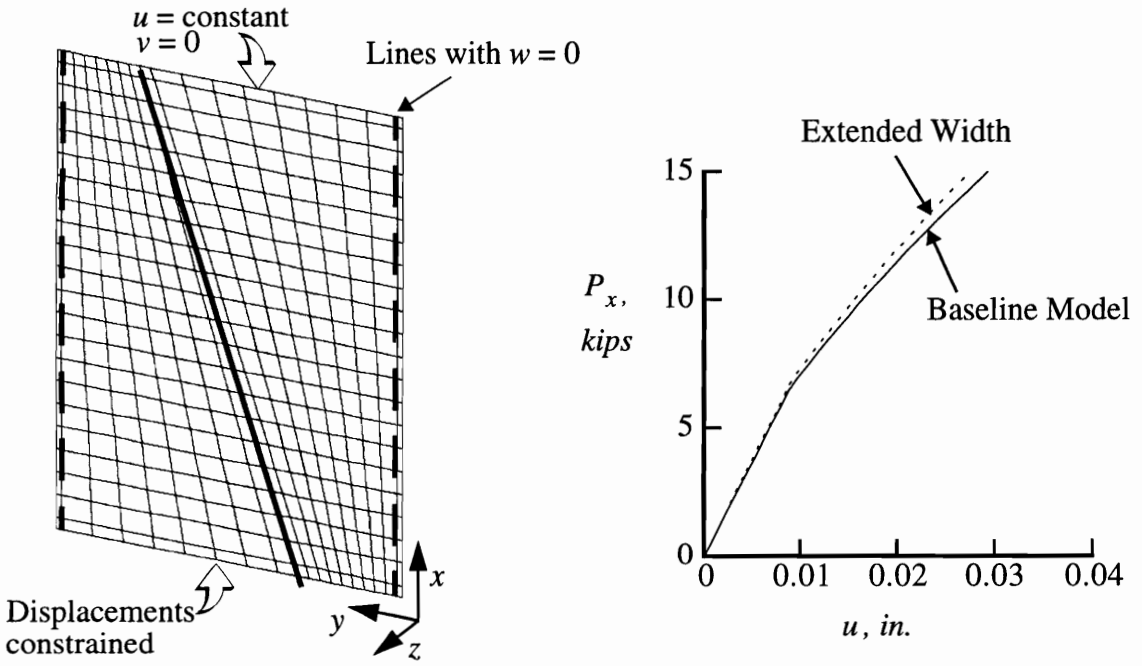

(a) Baseline model

(b) Axial load vs. end shortening response

Fig. 3-5 Extended width outside knife-edge supports

two models were similar, but the extended width model was stiffer for all loads. The difference in stiffness increased in the postbuckling response, as the buckled skin transferred load into the stiffener and the skin supported by the knife-edges.

3.2.4 Modified Material Properties

Earlier it was discussed how the ply thickness and fiber volume fraction were altered to provide better correlation between the axial load obtained by integrating the stress resultants, $P_x^{exp\,(int)}$, and the load cell data P_x^{exp}. The modified material properties were summarized in Table 2-2. A linear buckling analysis of the model which used the modified material properties predicted $(P_x)_{cr} = 4.97$ kips. The axial load vs. end shortening response for this model and the model with nominal material properties are compared in Fig. 3-6. Using the modified material properties reduced the prebuckling panel stiffness by

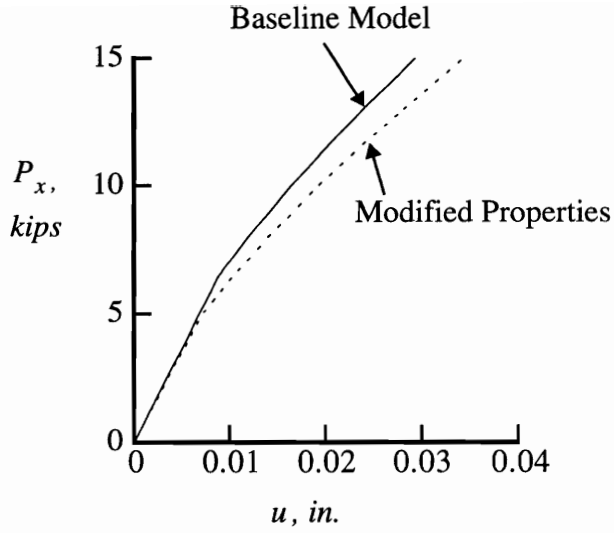

Fig. 3-6 Modified material properties: axial load vs. end shortening response

only 4.4%, but reduced the buckling load by 31%. The large reduction in the buckling load reflected the loss of local bending stiffness caused by reducing the ply thickness by 11%.

3.2.5 Unspecified *v*-displacement on the Top Edge

The baseline model had $v = 0$ on both of the loaded edges. For panel B2,2 subjected to end shortening, this constraint caused the force coupling shown in Fig. 2-15(a). If the model was modified so that the *v*-displacement of the top edge was uniform and unspecified, then $P_{xy} = 0$ and the displacement coupling situation in Fig. 2-15(b) was created. A linear buckling analysis of the model which had the *v*-displacement unspecified predicted $(P_x)_{cr} = 5.83$ kips. The axial load vs. end shortening responses for this model and the baseline model are compared in Fig. 3-7(a). Releasing the constraint of the *v*-displacement lowered the buckling load and reduced the axial stiffness. The displacement coupling (v/u) for this model and the force coupling (P_{xy}/P_x) for the baseline model are compared in Fig. 3-7(b). The behavior of the coupling in the two cases was very similar. The coupling response was constant in prebuckling and increased substantially in postbuckling. The experimental results for panel B2,2 presented in Figs. 2-16 and 2-17, demonstrate a mixture of force coupling and displacement coupling, each to a lesser degree than shown in Fig. 3-7(b). The mixture of force coupling and displacement coupling indicates that the test machine imposed a constraint on the *v*-displacement that was between fixed and unconstrained.

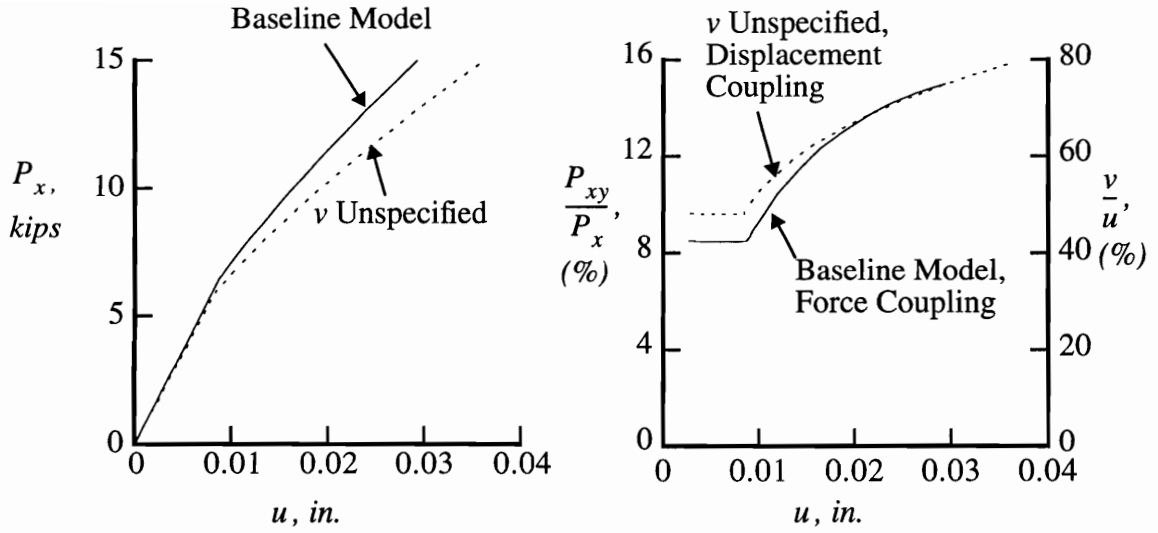

(a) Axial load vs. end shortening response

(b) Force coupling and displacement coupling

Fig. 3-7 Unspecified *v*-displacement

3.2.6 Initial Geometric Imperfections

When trying to correlate the response of the test panels with the predicted results, measured surface shape data were used to prescribe initial out-of-plane geometric imperfections. Surface shape data were obtained by the procedure described in Section 2.1.7. The procedure for including measured shape data is described below.

Converting Surface Shape Data into Mathematical Approximations of the Initial Geometric Imperfections

The measured surface shape data, $w_{measured}$, were used to compute Fourier series representations of the surface shape, $\hat{w}(x, y)$. Four different series representations were considered:

$$\hat{w}(x,y) = \sum_{m=1}^{NTERMS} \sum_{n=1}^{NTERMS} (FA)_{mn} cos\frac{(m-1)\pi x}{L} \cdot cos\frac{(n-1)\pi y}{W} \quad , \qquad (3.1)$$

$$\hat{w}(x,y) = \sum_{m=1}^{NTERMS} \sum_{n=1}^{NTERMS} (FB)_{mn} sin\frac{(m-1)\pi x}{L} \cdot sin\frac{(n-1)\pi y}{W} \quad , \qquad (3.2)$$

$$\hat{w}(x, y) = \sum_{m=1}^{NTERMS} \sum_{n=1}^{NTERMS} (FC)_{mn} \cos\frac{(m-1)\pi x}{L} \cdot \sin\frac{(n-1)\pi y}{W} \quad , \tag{3.3}$$

and

$$\hat{w}(x, y) = \sum_{m=1}^{NTERMS} \sum_{n=1}^{NTERMS} (FD)_{mn} \sin\frac{(m-1)\pi x}{L} \cdot \cos\frac{(n-1)\pi y}{W} \quad , \tag{3.4}$$

where $(FA)_{mn}$, $(FB)_{mn}$, $(FC)_{mn}$, and $(FD)_{mn}$ are Fourier coefficients computed by numerical integration using the trapezoidal rule, *NTERMS* is the range of terms in the series, and L and W are dimensions over which the surface shape was measured. To determine which Fourier series best represented the measured data, an error parameter was defined by

$$ERROR = \sqrt{\frac{\sum_{Ndata} (\hat{w} - w_{measured})^2}{\sum_{Ndata} (w_{measured})^2}} \quad . \tag{3.5}$$

This error parameter was computed for each series representation as a function of *NTERMS*. The variation of the error parameter with increasing value of *NTERMS* is shown for panel B2,2 in Fig. 3-8. The results in this figure indicate that the series given in Eq. (3.1) best represented the measured surface shape. A value of *NTERMS* = 7 was selected in order to avoid high frequency oscillations in the derivatives of $\hat{w}$. Contour plots of the measured surface shape and the computed Fourier representation of the shape are shown in Fig. 3-9. The magnitude of the imperfection is normalized by the skin thickness and exceeds half the skin thickness in both the positive and negative z-directions.

The surface shape was measured on the unstiffened side of the skin after the panels were potted. The potting and frame around the potting interfered with measuring the surface shape of the skin in locations that were within 0.25 in. from the potting and inside the potting. Thus the length L in the Fourier series representation of the measured data was equal to 20.5 in. When the Fourier series representation was applied to define the shape imperfection in the finite element models, part of the finite element model was located in the region where the shape could not be measured. At these locations in the model, the imperfection was computed by evaluating the Fourier series representation at the nearest point on the panel where the surface shape was measured. An external user-written subroutine

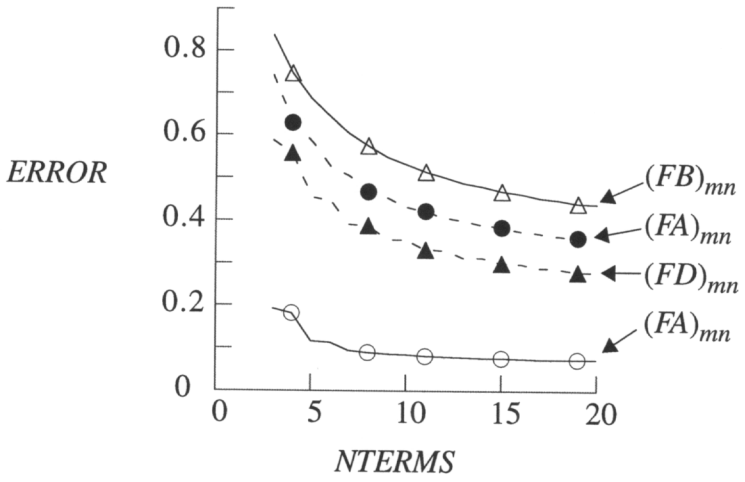

Fig. 3-8 Error parameter for approximation of surface shape: panel B2,2

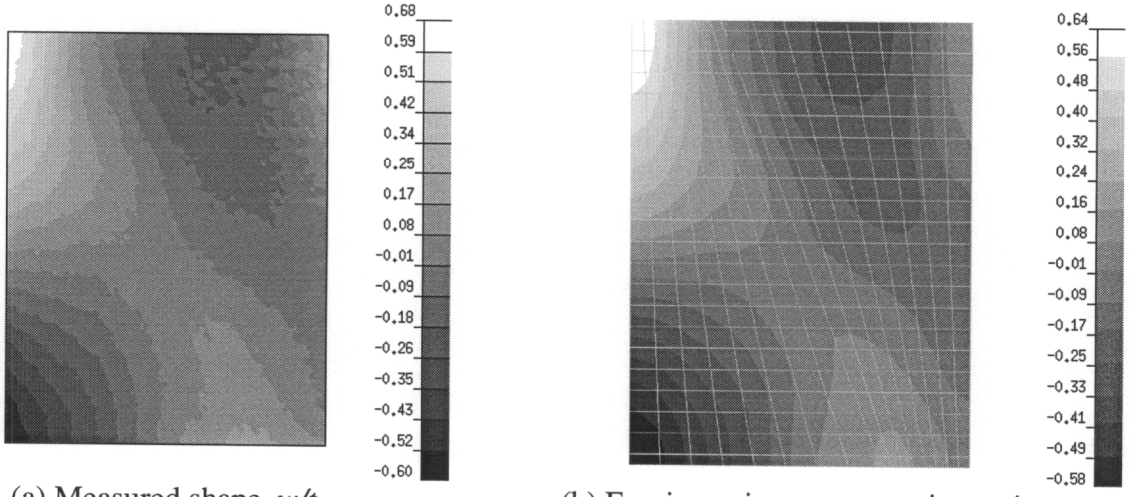

(a) Measured shape, *w/t*

(b) Fourier series representation, *w/t*

Fig. 3-9 Surface shape for panel B2,2

was used to define an initial geometric imperfection in the form of higher-order initial strain imperfections in the STAGS finite element analysis. Details of the implementation of the initial geometric imperfections can be found in Ref. 51.

Applying Shape Imperfections to Baseline Model

The flat baseline model was modified by introducing an initial geometric imperfection as defined by the measured surface shape. The axial load vs. end shortening response for the imperfect model and the baseline model are compared in Fig. 3-10. The measured imper-

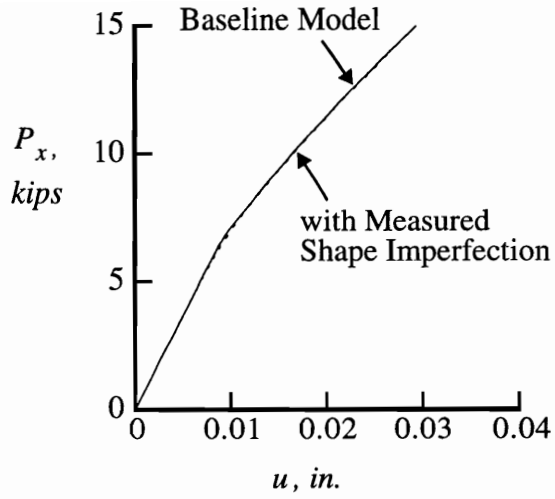

Fig. 3-10 Initial geometric imperfection: axial load vs. end shortening response

fection shape for this panel seemingly had little affect on the over-all response of the model. The bifurcation behavior of the flat baseline model created a buckling deformation that had little directional dependence, i.e., the baseline model may have buckled into a mode in the opposite direction of the buckling observed during the experiment. On the other hand, when an end shortening was applied to the imperfect model, compressive membrane stresses caused nonzero out-of-plane displacements prior to skin buckling. Near the buckling load the out-of-plane displacements of the imperfect panel grew smoothly and developed into a postbuckled pattern in the skin. The imperfection removed the bifurcation behavior observed with the baseline model, and increased the likelihood that the predicted and experimental deformations would be in the same direction.

3.3 The Advanced Model

Based on the model refinements just discussed, an advanced finite element model was developed to simulate the response of panel B2,2. This model is shown in Fig. 3-11(a). The stiffener was represented by branched plates, the entire length and width of the panel was included in the model, and the modified material properties in Table 2-2 were used. The measured shape data shown in Fig. 3-9(a) were converted into a Fourier series representation (Fig. 3-9(b)) and applied as an initial geometric imperfection. The question of the constraint on the v-displacement was addressed by specifying that the u- and v-dis-

placement of the top edge be defined by measured experimental data u^{exp} and v^{exp}.

A nonlinear postbuckling analysis of the advanced model of panel B2,2 was conducted. The axial load vs. end shortening response for the baseline model, advanced model, and the experiment are compared in Fig. 3-11(b). The advanced model accurately simulated the overall response of the panel in the prebuckling and postbuckling range of loading.

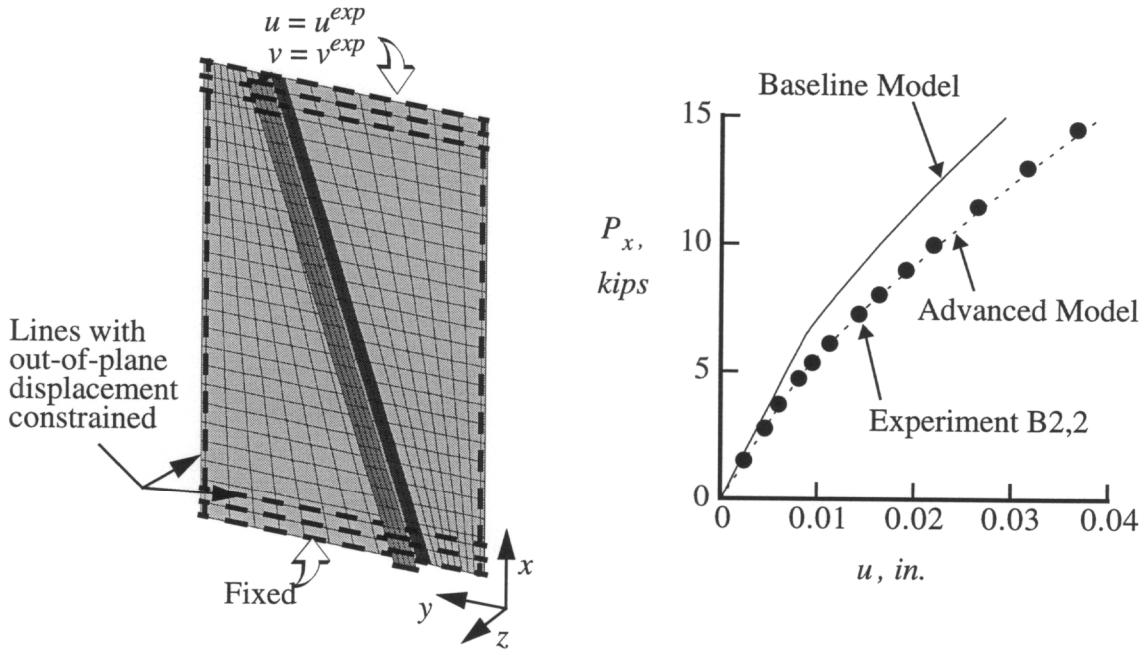

(a) Advanced model

(b) Axial load vs. end shortening response

Fig. 3-11 Advanced model and experiment B2,2

3.4 Nonuniform Initial Loading

Previous refinements to the finite element model were directed toward accurately predicting the overall response of a panel. Considering the local panel response, one more modification was introduced to the finite element model.

The experimental strain data for panel B2,2 indicated that the initial load introduction into the panel was nonuniform. Load introduction into the panel skin was monitored by strain gages located across the panel width, 4.0 in. from the top and bottom potting, as shown in Fig. 2-7. Load introduction into the stiffener was monitored by strain gages

located on the stiffener cap near the potted ends, shown in Fig. 2-9(b).

Numerically-predicted strains for an end shortening $u = 0.25u_{cr}$ were obtained from a nonlinear static analysis using the advanced finite element model. The predicted strains are compared to the measured strains in Fig. 3-12. The strains shown are normalized by the strain at buckling, i.e., $\varepsilon_x^* = \varepsilon_x / (u_{cr}/24)$. The measured strain values in the skin were low in the center of the panel. The measured strain values in the stiffener cap indicated bending, with the gages on the cap near the top potting showing a negative normalized strain, i.e., the stiffener cap was in tension when the remainder of the panel was in compression. In the experiment, the strain values in the stiffener cap remained tensile until just prior to buckling of the skin.

In an effort to better match the experimental load introduction, the finite element model was modified further by adding a nonuniform initial displacement to the uniform end shortening. The nonuniform initial displacement was defined on each end of the model and consisted of a nonuniform u-displacement and a rotation about the y-axis. Experimental data from strain gages on the skin were used to infer the shape of the nonuniform u-displacement, while data from strain gages on the stiffener cap were used to infer the end rotations.

The finite element analyses were conducted several times. After each analysis the predicted strains were compared to the measured strains, and a new nonuniform initial displacement was defined which reduced the discrepancy. After a few iterations the predicted strains correlated well with the measured strains for this single point in the loading history, namely about 25% of the panel buckling load. The predicted strains obtained with the nonuniform initial displacement model are compared to the experimental strains in Fig. 3-13. The magnitude of the nonuniform initial inplane displacement was small. The variation across the width of the skin was less than 0.001 in., and even with the end rotation included, the maximum nonuniform initial displacement was less than 0.003 in. These values are well within the tolerances held for machining and fixturing test specimens. However, a nonuniform initial displacement of 0.003 in. represented a significant percentage of the end shortening at buckling (see Table 2-1), and thus could be considered an important source of error.

To conduct analyses at higher loads, the nonuniform initial displacement was held constant, and a uniform end shortening was added. A nonlinear postbuckling analysis of the

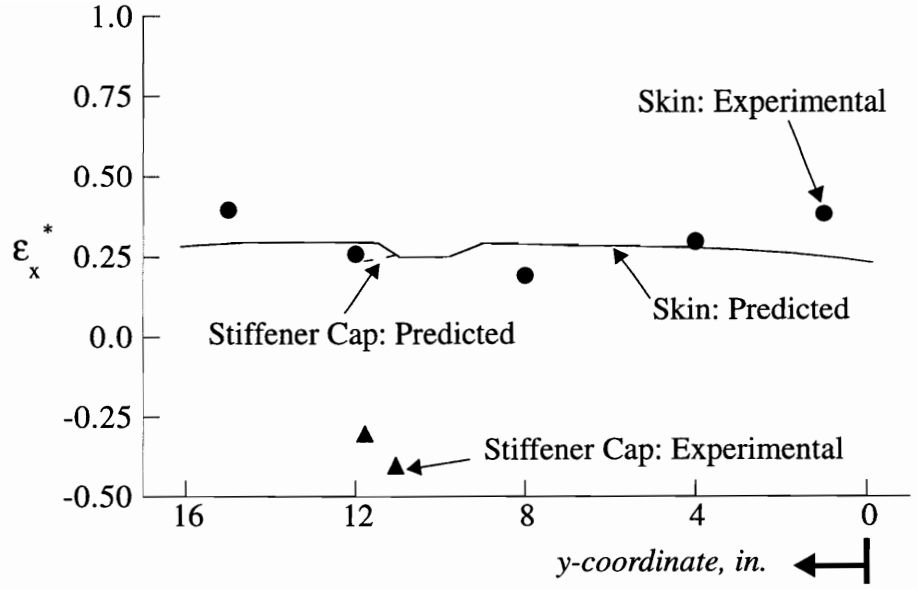

(a) Strains across width near top potting

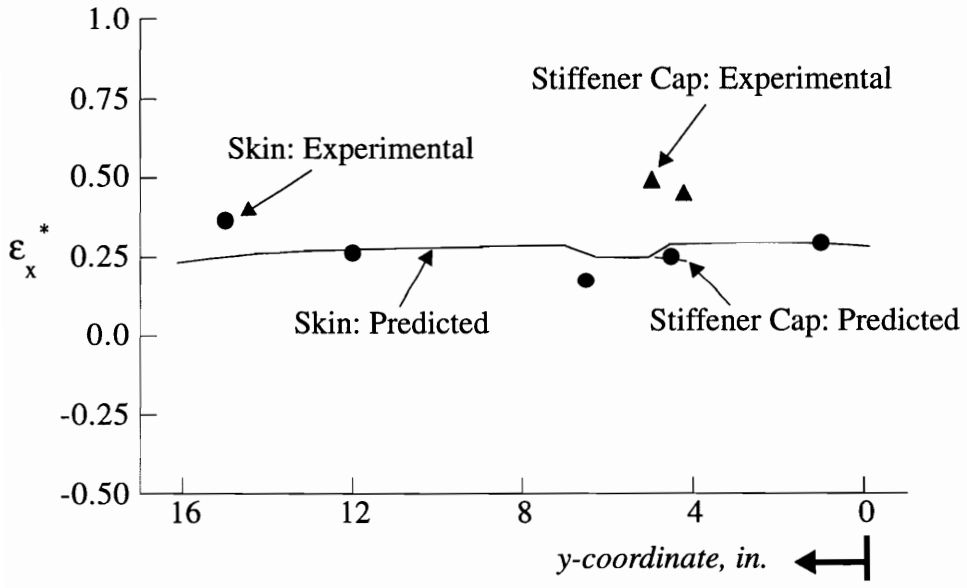

(b) Strains across width near bottom potting

Fig. 3-12 Comparison of experimental and predicted strains near loaded ends: advanced model

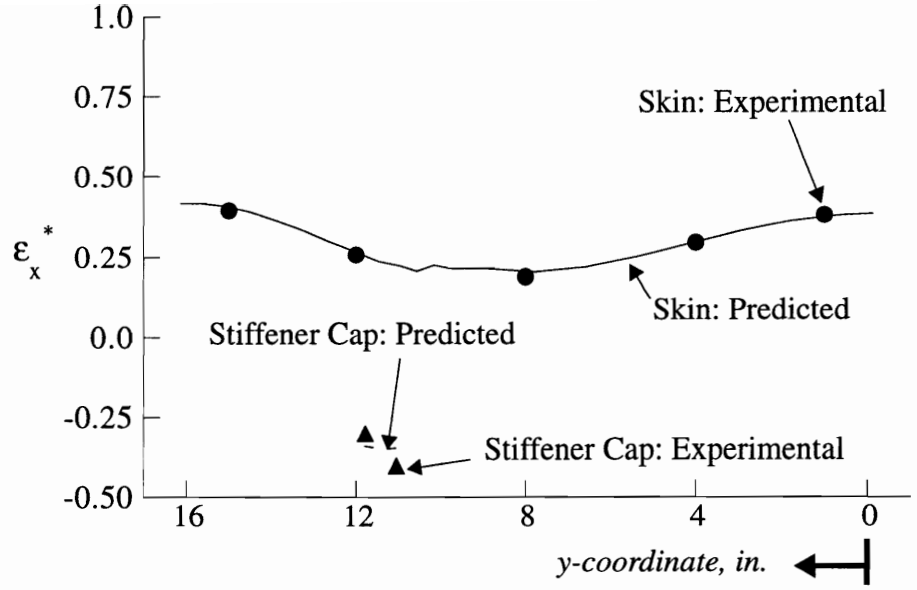

(a) Strains across width near top potting

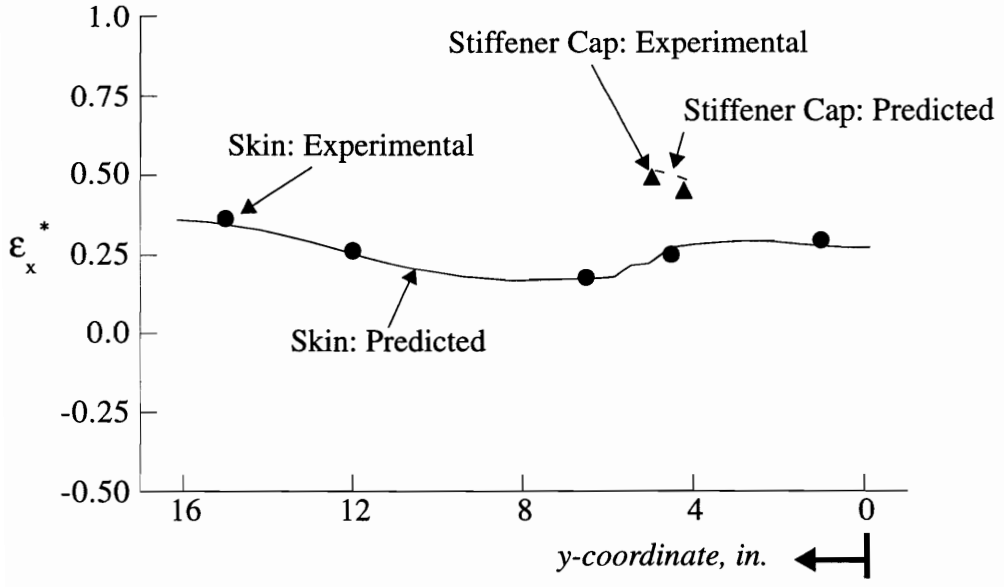

(b) Strains across width near bottom potting

Fig. 3-13 Comparison of experimental and predicted strains near loaded ends: nonuniform initial displacement

nonuniform initial displacement model of panel B2,2 was conducted. The axial load vs. end shortening response for the advanced model, the nonuniform initial displacement model, and the experiment are compared in Fig. 3-14. The results in Fig. 3-14 indicate that the nonuniform initial displacement which had a substantial effect on the local strain distribution shown in Fig. 3-13 had very little effect on the overall panel response.

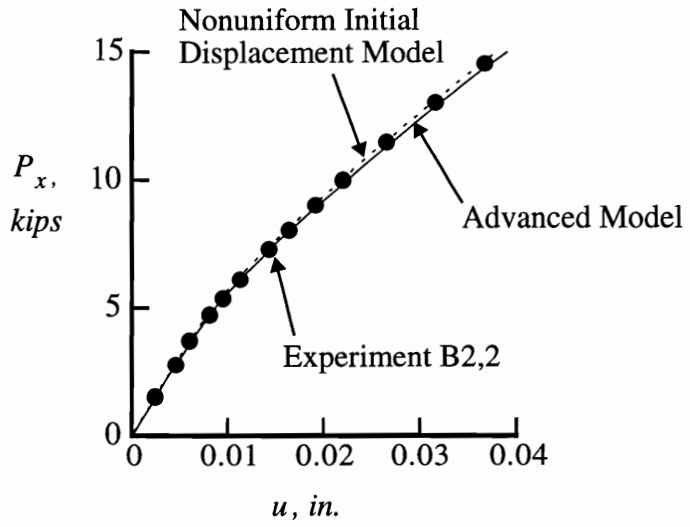

Fig. 3-14 Advanced model, nonuniform initial displacement model, and experiment B2,2: axial load vs. end shortening response

A contour plot of the out-of-plane skin displacement predicted by the nonuniform initial displacement model and a moiré-fringe pattern from the experiment are compared in Fig. 3-15 for an applied end shortening $u = 2.1u_{cr}^{exp}$. The shape, sign, and amplitude of the experimental and predicted out-of-plane skin displacements in the postbuckling equilibrium state correlated well.

The results presented above indicate that efforts to improve the correlation between the measured and predicted response were successful. By implementing a number of modeling refinements, a finite element model was developed which represented the physics of the response. In the process, valuable insight into the sensitivity of the model's response to each modeling refinement was gained by applying each refinement to a baseline model. The advanced model which includes nonuniform initial displacements is used in the next chapter.

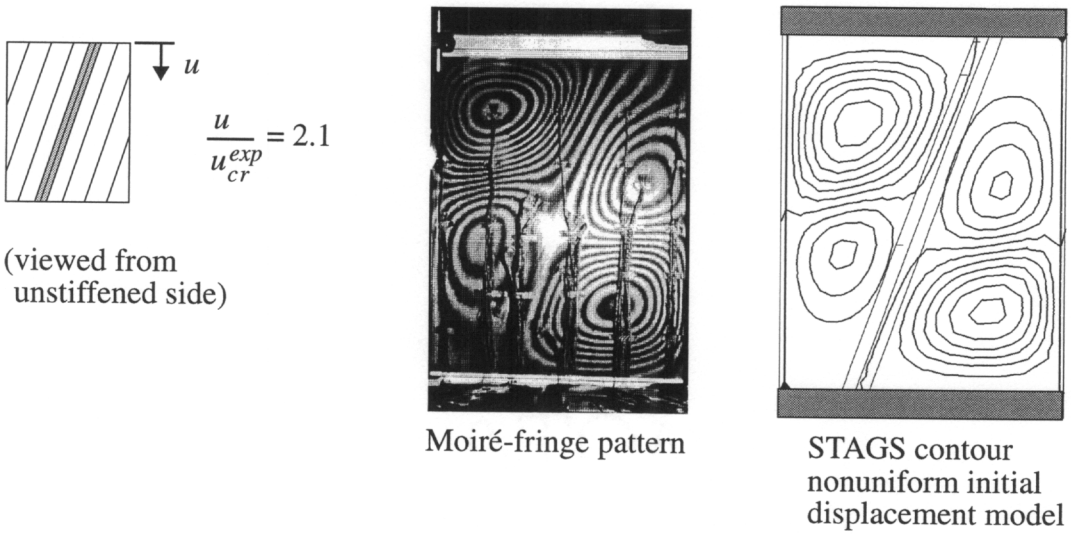

Fig. 3-15 Comparison of experimental and predicted out-of-plane skin displacement contours in the postbuckled state

4. Comparison Between Predicted and Experimental Results

The measured, observed, and predicted response of the individual panels in the prebuckling, buckling, and postbuckling load ranges are presented in this chapter. Applying the modeling techniques developed in Chapter 3, detailed finite element models were created for the five panels and the following structural analyses were conducted using the STAGS finite element analysis code:

- simplified linear bifurcation buckling analyses, ignoring measured shape imperfections and nonuniform initial loading, and setting the v-displacement on the top edge equal to zero
- nonlinear postbuckling analyses to simulate the experimental results, including measured shape imperfections (Sections 2.1.7 and 3.2.6) and nonuniform initial loading, (Section 3.4), and defining the u- and v-displacements at the top edge to be equal to the displacements u^{exp} and v^{exp}.

The primary objective of the current chapter is to verify the numerical models by comparing the predicted and measured results.

The results of the simplified linear bifurcation buckling analyses are presented first. The remainder of the chapter is dedicated to verifying the numerical models by comparing the predicted results from the nonlinear postbuckling analyses with the measured results from the experiments. The measured and predicted axial load vs. end shortening results are presented to demonstrate correlation of the overall panel responses over the entire range of loading, and are used to compute prebuckling stiffnesses, buckling loads, and initial postbuckling stiffnesses. The prebuckling stiffnesses and buckling loads from the experiments and the nonlinear analyses are compared to predicted values from the STAGS linear bifurcation buckling analyses. The observed postbuckling deflection patterns are presented and

compared to predictions obtained from the STAGS nonlinear postbuckling analyses. The measured and predicted axial-shear stiffness coupling responses of the panels are compared. The measured axial-shear stiffness coupling responses were reported in Section 2.3.3 and consisted of a mixture of force and displacement coupling. The predicted axial-shear stiffness coupling responses are reported in this chapter, and a method is developed to compute the net axial-shear stiffness coupling from a mixture of force and stiffness coupling.

4.1 Linear Bifurcation Buckling Results

The linear buckling response of each configuration is characterized by the buckling parameters $(P_x)_{cr}^{lin}$, u_{cr}^{lin}, and $(\varepsilon_x)_{cr}^{lin}$, where $(P_x)_{cr}^{lin}$ is the axial load which causes buckling, u_{cr}^{lin} is the end shortening at the buckling load, and $(\varepsilon_x)_{cr}^{lin}$ is the nominal compressive strain at buckling defined as u_{cr}^{lin} divided by the 24.0 in. length of the panel. The individual buckling parameters predicted for each configuration are summarized in Table 4-1. The results indicate that the predicted prebuckling axial stiffnesses of the five panels vary by only 7% relative to the baseline configuration, panel B0,0, while the predicted lin-

Table 4-1 Predicted Linear Stiffness and Linear Buckling Parameters

Configuration	Linear Stiffness, EA (kip)	Buckling Parameters		
		$(P_x)_{cr}^{lin}$ (kip)	u_{cr}^{lin} (mil)	$(\varepsilon_x)_{cr}^{lin}$ (με)
 B0,0	16,650	7.71	11.12	463
 B0,2	15,950	6.95	10.46	436
 B2,0	16,270	5.72	8.44	352
 B2,2	15,480	5.55	8.61	359
 B2,n2	15,550	5.22	8.07	336

ear buckling loads vary by as much as 32%. The configurations with the stiffener rotated 20° have buckling loads that are 25% lower, on average, than the buckling loads for the configurations with the unrotated stiffener. Rotating the stiffener increases the distance from the stiffener to the knife-edge support in two quadrants of the panel. The panel skin in these quadrants has a larger unsupported width, which causes the panel skin to buckle at a lower panel load.

The predicted buckling mode for each configuration is dominated by the out-of-plane displacement in the skin. Contour plots of the w component of the predicted buckling shape are shown in Fig. 4-1. The contour plots are shown as viewed from the stiffened side of the panel. The buckling modes are normalized with the maximum displacement equal to 1.0, and each contour represents a $\Delta w = 0.1$ in. The predicted buckling shapes are consistent with the observed deformations that were reported in Section 2.3.4 on page 54.

The values of $(\varepsilon_x)_{cr}^{lin}$ in Table 4-1 are a small fraction of the ultimate strain for the material. The ultimate strain of a composite material is dependent on the fiber orientation and the direction of loading. The results of material characterization tests of Hercules AS4-3502 graphite-epoxy reported in Ref. 3 gave a magnitude of the minimum ultimate strain to be 5500 με. Thus, at buckling the panels were not strength critical, and would be expected to exhibit considerable postbuckling load capacity.

4.2 Nonlinear Postbuckling Analyses and Experiments

As such, the nonlinear analyses constitute the core of the numerical effort. The linear buckling parameters reported in Table 4-1 are used to normalize some of the measured and predicted nonlinear results presented in this section. The specific scheme for normalizing is defined as the various predicted results are presented.

4.2.1 Axial Load vs. End Shortening Response: Full Range of Loading

The measured and predicted axial load vs. end shortening response of each configuration for the entire range of loading are compared in Fig. 4-2. The axial load and end shortening of each panel are normalized by $(P_x)_{cr}^{lin}$ and u_{cr}^{lin}, respectively, these values for each panel having been reported in Table 4-1. The axial load vs. end shortening results indicate that the predicted responses closely correlate with the measured responses. In all cases, the axial loads predicted by the nonlinear analyses are higher than the measured axial loads.

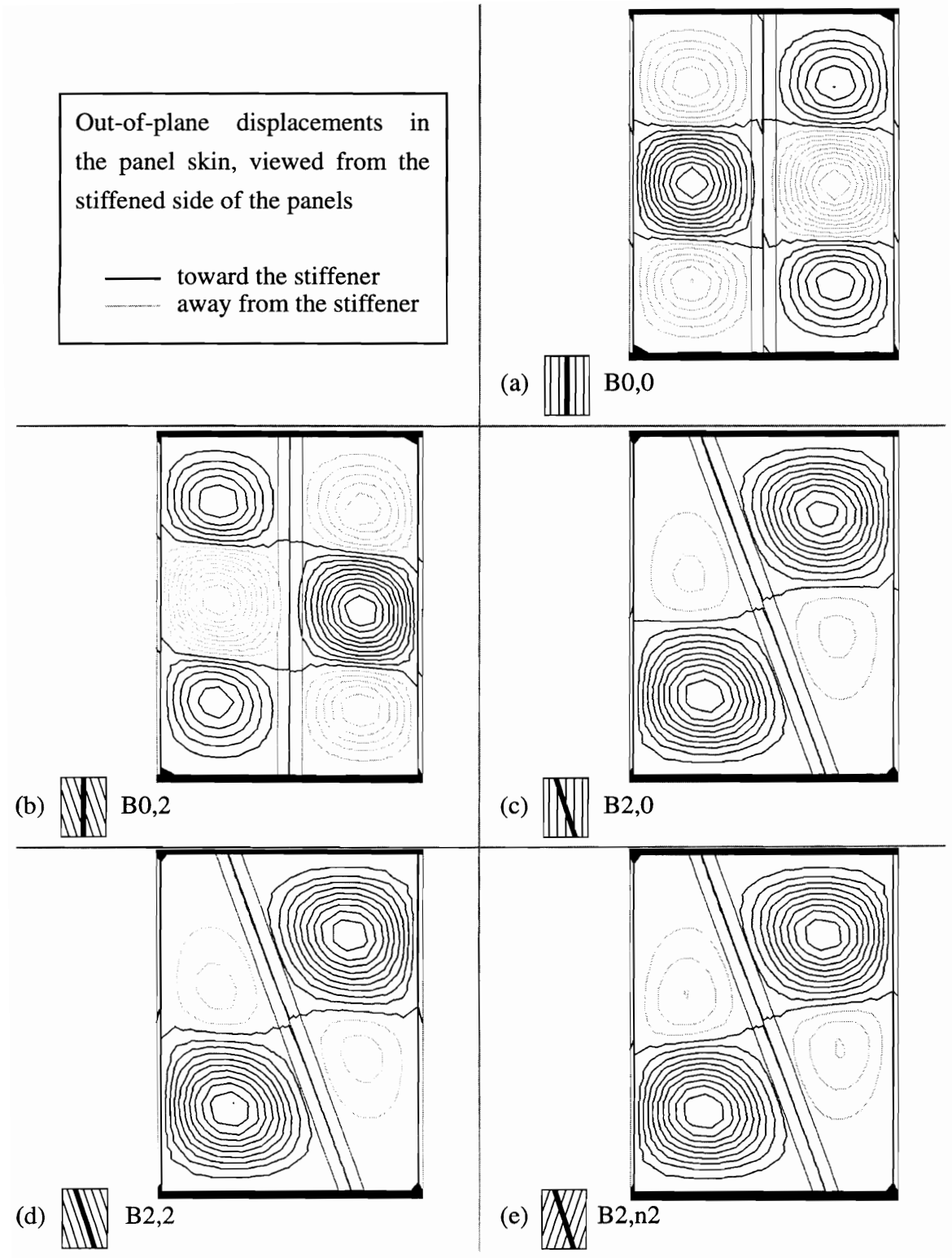

Fig. 4-1 Predicted buckling shapes from linear buckling analyses with $\nu = 0$

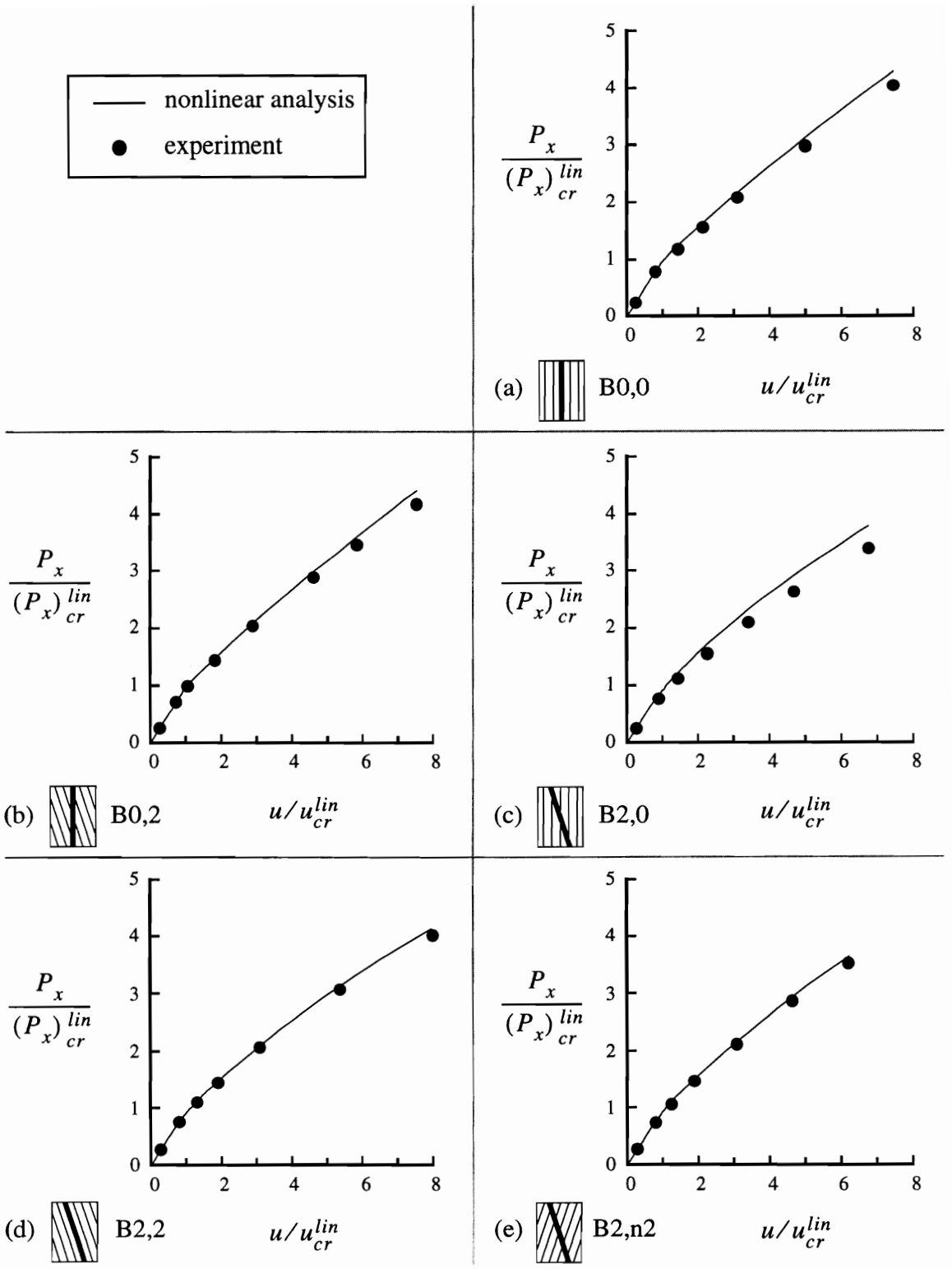

Fig. 4-2 Axial load vs. end shortening response: full range of loading

The predicted axial loads for panel B0,0, shown in Fig. 4-2(a), differ from the measured axial loads by a maximum of 8%. In Fig. 4-2(b) the predicted and measured axial loads for panel B0,2 differ by less than 6%. The results for panel B2,0 in Fig. 4-2(c) demonstrate the worst correlation, with the predicted and measured axial loads differing by up to 12%. The measured and predicted axial loads for panels B2,2 and B2,n2 shown in Figs. 4-2(d) and 4-2(e), respectively, differ by less than 5% for the entire range of loading.

4.2.2 Axial Load vs. End Shortening Response: Prebuckling and Initial Postbuckling

The axial load vs. end shortening responses shown in Fig. 4-2 are now considered in the prebuckling and initial postbuckling ranges of loading. The predicted and measured axial load vs. end shortening responses for a range of loading limited to 1.5 times the linear buckling load are shown for each configuration in Fig. 4-3. The responses in Fig. 4-3 are used to compute the predicted and measured prebuckling stiffnesses, buckling loads, and initial postbuckling stiffnesses. In the plotting software a least-squares algorithm is used to prescribe a linear approximation to the axial load vs. end shortening response for the load range $P_x / (P_x)_{cr}^{lin} = 0.5$ to 0.75. The prebuckling stiffness of the response is defined as the slope of the linear approximation times $(P_x)_{cr}^{lin} / u_{cr}^{lin}$, times the 24.0 in. length of the panels. The initial postbuckling stiffness is defined by applying a similar method to the axial load vs. end shortening response for the load range $P_x / (P_x)_{cr}^{lin} = 1.25$ to 1.50. The buckling parameters are defined by the intersection of the linear approximations to the prebuckling response and the initial postbuckling response. The predicted and measured prebuckling stiffnesses, initial postbuckling stiffnesses, and buckling parameters that were computed from the axial load vs. endshortening responses in Fig. 4-3 are summarized in Table 4-2. The measured results, from Table 2-1, are identified in Table 4-2 by "EXP", and the predicted results from the nonlinear analyses are identified by "STAGS." Next to all of the predicted results is a number in parentheses which indicates the percentage difference between the predicted results and the experimental results. The results in Table 4-2 indicate that the measured panel prebuckling and postbuckling stiffnesses are predicted to within 4% for all panels except for panel B2,0. For panel B2,0, the nonlinear analysis overpredicts the experimental prebuckling stiffness by 10%, and the postbuckling stiffness by 17%. The buckling parameters in Table 4-2 are reported as non-normalized values. The predicted and measured buckling parameters agree to within 8% for all panels except panel B0,0. For panel B0,0 the nonlinear analysis predicts buckling parameters that are 17% higher than the measured buckling parameters.

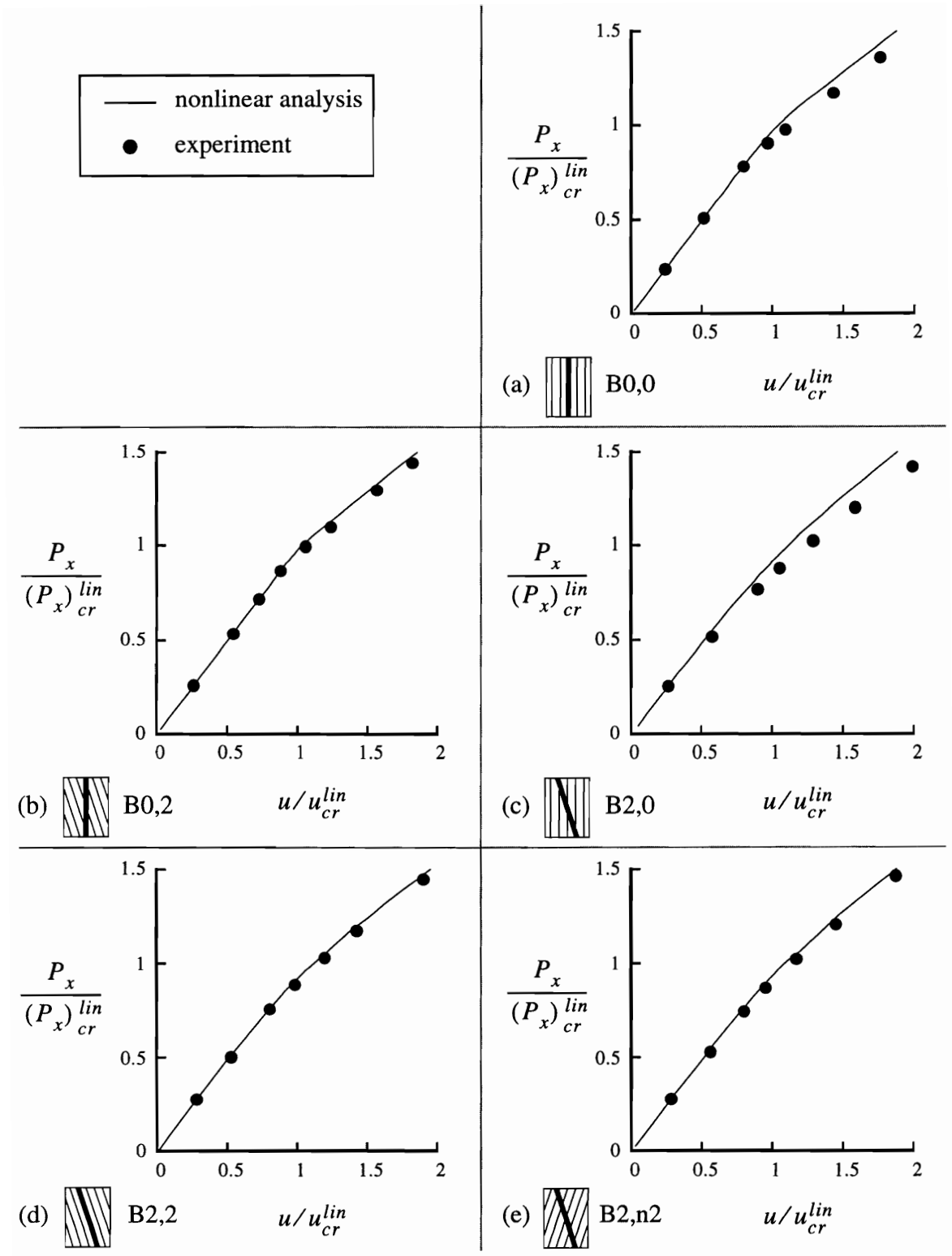

Fig. 4-3 Axial load vs. end shortening response: prebuckling and initial postbuckling

Table 4-2 Predicted and Measured Nonlinear Stiffness and Buckling Parameters Computed from the Axial Load vs. End Shortening Response

Configuration		EA (kip)		Buckling	
		Pre-buckled (% differ)	Post-buckled (% differ)	$(P_x)_{cr}$ kip (% differ)	$(u)_{cr}$ mil (% differ)
 B0,0	EXP	16,380	9,350	6.65	9.74
	STAGS	16,360 (0%)	9,660 (3%)	7.77 (17%)	11.35 (17%)
 B0,2	EXP	16,020	9,230	6.46	9.82
	STAGS	15,720 (2%)	9,410 (2%)	6.99 (8%)	10.65 (8%)
 B2,0	EXP	13,180	8,520	5.55	9.57
	STAGS	14,560 (10%)	9,950 (17)%	5.84 (5%)	9.29 (3%)
 B2,2	EXP	14,430	8,790	5.12	8.38
	STAGS	14,150 (2%)	8,930 (2%)	5.42 (6%)	8.90 (6%)
 B2,n2	EXP	13,840	9,300	5.16	8.62
	STAGS	14,430 (4%)	9,290 (0%)	5.34 (3%)	8.65 (0%)

The buckling loads that are experimentally-measured and predicted with nonlinear analyses (Table 4-2) and the buckling loads that are predicted with linear bifurcation analyses (Table 4-1) are summarized to assess the effect of rotating the stiffener or skin on the panels' buckling loads. Comparing the buckling loads for panel B0,0 and panel B2,0 indicates that rotating the stiffener 20° decreases the linear-predicted, nonlinear-predicted, and measured buckling loads by 17%, 15%, and 26%, respectively. Comparing the buckling loads for panel B0,0 and panel B0,2 indicates that rotating the skin 20° decreases the measured, nonlinear-predicted, and linear-predicted buckling loads by 3%, 10%, and 10%, respectively. The discrepancies between the measured and predicted reductions in the buckling load are attributed largely to a 17% discrepancy between the measured and nonlinear-predicted buckling loads for the baseline panel B0,0. Comparing the buckling loads for panel B2,0 and panel B2,2 indicates that for panels with the stiffener rotated 20°, rotating the skin 20° in the same direction decreases the measured, nonlinear-predicted, and linear-predicted buckling loads by 8%, 7%, and 3%, respectively. Comparing the buckling loads for panel B2,0 and panel B2,n2 indicates that for panels with the stiffener rotated 20°, rotating

the skin 20° in the opposite direction decreases the measured, nonlinear-predicted, and linear-predicted buckling loads by 7%, 9%, and 9%, respectively.

4.2.3 Linear vs. Nonlinear Analyses: Prebuckling and Buckling Response

The predicted prebuckling and buckling results from the linear analyses, reported in Table 4-1, and from the nonlinear analyses, reported in Table 4-2, are now compared. For the configurations with the unrotated stiffener, the prebuckling stiffness from the linear and nonlinear analyses agree to within 2%. For the configurations with the stiffener rotated 20°, the linear analyses overpredicts the prebuckling stiffness by 9%, on average, compared to the nonlinear analyses. The discrepancies in stiffness are most likely due to the prebuckling out-of-plane displacements that were present for the configurations with the stiffener rotated 20°. These prebuckling deformations are quantified and explained in the next section.

The buckling loads predicted by the linear buckling analyses are within 2% of the buckling loads predicted from the nonlinear analyses.

4.2.4 Out-of-Plane Deformations

The observed and predicted postbuckling shapes of each configuration are compared in Fig. 4-4. Postbuckling deformations for panels with the applied end shortening equal to approximately four times the critical end shortening are considered. The observed deformations are represented in Fig. 4-4(a) by moiré-fringe patterns that were photographed during the experiments. The "+" and "-" symbols that are superimposed on the moiré-fringe patterns indicate the direction of the out-of-plane deformations, with "+" being toward the stiffener. In each case, the direction of the deformation pattern was determined from DCDT readings. The predicted postbuckling deformations are represented in Fig. 4-4(b) by contour plots of the out-of-plane displacement from the nonlinear analyses. The dark contours correspond to $w \geq 0$, i.e., toward the stiffener, while the light contours correspond to $w < 0$. The first dark contour corresponds to $w = 0$, and each contour represents a $\Delta w = 0.020$in. The contour plots and moiré-fringe patterns are shown as viewed from the unstiffened side of the panel. The results shown in Fig. 4-4 demonstrate that for all of the panels, the predicted postbuckling deformations have the same shape and direction as the deformations observed during the tests.

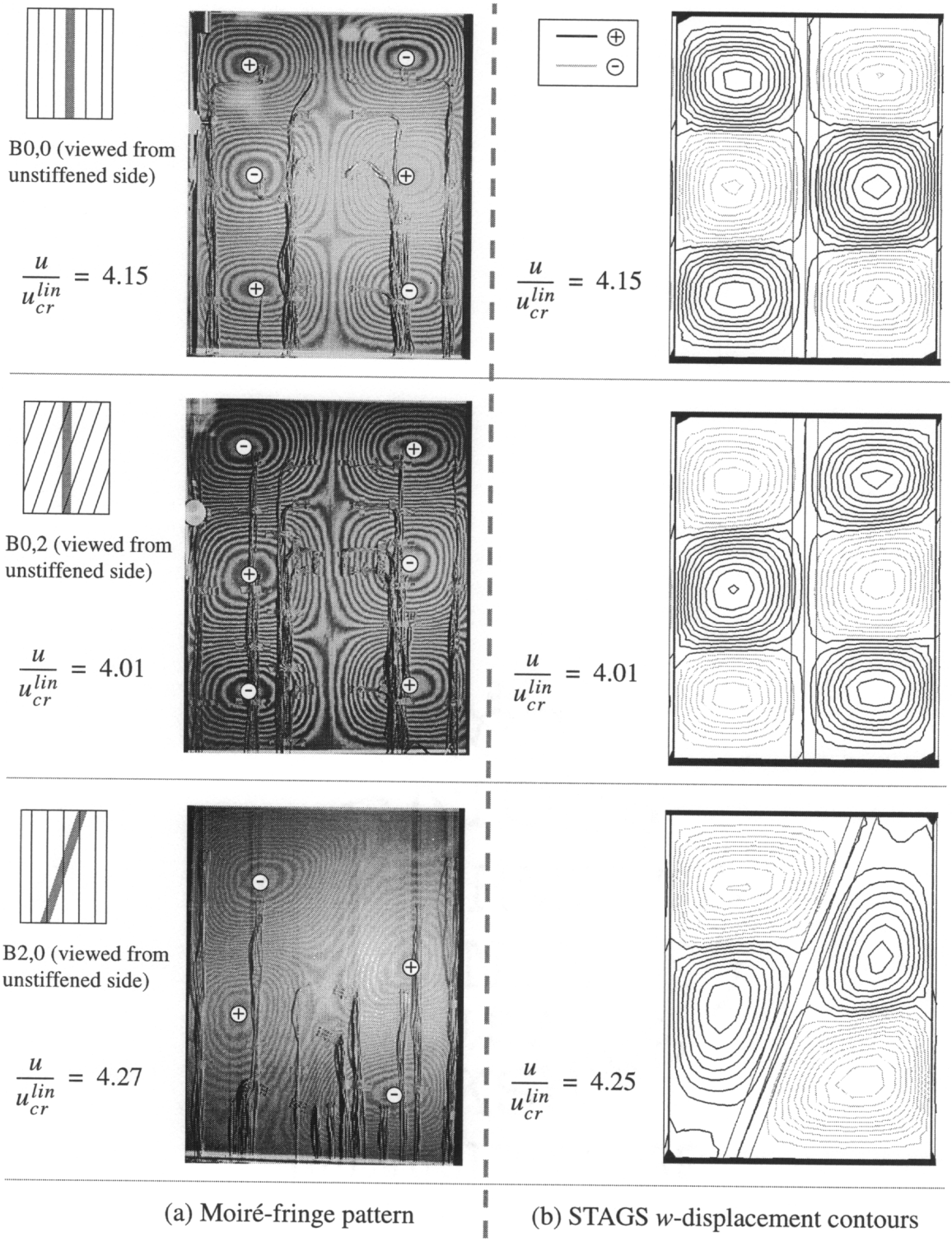

Fig. 4-4 Comparison of experimental and predicted out-of-plane displacement contours in the postbuckled state

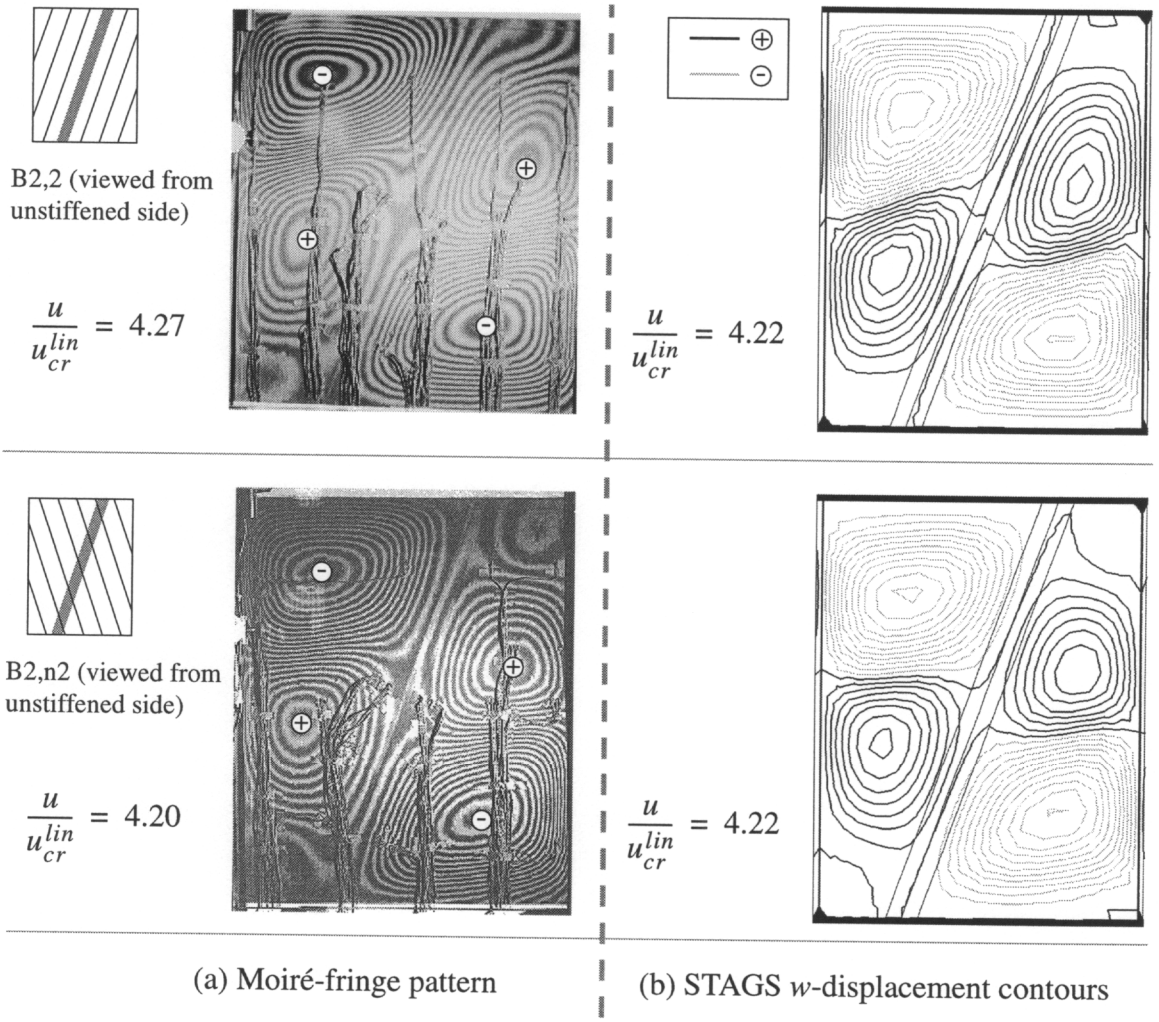

Fig. 4-4 Continued

An additional point that is evident in Fig. 4-4 is that all of the panels with the stiffener rotated 20° have postbuckling deformations in the same direction. The quadrants of the panel which have wider sections of skin have the largest out-of-plane displacement and always buckle away from the stiffener. The direction of the postbuckling deformation is directly related to the direction of the forces holding the skin and stiffener of the panel together. Having the largest skin deformations in a direction away from the stiffener may promote failure of the panel by separation of the skin and stiffener.

For the panels with a rotated stiffener, the tendency for the wider sections of skin to buckle in a direction away from the stiffener is driven by Poisson expansion of the skin. The sketch in Fig. 4-5 demonstrates how Poisson expansion in the skin can cause out-of-

plane deformations if the stiffener is rotated. The top and bottom ends of the panel are potted, as described in Section 2.1.5. The potting restrains Poisson expansion on the ends of the skin and restrains displacement in the y-direction of the stiffener cross section. When an end shortening displacement is applied to the panels, Poisson expansion causes the skin sections between the top and bottom potted ends to expand in the y-direction, giving local displacements that are away from the panel centerline. If the stiffener is not along the panel centerline, then the skin under the stiffener tends to displace in the direction away from the panel centerline. The eccentricity of the stiffener and the skin inplane displacement in the y-direction couple to produce a rotation of the stiffener attachment flange. A rotation of the stiffener attachment flange creates nonzero w-displacements in the panel skin, with the wider section of panel skin moving in the direction away from the stiffened side of the panel.

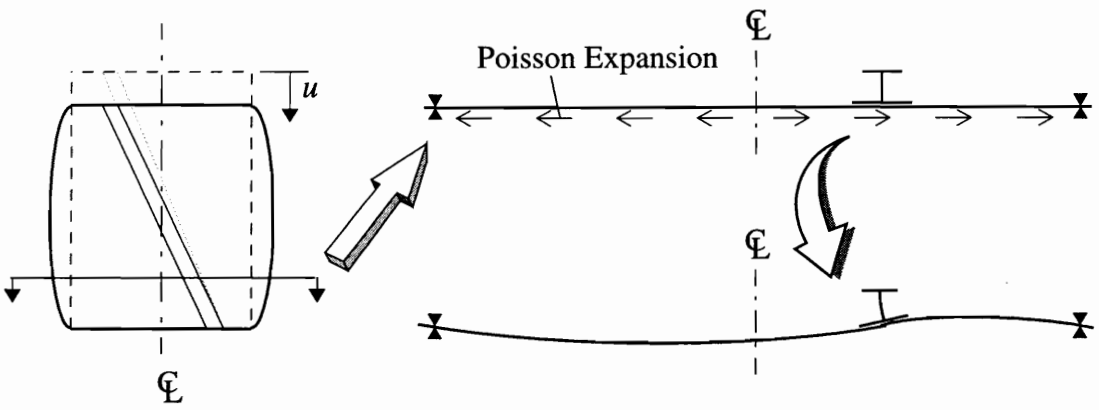

Fig. 4-5 Poisson expansion of panel skin influences direction of out-of-plane deformation

In addition to comparing the observed and predicted shapes of the postbuckling deformations, the magnitudes of the out-of-plane displacements at discrete locations on the panel skin are compared for the full range of loading. As indicated in Section 2.1.10, DCDT's were used to measure the out-of-plane displacements at several locations on the skin. The results from the nonlinear postbuckling analyses were interpolated to predict the out-of-plane displacements at the same locations where the measurements were taken with the DCDT's. The measured and predicted out-of-plane skin displacements at discrete locations on each panel are compared in Fig. 4-6. On the left side of Fig. 4-6 the contour plots from Fig. 4-4 are shown as viewed from the stiffened side of the panel, and the locations

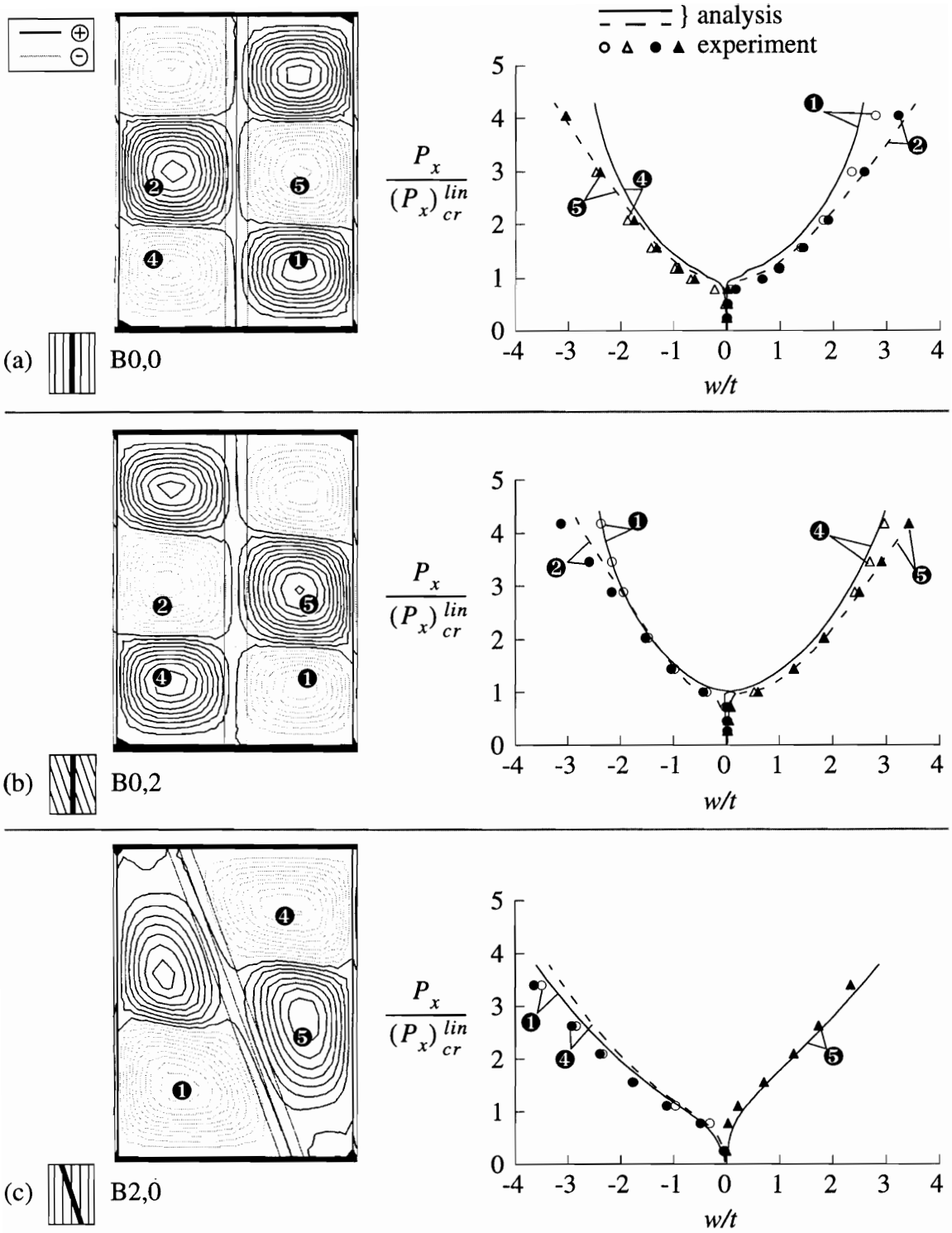

Fig. 4-6 Comparison of experimental and predicted out-of-plane displacement at discrete locations on the panel skin

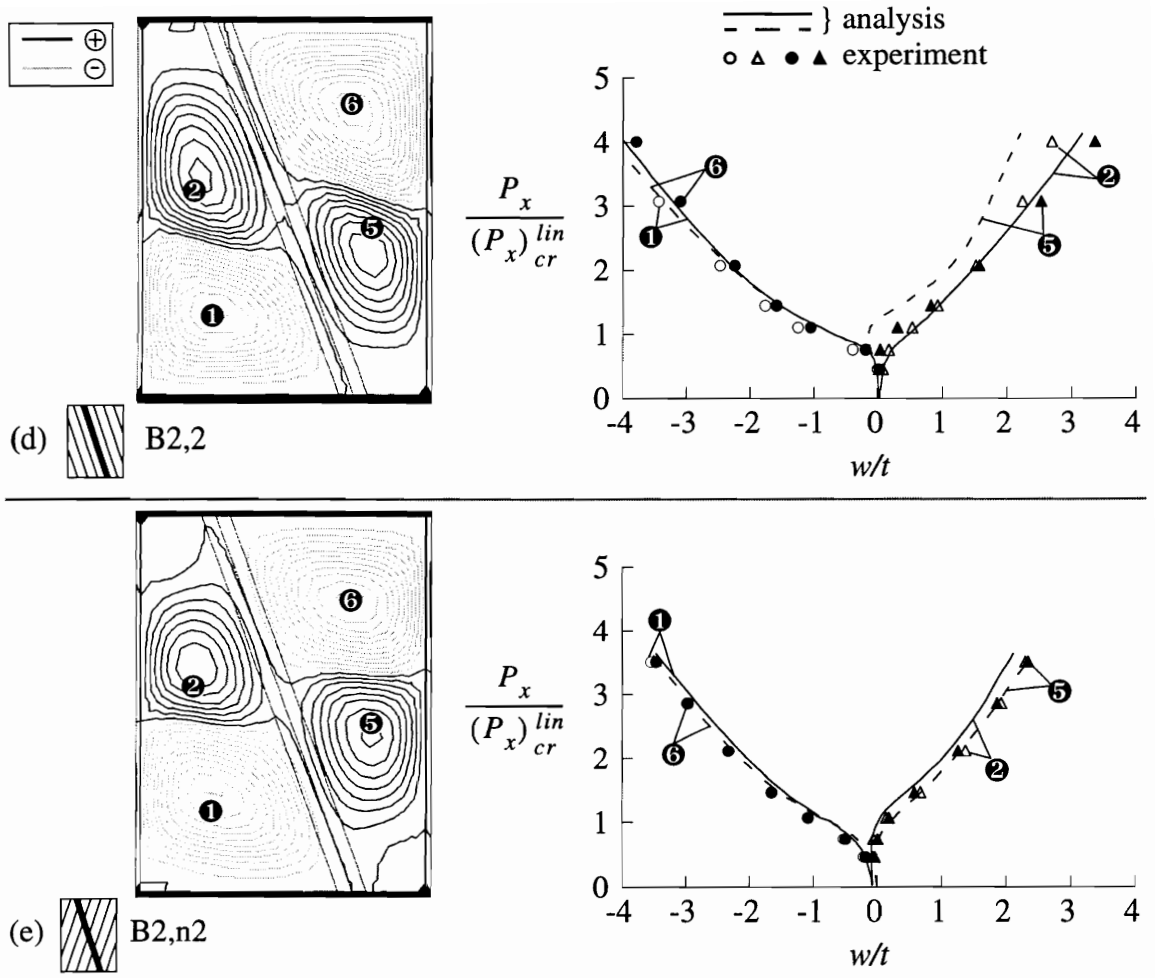

Fig. 4-6 Continued

on the panel skin where the DCDT measurements were taken are identified by numbered markers indicating the DCDT number from the experiment. The measured and predicted out-of-plane displacements at these locations are plotted as a function of the applied axial load on the right side of Fig. 4-6. In the plots the applied load P_x is normalized by the linear buckling load $(P_x)_{cr}^{lin}$ and the w-displacement is normalized by the thickness of the panel skin. In general a close correlation exists between the measured and predicted displacements. For the panels with the stiffener rotated 20°, the out-of-plane displacements start to develop at loads less than the linear buckling load. This is most evident for panel B2,0, shown in Fig. 4-6(c). The reason for the prebuckling out-of-plane deformation in the panels with the stiffener rotated was explained above in Fig. 4-5.

4.2.5 Axial-Shear Force and Displacement Coupling

The measured axial-shear stiffness coupling responses consisted of a mixture of force and displacement coupling. The measured values of force and displacement coupling were reported in Section 2.3.3. Since the experimental data u^{exp} and v^{exp} were used to prescribe the u- and v-displacements at the top edge of the numerical model, the predicted and measured displacement couplings are identically equal. The measured force coupling, previously reported in Fig. 2-16, is now compared to the predicted force coupling from the nonlinear analysis. Nonuniform initial loading, observed in the experiments and simulated in the analyses, caused the force coupling to be erratic during the initial loading. The force coupling results for $u/u^o_{cr} < 0.5$ have been eliminated from the following plots, since the initial loading response was not representative of the overall panel response.

Force coupling was defined in Section 2.3.3 as the ratio of the shear force P_{xy} to the axial force P_x. In the experiments, P^{exp}_x is the load cell reading, while P^{exp}_{xy} is computed from strain gage data using the numerical integration procedure described in Section 2.3.2. The predicted axial and shear forces from the nonlinear analyses were computed by summing the nodal forces for all the nodes on one end of the panel model. The measured and predicted force coupling vs. end shortening responses of each panel are compared in Fig. 4-7. The force coupling is presented as a percentage, and the end shortening is normalized by u^o_{cr}, the end shortening corresponding to linear buckling of the baseline configuration, B0,0. The force couplings predicted by the analyses are shown as dark solid and dashed lines. The measured force couplings are represented by filled symbols. To assist in identifying the experimental data for a single configuration, the filled symbols are connected by light solid lines.

The measured and predicted force coupling results shown in Fig. 4-7 are difficult to compare. The force coupling is near zero for the configurations with the unrotated stiffener. The configurations with the stiffener rotated 20° have force couplings that are greater than zero and increase in the postbuckling load range. If the results for one configuration are considered, then the measured and predicted force coupling responses follow similar trends as the loading is increased. When the results for the three configurations with the stiffener rotated 20° are compared, the results from the different configurations overlap. If these three configurations were to be ranked according to the amount of force coupling, the order of the ranking would vary with load and would also depend on whether the measured or predicted results were used for the ranking.

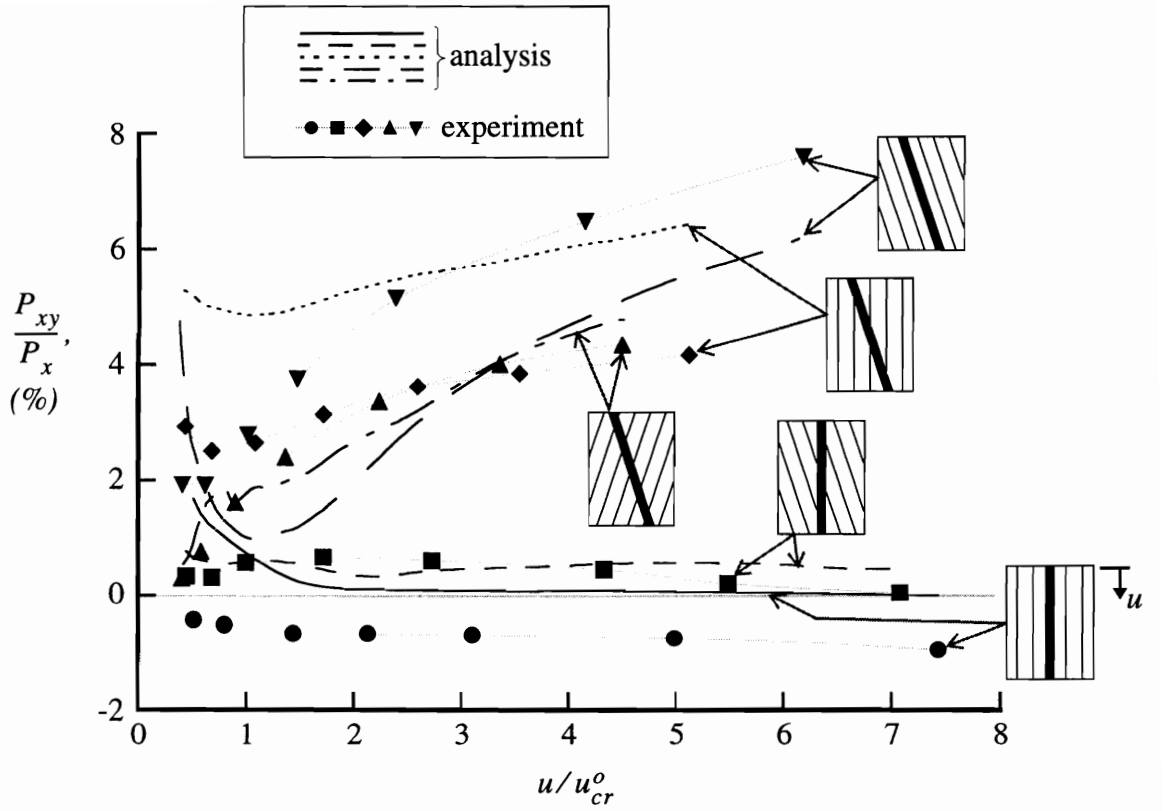

Fig. 4-7 Experimental and predicted force coupling vs. end shortening response

The results presented in Fig. 4-7 indicate that the force coupling of the test panels was difficult to predict. If only these results are considered, then the accuracy of the numerical model would seem to be in question. Before any judgement is passed regarding the accuracy of the numerical model, consider that the axial-shear coupling response of each panel is a combination of force and displacement coupling. The results presented in Fig. 4-7 were obtained by equating the displacement coupling in the experiment and the analysis, and then comparing the force coupling. The force coupling is only a fraction of the total axial-shear coupling response. By specifying the displacement coupling, the discrepancies in the force coupling may appear large, while the total axial-shear coupling responses of the experiment and the analysis may agree quite well.

To demonstrate the effect of considering only a portion of the total response, consider the following analogy. Say that there are two jars on a table. The first jar contains 80 red marbles and 20 blue marbles and the other jar contains 80 red marbles and 15 blue marbles. If the total number of marbles in each jar are compared, the totals differ by only 5%.

If only the blue marbles are considered, then the number of blue marbles in each jar differs by 25%. In this analogy, as will be seen, the displacement coupling corresponds to the red marbles, while the force coupling corresponds to the blue. Thus, to evaluate the accuracy of the numerical model in predicting the axial-shear coupling response of the panels, the sum of the force and displacement coupling should be considered. The predicted and measured total axial-shear coupling responses are compared by defining a predicted pure force coupling from the analyses and an equivalent pure force coupling using the measured test data.

Predicted Pure Force Coupling

As was stated, the nonlinear analyses of the preceding section were conducted with the u- and v-displacements at the top edge specified to correspond with measured experimental data u^{exp} and v^{exp}. If the nonlinear analyses are repeated with $v = 0$, and all the other modeling parameters (initial imperfections and nonuniform initial loading) are unchanged, then the predicted responses have no displacement coupling (v/u is identically equal to zero), and they consist entirely of pure force coupling, i.e, $(P_{xy}/P_x)_{pure}$. The predicted pure force coupling responses from these analyses are shown in Fig. 4-8. The predicted pure force coupling is presented as a percentage, and the end shortening is normalized by u^o_{cr}.

Equivalent Pure Force Coupling

As the measured test data represents a mixture of force and displacement coupling, the two forms of coupling in the experiments are combined into a single parameter, namely the equivalent pure force coupling $(P_{xy}/P_x)^{equ}_{pure}$. For this, it is assumed that the experimental displacement coupling can be multiplied by some scale factor Φ and then added to the experimental force coupling to form the equivalent pure force coupling, namely,

$$\left(\frac{P_{xy}}{P_x}\right)^{equ}_{pure} = \frac{P^{exp}_{xy}}{P^{exp}_{x}} + \Phi\left(\frac{v^{exp}}{u^{exp}}\right) \quad . \tag{4.1}$$

The scale factor Φ is related to the panel's shear and axial stiffnesses and may be a function of the load range. The values for Φ are estimated numerically by assuming that the predicted force and displacement coupling can be combined in a similar manner, i.e.,

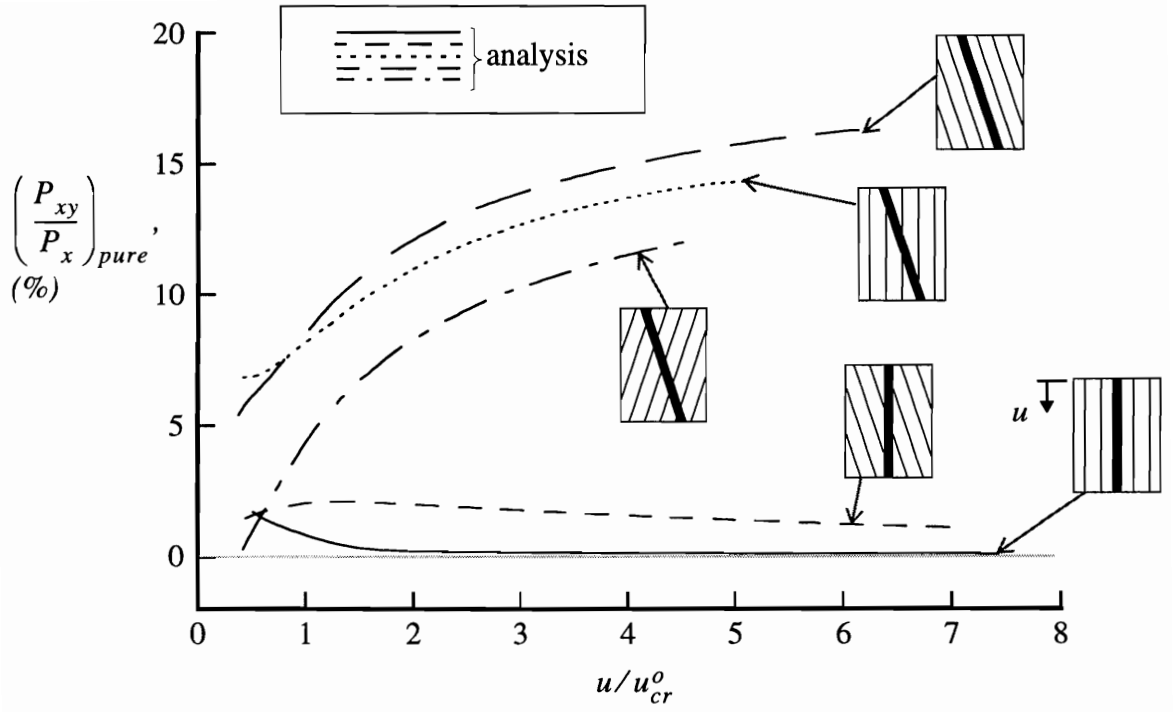

Fig. 4-8 Predicted pure force coupling vs. end shortening response

$$\left(\frac{P_{xy}}{P_x}\right)^{equ}_{pure} = \frac{P_{xy}}{P_x} + \Phi\left(\frac{v}{u}\right) \quad . \tag{4.2}$$

To evaluate Φ in Eq. (4.2), the two ideal boundary conditions on the transverse displacement originally shown in Fig. 2-15 are considered in the analyses. The first case assumes $v = 0$ and corresponds to pure force coupling. This case was considered in the previous section and produced the $(P_{xy}/P_x)_{pure}$ responses that were shown in Fig. 4-8. Evaluating the right side of Eq. (4.2) for this case gives

$$\left(\frac{P_{xy}}{P_x}\right)^{equ}_{pure} = \frac{P_{xy}}{P_x} \quad . \tag{4.3}$$

The second case assumes that v is uniform but unspecified. The finite element models with $v = 0$ were modified to correspond to this case. Nonlinear analyses with these modified boundary conditions predict a pure displacement coupling response, i.e., $(v/u)_{pure}$, with the force coupling equal to zero. The predicted pure displacement coupling response of each panel is shown in Fig. 4-9. The pure displacement coupling is presented as a percentage, and the end shortening is normalized by u^o_{cr}. The pure displacement couplings shown in

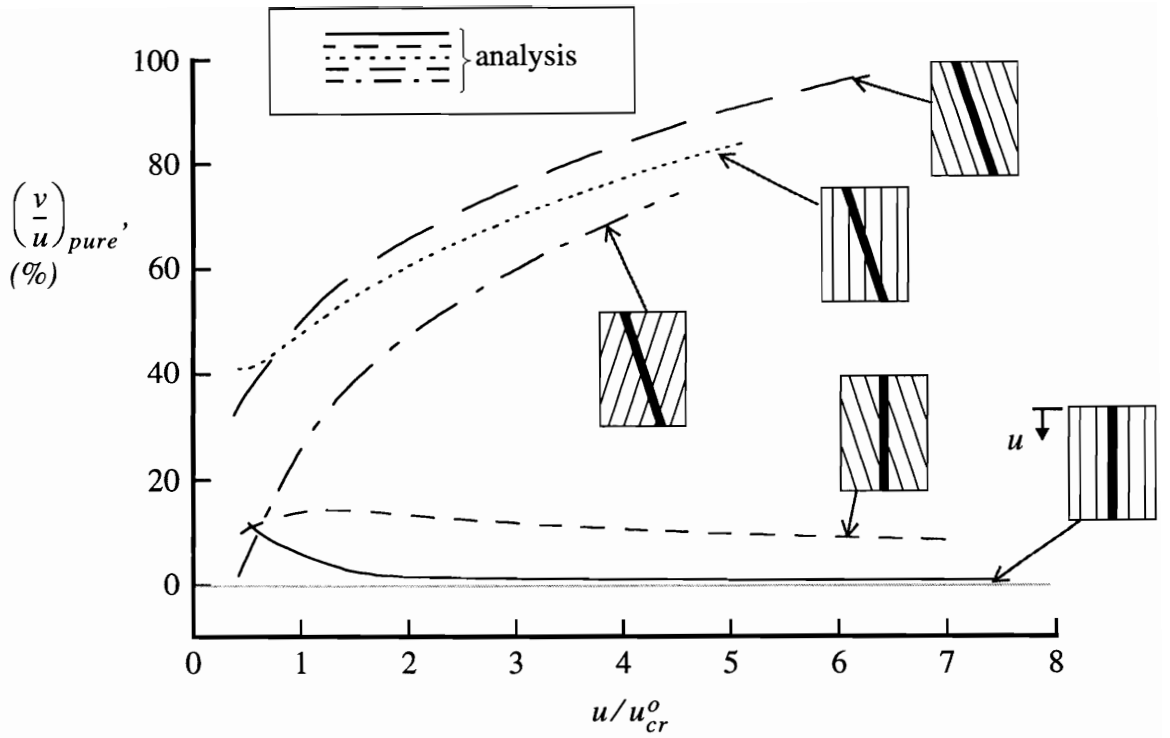

Fig. 4-9 Predicted pure displacement coupling vs. end shortening response

Fig. 4-9 have larger magnitudes than the pure force couplings shown in Fig. 4-8, but the shapes of the responses are nearly identical. Evaluating the right side of Eq. (4.2) for this case gives

$$\left(\frac{P_{xy}}{P_x}\right)^{equ}_{pure} = \Phi\left(\frac{v}{u}\right)_{pure} \quad . \tag{4.4}$$

Subtracting Eq. (4.4) from Eq. (4.3) and solving for Φ gives

$$\Phi = \frac{\left(\frac{P_{xy}}{P_x}\right)_{pure}}{\left(\frac{v}{u}\right)_{pure}} \quad . \tag{4.5}$$

Thus, the estimated values of Φ are obtained by dividing the results in Fig. 4-8 by the results in Fig. 4-9. The estimated values of Φ for each panel are shown in Fig. 4-10 as a function of the normalized end shortening. For the panels that were tested, the scale factor

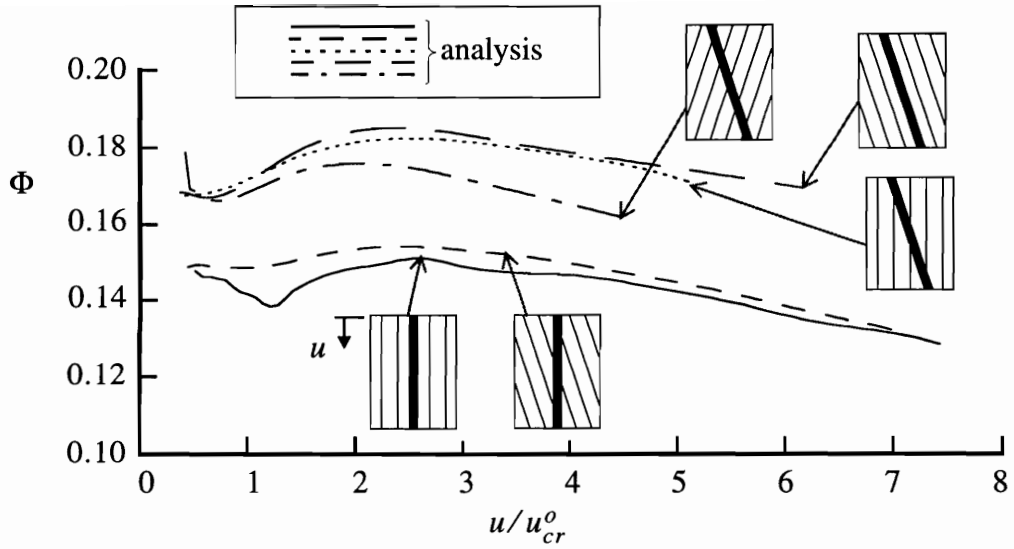

Fig. 4-10 Predicted scale factor vs. end shortening response for converting displacement coupling to an equivalent pure force coupling

Φ had values that ranged from 0.129 to 0.185, and the value of Φ for a single panel varied by less than 20% over the full range of the loading.

The estimated values of Φ and the measured force and displacement couplings are then applied to Eq. (4.1) to yield the equivalent pure force coupling for the experiments. The predicted pure force coupling results previously shown in Fig. 4-8 and the equivalent pure force coupling from the experiments are compared in Fig. 4-11. The pure force coupling is presented as a percentage, and the end shortening is normalized by u^o_{cr}. The pure force couplings predicted by the analyses are shown as dark solid and dashed lines. The equivalent pure force couplings that were computed using the experimental data are represented by filled symbols. To assist in identifying the experimental data for a single configuration, the filled symbols are connected by light solid lines. The pure force coupling results shown in Fig. 4-11 are a measure of the total axial-shear coupling response of the configurations that were tested. These results demonstrate that the numerical model was able to predict an axial-shear coupling response that compares well with the response that was observed in the experiments. There are some discrepancies in the measured and predicted values of the pure force coupling, but the nature of the response and the ranking of the configurations based on the levels of pure force coupling are consistent between the measured and predicted responses. The following conclusions may be made based on the results shown in Fig. 4-11.

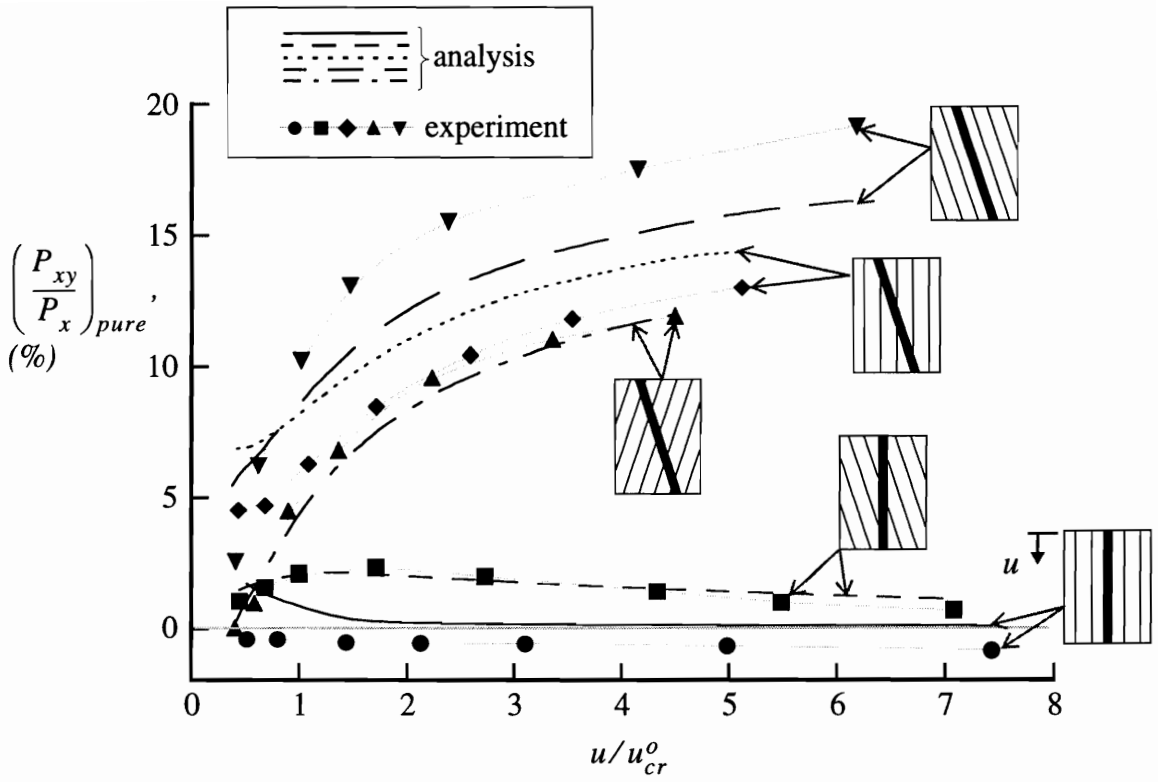

Fig. 4-11 Predicted pure force coupling and equivalent pure force coupling vs. end shortening response

- The axial-shear coupling response of the configuration with the unrotated stiffener and unrotated skin is near zero for all load ranges.
- The configuration with the unrotated stiffener and the skin rotated 20° demonstrates a small amount of axial-shear coupling response, and the amount of axial-shear coupling response diminishes in the postbuckling load range.
- The three configurations with the stiffener rotated 20° all exhibit a substantial increase in the axial-shear coupling response in the postbuckling load range. Rotating the skin orientation in the same direction as the stiffener rotation increases the axial-shear coupling response, and rotating the skin in the opposite direction of the stiffener rotation decreases the axial-shear coupling response.

This chapter has presented experimental data and numerical results from nonlinear structural analyses that were conducted to simulate the experimental responses. Measured and predicted values for the axial load vs. end shortening response, deformed shapes and out-

of-plane displacements, and axial-shear coupling responses have been compared. The numerical results compare well with the experimental results, and thus the accuracy of the numerical models have been verified.

5. Failure of Stiffened Panels

When the panels were compressed, the skins buckled and out-of-plane displacement patterns developed in the skins. The stiffener participated in the buckling deformation by way of the attachment flanges bending and twisting, but the overall out-of-plane displacements of the stiffener were negligible. Stresses developed in the interface between the skin and the stiffener attachment flange as a result of the out-of-plane deformations, stiffness discontinuity, and attachment flange eccentricity. As the load on the panels increased, the stresses required to keep the skin and stiffener together grew until they exceeded the strength of the interface. Then the skin and stiffener separated. The failure loads for the experiments were listed in Table 2-1. The average failure load of the panels with the unrotated stiffener was 30.1 kips, while the average failure load for the panels with the stiffener rotated 20° was 20.1 kips. These failure loads indicate that rotating the stiffener by 20° caused an average of 33% reduction in panel strength.

As reported in the literature review, the most common failure mode of postbuckled composite stiffened panels is stiffener disbonding, i.e., skin-stiffener separation, although experimental studies of postbuckled stiffened panels typically have not expanded on this mode of failure. Several papers that address the interlaminar normal and shear stresses at the skin-stiffener interface are Refs. 54 - 61. In general, the current methods for predicting skin-stiffener interface stresses fall short of reliable prediction of failure due to skin-stiffener disbonding of stiffened panels under general loading.

It is recognized that the stress state in the skin-stiffener interface is complex, consisting of interlaminar shear stresses in two directions, and an interlaminar normal stress. Stiffness discontinuity in the interface results in high stress gradients and singularities. Finite element analyses using three-dimensional elements which can account for possible singular stress behavior would have been required to predict the interface stresses in the panels

considered in this investigation. Conceding that a detailed stress analysis of the skin-stiffener interface is beyond the scope of the current research project, it may be possible, however, to obtain information from a simplified analysis based on two-dimensional plate elements that will give insight into the tendency for skin-stiffener separation to occur. The information available from a simplified analysis is discussed in what follows.

The premise that is applied in this simplified analysis is that the stresses at the interface are a result of the local load transfer between the skin and stiffener, and that the forces and moments (as opposed to the stresses) between the skin and stiffener can be explained, at least qualitatively, with results obtained from an analysis which is based on plate elements. After all, the integral of the interface stresses should be equal to the net forces and moments holding the skin and stiffener together. Crude approximations of the stress distribution associated with each force component are introduced only to assess the relative significance of each force component. By computing the forces and moments at the interface in the models using plate elements, it may be possible to explain why the panels with the skewed stiffeners failed at an average ultimate load that was 33% lower than the average ultimate load for panels with the unrotated stiffener. The purpose of this approach is not to predict failure quantitatively, but rather to provide some method for assessing the effect of stiffness tailoring on the tendency for skin-stiffener separation, at least in a comparative sense. The validity of this approach is evaluated by performing STAGS analyses of the five panels at loads corresponding to failure, and looking for some commonality in the forces or moments at the skin-stiffener interface. The predicted skin-stiffener attachment forces and moments from the analyses are presented in the following sections.

5.1 Approach to Predict Skin-Stiffener Attachment Forces and Moments

Though not specifically mentioned earlier, the finite element models that were used to compute the numerical results presented in Chapter 4 were specifically designed to obtain skin-stiffener attachment forces and moments. Rather than representing the attachment flange of the stiffeners and the skin under the stiffener as a single built-up laminate, the attachment flange and skin were modeled as separate laminates with displacement compatibility enforced between the laminates. A sketch which demonstrates the finite element model of the skin and stiffener cross section is shown in Fig. 5-1. In the model the reference surfaces for the skin and attachment flange are located at the midplane of the skin.

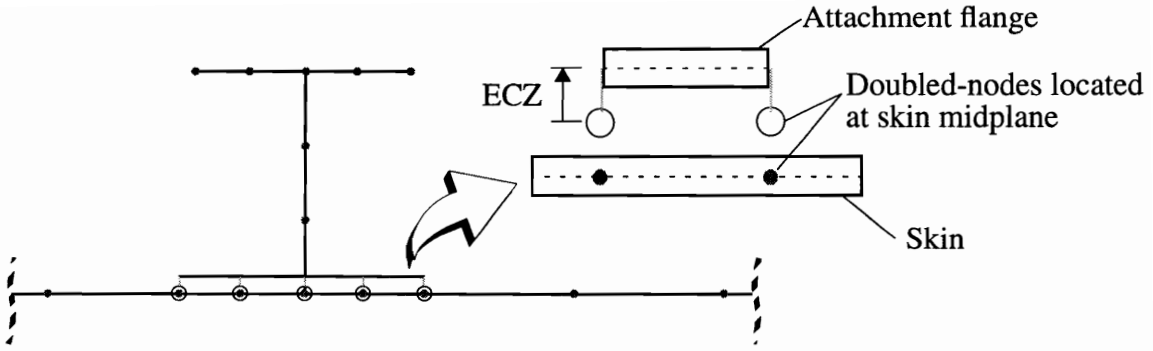

Fig. 5-1 Finite element model of skin-stiffener attachment

The nodes on the reference surface of the attachment flange are coincident with nodes on the skin reference surface, forming a series of doubled-node pairs. Displacement compatibility is then applied to the translations and rotations of the doubled-nodes, thereby connecting the attachment flange to the skin. The eccentricity of the attachment flange relative to the skin midplane is modelled by specifying that the plate elements representing the attachment flange have an eccentricity ECZ equal to half the skin thickness plus half the thickness of the attachment flange.

After a solution is obtained with the STAGS analysis code, the external forces and moments on the nodes can be computed. The forces and moments computed for the skin nodes under the attachment flange are the skin-stiffener forces and moments applied by the attachment flange to the skin midplane. The forces and moments applied at the interface between the attachment flange and the skin are obtained by determining a statically equivalent force-couple system at the interface location. The equivalent force-couple system at the interface location results in the same forces, but the moments reflect the moments created by changing the z-location of the forces by half the thickness of the skin.

Numerical solutions for the response of each panel for applied u and v displacements equal to the displacements at failure, u_{ult}^{exp} and v_{ult}^{exp}, respectively, are presented below. Recall, the experimentally-measured ultimate loads $(P_x)_{ult}^{exp}$ and the corresponding displacements u_{ult}^{exp} and v_{ult}^{exp} were reported in Table 2-1.

5.2 Nomenclature and Normalization of Forces and Moments

The forces and moments presented in this chapter represent the forces and moments applied to the skin by the stiffener at the skin-stiffener interface. The forces and moments are presented in a local rectangular coordinate system which is aligned with the stiffener axis. The *xs* direction is along the axis of the stiffener, the *ys*-direction is perpendicular to the stiffener and parallel to the skin surface, and the *zs*-direction is normal to the skin surface. For the panels with the unrotated stiffeners, the *xs*-, *ys*-, and *zs*-coordinate directions are aligned with the global *x*-, *y*-, and *z*-axes. At each node on the skin-stiffener interface the forces in the *xs*-, *ys*-, and *zs*-directions are denoted by F_{xs}, F_{ys}, and F_{zs}, respectively, and the moments about the *xs*-, *ys*-, and *zs*-coordinate axes are denoted by M_{xs}, M_{ys}, and M_{zs}, respectively. A schematic which shows the positive directions of the forces and moments for a case with the stiffener rotated 20° is shown in Fig. 5-2.

The finite element discretization in the skin-stiffener attachment region that was used to obtain the numerical results is shown in Fig. 5-3. The mesh with the unrotated stiffener and the mesh with the stiffener rotated 20° are shown in Figs. 5-3(a) and 5-3(b), respectively. Both meshes have four elements across the 1.5 in. width of the stiffener attachment flange, and an element length in the *x* direction of 1.0 in. Therefore, the elements in the mesh with the unrotated stiffener have an element length in the *xs*-direction of 1.0 in., while the elements in the mesh with the stiffener rotated 20° have an element length in the

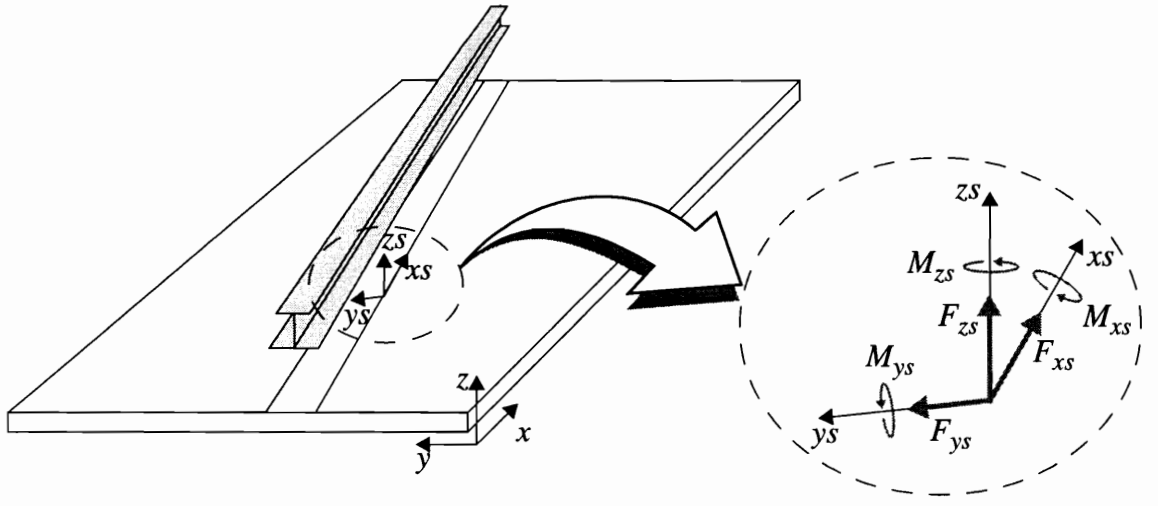

Fig. 5-2 Skin-stiffener attachment forces and moments on skin surface in stiffener *xs-ys-zs* coordinate system

xs direction of 1.064 in. To allow comparison of the results obtained from the two meshes, the forces and moments that were computed with the stiffener rotated 20° were divided by 1.064, thus scaling the results to be equivalent to a 1.0 in. element spacing along the *xs*-axis.

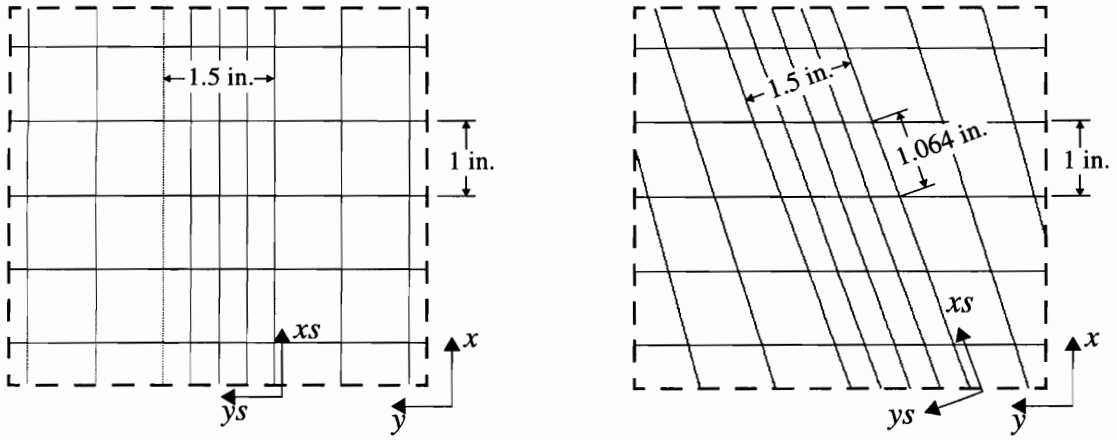

(a) Unrotated stiffener (b) Stiffener rotated 20°

Fig. 5-3 Mesh discretization of the skin-stiffener attachment region

Panel B0,0, with the unrotated stiffener and unrotated skin, is considered the baseline configuration against which the other configurations are compared. The predicted maximum magnitude of the forces and moments for panel B0,0 at failure are denoted by $\overline{F}_{xs}$, $\overline{F}_{ys}$, $\overline{F}_{zs}$, $\overline{M}_{xs}$, $\overline{M}_{ys}$, and $\overline{M}_{zs}$, and their values are listed in Table 5-1.The primary objectives of examining the skin-stiffener attachment forces and moments are to identify the locations within a given panel where the forces and moments are the largest, and to compare the predicted forces and moments in each of the panels at failure. To assist in comparing results, the skin-stiffener forces and moments F_{xs}, F_{ys}, F_{zs}, M_{xs}, M_{ys}, and M_{zs} for all panels are presented as a percentage of $\overline{F}_{xs}$, $\overline{F}_{ys}$, $\overline{F}_{zs}$, $\overline{M}_{xs}$, $\overline{M}_{ys}$, and $\overline{M}_{zs}$, respectively.

5.3 Predictions of Skin-Stiffener Attachment Forces and Moments

Results for the panel with the unrotated skin and unrotated stiffener are presented first. This panel has the most benign configuration, and its skin-stiffener attachment forces and moments are the most easily explained by examining the postbuckled deformations of the panel. While presenting the forces and moments for this panel, some comments are made regarding the stress distributions associated with skin-stiffener forces and moments.

Table 5-1 Maximum Magnitude of Skin-Stiffener Forces and Moments for Panel B0,0

Force, Moment	Maximum Magnitude
$\overline{F}_{xs}$	951 lbs
$\overline{F}_{ys}$	401 lbs
$\overline{F}_{zs}$	114 lbs
$\overline{M}_{xs}$	17 in-lbs
$\overline{M}_{ys}$	36 in-lbs
$\overline{M}_{zs}$	23 in-lbs

5.3.1 Panel B0,0: 

The experimentally-measured ultimate load for panel B0,0 was $(P_x)_{ult}^{exp} = 31.2$ kips (see Table 2-1). When the displacements u_{ult}^{exp} and v_{ult}^{exp} were applied to the finite element model, the predicted load in the x-direction was $(P_x)_{ult}^{FE} = 33.1$ kips. A contour plot of the predicted out-of-plane displacement and the moiré-fringe pattern photographed just prior to failure of the panel are compared in Fig. 5-4. The contour plots and moiré-fringe patterns are shown as viewed from the unstiffened side of the panel. In the contour plot in Fig. 5-4(a), the dark contours correspond to $w \geq 0$, i.e., toward the stiffener, while the light contours correspond to $w < 0$. The outermost dark contour corresponds to $w = 0$, and each contour represents a $\Delta w = 0.020$ in. The results in Fig. 5-4 show that the out-of-plane deformations are largest in the postbuckled skin and are near zero along the centerline of the stiffener. A close examination of Fig. 5-4 shows contour lines on the skin and attachment flange region of the stiffener. It can therefore be concluded that although the centerline of the stiffener has minimal out-of-plane displacements, the stiffener attachment flange deforms. The out-of-plane deformations in the skin-stiffener attachment region are a direct result of skin buckling and are largely responsible for the generation of skin-stiffener attachment forces and moments.

For panel B0,0 the predicted forces and moments on the skin at the skin-stiffener interface at the ultimate load are shown in Fig. 5-5. Each force and moment are shown separately as vector plots. The lengths of the vectors are scaled proportional to the magnitude of the force, or moment, and the directions of the vectors indicate the direction of the force, or moment, applied to the skin by the stiffener attachment flange.

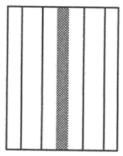

(viewed from unstiffened side)

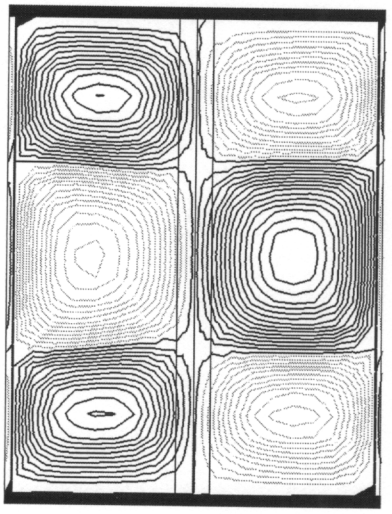

(a) STAGS contour

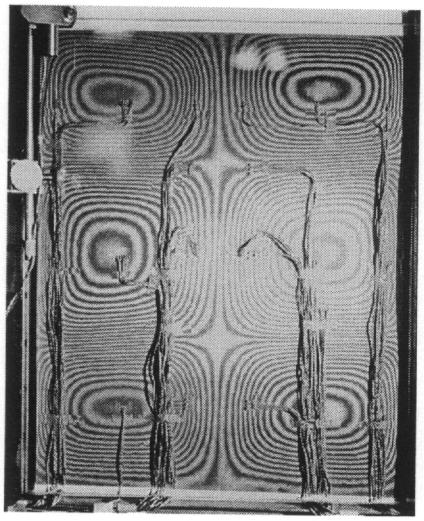

(b) Moiré-fringe pattern

Fig. 5-4 Panel B0,0: comparison of predicted out-of-plane skin displacement contours at ultimate load

The results that are presented do not display any strong form of symmetry. Symmetry in the response does not exist because

- the panel is stiffened on one side only
- unsymmetric initial geometric imperfections are included in the analysis
- unsymmetric nonuniform initial loading is included in the analysis

To aid in interpretation of the results, two contour plots of the predicted out-of-plane displacement are shown on the left side of the figure. The smaller contour plot is of the entire panel skin with contour intervals of $\Delta w = 0.06$ in., and the larger contour plot is of the skin under the attachment flange with contour intervals of $\Delta w = 0.01$ in. These contour plots are shown as viewed from the stiffened side of the panel, and, as before, the dark contours correspond to $w \geq 0$, i.e., toward the stiffener, while the light contours correspond to $w < 0$. Locations where the skin-stiffener forces and moments are a maximum are identified on the larger contour plot by the letters $\mathbb{A}$, $\mathbb{B}$, and $\mathbb{C}$.

The force on the skin in the direction of the stiffener axis, F_{xs}, is shown in Fig. 5-5(a). The maximum values of F_{xs} occur on the edges of the skin-stiffener interface at nodelines in the w displacement. The point of maximum force is circled and corresponds to point $\mathbb{A}$

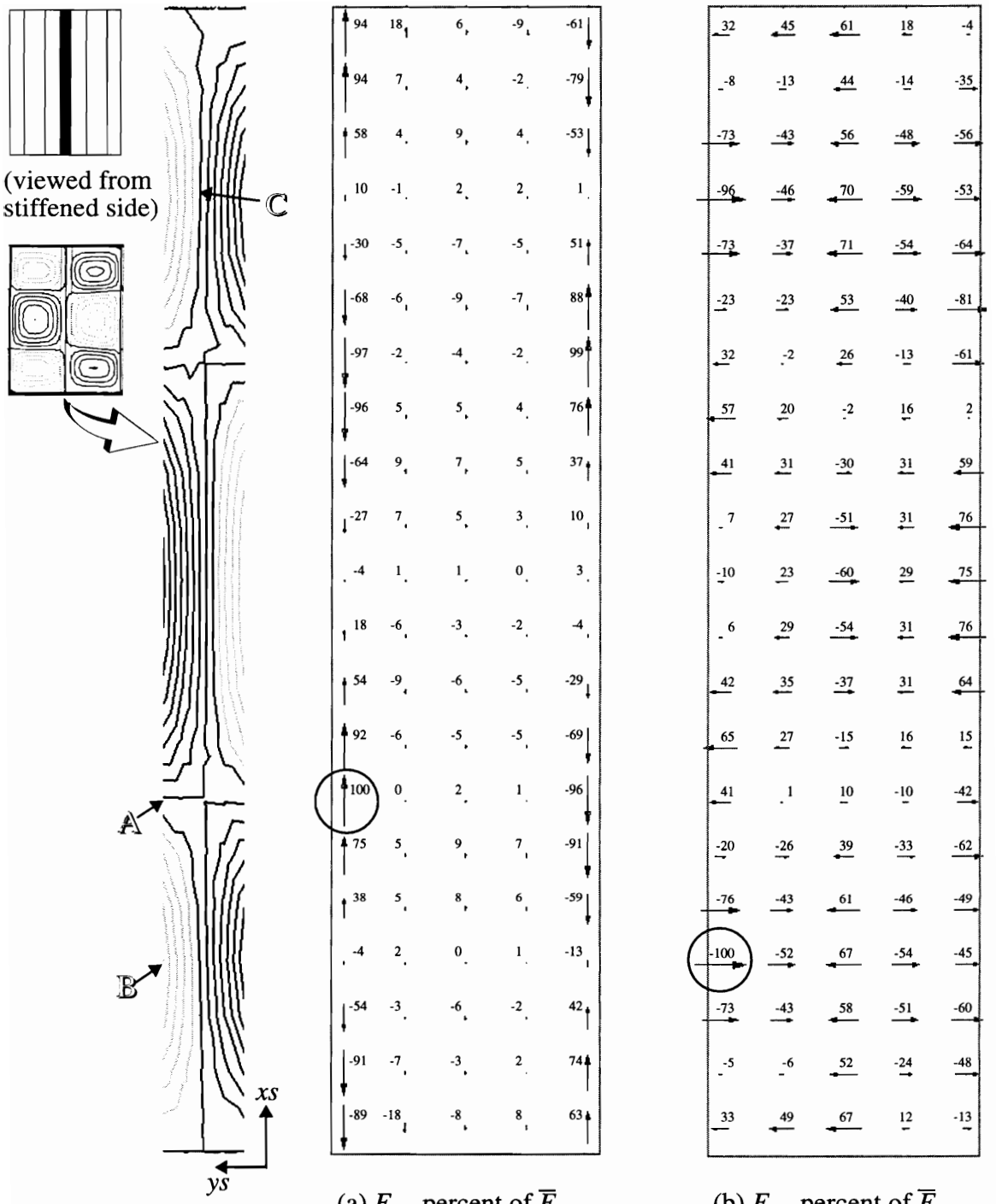

(a) F_{xs}, percent of $\overline{F}_{xs}$

(b) F_{ys}, percent of $\overline{F}_{ys}$

Fig. 5-5 Panel B0,0: predicted forces and moments on skin at skin-stiffener interface at failure, $(P_x)_{ult}^{exp}$ = 31.2 kips

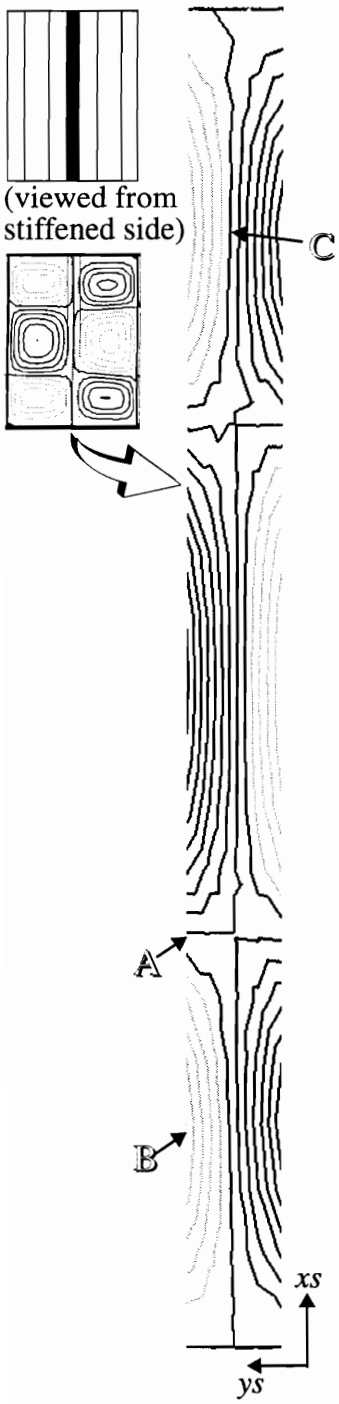

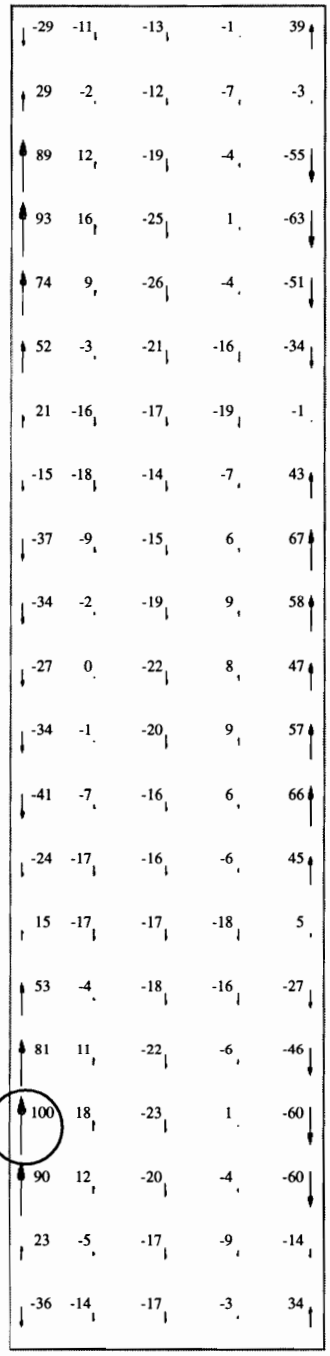

(c) F_{zs}, percent of $\overline{F}_{zs}$

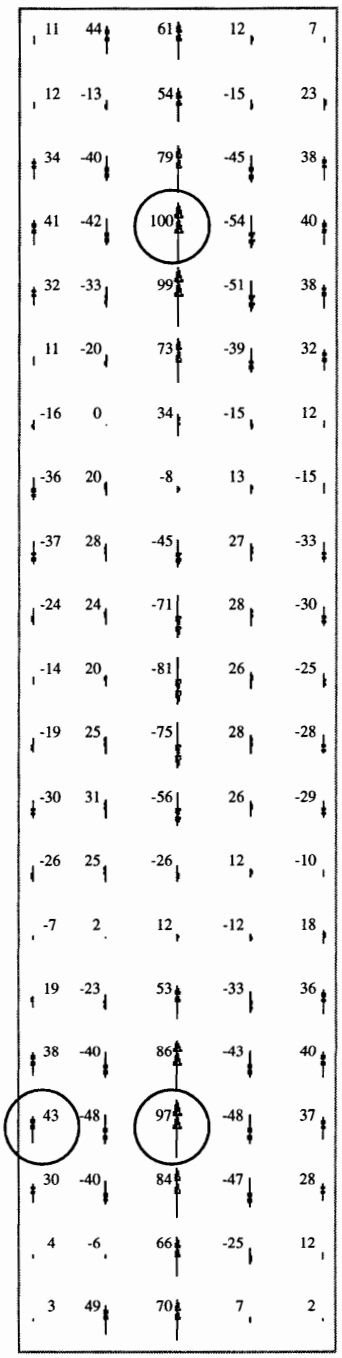

(d) M_{xs}, percent of $\overline{M}_{xs}$

Fig. 5-5 Continued

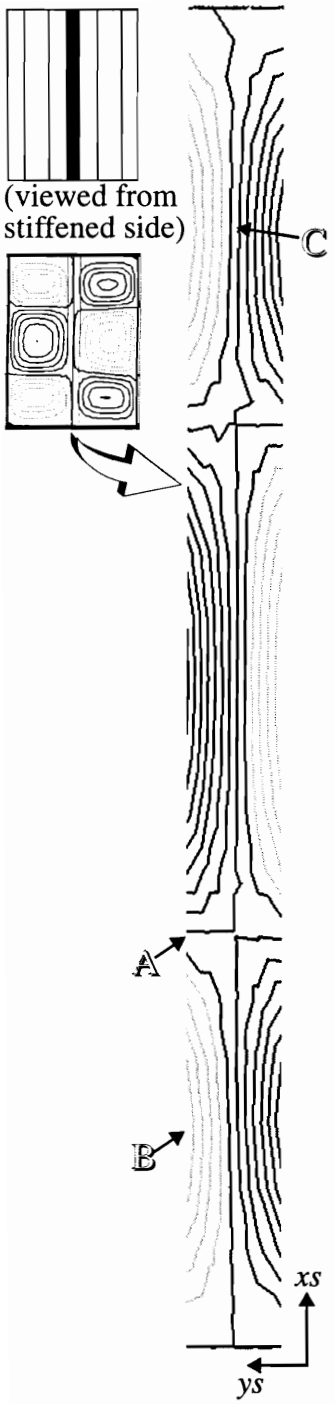

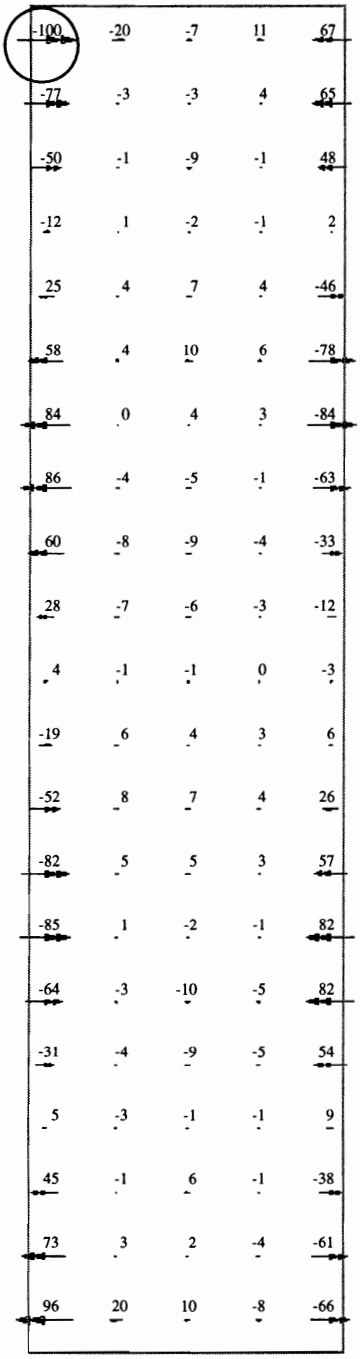

(e) M_{ys}, percent of $\overline{M}_{ys}$

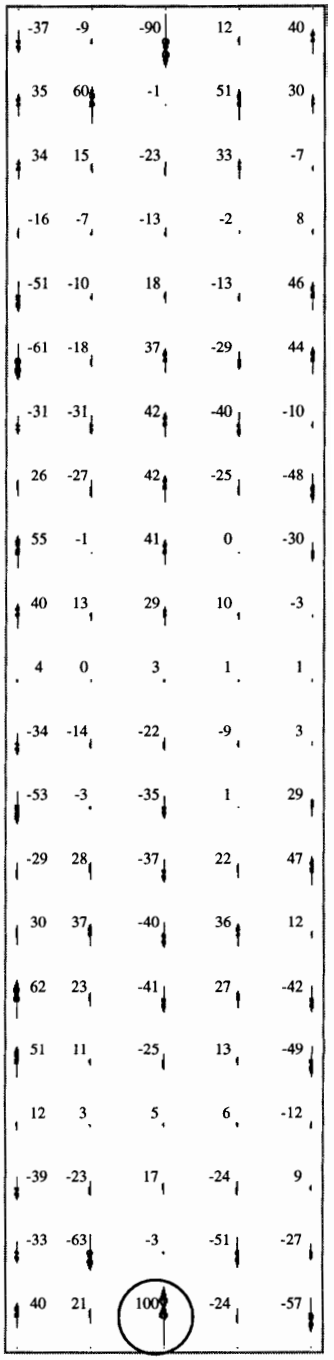

(f) M_{zs}, percent of $\overline{M}_{zs}$

Fig. 5-5 Continued

on the contour plot of the *w* displacement. The forces on the skin on both edges of the interface region are in the direction of increasing w displacement, and therefore are opposite in direction on the right and left edges. Force F_{xs} is a result of the twisting moment about the *ys*-direction that is created by the postbuckled skin intersecting the stiffener. The sketch in Fig. 5-6(a) shows a twisting moment M_{xy} that exists in the skin near the nodeline in the postbuckled skin. At the location where the attachment flange is over the skin, the neutral axis of the net section shifts upward. In Fig. 5-6(b) the twisting moment causes a rotation of the net section. Displacement compatibility at the skin-stiffener interface causes the midplane of the attachment flange to move in the (*-xs*)-direction, and the midplane of the skin to move in the (*+xs*)-direction. The forces and moments between the skin and attachment flange which keep the surfaces together are shown in Fig. 5-6(b). Force F_{xs} on the skin is in the direction of increasing *w* displacement, which is consistent with Fig. 5-5(a). There are M_{ys} moments shown in Fig. 5-6(b). These moments are the result of determining a statically equivalent force-couple system at the skin-stiffener interface, and are due to changing the location of the forces to the interface. The distribution of M_{ys} for

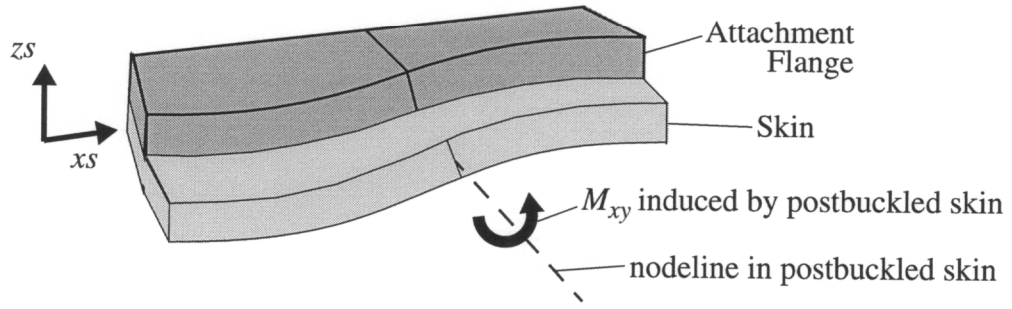

(a) Twisting moment in skin

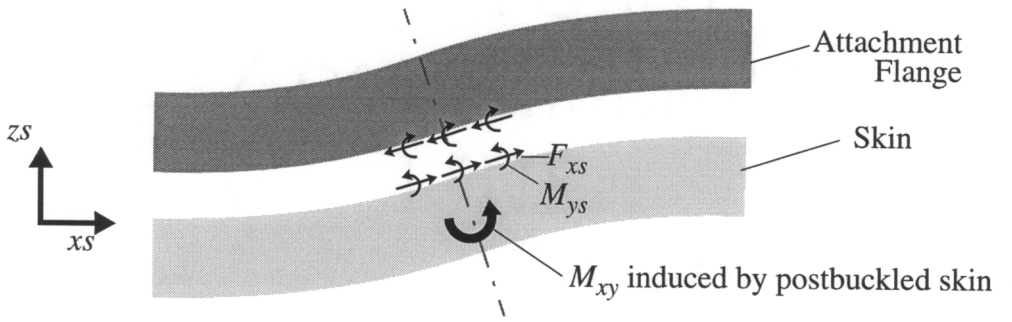

(b) Cross section deformation at edge of attachment flange

Fig. 5-6 Twisting moment in the skin creates F_{xs} and M_{ys}

panel B0,0 is shown in Fig. 5-5(e). The largest values of M_{ys} are located on the edge of the skin-stiffener interface, at nodelines in the postbuckled skin.

Forces F_{ys} and F_{zs} and moment M_{xs} are shown in Figs. 5-5(b), 5-5(c), and 5-5(d), respectively. The maximum values of each component are circled and are located along the stiffener where the out-of-plane skin displacements of the skin are a maximum.

Forces F_{ys} and F_{zs} have maximum values at point $\mathbb{B}$ indicated on the contour plot of the w displacement. In the vector plot of F_{zs} in Fig. 5-5(c), a vector pointing toward the top of the page indicates a force on the skin in the $(+zs)$-direction and corresponds to a tensile stress in the skin-stiffener interface. Moment M_{xs} shown in Fig. 5-5(d) is the moment about the stiffener axis. The maximum value of M_{xs} is located at point $\mathbb{C}$ on the centerline of the skin-stiffener interface, under the stiffener web. Moment M_{xs} is also large under the stiffener web near point $\mathbb{B}$. The maximum value of M_{xs} on the edge of the interface is located at point $\mathbb{B}$.

Moment M_{zs} shown in Fig. 5-5(f) is the moment about the normal to the skin surface. In the vector plot of M_{zs}, a vector pointing toward the top of the page indicates a moment on the skin about the $(+zs)$-direction. The maximum values of M_{zs} are located at the ends of the stiffener.

The existence of forces F_{ys} and F_{zs} and moment M_{xs} in the postbuckled panel is explained by the sketch of the skin-stiffener cross section at point $\mathbb{B}$ on the stiffener shown in Fig. 5-7. Consider first the left side of the cross section shown in Fig. 5-7. The postbuckled skin on this side of the stiffener has a negative w displacement. The attachment flange resists the out-of-plane displacement and thus the shear resultant Q_y and bending resultant M_y are created in the skin. The bending moment in the skin causes the skin to bend about its midplane. At the location where the attachment flange is over the skin, the neutral axis of the net section shifts upward. The bending moment caused by M_y and Q_y creates bending of the net section, and puts the attachment flange in inplane tension and the skin under the attachment flange in inplane compression, both in the ys-direction. This inplane compression in the skin under the left attachment flange is generated through interface forces F_{ys}. The tensile normal force F_{zs} and the bending moment M_{xs} at the edge of the attachment flange are a result of the skin trying to pull away and peel away from the attachment flange. On the right side of the stiffener the skin has a positive w displacement. The attachment flange resists the out-of-plane displacement and creates the shear and

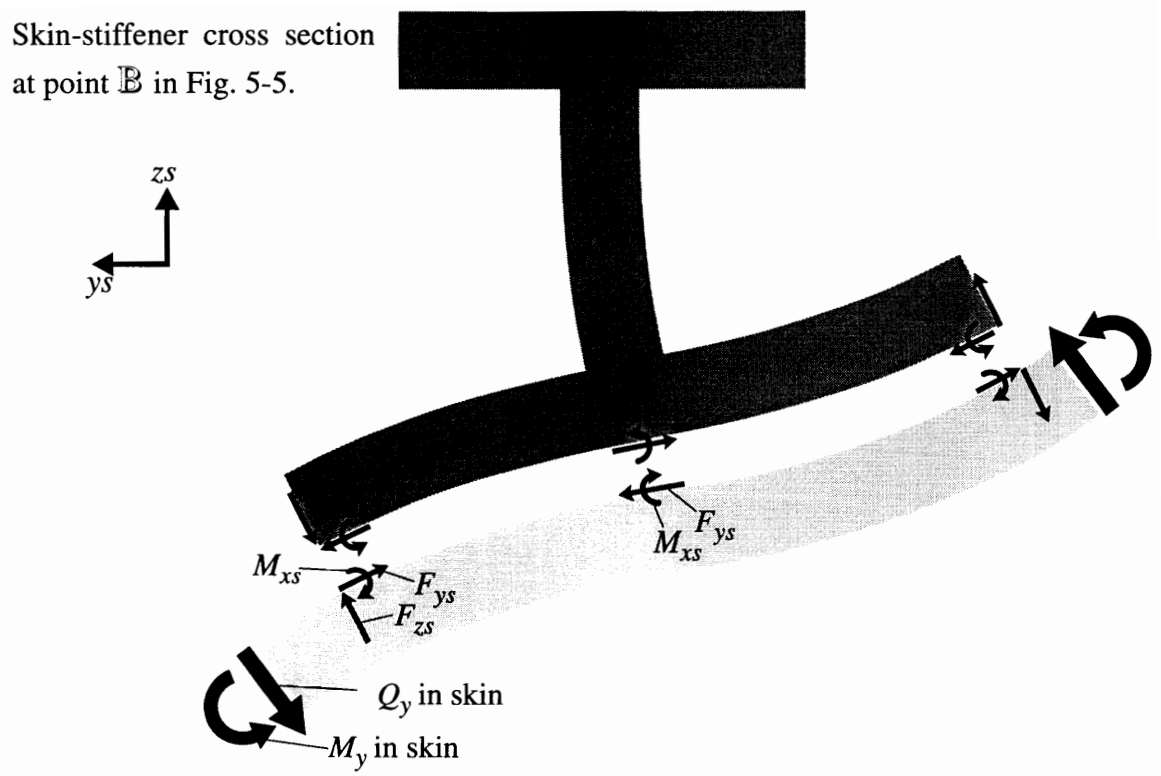

Fig. 5-7 Shear Q_y and bending moment M_y in the skin create F_{ys}, F_{zs}, and M_{xs}

bending moments in the skin. The loads in the skin on the right side of stiffener are reversed in nature relative to the skin forces on the left side of the stiffener. On the right edge of the attachment flange the normal force F_{zs} and the bending moment M_{xs} cause interface normal stresses that are in compression, and therefore do not invoke skin-stiffener separation. The bending of the skin-attachment flange section induces interface forces F_{ys} which put the skin under the attachment flange in inplane tension. In the center of the interface region, under the stiffener web, force F_{ys} on the skin is to the left, so that the skin under the attachment flanges are in inplane compression on the left, and in inplane tension on the right. Moment M_{xs} under the stiffener web results from the stiffener web and cap resisting torsional deformation of the attachment flange.

Looking again at forces F_{ys} and F_{zs} and moment M_{xs} shown in Figs. 5-5(b), 5-5(c), and 5-5(d), respectively, note that the forces and moments are larger in magnitude on the side where the skin has negative w displacements, i.e., where the skin is moving away from the stiffener. The differences in the magnitudes are due to the N_y distribution that develops in the postbuckled skin. Contour plots of the predicted w displacement and the stress result-

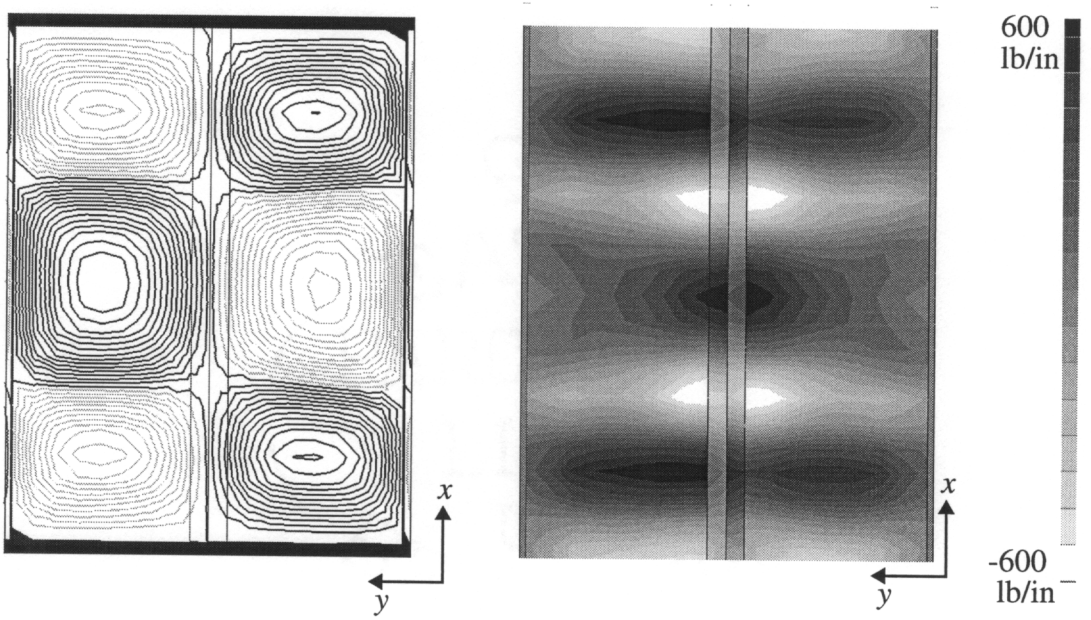

(a) STAGS w displacement (b) STAGS N_y stress resultant

Fig. 5-8 Panel B0,0: predicted N_y stress resultant at failure

ant N_y in the skin for panel B0,0 at the load corresponding to failure are shown in Fig. 5-8. These plots indicate that the skin has tensile N_y across the width where the out-of-plane displacements are large, and a compressive N_y along the nodelines in the buckled pattern. At the location on the stiffener previously identified as point $\mathbb{B}$, the skin experiences tensile N_y on both sides of the stiffener. The skin-stiffener interface forces and moments created by applying only tensile N_y to a stiffened panel that has similar skin and attachment flange stiffnesses are shown in Fig. 5-9. If the forces and moments on the skin-stiffener interface in Fig. 5-9 are added to the forces and moments in Fig. 5-7, the resultant forces and moments will have a larger magnitude on the left edge of the interface, i.e., where the w displacement is away from the stiffener.

Stress distributions associated with skin-stiffener interface forces and moments

As a point of general information, some comments are now made concerning the character of the three-dimensional stress distributions that lead to the skin-stiffener interface forces and moments just discussed. These comments are meant to reflect the general nature of the stress distributions only. The stress distributions have singularities associated with discontinuous stiffnesses. Typically, the attenuation length for the singularity is of the order of the thickness of the attachment flange.

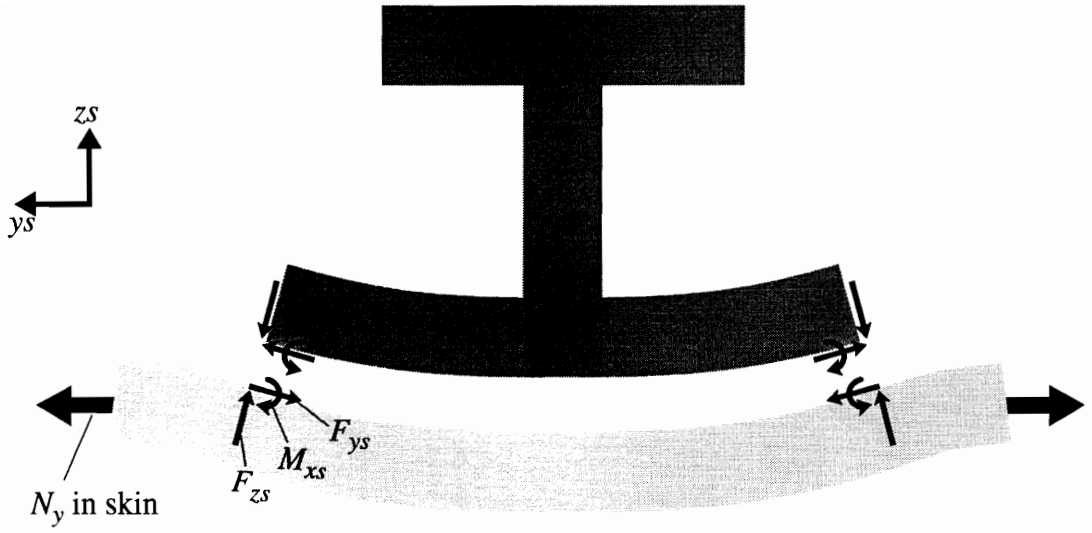

Fig. 5-9 Skin-stiffener interface forces and moments caused by N_y stress resultant

A single F_{xs} force along the edge of the interface is the result of a distribution of σ_{xz} of the form shown in Fig. 5-10(a). Force F_{ys} perpendicular to the stiffener edge may originate from a distribution of σ_{yz} of the form shown in Fig. 5-10(b). The σ_{yz} distribution goes to zero on the edge of the interface. Force F_{zs} and moment M_{xs} are the result of a distribution of σ_z in the interface. The distribution of σ_z that would be equivalent to the normal force and the peeling moment at the edge of the interface is shown in Fig. 5-10(c), and the distribution of σ_z that would be equivalent to moment M_{xs} under the web of the stiffener is shown in Fig. 5-10(d).

The predicted skin-stiffener forces and moments for panel B0,0 have been presented, and an attempt has been made to identify the mechanics of the postbuckled response that create the skin-stiffener attachment forces and moments. The results from finite element analyses of the other panels will be reviewed and compared to the results for panel B0,0. The interface forces and moment that are examined are F_{xs}, F_{ys}, F_{zs}, and M_{xs}, since these components may be proportional to the interface stresses.

5.3.2 Panel B0,2:

The experimentally-measured ultimate load for panel B0,2 panel was $(P_x)_{ult}^{exp} = 29.0$ kips. When the displacements u_{ult}^{exp} and v_{ult}^{exp} were applied to the finite element model, the predicted load in the x-direction was $(P_x)_{ult}^{FE} = 30.7$ kips. A contour plot of the predicted

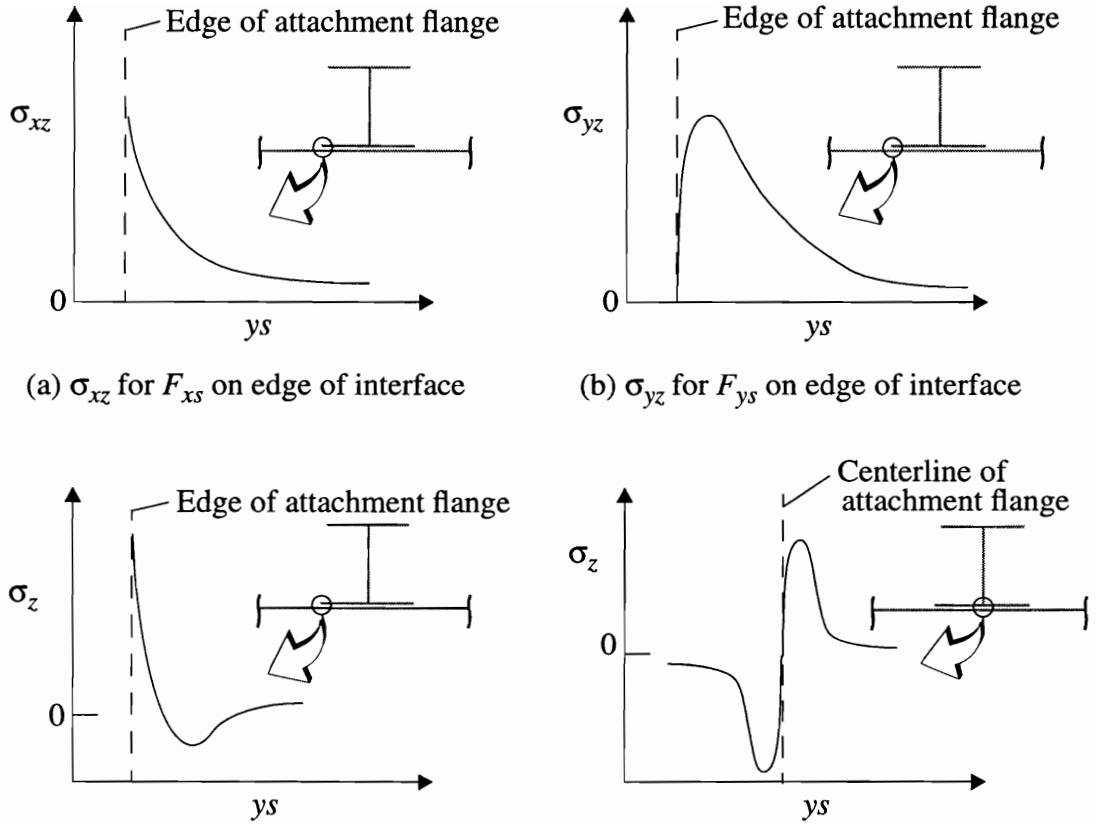

(a) σ_{xz} for F_{xs} on edge of interface

(b) σ_{yz} for F_{ys} on edge of interface

(c) σ_z for F_{zs} and M_{xs} on edge of interface

(d) σ_z for M_{xs} on centerline of interface, under stiffener web

Fig. 5-10 Possible interface shear and normal stress distributions resulting in interface forces and moments

out-of-plane displacement, and the moiré-fringe pattern photographed just prior to failure of the panel, are compared in Fig. 5-11.

The predicted forces and moments on the skin at the skin-stiffener interface at the ultimate load are shown in Fig. 5-12. The forces and moments for panel B0,2 are very similar in nature to those reported for panel B0,0. Note that because the out-of-plane deflection pattern for panel B0,2 is 'reversed' from the pattern of panel B0,0, the directions of the maximum interface forces and moments for panel B0,2 are opposite the directions for panel B0,0, and for the most part they occur on opposite sides of the stiffener flange, i.e., left vs. right side of the flange. Force F_{xs} has a maximum magnitude of 96 at the nodeline in the postbuckled skin, identified in Fig. 5-12 by point 𝔸. The maximum magnitudes for F_{ys} and F_{zs}, 118 and 100, respectively, are located at point 𝔹 where the skin out-of-plane

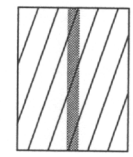

(viewed from unstiffened side)

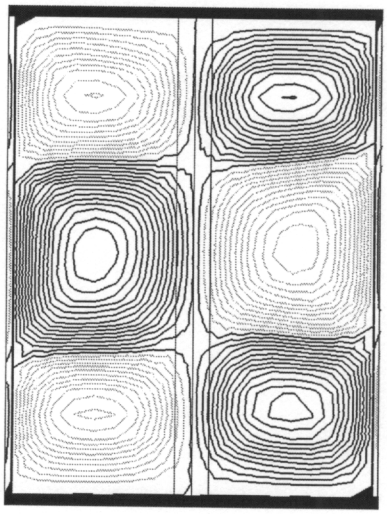

(a) STAGS contour

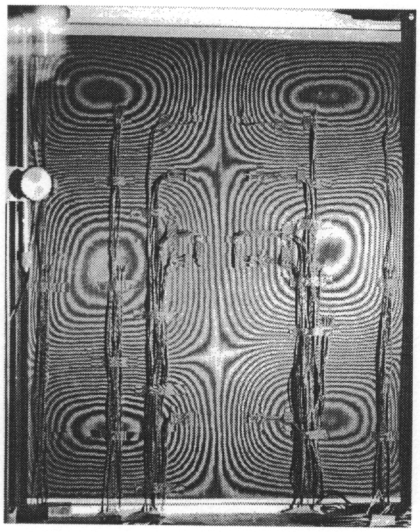

(b) Moiré-fringe pattern

Fig. 5-11 Panel B0,2: comparison of predicted out-of-plane skin displacement contours at ultimate load

displacement has a maximum negative value. The maximum magnitude of moment M_{xs}, 104, is located under the stiffener web at point $\mathbb{C}$, near point $\mathbb{B}$, and the maximum magnitude of the peeling moment on the edge of the interface, 58, is located at point $\mathbb{B}$.

5.3.3 Panel B2,0: 

The experimentally-measured ultimate load for panel B2,0 was $(P_x)_{ult}^{exp} = 19.43$ kips. When the displacements u_{ult}^{exp} and v_{ult}^{exp} were applied to the finite element model, the predicted load in the x-direction was $(P_x)_{ult}^{FE} = 21.6$ kips. A contour plot of the predicted out-of-plane displacement, and the moiré-fringe pattern photographed just prior to failure of the panel, are compared in Fig. 5-13. The maximum out-of-plane displacements are for $w < 0$. The displacement pattern of the postbuckled skin for panel B2,0 is quite different from the displacement pattern of the panels with the unrotated stiffener. A contour plot of the out-of-plane displacement of the skin under the attachment flange is shown to the left of the force vector plots in Fig. 5-14. As shown in the contour plot, at the stiffener midlength the skin has an out-of-plane displacement that is positive, i.e., toward the stiffener, across the entire width of the stiffener, and the w displacement on each side of the stiffener is also positive.

The predicted forces and moments on the skin at the skin-stiffener interface at the ulti-

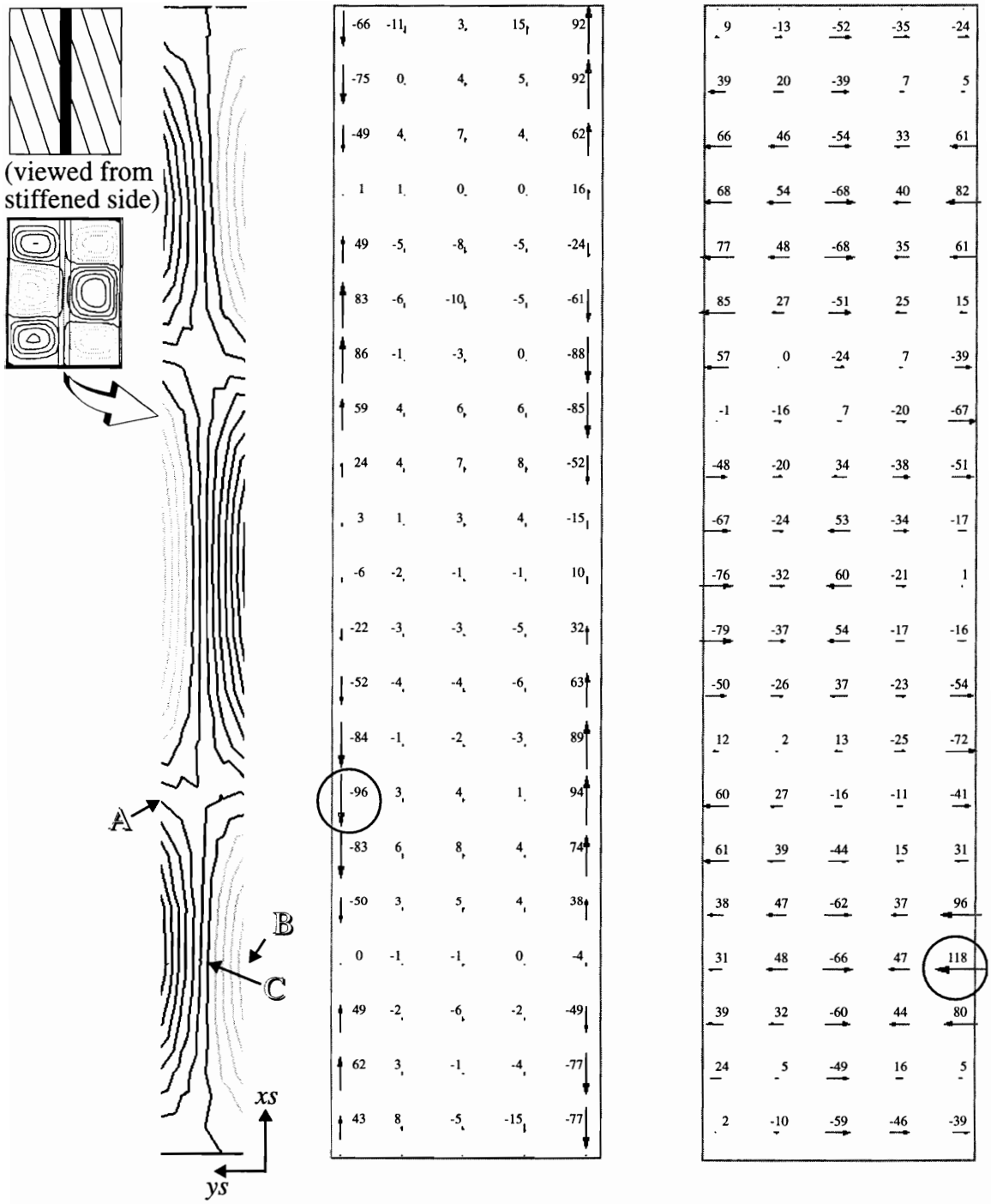

(a) F_{xs}, percent of $\overline{F}_{xs}$ (b) F_{ys}, percent of $\overline{F}_{ys}$

Fig. 5-12 Panel B0,2: predicted forces and moments on skin at skin-stiffener interface at failure, $(P_x)_{ult}^{exp}$ = 29.0 kips

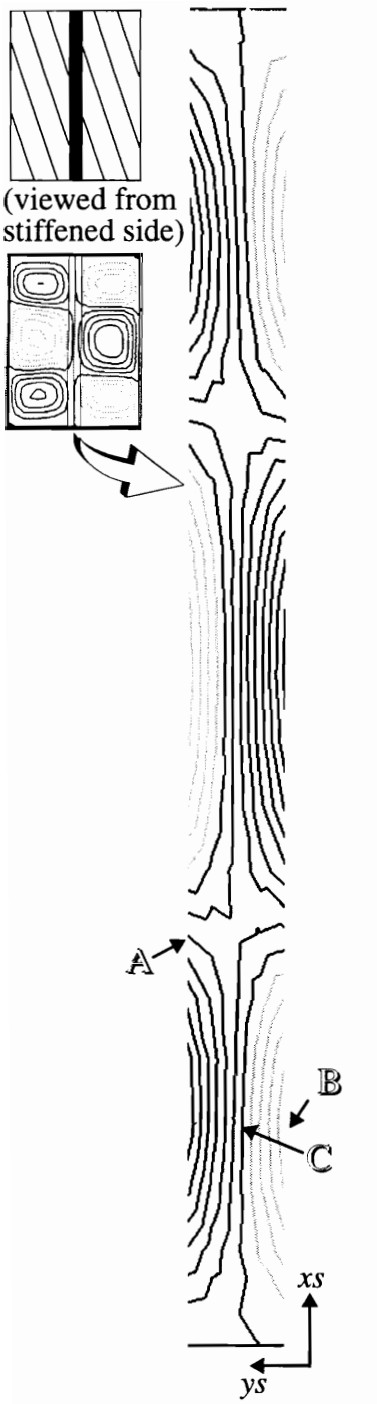

27	-5	-17	-12	-17
-11	-9	-17	-6	20
-50	-3	-22	8	73
-58	3	-23	15	84
-50	-2	-21	9	69
-24	-13	-15	-2	50
12	-14	-10	-14	23
41	-4	-10	-14	-16
52	3	-15	-4	-43
49	7	-20	2	-40
55	11	-19	1	-27
68	13	-16	-2	-24
57	3	-17	-9	-25
20	-14	-22	-18	-16
-12	-22	-24	-19	5
-29	-16	-23	-6	43
-49	-5	-22	8	81
-63	0	-19	14	100
-43	-3	-12	10	85
8	-4	-5	-2	26
28	2	-7	-6	-31

(c) F_{zs}, percent of $\overline{F}_{zs}$

-4	-9	-52	-31	-4
-20	22	-51	8	-17
-42	45	-80	30	-42
-44	51	-102	37	-44
-39	47	-100	31	-31
-36	28	-74	22	-7
-19	3	-31	5	24
12	-12	15	-21	41
30	-17	53	-37	34
29	-22	77	-32	16
28	-31	85	-20	10
34	-35	78	-15	24
28	-22	58	-20	41
-1	6	23	-24	37
-36	28	-22	-14	7
-51	36	-66	10	-30
-43	40	-97	31	-55
-32	41	-104	42	-58
-22	28	-90	41	-30
-1	7	-64	16	10
11	-4	-63	-46	0

(d) M_{xs}, percent of $\overline{M}_{xs}$

Fig. 5-12 Continued

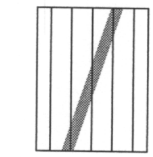

(viewed from unstiffened side)

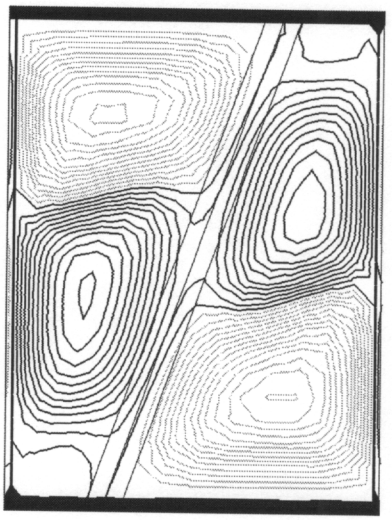

(a) STAGS contour

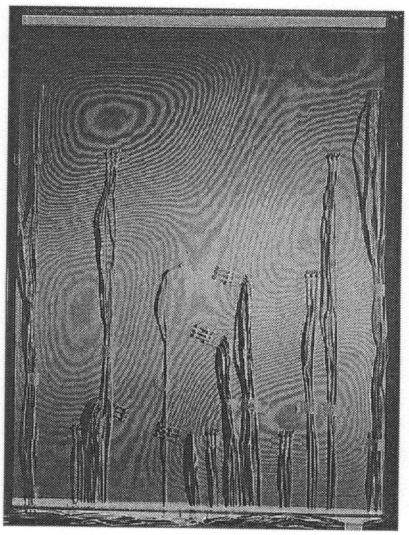

(b) Moiré-fringe pattern

Fig. 5-13 Panel B2,0: comparison of predicted out-of-plane skin displacement contours at ultimate load

mate load are shown in Fig. 5-14. As expected from the deformations shown in Fig. 5-13, the interface forces and moments for panel B2,0 are quite different than they were for the panels with the unrotated stiffener. Force F_{xs} shown in Fig. 5-14(a) has a maximum magnitude near the ends of the stiffener at the location identified in Fig. 5-14 by point $\mathbb{A}$. The maximum magnitudes for F_{ys} and M_{xs} are located at point $\mathbb{B}$ where the skin is bending toward the stiffener on each side of the stiffener. The directions of F_{zs} and M_{xs} at point $\mathbb{B}$ indicate that the normal stress in the skin-stiffener interface is compressive at this location. The maximum force $F_{zs,}$ the largest peeling moment M_{xs}, and large values for force F_{ys}, are located near point $\mathbb{C}$ on the edge of the interface where the out-of-plane displacement away from the stiffener is a maximum.

5.3.4 Panel B2,2: 

The experimentally-measured ultimate load for panel B2,0 was $(P_x)_{ult}^{exp} = 22.3$ kips. When the displacements u_{ult}^{exp} and v_{ult}^{exp} were applied to the finite element model, the predicted load in the x-direction was $P_x^{FE} = 23.0$ kips. A contour plot of the predicted out-of-plane displacement, and the moiré-fringe pattern photographed just prior to failure of the panel, are compared in Fig. 5-15.

The predicted forces and moments on the skin at the skin-stiffener interface at the ulti-

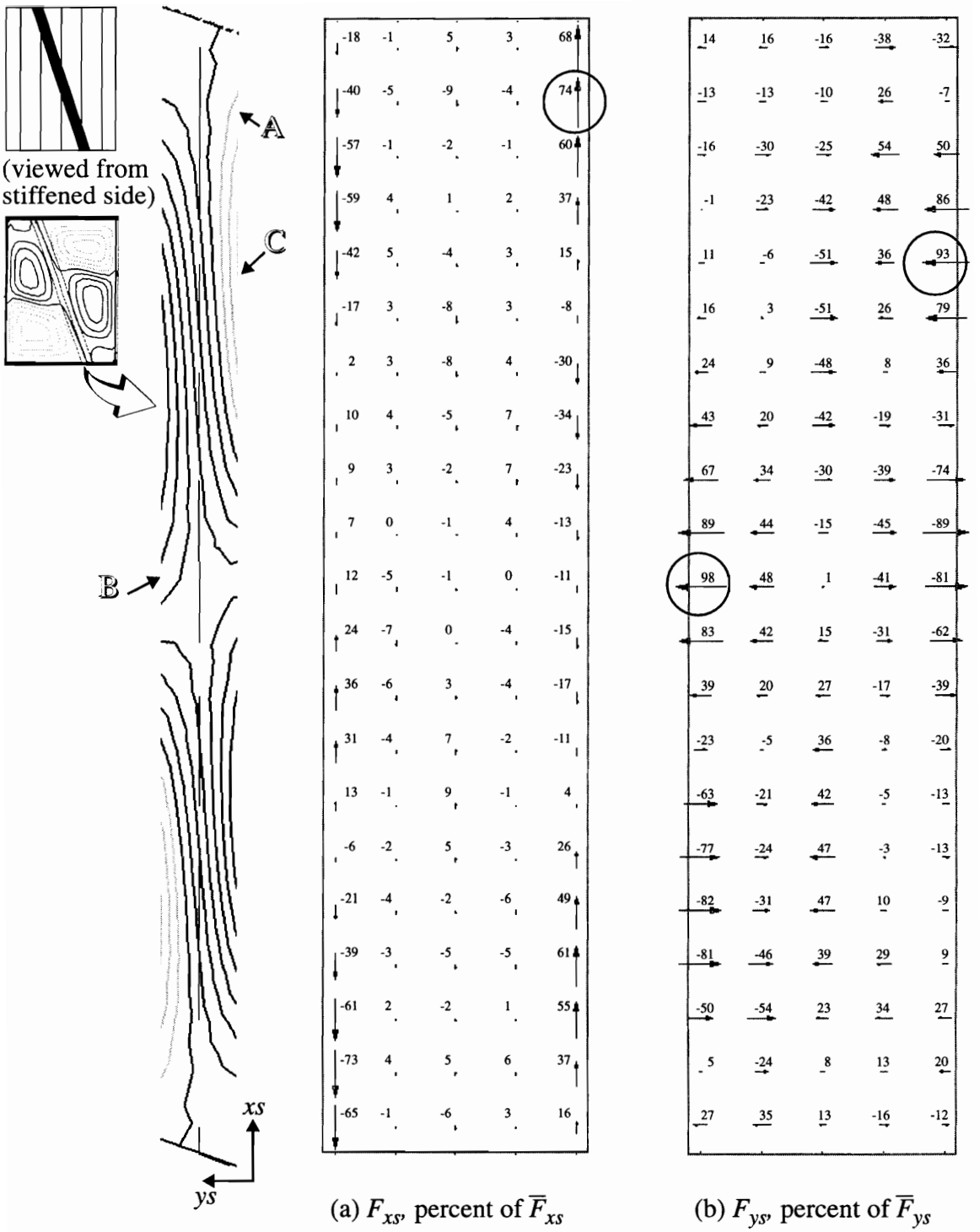

(a) F_{xs}, percent of $\overline{F}_{xs}$

(b) F_{ys}, percent of $\overline{F}_{ys}$

Fig. 5-14 Panel B2,0: predicted forces and moments on skin at skin-stiffener interface at failure, $(P_x)_{ult}^{exp}$ = 19.43 kips

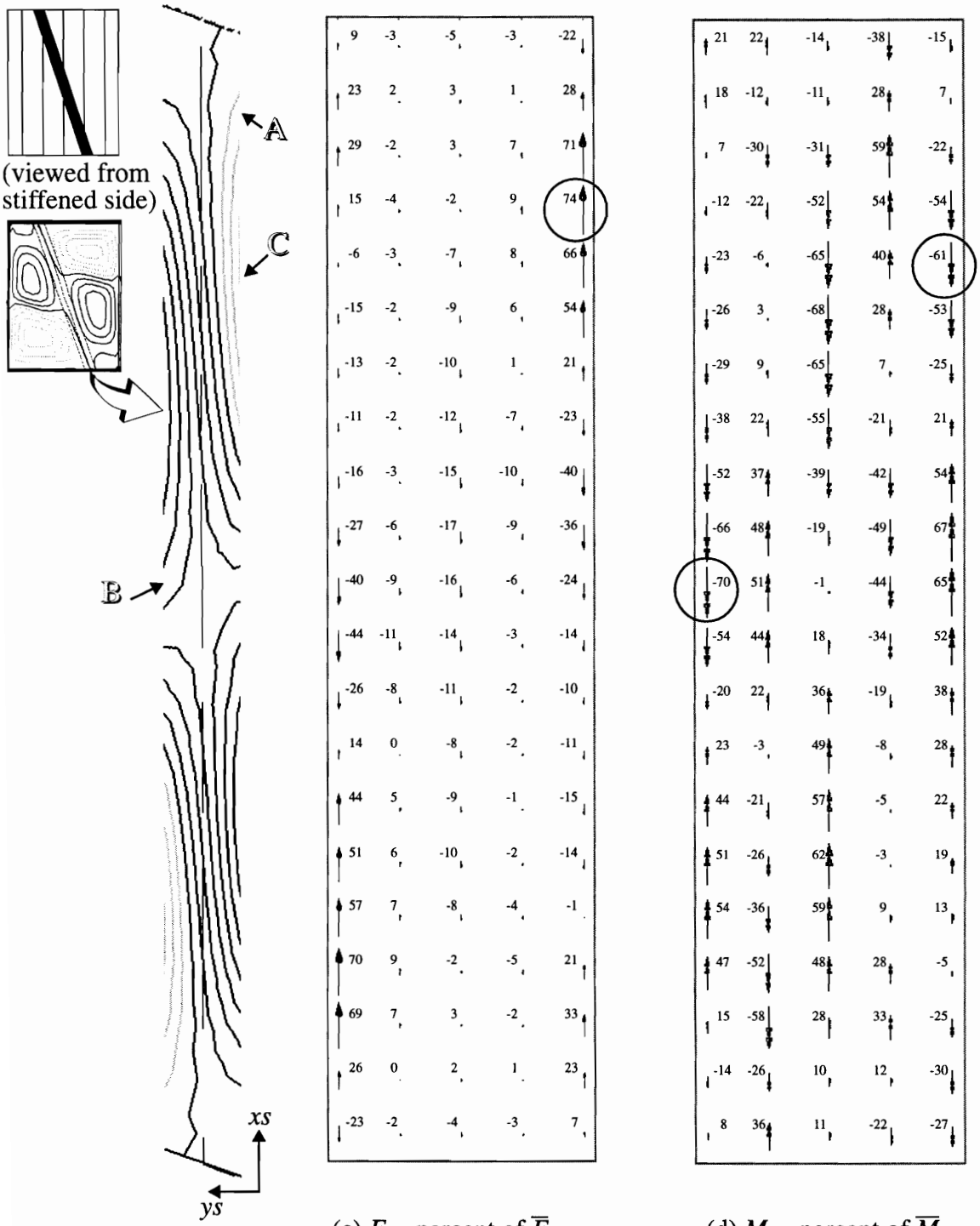

(c) F_{zs}, percent of $\overline{F}_{zs}$

(d) M_{xs}, percent of $\overline{M}_{xs}$

Fig. 5-14 Continued

(viewed from unstiffened side)

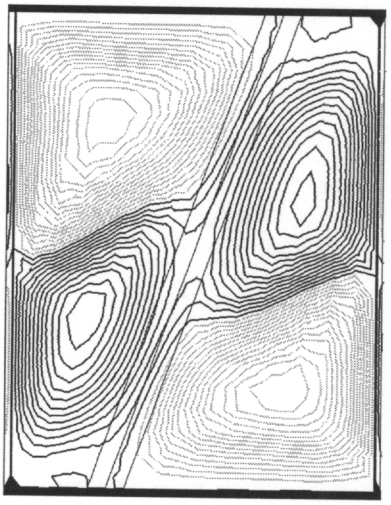

(a) STAGS contour

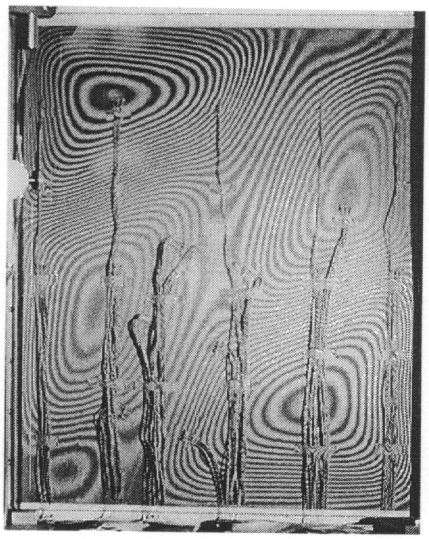

(b) Moiré-fringe pattern

Fig. 5-15 Panel B2,2: comparison of predicted out-of-plane skin displacement contours at ultimate load

mate load are shown in Fig. 5-16. Force F_{xs} shown in Fig. 5-16(a) has a maximum magnitude near the ends of the stiffener, and the location is identified in Fig. 5-16 by point $\mathbb{A}$. The maximum values for F_{ys} and M_{xs} are located at point $\mathbb{B}$ where the skin is bending toward the stiffener on each side of the stiffener. The direction of F_{ys} and M_{xs} at point $\mathbb{B}$ indicates that the skin and attachment flange are being pushed together at this location, rather than being pulled apart. The maximum values for F_{zs} and the peeling moment M_{xs}, and large values for F_{ys}, are located near point $\mathbb{C}$ on the edge of the interface where the out-of-plane displacement away from the stiffener is a maximum. Similar features were also observed for case B2,0.

5.3.5 Panel B2,n2: 

The experimentally-measured ultimate load for panel B2,n2 was $(P_x)_{ult}^{exp} = 18.44$ kips. When the displacements u_{ult}^{exp} and v_{ult}^{exp} were applied to the finite element model, the predicted load in the x-direction was $(P_x)_{ult}^{FE} = 19.07$ kips. A contour plot of the predicted out-of-plane displacement, and the moiré-fringe pattern photographed just prior to failure of the panel, are compared in Fig. 5-17.

The predicted forces and moments on the skin at the skin-stiffener interface at the ultimate load are shown in Fig. 5-18. Force F_{xs} shown in Fig. 5-18(a) has a maximum value

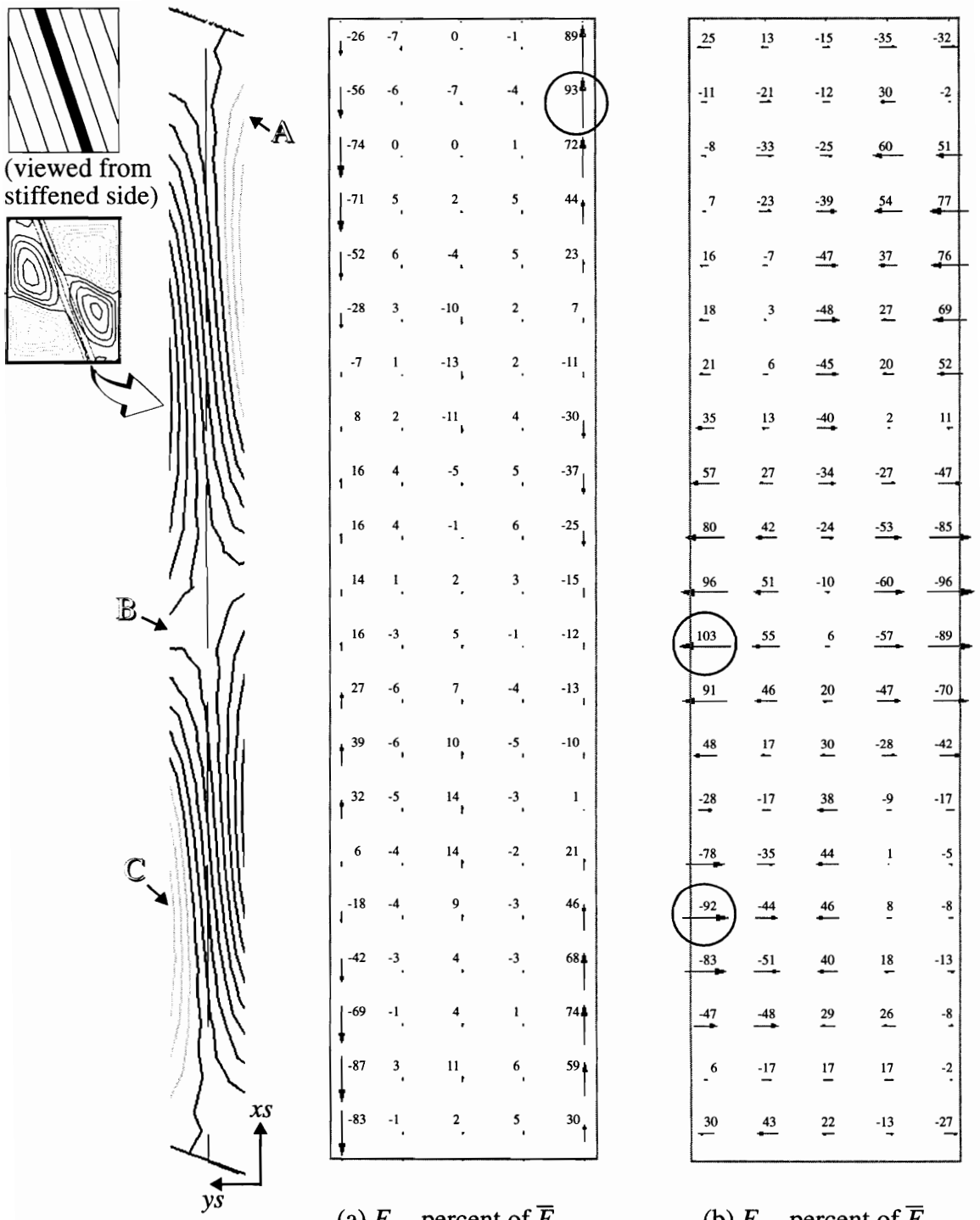

(a) F_{xs}, percent of $\overline{F}_{xs}$

(b) F_{ys}, percent of $\overline{F}_{ys}$

Fig. 5-16 Panel B2,2: predicted forces and moments on skin at skin-stiffener interface at failure, $(P_x)_{ult}^{exp}$ = 22.3 kips

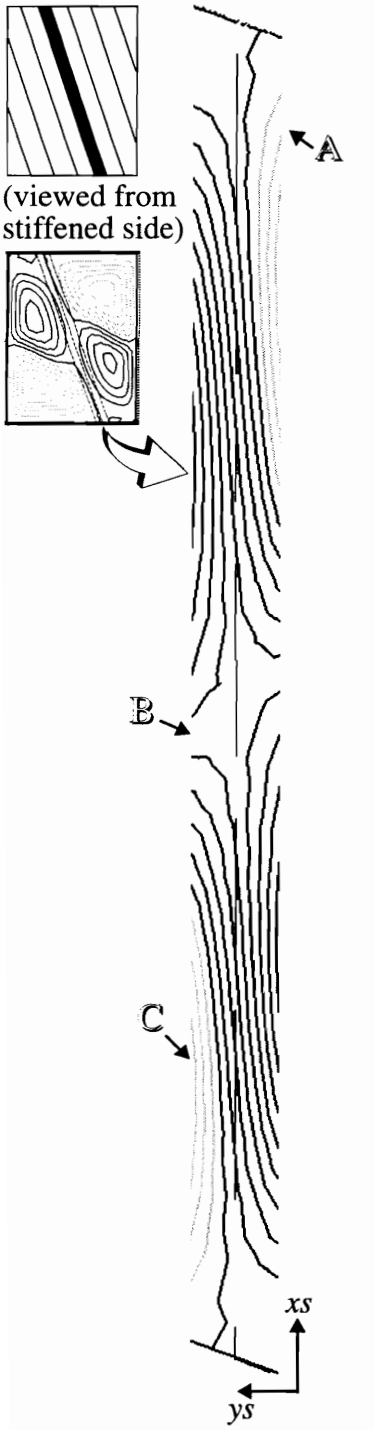

15	-1	-6	-4	-17
33	0	2	3	33
33	-4	1	12	77
16	-6	-6	14	78
-1	-4	-11	10	63
-9	-2	-12	8	52
-11	-1	-11	6	42
-12	-1	-11	-1	12
-15	-1	-14	-11	-29
-22	-4	-18	-16	-50
-32	-8	-19	-12	-45
-45	-13	-20	-7	-34
-48	-16	-18	-2	-25
-25	-10	-13	0	-18
30	3	-8	-1	-14
65	10	-9	-3	-10
76	12	-9	-4	-4
80	13	-6	-5	10
67	9	-1	-4	27
21	0	0	0	31
-19	-4	-7	-1	17

(c) F_{zs}, percent of $\overline{F}_{zs}$

25	20	-12	-33	-18
11	-19	-14	31	-8
-4	-33	-30	63	-28
-21	-22	-46	58	-45
-28	-6	-56	40	-48
-27	3	-59	29	-45
-26	7	-56	20	-34
-31	14	-51	1	-11
-40	29	-42	-29	26
-52	45	-28	-55	48
-62	55	-10	-64	58
-63	59	7	-61	55
-53	49	25	-49	46
-29	20	39	-28	35
16	-15	50	-8	26
44	-35	56	2	22
50	-46	57	9	21
40	-55	50	18	18
17	-51	35	25	7
-5	-19	19	14	-7
8	42	19	-21	-21

(d) M_{xs}, percent of $\overline{M}_{xs}$

Fig. 5-16 Continued

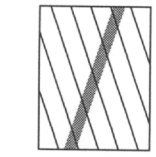

(viewed from unstiffened side)

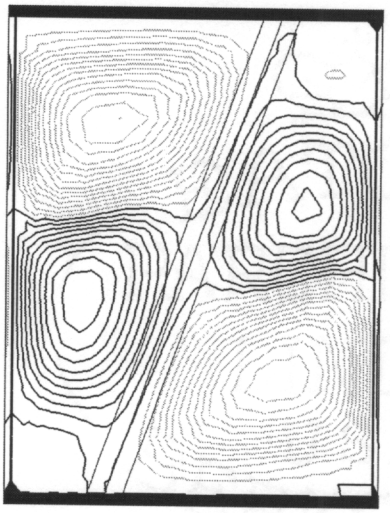

(a) STAGS contour

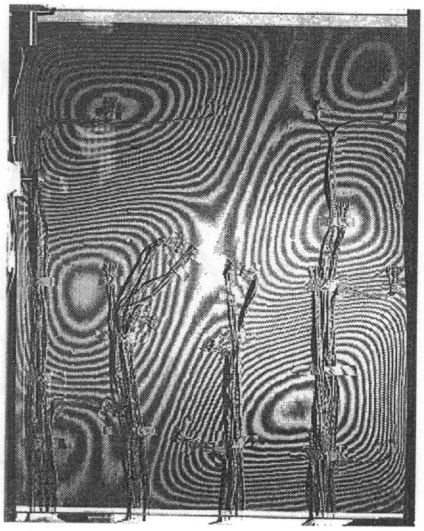

(b) Moiré-fringe pattern

Fig. 5-17 Panel B2,n2: comparison of predicted out-of-plane skin displacement contours at ultimate load

near the ends of the stiffener and the location is identified in Fig. 5-18 by point 𝔸. The maximum forces F_{ys} and F_{zs}, and the largest peeling M_{xs} moment, are located near point 𝔹 on the edge of the interface where the out-of-plane displacement away from the stiffener is a maximum.

5.3.6 Summary of Predicted Skin-Stiffener Attachment Force 'Hot Spots'

The maximum values of F_{xs}, F_{ys}, F_{zs}, and M_{xs} that were reported in previous sections are summarized in Table 5-2. In the last column of Table 5-2 there are comments next to the value of moment M_{xs} that indicate the nature of the interface normal stresses associated with the moment. The comment 'web' indicates that the moment is for a point under the stiffener web, and the corresponding normal stress distribution is of the form shown in Fig. 5-10(d). The comment 'peel' indicates that the moment is for a point on the edge of the interface, and the corresponding normal stress distribution is of the form shown in Fig. 5-10(c) with a tensile normal stress at the edge of the interface. The comment 'no peel' indicates that the moment is for a point on the edge of the interface, but the sign of the moment is reversed. Therefore, the corresponding normal stress distribution is of the form shown in Fig. 5-10(c) but the sign is reversed and the normal stress at the edge of the interface is compressive.

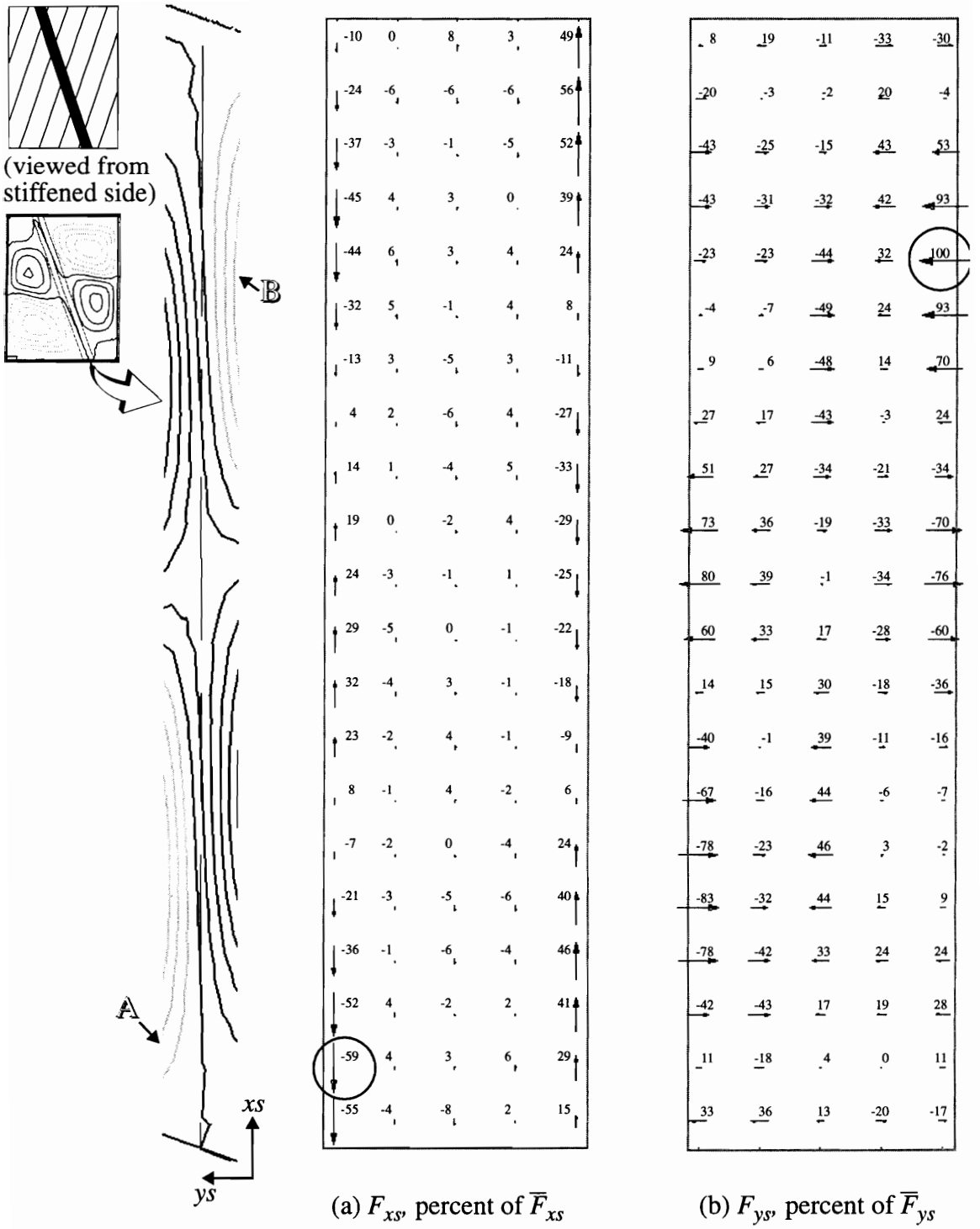

(a) F_{xs}, percent of $\overline{F}_{xs}$

(b) F_{ys}, percent of $\overline{F}_{ys}$

Fig. 5-18 Panel B2,n2: predicted forces and moments on skin at skin-stiffener interface at failure, $(P_x)_{ult}^{exp}$ = 18.44 kips

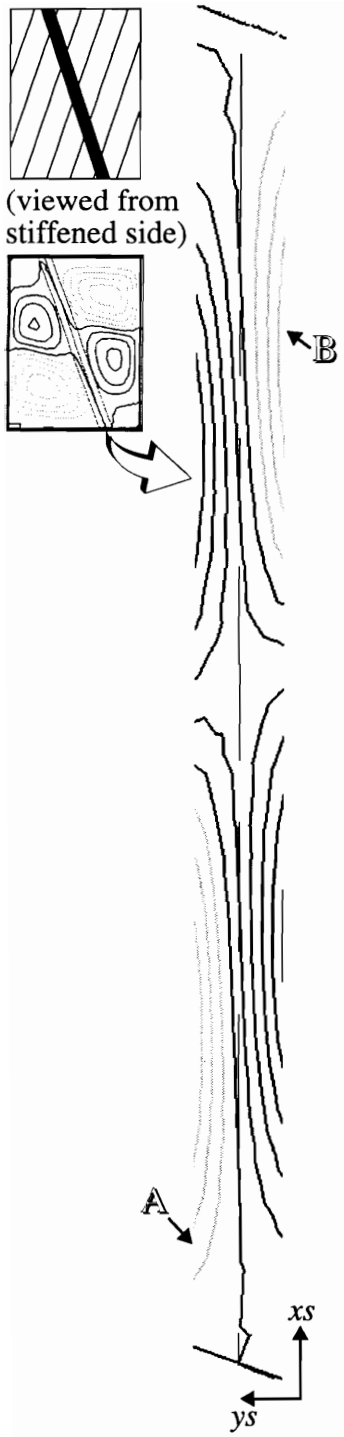

4	-2	-6	-1	-15
12	0	0	-1	20
23	-2	3	1	55
23	-4	1	4	64
11	-4	-2	6	58
-5	-2	-6	5	51
-15	-1	-8	2	36
-18	-1	-10	-3	6
-19	-2	-12	-7	-19
-23	-4	-13	-8	-28
-30	-7	-13	-6	-24
-30	-9	-12	-4	-17
-13	-6	-11	-2	-14
14	-2	-9	-1	-14
36	3	-8	-1	-14
47	6	-7	-1	-9
54	7	-3	-3	3
62	6	0	-4	15
55	2	2	-3	19
21	-1	-1	0	11
-15	-2	-6	-3	4

(c) F_{zs}, percent of $\overline{F}_{zs}$

19	22	-9	-33	-6
31	-3	-3	22	7
42	-24	-18	49	-34
33	-29	-37	50	-70
10	-20	-54	39	-76
-9	-7	-65	27	-70
-18	5	-69	13	-54
-27	16	-64	-6	-24
-38	27	-50	-24	22
-50	37	-28	-36	51
-51	41	-2	-36	59
-31	35	23	-29	49
1	18	42	-18	34
40	0	55	-10	21
51	-16	62	-5	13
56	-26	63	3	8
58	-37	57	14	-6
50	-48	42	23	-26
16	-47	23	20	-36
-21	-20	6	0	-28
0	37	11	-24	-19

(d) M_{xs}, percent of $\overline{M}_{xs}$

Fig. 5-18 Continued

Table 5-2 Summary of Predicted Skin-Stiffener Attachment Forces and Moments at Ultimate Load

Panel	Location on interface	F_{xs}, percent of $\overline{F}_{xs}$	F_{ys}, percent of $\overline{F}_{ys}$	F_{zs}, percent of $\overline{F}_{zs}$	M_{xs}, percent of $\overline{M}_{xs}$
 B0,0	Fig. 5-5				
	Point 𝔸	100	41	15	-7 (no peel)
	Point 𝔹	-4	-100	100	43 (peel)
$(P_x)_{ult}^{exp} = 31.2$ kips	Point ℂ	2	70	-25	100 (web)
 B0,2	Fig. 5-12				
	Point 𝔸	-96	60	-12	-36 (no peel)
	Point 𝔹	-4	-118	100	-58 (peel)
$(P_x)_{ult}^{exp} = 29.0$ kips	Point ℂ	-1	-66	-19	-104 (web)
 B2,0	Fig. 5-14				
	Point 𝔸	74	-7	28	7 (no peel)
	Point 𝔹	12	98	-40	-70 (no peel)
$(P_x)_{ult}^{exp} = 19.43$ kips	Point ℂ	15	93	66	-61 (peel)
 B2,2	Fig. 5-16				
	Point 𝔸	93	-2	33	-8 (peel)
	Point 𝔹	16	103	-45	-63 (no peel)
$(P_x)_{ult}^{exp} = 22.3$ kips	Point ℂ	-18	-92	76	50 (peel)
 B2,n2	Fig. 5-18				
	Point 𝔸	-59	11	21	-21 (no peel)
	Point 𝔹	24	100	58	-76 (peel)
$(P_x)_{ult}^{exp} = 18.44$ kips					

The skin-stiffener forces and moments summarized in Table 5-2 are compared to see if any comments can be made to suggest why the panels with the stiffener rotated 20° had failure loads that were an average of 33% lower that the failure loads of the panels with the unrotated stiffener. Comparing the forces or moments in a single component direction may provide some insight into the variation in response from one panel to another. No attempts have been made to combine the force components into a single measure of the tendency for skin-stiffener separation. If the mode of failure varies from panel to panel, then comparing the forces and moments in a single component direction may not provide an accurate indication of the tendency for skin-stiffener separation, even in a comparative sense.

Consider first the force along the axis of the stiffener, F_{xs}, which is listed in column 3 of Table 5-2. The maximum values of F_{xs} occur at location $\mathbb{A}$ on each panel. The maximum magnitudes of F_{xs} range from 100 to 59, and the maximum values of F_{xs} for the panels with the stiffener rotated 20° are 23% lower, on average, than the maximum values of F_{xs} for the panels with the unrotated stiffener. The reduction in the maximum value of F_{xs} for the panels with the stiffener rotated 20° suggests that these panels did not fail due to force F_{xs}, or the associated interlaminar shear stress, σ_{xz}.

The maximum values of force F_{ys} occur at location $\mathbb{B}$ on each panel. The maximum magnitudes of F_{ys} range from 118 to 98, and the maximum values of F_{ys} for the panels with the stiffener rotated 20° are only 9% lower, on average, than the maximum values of F_{ys} for the panels with the unrotated stiffener. The small variation in the maximum value of F_{ys} suggests that all of the panels may have failed due to force F_{ys}, or the associated interlaminar shear stress, σ_{yz}.

The maximum values of force F_{zs} occur at location $\mathbb{B}$ on panels B0,0, B0,2, and B2,n2, and at location $\mathbb{C}$ on panels B2,0, and B2,2. The maximum magnitudes of force F_{zs} range from 100 to 58, and the maximum values of F_{zs} for the panels with the stiffener rotated 20° are 33% lower, on average, than the maximum values of F_{zs} for the panels with the unrotated stiffener. The reduction in the maximum value of F_{zs} for the panels with the stiffener rotated 20° may suggests that these panels did not fail due to force F_{zs}, or the associated interlaminar normal stress, σ_z.

When considering moment M_{xs}, the location and direction of the moment are important. The maximum values of M_{xs} for panels B0,0 and B0,2 occur at location $\mathbb{C}$, which is located under the stiffener web. None of the panels with the stiffener rotated 20° had large

moments under the web, which suggests that these panels did not fail due to moment M_{xs} under the stiffener web.

Looking at moment M_{xs} on the edge of the interface, and considering only moments which create 'peel' stresses, the maximum values of moment 'peel' M_{xs} occur at location $\mathbb{B}$ on panels B0,0, B0,2, and B2,n2, and at location $\mathbb{C}$ on panels B2,0 and B2,2. The maximum magnitudes of 'peel' M_{xs} range from 43 to 76, and the maximum values of 'peel' M_{xs} for the panels with the stiffener rotated 20° are 23% higher, on average, than the maximum values of 'peel' M_{xs} for the panels with the unrotated stiffener. However, the range of values for M_{xs} for the rotated and unrotated stiffeners prevents any solid conclusions regarding failure due to M_{xs} alone. Noting that the interlaminar normal stress σ_z on the edge of the interface is a result of force F_{zs} and moment 'peel' M_{xs}, the variations in these quantities should be considered together. As noted above, the maximum values of F_{zs} and 'peel' M_{xs} occur at location $\mathbb{B}$ on panels B0,0, B0,2, and B2,n2, and at location $\mathbb{C}$ on panels B2,0 and B2,2. As noted above, for the panels with the stiffener rotated 20°, on average the maximum values of F_{zs} are 33% lower, and the maximum values of 'peel' M_{xs} are 23% higher, than the same quantities for the panels with the unrotated stiffener. Recall from Fig. 5-10(c) that the interlaminar normal stress distribution, σ_z, is influenced by F_{zs} and M_{xs}. If moment M_{xs} influences the interlaminar normal stress distribution more severely than force F_{zs}, then the panels with the stiffener rotated 20° may fail due to a combination of the force F_{zs} and moment 'peel' M_{xs}, or the associated interlaminar normal stress, even though the values of F_{zs} are 33% lower.

Based on the results presented above, it is postulated that panels B0,0 and B0,2 failed due to skin-stiffener separation that initiated at point $\mathbb{B}$ on the these panels, where F_{ys}, F_{zs}, and 'peel' M_{xs} are maxima. For panels B2,0 and B2,2 it is postulated that failure may have initiated at location $\mathbb{B}$ where F_{ys} is a maximum, but it seems more likely that failure would have initiated at location $\mathbb{C}$ on these panels, where the F_{ys} forces are nearly as high, and F_{zs} and 'peel' M_{xs} are maxima. For panel B2,n2 it is postulated that skin-stiffener separation would occur at location $\mathbb{B}$ where force F_{ys} and moment 'peel' M_{xs} are maxima. Based upon the limited information that was available from the numerical model, if all the panels fail from the same mechanism, it seems likely that failure initiated in all panels at locations on the edge of the skin-stiffener interface at locations were the w displacement was a maximum in the negative direction, i.e., away from the stiffener. Moreover, with their respective experimentally-measured ultimate loads applied to each panel, compara-

ble skin-stiffener forces and moments were computed for all panels. Thus, the reduction in panel strength observed experimentally when the stiffener was rotated 20° seems to be supported by the numerical results.

On a final note, a possible explanation is offered as to why the skin-stiffener forces and moments in all the panels are comparable, even though the applied panel loads are substantially different. A simplistic answer is that the deformation states are different. Contour plots of the predicted w displacement and the stress resultant N_{ys} in the skin for panels B0,0 and B2,0 at the experimentally-measured failure loads are shown in Fig. 5-19. The stress resultant N_{ys} is the membrane stress resultant in the skin in the ys-direction, i.e., perpendicular to the stiffener axis. The results are shown for the skin only, as viewed from the stiffened side of the panel. The predicted critical locations, point $\mathbb{B}$ on panel B0,0 and point $\mathbb{C}$ on panel B2,0, are identified on the contour plots of the out-of-plane deformation.

The displacement pattern for panel B0,0 is nearly antisymmetric with respect to the stiffener. At the predicted critical location identified as point $\mathbb{B}$ on panel B0,0, the out-of-plane displacements on each side of the stiffener cause a tensile load to exist in the skin, on both sides of the stiffener, in a direction that is perpendicular to the stiffener axis. The stress resultant N_{ys} in the skin of panel B0,0, shown in Fig. 5-19(b), has a maximum tensile value at point $\mathbb{B}$. In the skin location directly across the stiffener from point $\mathbb{B}$, the stress resultant N_{ys} also has a local tensile maximum. The tensile stress resultants in the skin on each side of the stiffener are aligned and partially offset each other, reducing the net transverse load on the stiffener. Also, moment M_{xs} that was reported in Fig. 5-5(d) is nearly equal on each side of the stiffener, with the moments on each side tending to rotate the stiffener in the same direction.

The displacement pattern for panel B2,0 is not antisymmetric with respect to the stiffener. For example, the out-of-plane displacements away from the stiffener are larger than the displacements toward the stiffener, and the nodelines on the left and right sides of the stiffener do not intersect the stiffener at the same distance along the length of the stiffener. As shown in Fig. 5-19(b), the stress resultant N_{ys} is not as symmetric across the stiffener. At the predicted critical location identified as point $\mathbb{C}$ on panel B2,0, the lack of asymmetry in the response causes a tensile load in the skin on the right side of the stiffener that is not directly aligned with a tensile load in the skin on the left side of the stiffener. Likewise, moment M_{xs} reported in Fig. 5-14(d) is notably larger on the right side of the stiffener than on the left side. It is suggested that the lack of symmetry and/or lack of antisymmetry in

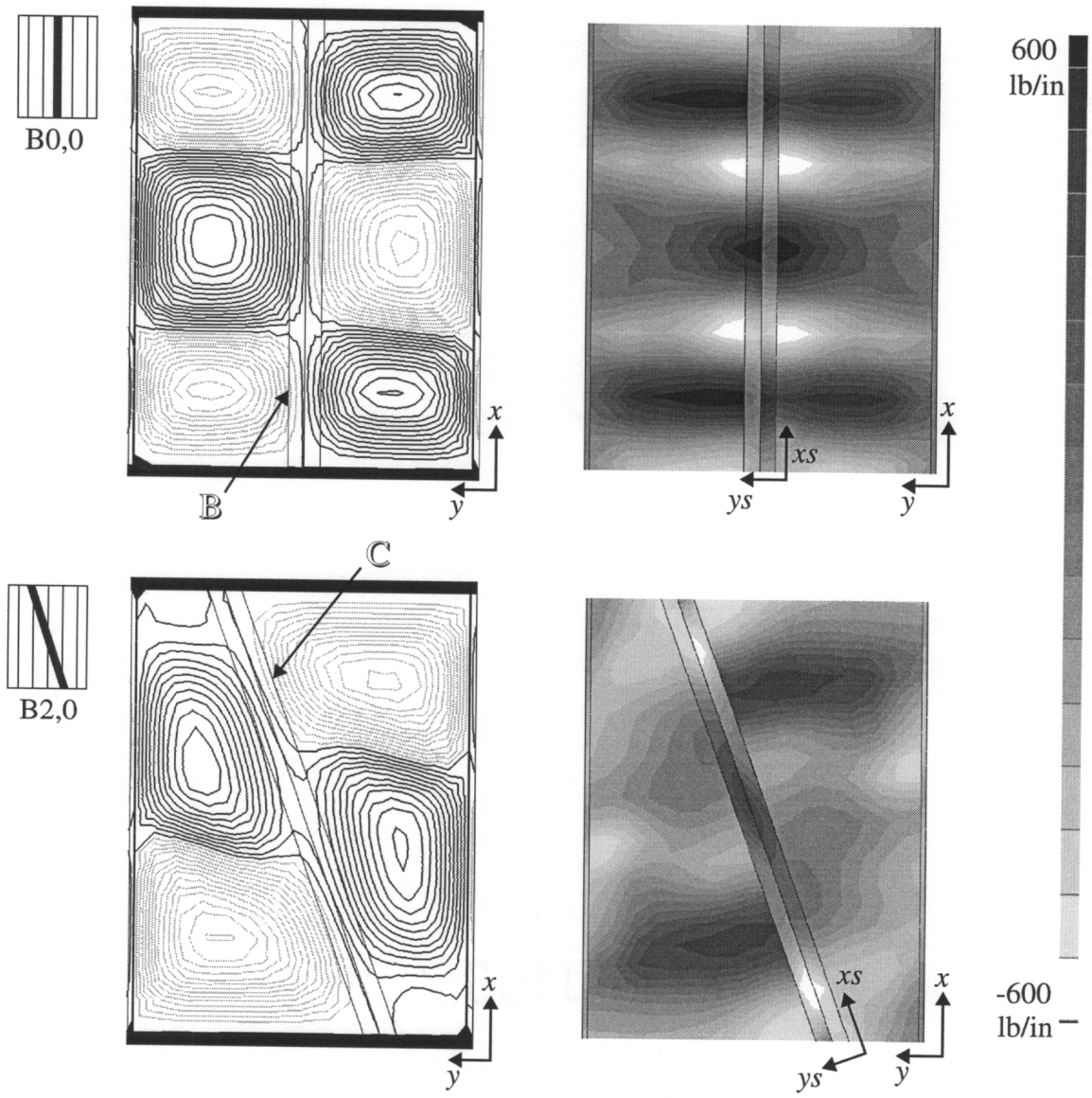

(a) STAGS *w* displacement

(b) STAGS stress resultant N_{ys}

Fig. 5-19 Panels B0,0 and B2,0: comparison of predicted out-of-plane displacements and N_{ys} stress resultant in the panel skin at failure

the response is what causes the skin-stiffener forces and moments for panel B2,0 to be more severe and causes failure of panel B2,0 at loads well below the ultimate load for panel B0,0.

6. Exploring Axial-Shear Stiffness Coupling

The results of experiments and numerical simulations of the experimental responses were presented in Chapter 4. The primary objectives in Chapter 4 were to describe the overall response of the panels, and to verify the numerical models by correlating the measured and predicted panel responses. It was observed that the axial-shear coupling response of the panels was significantly altered by rotating the stiffener and/or rotating the principal direction of orthotropy of the skin, and that the response was load dependent.

In this chapter the potential for tailoring the axial-shear coupling response is examined in greater depth. The mechanisms which influence the axial-shear coupling response are identified, and additional panel configurations which exploit the contributing mechanisms are considered. The numerical models that were verified by comparing the measured and predicted responses were used to analyze these additional panel configurations. Nonlinear postbuckling analyses were conducted with an applied end shortening u and with $v = 0$. Hence the pure force coupling response, $(P_{xy}/P_x)_{pure}$, was computed. Solutions were obtained for applied end shortening up to four times u_{cr}. The singular solution that exists at the bifurcation load of a perfect panel was removed by applying an initial geometric imperfection in the shape of the linear bifurcation buckling mode with an amplitude of 0.001 in. For each configuration that was considered, the prebuckling stiffness, EA, the linear buckling parameters, $(P_x)_{cr}^{lin}$ and u_{cr}^{lin}, the postbuckled deformation shape, and the prebuckling and postbuckling force coupling response are reported below. Partial numerical results are included in the chapter text, and all numerical results are summarized in Table 6-2 at the end of the chapter.

Before proceeding with additional panel configurations, the axial-shear coupling responses for the panel configurations that were tested are reviewed. Recall that results of simplified linear bifurcation buckling analyses of the test panels (omitting measured shape

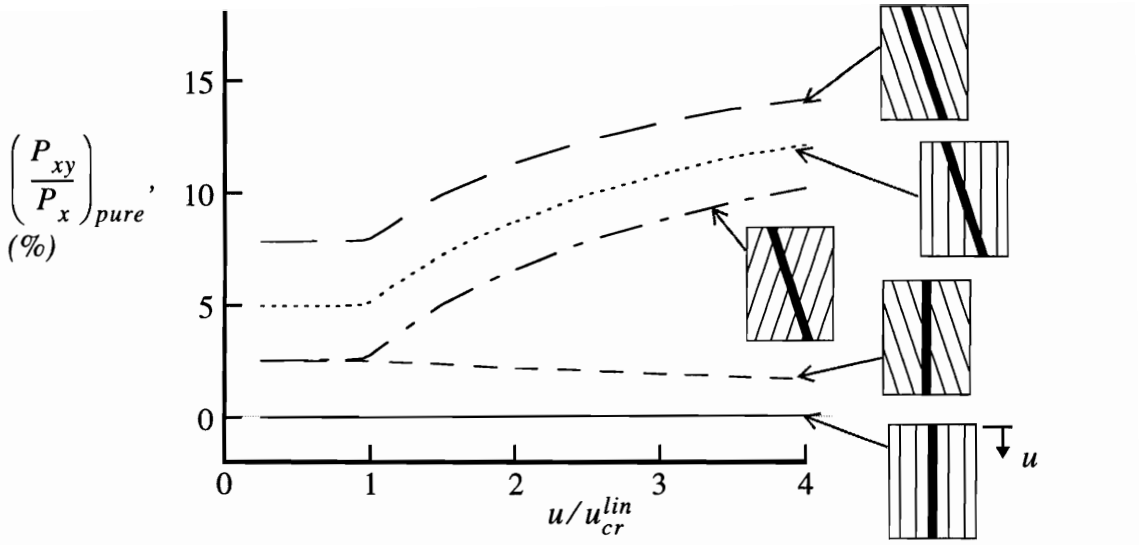

Fig. 6-1 Pure force coupling response of configurations that were tested: omitting measured shape imperfections and nonuniform initial loading

imperfections and nonuniform initial loading, and setting $v = 0$) were reported at the beginning of Chapter 4. The prebuckling stiffness and linear buckling parameters for these panels were reported in Table 4-1. The numerical results for pure force coupling that were presented in Fig. 4-11 included the effects of measured shape imperfections and nonuniform initial loading. If the measured shape imperfections and nonuniform initial loading are omitted from the nonlinear postbuckling analyses, then the pure force coupling versus end shortening responses for the test panels vary as shown in Fig. 6-1. In this figure, the end shortening of each panel is normalized by the end shortening at buckling, u_{cr}^{lin}, for the respective panel, and results are presented for $u/u_{cr}^{lin} \leq 4$. Contour plots of the out-of-plane displacement in the skin at $u/u_{cr}^{lin} = 4$ are shown in Fig. 6-2. Note the overall similarity of Fig. 6-2 when compared with Fig. 4-4, the postbuckled out-of-plane deflections predicted by the most refined nonlinear analysis. Also, when comparing Fig. 6-1 with Fig. 4-11, it is seen that including measured shape imperfections and nonuniform initial loading do not have a large effect on force coupling predictions in the postbuckling load range. The ranking of the effects of rotated stiffeners and rotated skins on the force coupling predictions is unaffected, and the coupling percentages are comparable. The pure force coupling results shown in Fig. 6-1 support the following conclusions:

- The force coupling response of the configuration with the stiffener and skin unrotated is approximately zero for all load ranges.

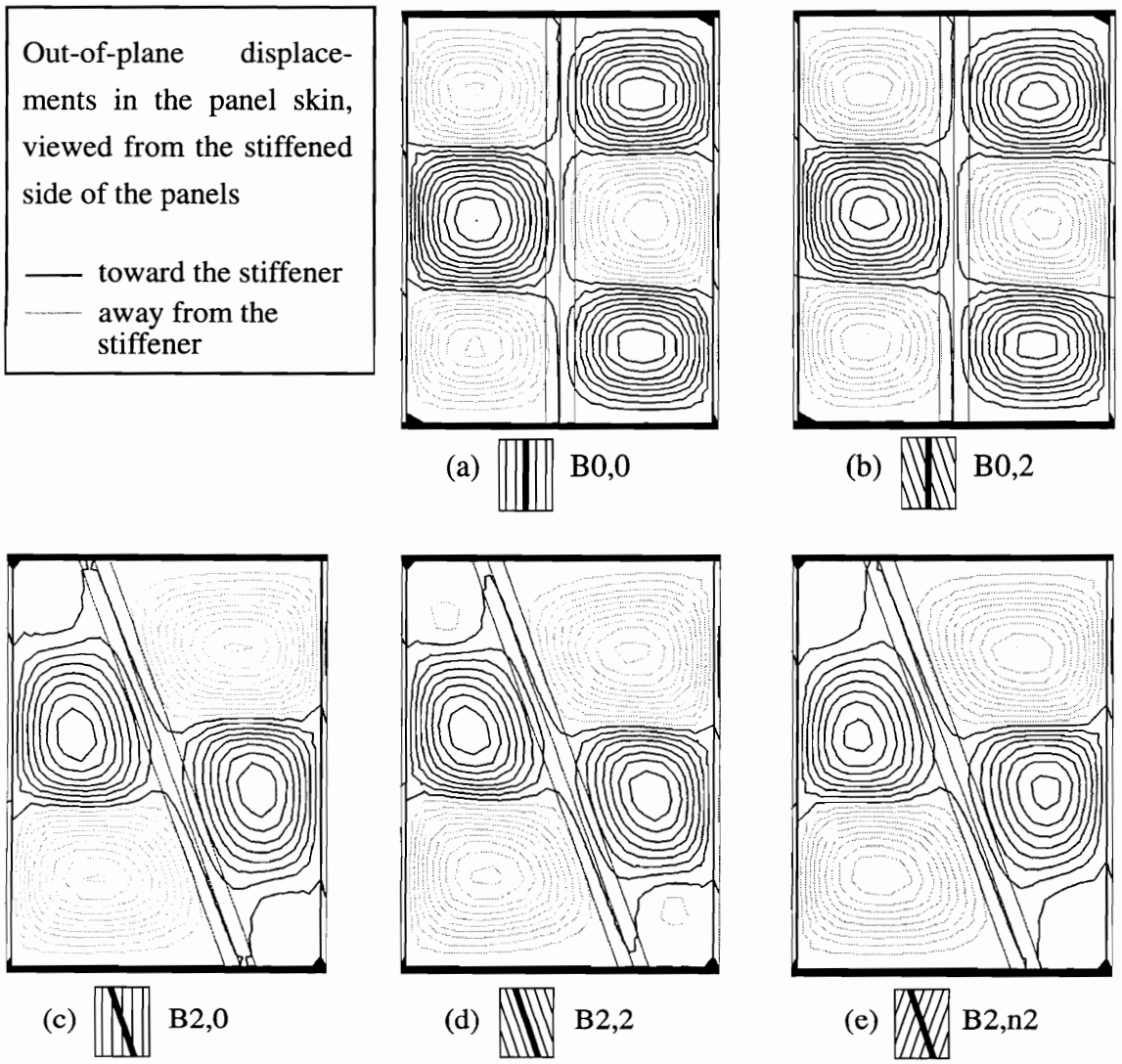

Fig. 6-2 Postbuckling shapes of the configurations that were tested: simplified nonlinear analyses with $\nu = 0$ and $u/u_{cr}^{lin} = 4$

- The configuration with the unrotated stiffener and the skin rotated exhibits axial-shear stiffness coupling due to skin anisotropy. The amount of force coupling is constant in prebuckling, and diminishes in the postbuckling load range (spectrum: 2.54% ⇨ 1.69%).
- The configuration with the stiffener rotated and the unrotated skin exhibits axial-shear stiffness coupling due to the skewed stiffener. The amount of force coupling is constant in prebuckling, and increases in the postbuckling load range (spectrum:

4.97% ➪ 12.15%). The entire force coupling response curve is shifted upward if the skin is rotated in the same direction as the stiffener rotation (spectrum: 7.84% ➪ 14.17%). Rotating the skin in the opposite direction of the stiffener rotation decreases the force coupling response (spectrum: 2.57% ➪ 10.24%).

Similar comments were made regarding the pure force coupling results presented at the end of Chapter 4. It is postulated that the mechanisms which control the axial-shear coupling response of the stiffened panels are:

1. stiffener properties
   - orientation
   - stiffness
2. skin anisotropy
   - membrane stiffness coupling
   - bending stiffness coupling

In the remainder of this chapter, additional configurations are considered which either address each of these mechanisms independently, or combine the different mechanisms to tailor the axial-shear coupling response in the prebuckling and postbuckling load ranges. Since all results reported in this chapter are from analyses with $\nu = 0$, references in the text to the force coupling response always allude to the pure force coupling response.

6.1 Stiffener Properties

To independently examine the effect of the stiffener orientation and stiffness on the axial-shear coupling response of the stiffened panels, panel configurations are considered which are constructed entirely from 2024 aluminum alloy (E = 10.5 Msi, ν = 0.33). The isotropic material is selected to eliminate any suspicions that the computed responses for these panels are related in any way to material anisotropy.

6.1.1 Stiffener Orientation

The first configurations that are considered are sized to have the same axial stiffness as panel B0,0. To match the axial stiffness, i.e., the EA, of the $[\pm 45/\mp 45/0_3/90]_s$ graphite-epoxy laminate, the aluminum skin thickness is set to 0.0771 in. The axial stiffness of

the graphite-epoxy stiffener, with $[\pm 45/0/90]_{2s}$ laminates and 0° pre-preg filling the triangular-shaped voids at the top and bottom of the stiffener web, is matched by an aluminum stiffener with the same stiffener dimensions as shown in Fig. 2-1(a), and component thicknesses equal to 0.0678 in. Three panel configurations are analyzed that utilize these skin and stiffener dimensions. The panels, identified as Al-B0, Al-B1, and Al-B2, designate all-aluminum panel configurations with the stiffener rotated 0°, 10°, and 20°, respectively. The prebuckling stiffnesses for these panels are 16,630, 16,530, and 16,270 kips, respectively. The reduction in axial stiffness that occurs when the stiffener is rotated reflects the fact that the stiffener axis is not aligned with the principle loading direction. The linear buckling loads of the three panels are 8.25, 7.70, and 6.48 kips, respectively. Thus, rotating the stiffener by 10° and 20° causes reductions in the buckling load of 7% and 21%, respectively, relative to the panel with the unrotated stiffener. The reduction in buckling load that occurs when the stiffener is rotated is partially associated with the reduction in the load carried in the stiffener, but is mostly due to the increase in the width of the skin sections that is introduced when the stiffener is rotated. Contour plots of the out-of-plane displacement in the skin at $u/u_{cr}^{lin} = 4$ are shown in Fig. 6-3. It was noted earlier that the postbuckling deformations of the panels with the stiffener rotated 20° differ substantially from the cases with the unrotated stiffener. The contour plots in Fig. 6-3 indicate that for the all-aluminum panels, the postbuckling deformations have three axial half-

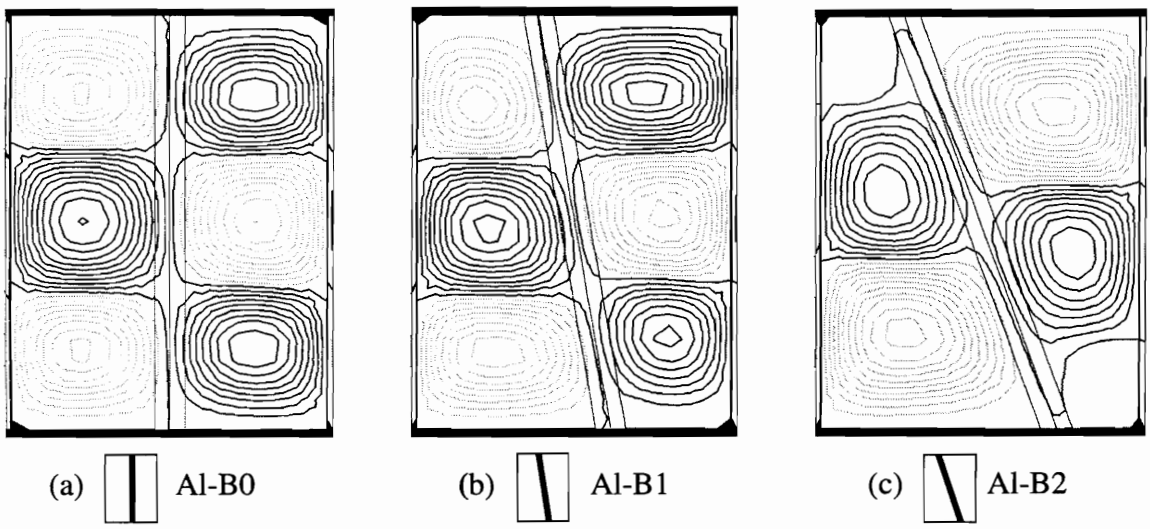

Fig. 6-3 Postbuckling shapes of all-aluminum panels with the stiffener rotated 0°, 10°, and 20°

waves when the stiffener is unrotated and rotated 10°, and two axial half-waves when the stiffener is rotated 20°. In Section 4.2.4 it was observed that when the stiffener is rotated 20°, Poisson expansion of the skin causes the wider sections of skin to buckle in a direction away from the stiffener. This effect is less pronounced when the stiffener is only rotated 10°, and did not control the direction of the skin deformation shown in Fig. 6-3(b). The force coupling versus end shortening responses for these panels are shown in Fig. 6-4. The force coupling for panel Al-B0 is zero, as expected. When the stiffener is rotated 10°, the force coupling response is 2.63% in the prebuckling load range, and increases to 7.33% in the postbuckling load range. The force coupling response of panel Al-B2 varies from 4.95% to 11.77% and is very similar to the response for panel B2,0 (spectrum: 4.97% ⇨ 12.15%).

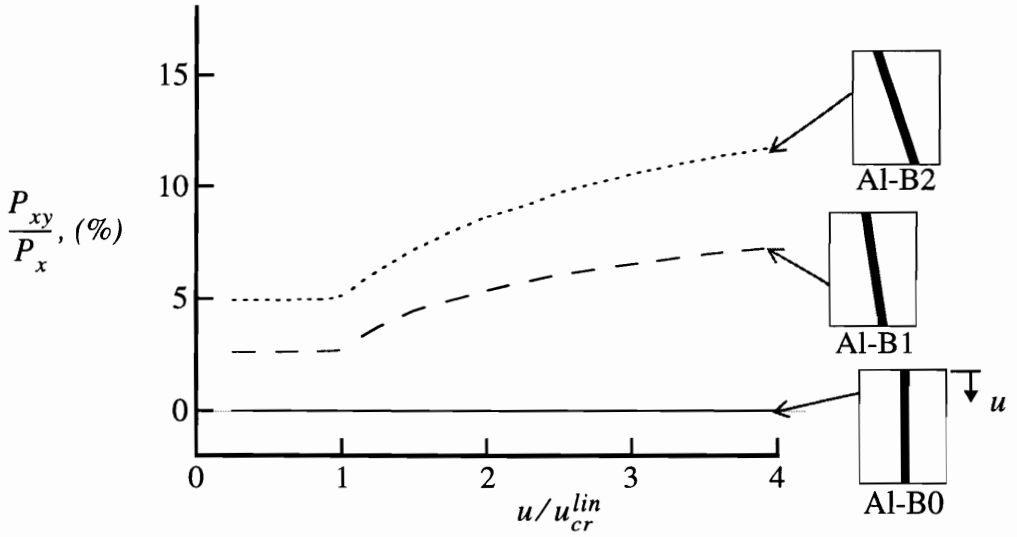

Fig. 6-4 Force coupling response of all-aluminum panels with stiffener rotated 0°, 10°, and 20°

6.1.2 Stiffener 'Stiffness'

The effect of the stiffness of the stiffener on the axial-shear coupling response of the panels with skewed stiffeners is examined by considering all-aluminum panels with the thickness of the stiffener components doubled to 0.1356 in., while keeping the skin thickness equal to 0.0771 in. The panels, identified as Al-C1 and Al-C2, designate all-aluminum panel configurations with the more-rigid stiffener rotated 10°, and 20°, respectively. The prebuckling stiffnesses for panels Al-C1 and Al-C2 are 19,430, and 18,820 kips, respectively. The linear buckling loads of the panels are 9.88, and 8.15 kips, respectively. Con-

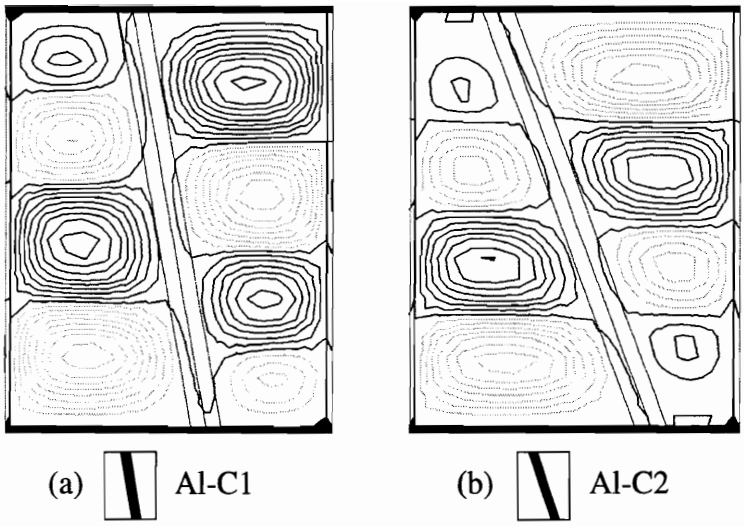

Fig. 6-5 Postbuckling shapes of all-aluminum panels with more-rigid stiffener rotated 10° and 20°

tour plots of the out-of-plane displacement in the skin at $u/u_{cr}^{lin} = 4$ are shown in Fig. 6-5. The contour plots in Fig. 6-5 show that the panels with more-rigid stiffeners have postbuckling deformations with a higher number of half-waves in the axial direction, and smaller out-of-plane deformations in the skin-stiffener attachment region. The change in the deformation shape could strongly influence failure by skin-stiffener separation. The force coupling versus end shortening responses for panels Al-B1, Al-B2, Al-C1, and Al-C2 are compared in Fig. 6-6. The more-rigid stiffener causes the force coupling response to be higher, compared to the response for the original stiffener, over the entire range of loading. The force coupling response has a spectrum of 4.71% to 8.57% for panel Al-C1, and 8.90% to 17.00% for panel Al-C2.

6.1.3 Rotated Stiffener and Variations in Force Coupling Response in the Postbuckling Load Range

There have been no surprises in any of the results for the all-aluminum panels. The force coupling responses of the panels with the stiffener rotated all demonstrate the same general behavior. In all cases with the stiffener rotated the force coupling is constant in the prebuckling load range and increases nonlinearly in the postbuckling load range. This increase in the force coupling response in the postbuckling load range was also observed in the experiments for the composite panels with the rotated stiffeners, and was reported earlier. The contour plots of the out-of-plane deformation have indicated that the deforma-

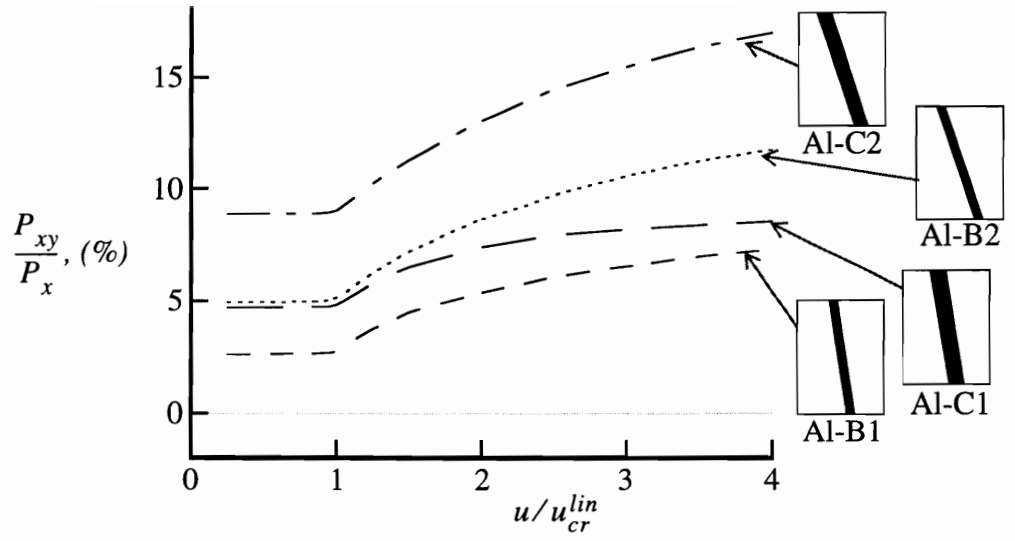

Fig. 6-6 Force coupling response of all-aluminum panels with original and more-rigid stiffener

tions in the skin-stiffener attachment region are small, and rotating the stiffener causes the deformations in the postbuckled skin to be skewed, particularly in the regions of the skin that are directly adjacent to the stiffener. Since the deformations of the stiffener are small, the stiffener contribution to the response is expected to be linear over the entire range of loading. It is postulated that the increase in force coupling response is related to the nonlinear response and skewed deformations of the postbuckled skin. To independently assess the effect of the skewed deformation state in the skin on the axial-shear coupling response, two cases are considered in which the rotated stiffeners are eliminated, and the out-of-plane displacements are constrained in the skin along a line where the stiffener used to be. Panel Al-w2 is created by eliminating the stiffener from panel Al-B2, and setting the *w* displacement to zero for the nodes in the skin that were originally under the stiffener web. Constraining the *w* displacement along a line simulates the out-of-plane support that a stiffener with a somewhat flexible cross section might provide. Panel Al-wdw2 is created to be similar to panel Al-w2, but the *w* displacement and the out-of-plane rotations, *Ru* and *Rv*, are constrained along the same line to simulate the support which a more-rigid stiffener would supply. Thus, these models simulate the out-of-plane support that a stiffener would supply, without including the inplane stiffness of the stiffener. Contour plots of the out-of-plane displacement in the skin at $u/u_{cr}^{lin} = 4$ are shown for panels Al-w2, and Al-wdw2 in Fig. 6-7. The contour plots shown in Figs. 6-7(a) and 6-7(b) closely resemble the con-

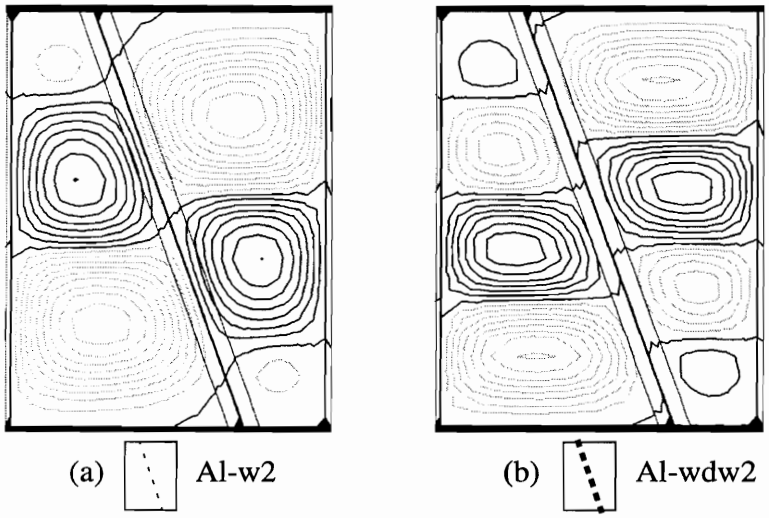

Fig. 6-7 Postbuckling shapes of all-aluminum panels with the rotated stiffener replaced with out-of-plane displacement constraints

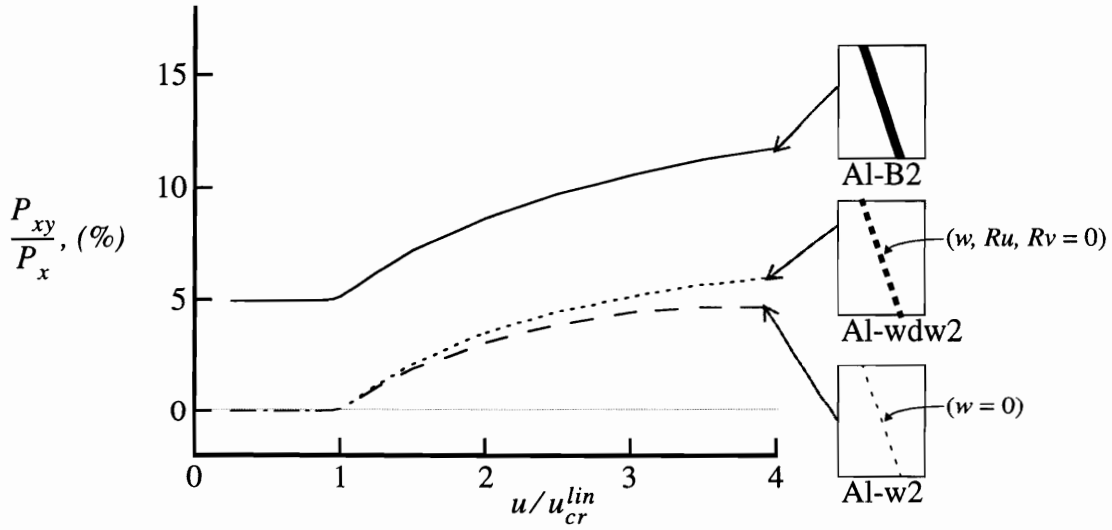

Fig. 6-8 Force coupling responses of all-aluminum panel with original stiffener, and panels with the stiffener replaced with out-of-plane displacement constraints

tour plots for panels Al-B2 and Al-C2, shown in Figs. 6-3(c) and 6-5(c), respectively. The force coupling versus end shortening responses for panels Al-B2, Al-w2, and Al-wdw2 are compared in Fig. 6-8. The force coupling responses for panels Al-w2 and Al-wdw2 are zero in the prebuckling load range, and increase to 4.71% and 6.07%, respectively, in the postbuckling load range. These results indicate similar increases in the force coupling responses for panels Al-B2, Al-w2 and Al-wdw2, and support the postulate that the

increase in the force coupling response that is observed after skin buckling in panels with a rotated stiffener is due largely to the skewed deformations of the postbuckled skin. The issue of how skewness in the postbuckling deformation of the skin causes force coupling is now considered. In the unstiffened panels with displacement constraints considered above, the shear load P_{xy} is simply the integral of the shear stress resultant N_{xy} across the width of the panel. The panels are made of isotropic material, so A_{16} and A_{26} are zero, and Eq. (1.1) gives

$$N_{xy} = A_{66}\gamma^o_{xy} \quad . \tag{6.1}$$

If P_{xy} is to be nonzero, then

$$\int \gamma^o_{xy} dy \neq 0 \quad . \tag{6.2}$$

If von Kármán nonlinear plate theory is applied, then from Eq. (A.22),

$$\gamma^o_{xy} = \frac{\partial u_o}{\partial y} + \frac{\partial v_o}{\partial x} + \left(\frac{\partial w}{\partial x}\right)\left(\frac{\partial w}{\partial y}\right) \quad . \tag{6.3}$$

Skewness of the postbuckled shape affects the distribution of $(\partial w/\partial x)(\partial w/\partial y)$. For example, consider the contours of the skin out-of-plane displacements shown in Figs. 6-3(a) and 6-3(b). Close-up views of the contour plots at the midlength of panels Al-B0 and Al-B1 are shown in Figs. 6-9(a) and 6-9(b), respectively. The deformation in panel Al-B0 is not

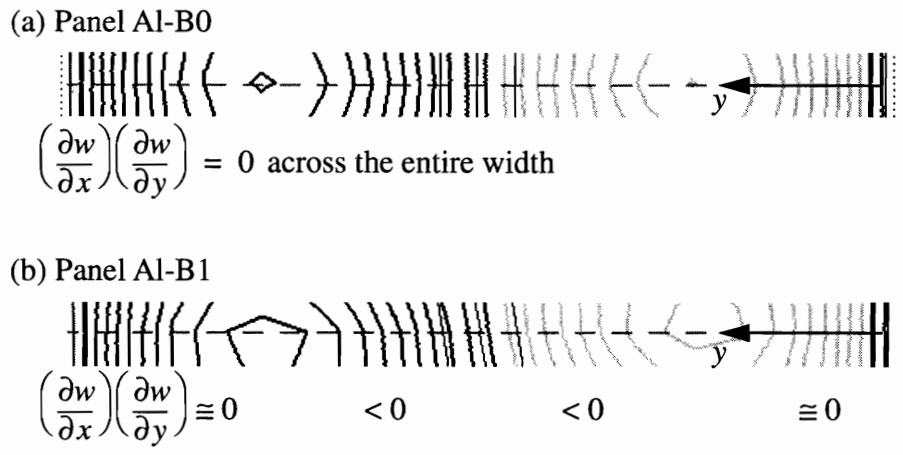

Fig. 6-9 Skewness in the out-of-plane displacements of the skin at panel midlength

skewed and $(\partial w/\partial x)(\partial w/\partial y) = 0$ across the entire width at the panel midlength. At cross sections above and below the midlength of panel Al-B0, $(\partial w/\partial x)(\partial w/\partial y)$ has nonzero values, but the integral of $(\partial w/\partial x)(\partial w/\partial y)$ across the width of the panel is zero. The displacement contours for panel Al-B1 are skewed due to the support of the rotated stiffener. The quantity $(\partial w/\partial x)(\partial w/\partial y)$ at the panel midlength is approximately zero on the left and right sides of the panel, but less than zero in the middle of the panel. This distribution of $(\partial w/\partial x)(\partial w/\partial y)$ creates a shear strain that does not integrate to zero, and thus, the panel shear load P_{xy} is nonzero.

The results presented above have shown that rotating the stiffener can create a force coupling response that is constant in the prebuckling load range, and increases nonlinearly in the postbuckling load range. While the results have shown that rotating the stiffener by a positive angle, i.e., $\alpha > 0$, creates positive values of force coupling P_{xy}/P_x, it follows that rotating the stiffener by a negative angle creates negative values of force coupling. In regards to the *nonlinear* increase in force coupling after skin buckling, it is informative to examine the behavior of the forces P_x and P_{xy} independently. For example, consider the force coupling response for panel Al-B2 that was shown in Fig. 6-4. The individual force components, P_x and P_{xy}, versus end shortening responses for this panel are shown in Figs. 6-10(a) and 6-10(b), respectively. The forces and end shortening are normalized by the linear buckling parameters, $(P_x)_{cr}^{lin}$ and u_{cr}^{lin}, respectively. The axial force vs. end shortening response shown in Fig. 6-10(a) displays a reduction in slope at the buckling load, indicating a reduction in axial stiffness that is typical of buckled stiffened panels. The response curve is nearly bilinear, with additional reductions in stiffness as the loading increases. When $u = 4.0\, u_{cr}$ the panel's axial stiffness is approximately 50% of its prebuckling axial stiffness. The shear force vs. end shortening response shown in Fig. 6-10(b) displays a increase in slope at the buckling load, and the response curve appears to be exactly bilinear. The force coupling response that has been used throughout this study was defined as the ratio of the shear force to the axial force. This definition provides a secant-type measure of the response at a given value of end shortening, but does not directly indicate the incremental (tangent) local behavior of the response. The secant force coupling response P_{xy}/P_x, and the tangent force coupling response $\Delta P_{xy}/\Delta P_x$, are computed for panel Al-B2 and compared in Fig. 6-10(c). Structural designers may be more interested in the tangent force coupling if they are concerned with controlling the incremental response of a structure as it is subjected to incremental loads. As indicated in Fig. 6-10(c), the tangential force coupling response can vary quickly when the skin buckles.

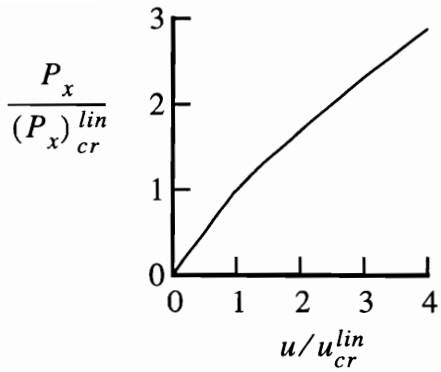

(a) Axial force vs. end shortening

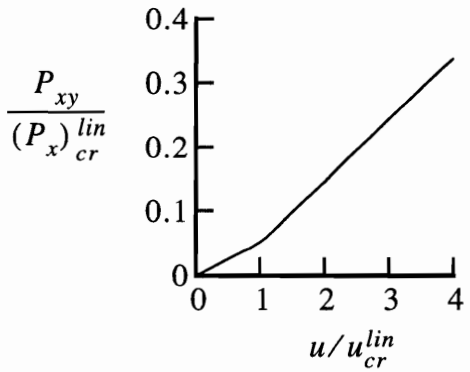

(b) Shear force vs. end shortening

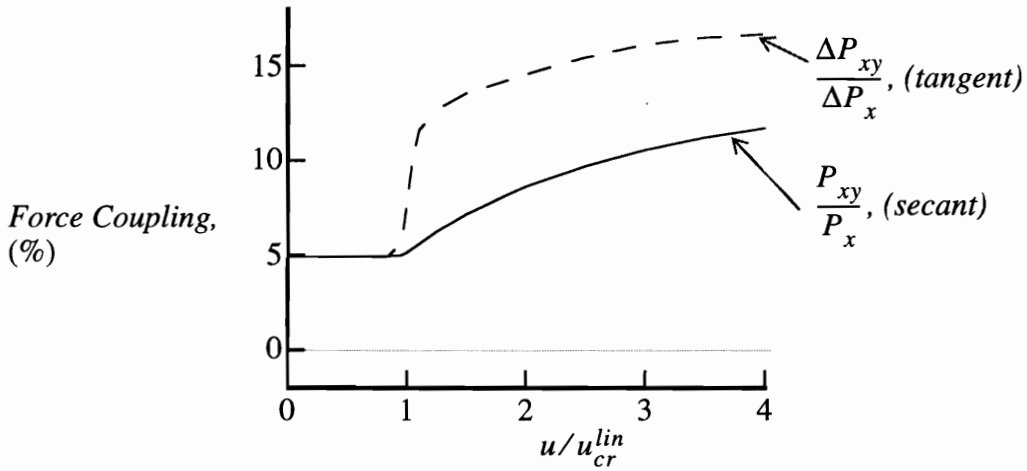

(c) Axial-shear force coupling vs. end shortening

Fig. 6-10 Force coupling for panel Al-B2: individual force components and secant versus tangent force coupling

6.2 Skin Anisotropy

To examine the effect of the skin anisotropy on the axial-shear coupling response of the stiffened panels, panel configurations are considered which have the unrotated stiffener. The panels are assumed to be constructed entirely from Hercules, Inc. AS4-3502 graphite-epoxy unidirectional preimpregnated tape, with the modified material properties in Table 2-2 applied. The stiffener definition for these panels is the same as for the panels that were tested, i.e., a graphite-epoxy stiffener with $[\pm 45/0/90]_{2s}$ laminates and the cross section shown in Fig. 2-1(a).

For the panel configurations that were tested, a nominal skin laminate construction was specified, and the entire laminate was rotated relative to the principal loading direction. As was demonstrated in Section 1.1.4, rotating a laminate typically modifies the membrane and bending stiffnesses. The skin constructions that are considered in this chapter are not specified and then rotated, but rather are prescribed exactly to isolate specific membrane and bending stiffness coupling terms. A few parameters are useful to quantify the degree of anisotropy in a laminate. The amount of membrane stiffness coupling is reflected by the value of the equivalent membrane coefficient of mutual influence $\eta^{o}_{xy,\,x}$, previously defined in Eq. (1.11). The amount of bending stiffness coupling is reflected by the value of the equivalent flexural coefficient of mutual influence $\eta^{f}_{xy,\,x}$, previously defined in Eq. (1.21), and the values of the anisotropic parameters,

$$\gamma = \frac{D_{16}}{(D_{11}^3 D_{22})^{0.25}} \qquad \delta = \frac{D_{26}}{(D_{11} D_{22}^3)^{0.25}} \quad , \tag{6.4}$$

defined by Nemeth in Ref. 27. Results are presented below for four different skin laminates. All of the skin laminates are 16 ply symmetric laminates. The laminates have two 0° plies, two 90° plies, and the remaining twelve plies are split between 30° and -30° orientations. The anisotropy of the laminates is altered by replacing -30° plies with 30°plies, and by changing the stacking sequence. The stacking sequences for the selected laminates and values of the parameters which reflect their various degrees of anisotropy are listed in Table 6-1.The skin laminate 'c' has minimal anisotropy, and serves as a benchmark configuration. Laminate 'd' has a higher number of 30° plies to create membrane stiffness coupling, yet has a stacking sequence which minimizes the bending stiffness coupling. Note that $\eta^{o}_{xy,\,x}$ for laminate 'd' is negative, thus indicating negative membrane stiffness coupling. Laminate 'e' has zero membrane stiffness coupling, but has large negative bending stiffness coupling, as reflected in Table 6-1 by the negative value of $\eta^{f}_{xy,\,x}$. Laminate 'f' includes both negative membrane and negative bending stiffness coupling.

The panels, identified as B0c, B0d, B0e, and B0f, designate panel configurations with the unrotated stiffener, and skin laminates 'c', 'd', 'e', and 'f', respectively. The prebuckling stiffnesses for these panels are 17,250, 16,290, 17,250, and 16,290 kips, respectively. The linear buckling loads are 7.04, 6.37, 6.02, and 5.69 kips, respectively. Thus, the reductions in buckling load due to skin membrane stiffness coupling, bending stiffness coupling, and combined membrane and bending stiffness coupling, are 9%, 14%, and 19%,

Table 6-1 Laminates with Various Types of Anisotropy

Skin ID.	Lay-up	$\eta^{o}_{xy,\,x}$	$\eta^{f}_{xy,\,x}$	γ	δ
c	$[\pm 30/90/\mp 30/0/\mp 30]_s$	0.00	-0.03	0.02	0.01
d	$[-30/90/30_2/0/30_3]_s$	-0.76	0.03	0.01	0.01
e	$[30_3/90/0/-30_3]_s$	0.00	-1.06	0.45	0.25
f	$[30_3/90/30_2/0/-30]_s$	-0.76	-1.30	0.56	0.31

respectively, relative to the benchmark panel with minimal anisotropy. The reductions in the buckling load that occur when the skin laminate is highly anisotropic are consistent with the findings reported in Refs. 27 and 41. Contour plots of the out-of-plane displacement in the skin at $u/u_{cr}^{lin} = 4$ are shown in Fig. 6-11. Panel B0c has the most symmetric deformation shape. The membrane stiffness coupling in panel B0d causes the skin to buckle under combined compression and shear. The shear load causes slight skewing of the deformation pattern for panel B0d. Bending stiffness coupling in panels B0e and B0f causes the skin deformations to have substantial skewing, but in the opposite direction of the skewing shown for panel B0d.

The force coupling versus end shortening responses for these panels are shown in Fig. 6-12. The force coupling for panel B0c is approximately zero, as expected. The negative membrane stiffness coupling in panel B0d produces a force coupling response that is 12.00% in the prebuckling load range, and decreases to 6.05% in the postbuckling load range. The negative bending stiffness coupling in panel B0e does not produce any force coupling until the skin buckles, and then the force coupling increases to 2.88% in the postbuckling load range. Panel B0f has the same membrane stiffness coupling as panel B0d, and thus has an equal amount of force coupling in the prebuckling response. The force coupling response of panel B0f reduces after the skin buckles, but the negative bending stiffness coupling causes the reduction in force coupling to be less for panel B0f than it was for panel B0d. The force coupling response for panel B0f ranges from 12.01% to 9.50%, and resembles the sum of the responses for panels B0d and B0e.

The axial-shear coupling response for panel B0f described above is very significant. Recall that this panel has negative membrane stiffness coupling and negative bending stiffness coupling, each of which creates a positive contribution to the force coupling response. Recall that negative membrane stiffness coupling becomes less effective in cre-

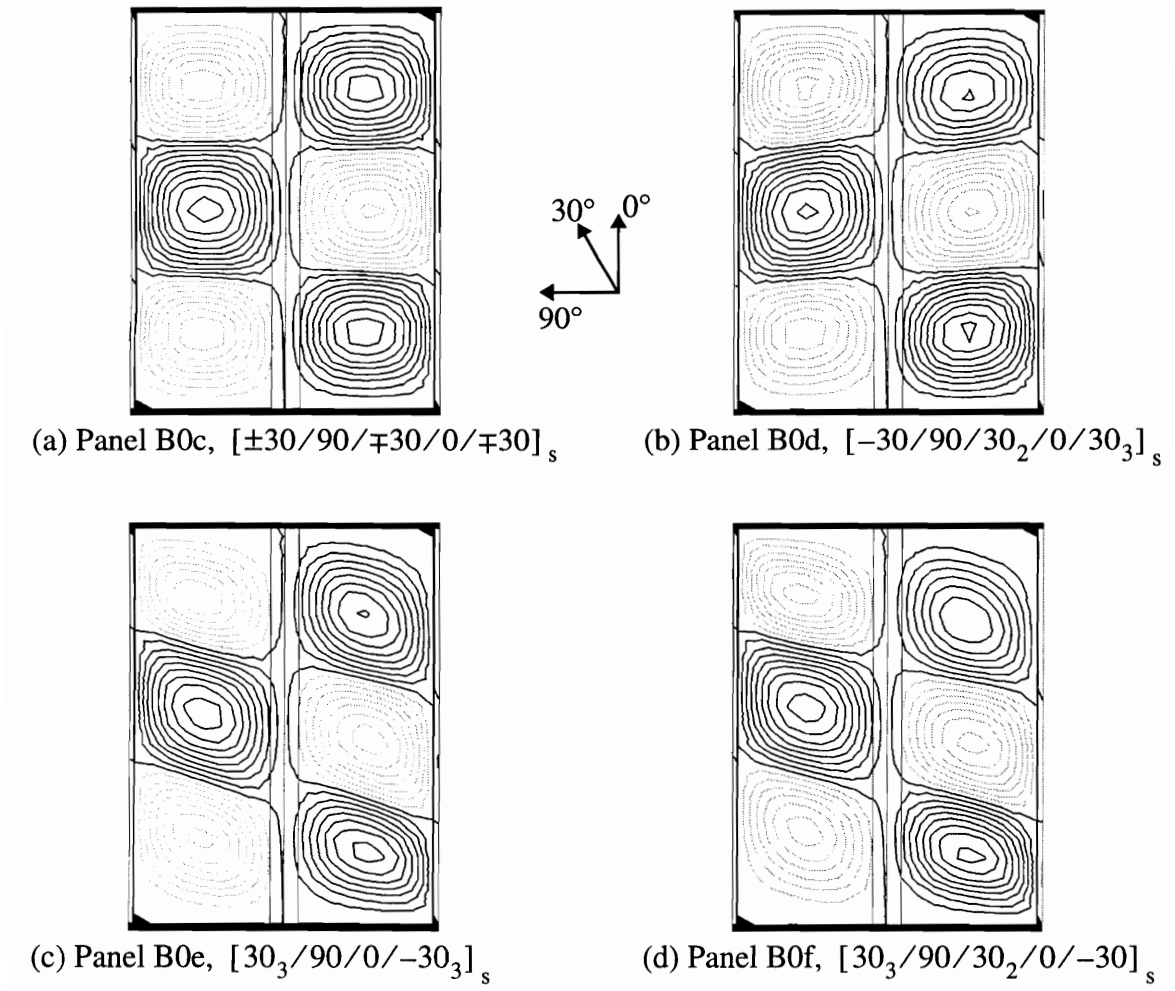

(a) Panel B0c, $[\pm 30/90/\mp 30/0/\mp 30]_s$ (b) Panel B0d, $[-30/90/30_2/0/30_3]_s$

(c) Panel B0e, $[30_3/90/0/-30_3]_s$ (d) Panel B0f, $[30_3/90/30_2/0/-30]_s$

Fig. 6-11 Postbuckling shapes of panels with the unrotated stiffener and anisotropic skins

ating force coupling, i.e., the force coupling response decreases, after the skin buckles. In contrast, negative bending stiffness coupling becomes more effective in creating force coupling, i.e., the force coupling response increases, after the skin buckles. By applying both mechanisms, negative membrane stiffness coupling and negative bending stiffness coupling, in the same panel, the loss in effectiveness of one mechanism is offset in part by the increase in effectiveness of the second mechanism, and the net effect is that the force coupling response is more uniform over the entire range of loading. Note that the membrane and bending stiffness coupling terms can be tailored somewhat independently. As was discussed in Section 1.1.4, the membrane stiffness terms A_{ij}, in Eq. (A.31) represent a simple summation of lamina properties that is independent a the z-location of each lamina.

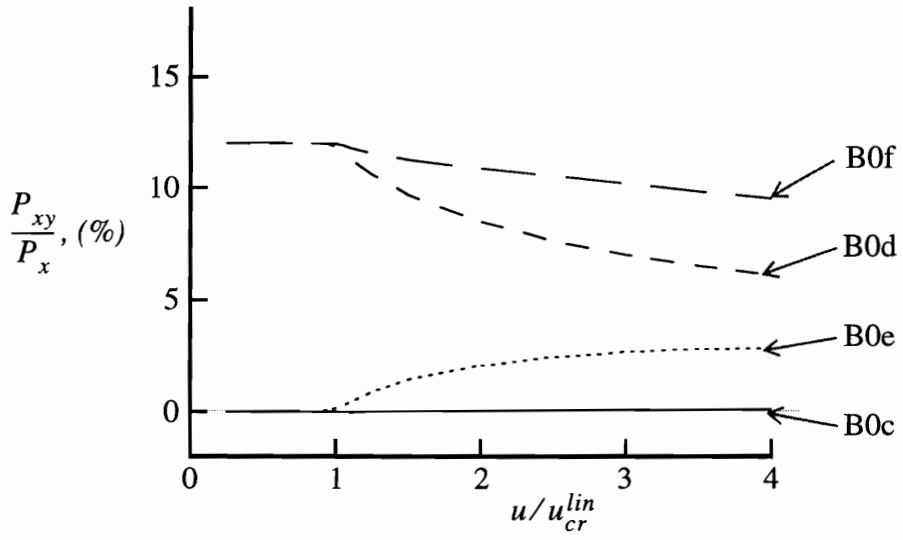

Fig. 6-12 Force coupling response of panels with the unrotated stiffener and anisotropic skins

In contrast, the bending stiffness terms D_{ij} are defined such that the contribution of each lamina to D_{ij} is weighted by the square of the z-location of the lamina. Therefore, it is possible to prescribe the percentage of lamina in specific orientations to tailor the A_{ij} terms, and then adjust the z-locations of the lamina by specifying the stacking sequence to tailor the D_{ij} terms. In panel B0f, the number of 30°plies is greater than the number of -30° plies to provide negative membrane stiffness coupling, and the -30° plies are located at the midplane of the laminate, while the 30° plies a located closer to the upper and lower surface of the laminate, to provide negative bending stiffness coupling.

6.2.1 Skin Anisotropy and Variations in Force Coupling Response in the Postbuckling Load Range

In the results shown above, negative bending stiffness coupling was responsible for increases in force coupling after skin buckling. Bending stiffness coupling causes skewing of the skin deformations, as was shown in Fig. 6-11(c), and also much earlier in Fig. 1-3. When presenting the results for rotated stiffeners above, it was explained how skewing of the skin deformations can increase the force coupling response in the postbuckling load range. In contrast, results have shown that negative membrane stiffness coupling in the skin creates a force coupling response that is uniform in the prebuckling load range and reduces nonlinearly after skin buckling. To explain this behavior, the force coupling response for panel B0d is examined closely in Fig. 6-13. The individual force components,

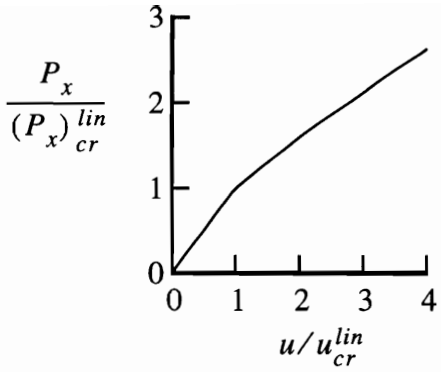

(a) Axial force vs. end shortening

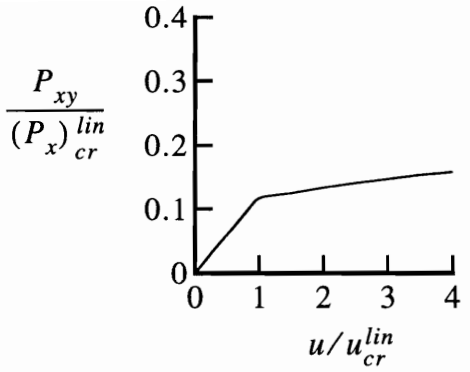

(b) Shear force vs. end shortening

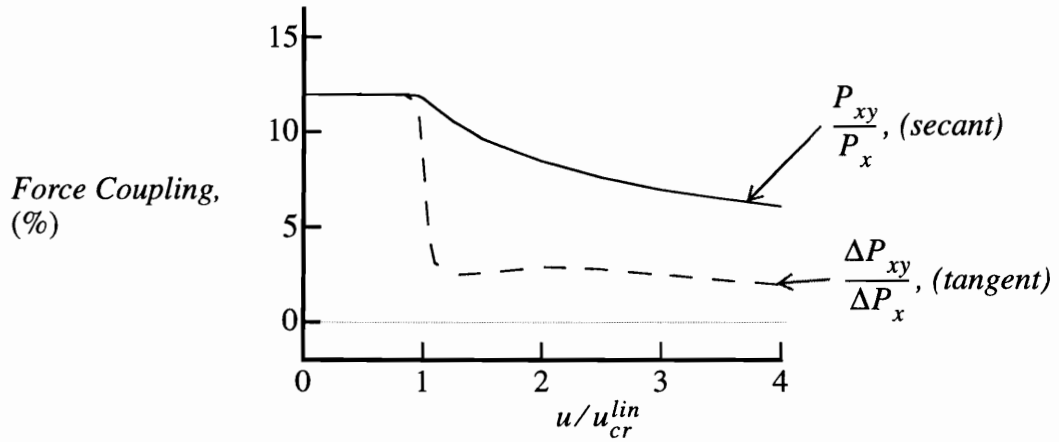

(c) Axial-shear force coupling vs. end shortening

Fig. 6-13 Force coupling for panel B0d: individual force components and secant versus tangent force coupling

P_x and P_{xy}, versus end shortening responses for panel B0d are shown in Figs. 6-13(a) and 6-13(b), respectively. The axial force vs. end shortening response shown in Fig. 6-13(a) displays the typical reduction in slope at the buckling load. The response curve is nearly bilinear, with additional reductions in stiffness as the loading increases. The shear force vs. end shortening response shown in Fig. 6-13(b) displays a sharp decrease in slope at the buckling load. This decrease in slope strongly contrasts the increase in slope of the shear force response for the panel with a rotated stiffener, shown in Fig. 6-13(b). The secant force coupling response, P_{xy}/P_x, and tangent force coupling response, $\Delta P_{xy}/\Delta P_x$, are compared in Fig. 6-13(c). The large reduction in the tangential force coupling response after skin buckling reflects the very low slope of the shear force response curve and represents a

substantial change in the behavior of the incremental response of the panel. The reduction in shear stiffness reported above resembles the results presented by Stein[36] on the postbuckling response of unstiffened plates in combined compression and shear. As was noted in the literature review, Stein observed that plates buckled in compression can display very large reductions in shear stiffness.

The results presented above have shown that anisotropy in the skin laminate creates a force coupling response that is constant in the prebuckling load range. After the skin buckles, the force coupling due to negative membrane stiffness coupling decreases, while the force coupling due to negative bending stiffness coupling increases. While laminates were considered which created positive values of force coupling P_{xy}/P_x, negating the fiber orientations of these laminates would reverse the membrane and bending stiffness couplings and create negative values of force coupling.

Panel configurations have been considered which examined the effect on the force coupling responses of independently applying skewed stiffeners and anisotropic skins. The results have indicated that the amount of force coupling, and the behavior of the response in the postbuckling load range, is dependent upon which mechanism is employed to create stiffness coupling. Additional cases are now considered which combine the mechanisms to tailor the axial-shear coupling response in the prebuckling and postbuckling load ranges.

6.3 Combining Skewed Stiffeners and Anisotropic Skins

Panel configurations which have the stiffener rotated 20° and have skin laminates with membrane and bending stiffness coupling are considered. The original graphite-epoxy stiffener definition shown in Fig. 2-1(a) was used for these panels. Results are presented below for five skin laminates. Three of the laminates are laminates 'c', 'd', and 'e', which were defined in the preceding section. The stacking sequences for these laminates were listed in Table 6-1. Two additional laminates, designated as laminates 'dr' and 'er', are prescribed by negating the fiber orientations of laminates 'd' and 'e', respectively, to change the signs of the stiffness couplings of the laminates. Laminate 'dr' has a stacking sequence of $[30/90/-30_2/0/-30_3]_s$, and has large positive membrane stiffness coupling and minimal bending stiffness coupling. Laminate 'er' has a stacking sequence of $[-30_3/90/0/30_3]_s$, and has large positive bending stiffness coupling and minimal

membrane stiffness coupling.

The panels, identified as B2c, B2d, B2dr, B2e, and B2er designate panel configurations with the stiffener rotated 20° and skin laminates 'c', 'd', 'dr', 'e', and 'er', respectively. Of these five panels, panel B2c is considered the benchmark configuration since skin 'c' has minimal anisotropy. The prebuckling stiffnesses for these panels are 16,880, 15,960, 15,860, 16,880, and 16,880 kips, respectively. The linear buckling loads are 5.44, 6.07, 4.45, 4.14, and 5.22 kips, respectively. Thus, when the stiffener is rotated, the panel with negative membrane stiffness coupling of the skin laminate has a linear buckling load that is 12% higher, and the panel with positive membrane stiffness coupling has a linear buckling load that is 18% lower, as compared to the benchmark configuration with minimal anisotropy in the skin. The panels with skin laminates with negative and positive bending stiffness coupling show decreases in the buckling load of 24% and 4%, respectively. Contour plots of the out-of-plane displacement in the skin at $u/u_{cr}^{lin} = 4$ are shown in Fig. 6-14.

The force coupling versus end shortening responses for these panels are shown in Fig. 6-15. The force coupling responses for the panels that combine a rotated stiffener and anisotropic skin are shown in separate plots so that they can be compared to the force coupling responses that are obtained when the rotated stiffener and anisotropic skins were applied separately. For example, the force coupling response for panel B2d is compared to the force coupling responses for panels B2c and B0d in Fig. 6-15(a). Panel B2c, which has the stiffener rotated 20° and negligible anisotropy, has a force coupling response that is 4.81% in the prebuckling load range, and increases to 12.29% in the postbuckling load range. Panel B0d, considered in the previous section, has an unrotated stiffener and negative membrane stiffness coupling, and has a force coupling response that is 12.00% in the prebuckling load range, but decreases to 6.05% in the postbuckling load range. When the rotated stiffener and negative membrane stiffness coupling are combined in panel B2d, it appears as if the responses of panels B2c and B0d are superimposed. The prebuckling responses add to give a larger response, and the increasing and decreasing responses after buckling partially offset each other. The net affect is that panel B2d has a large force coupling response that varies by a small amount over the entire range of loading. The force coupling response for panel B2d is 17.48% before buckling, and increases to 19.42% in the postbuckling load range. .

The case which combines a rotated stiffener with a skin laminate with positive mem-

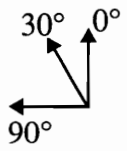

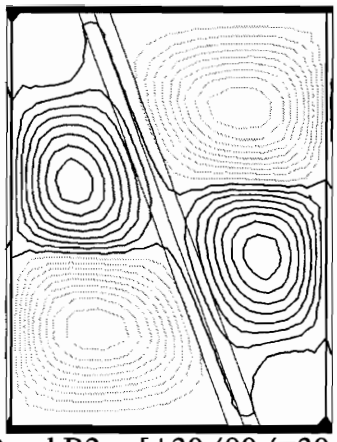

(a) Panel B2c, $[\pm 30/90/\mp 30/0/\mp 30]_s$

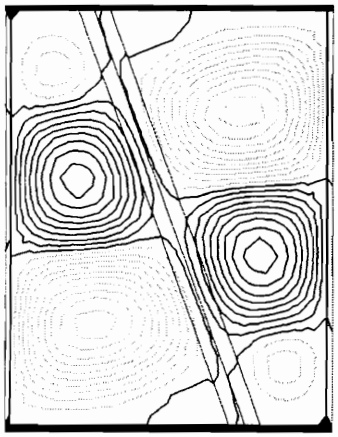

(b) Panel B2d, $[-30/90/30_2/0/30_3]_s$

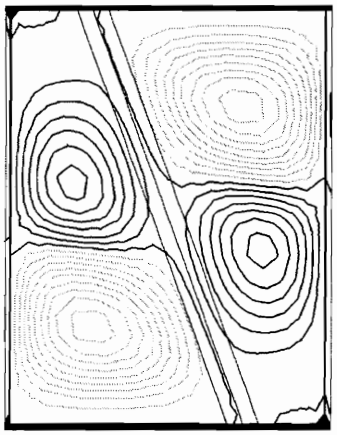

(c) Panel B2dr, $[30/90/-30_2/0/-30_3]_s$

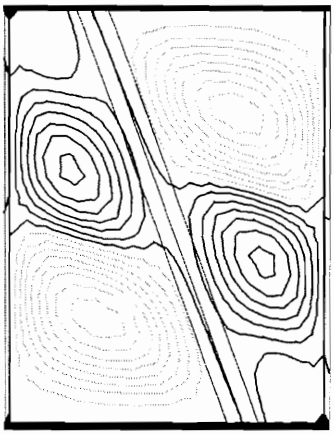

(d) Panel B2e, $[30_3/90/0/-30_3]_s$

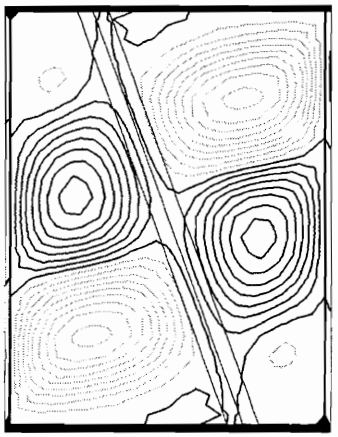

(e) Panel B2er, $[-30_3/90/0/30_3]_s$

Fig. 6-14 Postbuckling shapes of panels with the stiffener rotated 20° and anisotropic skins

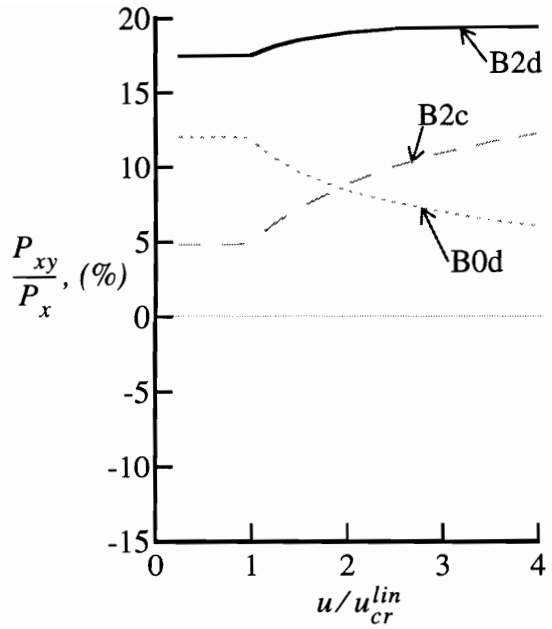

(a) Rotated stiffener and negative membrane stiffness coupling

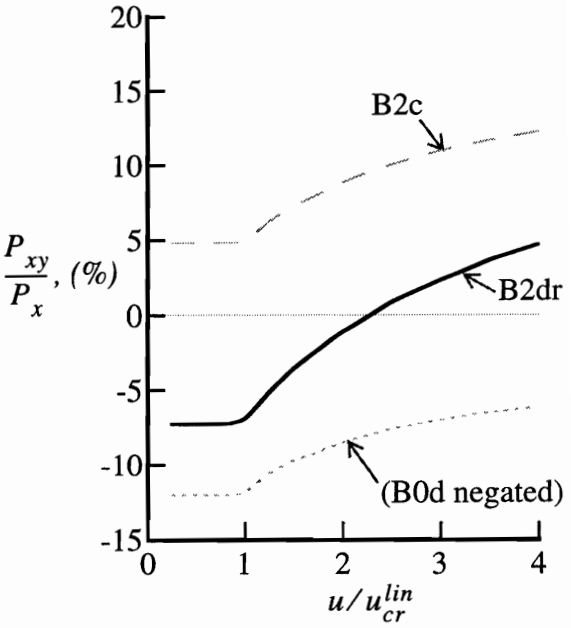

(b) Rotated stiffener and positive membrane stiffness coupling

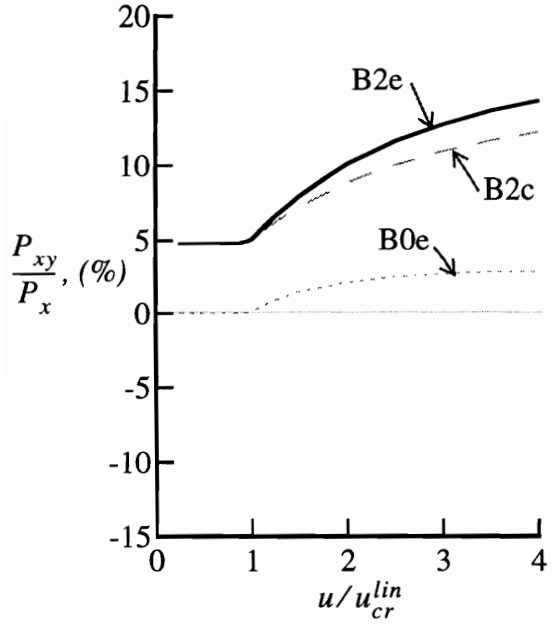

(c) Rotated stiffener and negative bending stiffness coupling

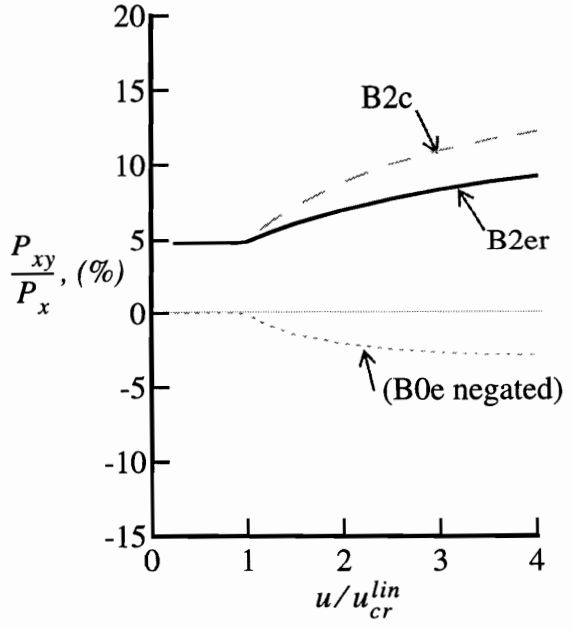

(d) Rotated stiffener and positive bending stiffness coupling

Fig. 6-15 Force coupling response of panels which combine a rotated stiffener and anisotropic skins

brane stiffness coupling is considered in Fig. 6-15(b). If an analyses were conducted with an unrotated stiffener and skin laminate 'dr', then the force coupling response would be equal to the 'B0d negated' response shown in Fig. 6-15(b). The 'B0d negated' response is negative before buckling, and becomes less negative, i.e., increases, after skin buckling. When the rotated stiffener and positive membrane stiffness coupling are combined in panel B2dr, it appears as if the responses of panels B2c and 'B0d negated' are superimposed. The prebuckling responses partially offset each other, and the increasing responses after buckling are additive. The net affect is that panel B2dr has a force coupling response that is -7.28% before buckling, and increases to 4.74% in the postbuckling load range. The individual force components, P_x and P_{xy}, versus end shortening responses for panel B2dr are shown in Figs. 6-16(a) and 6-16(b), respectively. The axial force vs. end shortening response shown in Fig. 6-16(a) is typical of all of the panels. The shear force vs. end shortening response shown in Fig. 6-16(b) is unique in that it has a negative slope during the initial loading and a positive slope after the skin buckles. The incremental shear force is positive immediately after the skin buckles, while the net shear force on the panel does not become positive until further into the postbuckling load range. The force coupling response of panel B2dr, shown in Fig. 6-15(b), becomes positive when the shear force P_{xy} becomes positive.

The case which combines a rotated stiffener with a skin laminate with negative bending stiffness coupling is considered in Fig. 6-15(c). Panel B0e, considered in the previous section, has an unrotated stiffener and negative bending stiffness coupling, and has a force coupling response that is zero in the prebuckling load range, but increases to 2.88% in the postbuckling load range. When the rotated stiffener and negative bending stiffness coupling are combined in panel B2e, it appears as if the responses of panels B2c and B0e are superimposed. Comparing the results for panels B2c and B2e shows that the negative bending stiffness coupling in panel B2e does not affect the force coupling response before buckling occurs, but it does increase the force coupling response in the postbuckling load range. The force coupling response for panel B2e is 4.81% before buckling, and increases to 14.40% in the postbuckling load range.

The case which combines a rotated stiffener with a skin laminate with positive bending stiffness coupling is considered in Fig. 6-15(d). If an analyses were conducted with an unrotated stiffener and skin laminate 'er', then the force coupling response would be equal to the 'B0e negated' response shown in Fig. 6-15(d). When the rotated stiffener and posi-

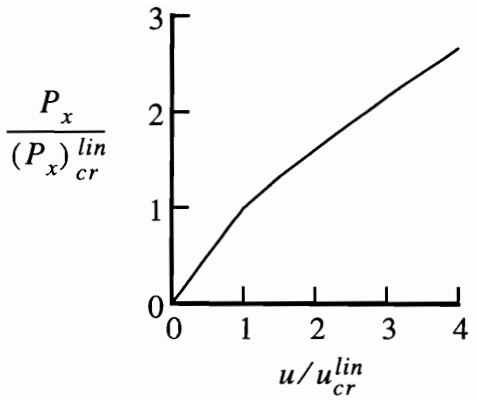

(a) Axial force vs. end shortening

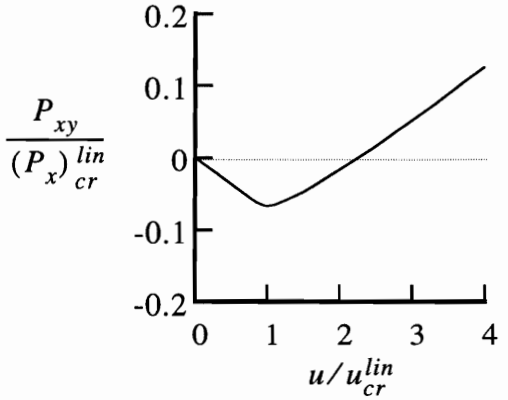

(b) Shear force vs. end shortening

Fig. 6-16 Individual force components for panel B2d

tive membrane stiffness coupling are combined in panel B2er, the positive bending stiffness coupling does not affect the force coupling response before buckling occurs, but it does reduce the amount of increase in the force coupling response in the postbuckling load range. The force coupling response for panel B2er is 4.81% before buckling, and increases to 9.30% in the postbuckling load range.

6.4 Summary of Cases Considered

For each stiffened panel configuration that was considered, the panel description, prebuckling stiffness, EA, the linear buckling parameters, $(P_x)^{lin}_{cr}$ and u^{lin}_{cr}, and the force coupling response, (P_{xy}/P_x), in the prebuckling and postbuckling load ranges, are summarized in Table 6-2. The force coupling response in the postbuckling load range is defined as (P_{xy}/P_x) at $u = 4.0\ u_{cr}$. In Table 6-2, the panels are listed by their 'I.D.,' or panel identification code. The stiffener cross section of each panel is identified by code. Cross sections 'Al-B' and 'Al-C' refer to the nominal and more-rigid aluminum stiffeners, respectively. Cross section 'B' refers to the nominal graphite-epoxy stiffener that was used for all of the composite panels. The all-aluminum panels are listed first in Table 6-2, followed by the composite panels that were tested, and then the additional composite panels that were discussed above. Table 6-2 also includes numerical results for additional composite panel which were not discussed above. These final cases all had an unrotated stiffener and considered various skin laminates. Comments on these additional cases are included below.

Table 6-2 Summary of Parametric Study

I.D.	Stiffener		Skin Laminate	EA (kip)	Linear Buckling		P_{xy}/P_x, (%)	
	Cross Section	α (deg)			$(P_x)_{cr}^{lin}$ (kip)	u_{cr}^{lin} (mil)	Pre-buckle	Post-buckle
Al-B0	Al-B	0	Al-2024, t = 0.0771 in.	16,630	8.25	11.90	0.000	0.000
Al-B1	Al-B	10	Al-2024, t = 0.0771 in.	16,530	7.70	11.17	2.63	7.33
Al-B2	Al-B	20	Al-2024, t = 0.0771 in.	16,270	6.48	9.56	4.95	11.77
Al-C1	Al-C	10	Al-2024, t = 0.0771 in.	19,430	9.88	12.21	4.71	8.57
Al-C2	Al-C	20	Al-2024, t = 0.0771 in.	18,820	8.15	10.39	8.90	17.00
B0,0	B	0	$[\pm 45/\mp 45/0_3/90]_s$	16,650	7.71	11.12	0.000	0.080
B0,2	B	0	$[65/-25_2/65/20_3/-70]_s$	15,950	6.95	10.46	2.54	1.69
B2,0	B	20	$[\pm 45/\mp 45/0_3/90]_s$	16,270	5.72	8.44	4.97	12.15
B2,2*	B	20	$[65/-25_2/65/20_3/-70]_s$	15,580	5.62	8.66	7.84	14.17
B2,n2	B	20	$[25/-65_2/25/-20_3/70]_s$	15,550	5.22	8.06	2.57	10.24
B0c	B	0	$[\pm 30/90/\mp 30/0/\mp 30]_s$	17,250	7.04	9.79	0.000	0.080
B0d	B	0	$[-30/90/30_2/0/30_3]_s$	16,290	6.37	9.38	12.00	6.05
B0e	B	0	$[30_3/90/0/-30_3]_s$	17,250	6.02	8.37	0.000	2.88
B0f	B	0	$[30_3/90/30_2/0/-30]_s$	16,300	5.69	8.38	12.00	9.50
B2c	B	0	$[\pm 30/90/\mp 30/0/\mp 30]_s$	16,880	5.44	7.73	4.81	12.29
B2d	B	20	$[-30/90/30_2/0/30_3]_s$	15,960	6.07	9.13	17.48	19.42
B2dr	B	20	$[30/90/-30_2/0/-30_3]_s$	15,860	4.45	6.73	-7.28	4.74
B2e	B	20	$[30_3/90/0/-30_3]_s$	16,880	4.14	5.89	4.81	14.40
B2er	B	20	$[-30_3/90/0/30_3]_s$	16,880	5.22	7.42	4.81	9.30
B0g	B	0	$[-15/90/15_2/0/15_3]_s$	23,400	5.54	5.69	8.67	5.84
B0h	B	0	$[45_2/-45_2/15_3/-75]_s$	14,460	7.48	12.41	8.15	5.34
B0i	B	0	$[30_2/-60_2/15_3/-75]_s$	14,640	6.55	10.74	14.71	9.02
B0j	B	0	$[15_3/90/0/-15_3]_s$	24,200	5.24	5.19	0.000	0.91
B0k	B	0	$[45_4/-45_4]_s$	7,850	7.61	23.3	0.000	4.33
B0l	B	0	$[30_4/-30_4]_s$	15,020	5.64	8.97	0.000	4.26
B0m	B	0	$[-30_2/90/30_2/0/30_2]_s$	17,030	6.51	9.18	5.79	1.49
B0n	B	0	$[30_2/90/30_2/0/-30_2]_s$	17,030	6.04	8.51	5.79	5.80
B0o	B	0	$[-30_2/30_6]_s$	14,570	5.83	9.61	10.89	4.08
B0p	B	0	$[30_6/-30_2]_s$	14,570	5.05	8.32	10.89	10.00
B0q	B	0	$[30_6/-60_2]_s$	11,200	5.04	10.81	20.1	13.49

* The width of the stiffener cap is assumed to be 1.2 in.

Additional Composite Panels

B0g: This panel is similar to panel B0d except the 30° and -30° layers are replaced by 15° and −15 ° layers. As shown in Fig. 1-6, a unidirectional laminate rotated 15° has a very large value of $\eta^{o}_{xy,x}$. The values of $\eta^{o}_{xy,x}$ for panels B0d and B0g are -0.76 and -1.23, respectively, yet the force coupling response of panel B0d is larger than for panel B0g. The lower-than-expected force coupling response of panel B0g is credited to the reduction in shear stiffness of the 15° layers, and the panel boundary conditions which have shear loads applied at the top and bottom panel edges only.

B0h: Panel B0,2 was constructed by rotating a $[\pm 45/\mp 45/0_3/90]_s$ laminate by 20°. The force coupling response of panel B0,2 was only 2.54% in the prebuckling load range. Panel B0h has a similar construction, except only the 0° and 90° layers are rotated 15°, and the ±45° layers are not rotated. The prebuckling response of panel B0h has a force coupling response of 8.15%.

B0i: This panel is similar to panel B0h. In addition to rotating the 0° and 90° layers 15°, the ±45° layers are rotated −15 °. The force coupling response of panel B0i is 14.71% in the prebuckling load range.

B0j: This panel has zero membrane stiffness coupling and nonzero bending stiffness coupling. It is similar to panel B0e, except the 30° and -30° layers are replaced by 15° and −15 ° layers. As shown in Fig. 1-6, a unidirectional laminate rotated 15° has a very large value of $\eta^{f}_{xy,x}$. The values of $\eta^{f}_{xy,x}$ for panels B0e and B0j are -1.06 and -1.67, respectively, yet the force coupling response in the postbuckling load range for panel B0e is three times larger than for panel B0j. This indicates that $\eta^{f}_{xy,x}$ is not a very good parameter to predict the force coupling caused by bending stiffness coupling. The anisotropic parameters, γ and δ, defined in Eq. (6.4) provide better correlation with the force coupling response. The values of γ and δ are (0.45,0.25) for panel B0e, and (0.26,0.06) for panel B0j. One reason that γ and δ provide better correlation with the force coupling response better than $\eta^{f}_{xy,x}$ is that the buckling shape of the panels involves bending in both the x and y directions.

B0k, B0l: These panels both have zero membrane stiffness coupling and high bending stiffness coupling. Panel B0k has all 45° layers, which causes the panel to have a high buckling load, but a very low axial stiffness.

B0m: This panel has moderate negative membrane stiffness coupling and positive bending stiffness coupling.

B0n: This panel is equivalent to panel B0m, except the stacking sequence is modified so that panel B0n has negative bending stiffness coupling. The combination of negative membrane and negative bending stiffness coupling causes the force coupling response of panel B0n to be nearly constant over the entire range of loading.

B0o, B0p: These panels are two more examples of panels with membrane and bending stiffness coupling. Panel B0o has positive bending stiffness coupling and the force coupling response reduces substantially after skin buckling occurs. Panel B0p has the stacking sequence changed to give negative bending stiffness coupling, and has a force coupling response that is nearly constant over the entire range of loading.

B0q: The -30° layers of panel B0p are replaced with -60° layers to form panel B0q. Panel B0q has the highest force coupling response of all the panels considered, with a value of 20.12% in the prebuckling load range.

6.5 Closing Comments

As can be seen, there are an endless number of combinations of skin and stiffener parameters that can be used to provide a range of responses. Exploitation of this feature of composites can lead to structural responses simply not possible with metals. The next chapter summarizes the findings of this entire study, and sets the stage for further investigation of structural tailoring using rotated stiffeners and anisotropic skins.

7. Conclusions and Recommendations

In an attempt to promote the use of structural tailoring concepts in innovative design applications, the goal of the present work was to quantify and explain the buckling and postbuckling response of composite stiffened panels which are tailored to exhibit axial-shear stiffness coupling. Typical applications include structures consisting of stiffened panel sections where stiffness tailoring is utilized to control structural deformations. To achieve the stated goal, an experimental and numerical investigation of the prebuckling and postbuckling responses of composite plates with anisotropic skins and skewed stiffeners was conducted. The structural configuration considered was a flat rectangular graphite-epoxy laminated composite panel with a single centrally located I-shaped graphite-epoxy stiffener, subjected to a uniform end shortening. Axial-shear stiffness coupling was introduced by rotating the orientation of the stiffener, and/or prescribing skin laminates which had various degrees of membrane and bending stiffness coupling. As noted earlier, only one reference in the literature previously addressed structural tailoring by applying rotated stiffeners and anisotropic skins in the same study. In the reference, rotated stiffeners were applied in metallic structures and anisotropic skins were applied in composite structures. The current investigation is the first to apply both rotated stiffeners and anisotropic skins in a single design, and to consider the postbuckling response of such panels.

An exploratory experimental program consisting of five stiffened panels was conducted. The baseline test panel had an unrotated stiffener and a $[\pm 45/\mp 45/0_3/90]_s$ skin laminate. Two panels had either the stiffener or the entire skin laminate rotated 20°, and the remaining two panels had both the stiffener and the skin laminate rotated 20°, either in the same direction, or in opposite directions. Extensive experimental data were acquired electronically during quasi-static tests. Finite element models were defined which accurately represented the conditions in the experiments. Geometrically nonlinear finite element analyses were utilized to simulate the prebuckling and postbuckling responses of the pan-

els. The numerical models were verified by correlating the following measured and predicted panel responses: prebuckling and initial postbuckling axial stiffness, axial loads and end shortening displacements at skin buckling, axial load vs. end shortening relations, out-of-plane deformation patterns and displacements at discrete points, and the axial-shear coupling vs. end shortening response. A procedure was defined for computing a net axial-shear coupling response from a mixture of measured force and displacement coupling responses. The finite element analyses, based on two-dimensional plate elements, were utilized to estimate the skin-stiffener attachment forces for each panel for applied displacements equal to the displacements at failure. The predicted skin-stiffener attachment forces were studied to gain insight into the effect of stiffness tailoring on the tendency for skin-stiffener separation.

The observed and predicted axial-shear coupling responses of the panels that were tested were studied to identify the mechanisms that control the response. The numerical models that were verified by correlating the experimental results were employed to conduct a parametric study to investigate the sensitivity of the axial-shear coupling response to the different controlling mechanisms. The parametric study first considered panels which independently assessed the effects of stiffener rigidity, stiffener orientation, skin membrane stiffness coupling, and skin bending stiffness coupling on the panel's stiffness, buckling parameters, and axial-shear coupling response. Then, panels were considered which demonstrated combining the effects of more than one mechanism in a single panel.

7.1 Conclusions

The conclusions drawn from this investigation are presented according to three major efforts of the investigation, namely,

- accurate modeling and simulation of the response of the panels that were tested
- characterization of the effect of anisotropic skins and skewed stiffeners on the buckling response, postbuckling response and failure, and axial-shear coupling response of composite stiffened panels based on measured and predicted responses
- exploitation of the identified stiffness tailoring mechanisms to effectively tailor the structural response.

7.1.1 Accurate Modeling of Postbuckled Stiffened Panels

The following conclusions can be made regarding the structural modeling techniques required to predict accurately the prebuckling and postbuckling responses of the stiffened panels:

- Based on the observed deformations of the stiffener cross section, the stiffener should be modelled as a branched shell, rather than a discrete beam.
- The entire length and width of the test specimen should be modelled, including the portion of the specimen that is potted.
- The nominal material properties should be adjusted based on measured laminate thicknesses and the prebuckling response of the most benign panel that was tested. Laminate thicknesses strongly influence panel buckling loads.
- When testing panels with axial-shear stiffness coupling, the end shortening and transverse displacements of the load platens should be monitored. If the test machine is designed to apply compressive loads, it should not be assumed that the load frame applies a rigid constraint in the transverse direction. For example, during one of the tests that was conducted for this study the transverse displacement of the load platen was as much as 68% of the end shortening displacement. The model should have the ability to simulate a non-rigid constraint in the transverse direction.
- Although initial geometric imperfections have very little affect on the load vs. end shortening response, they may assist the numerical analyses in finding solutions near the bifurcation buckling load. If the imperfections are based on measured shape imperfection data of the test specimens, then the imperfections are likely to encourage numerical solutions with deformations that are of the same sign as the observed response.
- For thin shell structures with small values of u_{cr}, tolerances during machining and test fixturing may substantially affect the load introduction. Nonuniform initial displacements may be introduced in the numerical model in order to simulate local nonuniform load distributions during initial loading. These effects tend to influence the local response and may not affect the global response of a panel.

The above modeling techniques were applied to simulate the response of the five test specimens. Correlation of the measured and predicted responses was achieved to the following

degree for 4 of 5 panels:

- The values of the buckling parameters were within 8%.
- The prebuckling and initial postbuckling stiffnesses agreed to within 4%.
- The axial load vs. end shortening responses differed by a maximum of 8% over the entire range of loading.

In addition, linear bifurcation buckling analyses with $v = 0$ and nonlinear static analyses with $v = v^{exp}$ predicted buckling loads that were within 2% of each other. The predicted prebuckling stiffnesses agree to within 2% for the unrotated stiffener, but differed by 9%, on average, for panels with the stiffener rotated 20°. The results from linear and nonlinear analyses in the prebuckling load range are similar because the prebuckling responses are nearly linear. In contrast, postbuckling responses were unquestionably nonlinear, and therefore geometrically nonlinear analyses were required to predict the postbuckling behavior to within 8% over the entire range of loading as indicated above.

It was difficult to correlate the axial-shear coupling response of the tests, since the tests exhibited mixed force and displacement coupling. A procedure was defined to compute an equivalent pure force coupling response from the measured test data. The equivalent pure force coupling response reflected the total axial-shear coupling response and was compared with the predicted pure force coupling response. This type of procedure may have to be applied in any study that compares numerical results from models with ideal boundary conditions to experimental results which display less than ideal boundary conditions.

7.1.2 Characterization of the Effect of Skewed Stiffeners and Anisotropic Skins

The following conclusions can be made for the configuration and loading that were studied in this investigation. The conclusions are based on the measured and predicted responses for the panels that were tested and the panels that were considered for the parametric study. When referring to the panels that were tested, 'nonlinear-predicted' refers to numerical results that were computed from nonlinear analyses using the advanced finite element model, and 'linear-predicted' refers to results from linear bifurcation buckling analyses using a simplified model that ignored measured shape imperfections, nonuniform initial loading, and non-zero v displacement.

Buckling Response

Rotating the stiffener reduces the buckling load, partially because of the reduction in the

load carried in the stiffener, but mostly due to the related increase in the distance from the stiffener to the knife-edge support in two quadrants of the panel. In the all-aluminum panels with the nominal stiffener, rotating the stiffener by 10° and 20° caused reductions in the buckling load of 7% and 21%, respectively, relative to the panel with the unrotated stiffener. For the composite panels that were tested, rotating the stiffener 20° caused the measured, nonlinear-predicted, and linear-predicted buckling loads to reduce by 17%, 25%, and 26%, respectively.

For panels with an unrotated stiffener, skin anisotropy reduces the buckling load relative to panels with minimal skin anisotropy. For the panels with an unrotated stiffener that were tested, rotating the skin 20° caused the measured, nonlinear-predicted, and linear-predicted buckling loads to decrease by 3%, 10%, and 10%, respectively. In the parametric study (panels B0c, B0d, B0e, and B0f), the reductions in buckling load due to skin membrane stiffness coupling, bending stiffness coupling, and combined membrane and bending stiffness coupling, were 9%, 14%, and 19%, respectively, relative to the panel with minimal anisotropy.

When the stiffener is rotated 20°, skin anisotropy typically reduces the buckling load relative to panels that have the stiffener rotated 20° and skins with minimal anisotropy. For the panels with a rotated stiffener that were tested, rotating the skin 20° caused the measured, nonlinear-predicted, and linear-predicted buckling loads to decrease by 8%, 7%, and 3%, respectively. Rotating the skin -20° caused the measured, nonlinear-predicted, and linear-predicted buckling loads to decrease by 7%, 9%, and 9%, respectively. Panels in the parametric study with the stiffener rotated 20° and anisotropic skins (panels B2d, B2dr, B2e, and B2er) demonstrated that negative membrane stiffness coupling increased the buckling load by 12%, while positive membrane stiffness coupling decreased the buckling load by 18%, relative to a panel with minimum skin anisotropy (panel B2c). Negative and positive bending stiffness coupling caused reductions in the buckling load by 24% and 4%, respectively.

Postbuckling Response and Failure

The values of the geometric and material parameters of the skins and stiffeners that were considered in this investigation are representative of a lightly loaded stiffened panel with postbuckling strength. All of the panels buckled at strains that were a small fraction of the ultimate strain for the material. During loading each panel initially remained flat, and then

deformed smoothly from the flat prebuckled state to a stable postbuckling equilibrium state. The postbuckling response of the panels was characterized by reductions in the axial stiffness and substantial out-of-plane deformations in the skin.

When a panel's skin buckles, there is an immediate reduction in the panel's axial stiffness. For the panels that were tested, the initial postbuckling axial stiffness of each panel was 57% to 68% of the prebuckling axial stiffness for the same panel. As the loading increases, the axial stiffness continues to reduce slowly. For all of the configurations considered in this study, when $u = 4\ u_{cr}$ the panel's axial stiffness was approximately 50% of its prebuckling axial stiffness.

When the skin buckles, small increases in the axial load cause large increases in the out-of-plane deformations in the skin. The skin panel deforms into a shape with multiple half waves, and the development of the postbuckling deformation with increasing load is highly nonlinear. For the panels that were tested, the observed out-of-plane deformations in the skin were as large as 3 to 4 times the skin thickness. Based on the results presented in this study, the following conclusions may be drawn regarding the effects of stiffener rotation, stiffener rigidity, and skin anisotropy on the postbuckling deformation:

- Panels with unrotated stiffeners and skins with minimal anisotropy have postbuckling deformations that are essentially antisymmetric with respect to the panel centerline.
- The postbuckling deformation was largest in the skin. The open-section stiffeners participated in the buckling deformation by way of the attachment flanges bending and twisting, but the overall out-of-plane displacements of the stiffeners were negligible. The more-rigid stiffener displayed less cross-section deformation and caused the skin to buckle into a higher number of half waves.
- Rotating the stiffener causes the skin deformations to be skewed, particularly in the skin locations that are immediately adjacent to the rotated stiffener, and the out-of-plane displacements are not inversely symmetric with respect to the panel centerline or the stiffener centerline. For the all-aluminum panels with the nominal stiffener, rotating the stiffener 10° did not change the deformations by very much relative to the unrotated stiffener case, but rotating the stiffener 20° caused the deformations to change substantially. If the stiffener is rotated, the skin sections are tapered in width. The tapered width may cause the skin to buckle into a shape with fewer half waves,

and the out-of-plane deformations are larger and develop first in the quadrants of the panel where the unsupported width of the skin is larger. Poisson expansion of the skin causes transverse displacements in the skin which create prebuckling out-of-plane deformations when the stiffener is rotated.

- For panels with unrotated stiffeners and anisotropic skins, membrane stiffness coupling can create shear loads which cause slight skewing of the postbuckled out-of-plane deformation. Bending stiffness coupling can create substantial skewing in the postbuckling deformation. The direction of skewing in the skin deformation is reversed if the signs of the stiffness coupling terms are changed.
- For panels with rotated stiffeners and anisotropic skins, bending stiffness coupling in the skin can be used to create skewness in the postbuckling deformation that is either in the same direction, or the opposite direction, as the skewing caused by the rotated stiffener.

The shape of the postbuckling deformation is significant since it may influence the strength of the panel. In this study, as in nearly all experimental studies of postbuckled composite stiffened panels, the panels exhibited substantial postbuckling strength and failed due to skin-stiffener separation. The experimental failure loads reported in the current investigation indicated that rotating the stiffener 20° caused an average of 33% reduction in panel strength. Rather than attempt to predict the complex three dimensional stress state in the skin-stiffener interface, the current study examined results from analyses based on plate elements to assess the effect of structural tailoring on the tendency for skin-stiffener separation in the panels that were tested. The skin-stiffener attachment forces and moments were reported and related to the local deformations of the skin. The results indicated that even though the ultimate loads for the test panels with an unrotated stiffener and a rotated stiffener were quite different, the predicted skin-stiffener forces and moments were comparable. It is concluded that the shape of the postbuckling deformation significantly influences the stress state in the skin, deformations of the stiffener, and the stress state in the skin-stiffener attachment interface.

Axial-Shear Coupling Response

The most enlightening aspect of the current study was the unique axial-shear coupling responses that were obtained by rotating the stiffener and/or introducing anisotropy in the skin.

The experimental results provided the first evidence of unique structural behavior. The experimentally-measured axial-shear coupling responses consisted of a mixture of force and displacement coupling that made the responses difficult to interpret. To assess the total axial-shear coupling response, a method for combining the mixed response into a single equivalent force coupling response was suggested and validated. The equivalent and predicted pure force coupling responses for the panels that were tested supported the following initial conclusions:

- The configuration with a unrotated stiffener and an unrotated skin has very little force coupling.
- Rotating the stiffener only creates force coupling that increases after the skin buckles.
- Rotating the skin only creates force coupling that decreases after the skin buckles.
- The two effects may be superimposed by rotating the stiffener and the skin. If the stiffener and skin are rotated in the same direction, the net force coupling response is larger. If the stiffener and skin are rotated in opposite directions, the effects partially cancel and the net force coupling response is smaller.

A parametric study was conducted to isolate and examine the mechanisms which contribute to a panel's pure force coupling response. Based on the results of the parametric study, the following conclusions are drawn:

- Rotating the stiffener 10° creates a force coupling response that is constant in prebuckling and increases in magnitude after skin buckling.
- Rotating the stiffener 20° creates a force coupling response that has the same behavior and the magnitude of the response is larger.
- Increasing the rigidity of a rotated stiffener increases the magnitude of the force coupling response.
- Membrane stiffness coupling in the skin creates a force coupling response that is constant in prebuckling and decreases in magnitude after skin buckling. The force coupling in prebuckling correlates well with the value of $\eta^{o}_{xy,\,x}$ for the laminate.
- Bending stiffness coupling in the skin creates a force coupling response that is zero in prebuckling and increases in magnitude after skin buckling. The increase after skin buckling correlates well with the laminate's anisotropic parameters, γ and δ.

- The nonlinear increase in the magnitude of the force coupling response that occurs after skin buckling when the stiffener is rotated or the skin has bending stiffness coupling is attributed to skewing of the skin's postbuckling deformation.
- When more than one mechanism is applied, the contributions from each mechanism are superimposed.
- The force coupling responses of each mechanism are sign dependent. Changing the sign of the stiffener rotation, the skin's membrane stiffness coupling, or skin's bending stiffness coupling changes the sign of the force coupling contribution.

Since the stiffener rotation and rigidity, and skin membrane and bending stiffnesses can be tailored independently, panels may be designed to exhibit very unique axial-shear coupling responses. By applying rotated stiffeners and anisotropic skins, stiffened panels may be designed which have axial-shear coupling responses which are positive, or negative, and either increase, decrease, or remain constant after skin buckling. Two panels were shown in the study that demonstrated a force coupling response that was nearly constant throughout the entire load range. One panel combined a positive stiffener rotation and negative membrane stiffness coupling, while the second had an unrotated stiffener and a skin with negative membrane and negative bending stiffness coupling. Another example combined a positive stiffener rotation and a skin with positive membrane stiffness coupling to give a response that was negative in prebuckling and became positive in the postbuckling load range.

7.2 Recommendations for Further Research

The present study was the first experimental and numerical study to consider structural tailoring of composite stiffened panels by utilizing both skewed stiffeners and anisotropic skins, and the first to examine the axial-shear coupling response of panels in the postbuckling load range. There are a number of issues which are felt to be important but were not considered in the present study. Some suggestions for further research are:

1. The seemingly endless number of combinations of skin and stiffener parameters that may be applied to tailor the structural response suggests implementation of an optimization scheme. The behavior observed in the current study seems to be well behaved and should lend itself to optimization studies.

2. The laminates considered in the current study were symmetric and exhibited a constant axial-shear coupling response in the prebuckling load range. The current study could be extended to consider unsymmetric laminates where coupling between inplane extension and transverse bending would cause out-of-plane deformations and a nonconstant axial-shear coupling response in the prebuckling load range.
3. The current study concentrated on the effect of several tailoring mechanisms on the panel's global structural response. The subject of how different mechanisms affect the local load distribution and interaction of the structural components should be considered.
4. The issue of failure of stiffened panels by skin-stiffener separation is one local response that will require indepth analyses. Simplified analyses bases on plate elements may provide insight into the local deformations and net forces between structural components, but more sophisticated models are required to predict failure. A global-local modeling technique may prove to be useful for this purpose.
5. The axial-shear coupling response may be sensitive to the inplane boundary conditions. The current study considered cases which had no inplane load on the left and right edges of the panel. Cases with biaxial loads or shear loads on all four edges should be considered. Tailored axial-shear coupling responses may be particularly interesting in cases with mixed loading, especially if the ratio of the loads varies with increasing load level.
6. The present work should be extended to examine the postbuckling response of multi-bay panels and built-up structures with skewed stiffeners and anisotropic skins. A few suggested configurations for multi-bay panels are shown in Fig. 7-1. The panel shown

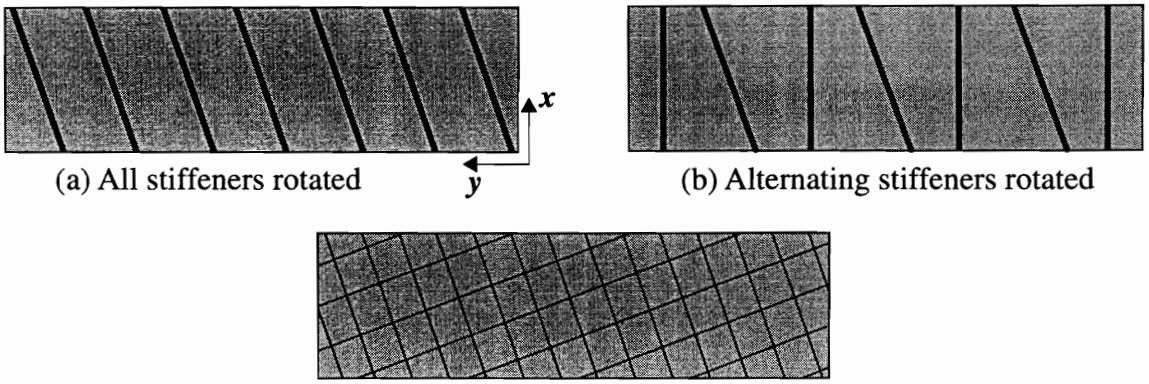

(a) All stiffeners rotated

(b) Alternating stiffeners rotated

(c) Rotated orthogrid

Fig. 7-1 Suggested multi-bay panels

in Fig. 7-1(a) has all the stiffeners rotated and the skin sections do not get wider when the stiffeners are rotated. Thus, the reduction in the buckling load associated with stiffener rotation that was observed in this study should not be as severe for this case.

7. Having demonstrated the use of innovative design concepts to obtain unique structural behavior, the challenging task of identifying applications which can benefit from the tailored response should be pursued.

References

1. Jones, R. M., Mechanics of Composite Materials, McGraw-Hill, New York, 1975.
2. Chia, C. Y., Nonlinear Analysis of Plates, McGraw-Hill, New York, 1980.
3. Sensmeier, M. D., Griffin, O. H., Jr., and Johnson, E. R., "Static and Dynamic Large Deflection Response of Graphite-Epoxy Beams," NASA CR-4118, 1988.
4. Anonymous, Product Data for Hercules Carbon Prepreg Tape AS4-3502, Number 855-2, Hercules Inc., Wilmington, DE 19894.

Structural Tailoring

5. Shirk, M. H., Hertz, T. J., and Weisshaar, T. A., "Aeroelastic Tailoring - Theory, Practice, and Promise," *Journal of Aircraft*, Vol. 23, No. 1, January 1986, pp. 6-18.
6. Diederick, F. W., and Budiansky, B., "Divergence of Swept Wings," NACA Technical Note 1680, 1948.
7. Mansfield, E. H., "Elasticity of a Sheet Reinforced by Stringers and Skew Ribs, with Applications to Swept Wings," R. & M. No. 2758, December 1949. (R.A.E. Report Structures 52).
8. Mansfield, E. H., "Some Structural Parameters for Aero-Isoclinic Wing," *Aircraft Engineering*, Vol. 24, No. 283, September 1952, pp. 263-264.
9. Soong, T. C., "Thermoelastic effect on Vibration and Flutter of Built-Up Delta-Wings with Arbitrarily Oriented Structural Components," AIAA Paper No. 72-174, January 1972.
10. Cooper, P. A., and Stroud, W. J., "Selective Reinforcement of Wing Structure for Flutter Prevention," *Journal of Aircraft*, Vol. 9, No. 11, November 1972, pp. 797-799.

11. Housner, J.M., and Stein, M., "Flutter Analysis of Swept-Wing Subsonic Aircraft with Parameter Studies of Composite Wings," NASA TN-D7539, September 1974.

12. Price, M. A., "HiMAT Structural Development Design Methodology," NASA CR-144886, October 1979.

13. Gratke, S. D., and Williams, J. G., "Analysis/Theory of Controlled Configured Structures (CCS)," AIAA Paper No. 77-1212, August 1977.

14. Gimmestad, D., "An Aeroelastic Optimization Procedure for Composite High Aspect Ratio Wings," AIAA Paper No. 79-0726, April 1979.

15. Krone, N. J., Jr., "Divergence Elimination with Advanced Composites," AIAA Paper No. 75-1009, August 1975.

16. Weisshaar, T. A., "Divergence of Forward Swept Composite Wings," *Journal of Aircraft*, Vol. 17, No. 6, June 1980, pp. 442-448.

17. Sherrer, V. C., Hertz, T. J., and Shirk, M. H., "Wind Tunnel Demonstration of Aeroelastic Tailoring Applied to Forward Swept Wings," *Journal of Aircraft*, Vol. 18, No. 11, November 1981, pp. 976-983.

18. Oyibo, G. A., "Generic Approach to Determine Optimum Aeroelastic Characteristics for Composite Forward-Swept-Wing Aircraft," *AIAA Journal*, Vol. 21, No. 1, January 1984, pp. 117-123.

Arbitrarily Orientated Stiffeners

19. Shastry, B. P., and Roa, G. V., "Vibrations of Thin Rectangular Plates with Arbitrarily Oriented Stiffeners," *Computers and Structures*, Vol. 7, 1977, pp.627-629.

20. Al-Shareedah, E. M., and Seireg, A. A., "Use of Undetermined Multipliers in the Design of Stiffened Plates," *Computers in Mechanical Engineering*, Vol. 4, No. 5, March 1986, pp. 57-64.

21. Phillips, J. L., and Gürdal, Z., "Structural Analysis and Optimum Design of Geodesically Stiffened Composite Panels," NASA CR-186944, 1990.

22. Won, C. J., "Stiffened Plates with Arbitrarily Oblique Stiffeners," *International Journal of Solids and Structures*, Vol. 26, No.7, July 1990, pp.779-799.

Buckling and Postbuckling: General Reviews, Handbooks

23. Becker, H., "Handbook of Structural Stability: Part II - Buckling of Composite Elements," NACA TN 3782, July 1957.

24. Kedward, K. T., Spier, E. E., and Arnold, R. R., "Stability Critical Compression Members," Handbook of Composites, Vol. 2 - Structure and Design, North-Holland, Amsterdam, 1989, pp. 583-622.

25. Arnold, R. R., and Kedward, K. T., "Stability Critical Stiffened Panels," Handbook of Composites, Vol. 2 - Structure and Design, North-Holland, Amsterdam, 1989, pp. 623-665.

26. Leissa, A. W., "Buckling of Laminated Composite Plates and Shell Panels," AFWAL-TR-85-3069, Air Force Wright Aeronautical Laboratories, June 1985.

27. Nemeth, M. P., "Importance of Anisotropy on Buckling of Compression-Loaded Symmetric Composite Plates," AIAA Journal, Vol. 24, No. 11, November 1986, pp. 1831-1835.

Postbuckling of Unstiffened Panels

28. Marguerre, K., "The Apparent Width of the Plate in Compression," NACA TM 833, 1937.

29. Levy, S., Goldenberg, D., and Zibritosky, G., "Simply Supported Long Rectangular Plate under Combined Axial Load and Normal Pressure," NACA TN 949, 1944.

30. Stein, M., "The Phenomenon of Change in Buckle Pattern in Elastic Structures," NASA TR R-39, 1959.

31. Stein, M., "Loads and Deformations of Buckled Rectangular Plates," NASA TR R-40, 1959.

32. Sharmon, P. W., and Humpherson, J., "An Experimental and Theoretical Investigation of Simply-Supported Thin Plates Subjected to Lateral Load and Uniaxial Compression," *The Aeronautical Journal of the Royal Aeronautical Society*, Vol. 72, May 1968, pp. 431-436.

33. Prabhakara, M. K., and Chia, C. Y., "Postbuckling of Angle-Ply and Anisotropic Plates," *Ingenieur-Archiv*, Bd. 45, H. 2, 1976, pp. 131-140.

34. Chan, D. P., "An Analytical Study of the Post Buckling of Laminated, Anisotropic Plates," *Fibre Science and Technology*, Vol. 11, 1978, pp. 165-187.

35. Feng, M., "An Energy Theory for Postbuckling of Composite Plates under Combined Loading," *Composites and Structures*, Vol. 16, No. 1-4, 1983, pp. 423-431.

36. Stein, M., "Postbuckling of Long Orthotropic Plates in Combined Shear and Compression," AIAA Paper No. 83-0876, May 1983.

37. Stein, M., "Postbuckling of Orthotropic Composite Plates Loaded in Compression," *AIAA Journal*, Vol. 21, No. 12, December 1983, pp. 1729-1735.

38. Zhang, Y., and Mathews, F. L., "Postbuckling Behavior of Anisotropic Laminated Plates Under Pure Shear and Shear Combined with Compressive Loading," *AIAA Journal*, Vol. 22, No. 2, February 1984, pp. 281-287.

39. Chia, C. Y., "Postbuckling of Composite Plates under Inplane Compressive and Shear Loading Having Edges Elastically Restrained against Rotation," *Composite Structures*, Vol. 3, 1985, pp. 278-289.

40. Rouse, M., "Postbuckling and Failure Characteristics of Selected Flat Rectangular Graphite-Epoxy Plates Loaded in Compression," AIAA Paper No. 85-0771, April 1985.

41. Jensen, D. W., and Lagace, P. A., "Influence of Mechanical Couplings On the Buckling and Postbuckling Behavior of Anisotropic Plates," AIAA Paper No. 86-0880, May 1986.

42. Jeffrey, G. L., "Postbuckling of Laminated Anisotropic Panels," NASA TM 100509, October 1987.

Postbuckling of Stiffened Panels

43. Dickson, J. N., Cole, R. T., and Wang, J. T. S., "Design of Stiffened Composite Panels in the Post-Buckling Range," Fibrous Composites in Structural Design, Plenum Press, New York, 1980, pp. 313-327.

44. Dickson, J. N., Biggers, S. B., and Starnes, J. H., Jr., "Stiffener Attachment Concepts for Graphite-Epoxy Panels Designed for Postbuckling Strength," AFWAL-TR-85-3094, June 1985, pp. v(a)95-v(a)109.

45. Wang, J. T.-S., and Biggers, S. B., "Skin/Stiffener Interface Stresses in Composite Stiffened Panels," NASA CR 172261, 1984.

46. Starnes, J. H., Jr., Knight, N. F., Jr., and Rouse, M., "Postbuckling Behavior of Selected Flat Stiffened Graphite-Epoxy Panels Loaded in Compression," *AIAA Journal*, Vol. 23, No. 8, August 1985, pp. 1236-1246.

47. Rouse, M., "Postbuckling and Failure Characteristics of Stiffened Graphite-Epoxy Shear Webs," AIAA Paper No. 87-0733-CP, April 1987.

48. Stein, M., "Postbuckling of Eccentric Open-section Stiffened Composite Panels," AIAA Paper No. 88-2215, April 1988.

49. Sheinman, I., and Frostig, Y., "Post-Buckling Analysis of Stiffened Laminated Panel," *Journal of Applied Mechanics*, Vol. 55, pp. 635-640.

STAGS finite element analysis code

50. Brogan, F. A., Rankin, C. C., and Cabiness, H. D., "STAGS Users Manual," Lockheed Palo Alto Research Laboratory, Report LMSC P032594, 1994.

51. Rankin, C. C., and Brogan, F. A., "Improved Plasticity and Imperfections in the STAGSC-1 Computer Code, Phase 2: Implementation," Lockheed Palo Alto Research Laboratory, Palo Alto, CA, LMSC-F386402, July, 1990.

52. Rankin, C. C., and Brogan, F. A., "The Computational Structural Mechanics Testbed Structural Element Processor ES5: STAGS Shell Element," NASA CR-4358, 1991.

PASCO analysis code

53. Anderson, M. S., and Stroud, W. J., "A General Panel Sizing Computer Code and Its Application to Composite Structural Panels," *AIAA Journal*, Vol. 17, No. 8, 1979, pp. 892-897.

Skin-Stiffener Interface Stresses

54. Goland, M., ans Reissner, E., "The Stresses in Cemented Joints," *Journal of Applied Mechanics*, March 1944, pp. A17-A26.

55. Wang, J. T.-S. and Biggers, S. B., "Skin/Stiffener Interface Stresses in Composite Stiffened Panels," NASA CR-172261, January 1984.

56. Arnold, R. R., "Disbond Criterion for Postbuckled Composite Panels," AIAA Paper No. 87-0732, 1987.

57. Hyer, M. W., and Cohen, D., "Calculation of Stresses in Stiffener Composite Panels," *AIAA Journal*, Vol. 26, No. 7, July 1988, pp. 852-858.

58. Hyer, M. W., Loup, D. C., and Starnes, J. H., Jr., "Stiffener/Skin Interactions in Pressure-Loaded Composite Panels," *AIAA Journal*, Vol. 28, No. 3, March 1990, pp. 532-537.

59. Cohen, D., and Hyer, M. W., "Influence of Geometric Nonlinearities on Skin-Stiffener Interface Stresses," *AIAA Journal*, Vol. 30, No. 4, April 1992, pp. 1055-1062.

60. Kassapoglou, C., and DiNicola, A. J., "Efficient Stress Solutions at Skin Stiffener Interfaces of Composite Stiffened Panels," AIAA Paper No. 91-1199-CP, 1991.

61. Hachenberg, D., and Kossira, H., "Stringer Peeling Effects at Stiffened Composite Panels in the Postbuckling Range," *Journal of Aircraft*, Vol. 30, No. 5, Sept.-Oct. 1993, pp. 769-776.

General

62. Lagace, P. A., Private Communication.

63. Young, R. D., Starnes, J. H., Jr. and Hyer, M. W., "Effects of Skewed Stiffeners and Anisotropic Skins on the Response of Compression-Loaded Composite Panels," Proceedings of the Tenth DoD/NASA/FAA Conference of Fibrous Composites in Structural Design, Hilton Head Island, SC, Nov. 1-4, 1993, Naval Air Warfare Center Report No. NAWACADWAR-94096060, Vol. 1, April 1994, pp. II-109 to II-123.

64. Noor, A. K., Starnes, J. H., Jr. and Peters, J. M., "Thermomechanical Buckling and Postbuckling Responses of Composite Panels with Skewed Stiffeners," AIAA Paper No. 96-1636-CP, April, 1996.

65. Sciammarella, C. A., "The Moiré Method - A Review," *Experimental Mechanics*, November 1982, pp. 418-433.

66. Tsai, S. W., Theory of Composites Design, Think Composites, Dayton OH, 1992, pp. 7.1-7.8.

Appendix A: Mechanics of Composite Plates

The term composite, as used in the context of materials for structural applications, generally describes a matrix material reinforced with continuous filaments. The terminology and nomenclature used in the field of composites varies from one reference to another. The current work contains equations taken primarily from the two textbooks, Mechanics of Composite Materials by R. M. Jones (Ref. A1), and Nonlinear Analysis of Plates by C. Y. Chia (Ref. A2).

A.1 Single-Layered Configurations

A lamina is a single layer of unidirectional or woven fibers impregnated by a matrix material. The fibers are typically strong and stiff, and are the primary load-carrying component. The matrix material may be organic, ceramic, or metallic, and functions primarily to support the fibers and provide a media for introducing load into the fibers and transferring load between fibers. A sketch of a lamina with unidirectional fibers is shown in Fig. A-1. The material principal directions are shown with the 1-axis along the fiber direction, the 2-axis perpendicular to the fibers and in the plane of the lamina, and the 3-axis perpen-

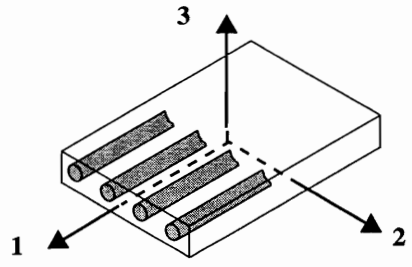

Fig. A-1 Lamina with unidirectional fibers; 1-2-3 material principal directions

dicular to the plane of the lamina. This lamina has material property symmetry in the 1-3 plane and the 1-2 plane. For structural level analyses the properties of the fibers and matrix material are smeared to define a homogeneous material with equivalent orthotropic material properties. Material behavior is assumed to be linear elastic. Typical material properties for a lamina made of unidirectional Hercules, Inc. AS4 fibers and Hercules, Inc. 3502 epoxy matrix material are given in Table A-1,

Table A-1 Typical Material Properties: Hercules AS4-3502 Graphite-Epoxy (Ref. A3)

E_1	19.40 Msi
E_2	1.48 Msi
G_{12}	0.82 Msi
ν_{12}	0.300
V_f	0.62 (Ref. A4)
t_{ply}	0.00550 in.

where

$$
\begin{aligned}
E_i &= \text{Young's moduli in the } i\text{-direction} \\
G_{ij} &= \text{shear moduli in the } i\text{-}j \text{ plane} \\
\nu_{ij} &= \text{Poisson's ratio for transverse strain in the} \\
&\quad\ j\text{-direction when stressed in the } i\text{-direction} \\
V_f &= \text{fiber volume fraction} \\
t_{ply} &= \text{nominal ply thickness}
\end{aligned}
\tag{A.1}
$$

For the lamina shown in Fig. A-1, a plane stress state is defined when the stress components σ_3, τ_{23}, and τ_{31} are zero. The stress-strain relations in principal material coordinates for an orthotropic lamina under plane stress, subjected to forces in the 1-2 plane, are

$$
\begin{Bmatrix} \sigma_1 \\ \sigma_2 \\ \tau_{12} \end{Bmatrix} = \begin{bmatrix} Q_{11} & Q_{12} & 0 \\ Q_{12} & Q_{22} & 0 \\ 0 & 0 & Q_{66} \end{bmatrix} \begin{Bmatrix} \varepsilon_1 \\ \varepsilon_2 \\ \gamma_{12} \end{Bmatrix} \quad , \tag{A.2}
$$

where the reduced stiffnesses, Q_{ij}, are defined in terms of engineering constants as

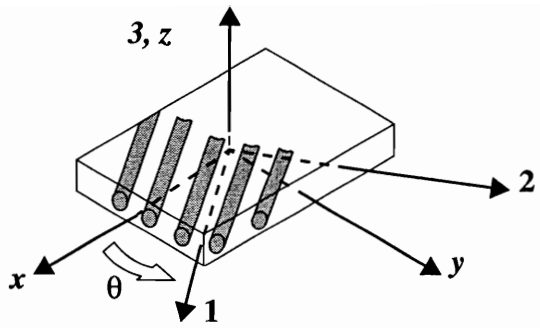

Fig. A-2 Lamina with unidirectional fibers rotated θ from *x-y-z* geometric coordinate axes

$$
\begin{aligned}
Q_{11} &= \frac{E_1}{1-\nu_{12}\nu_{21}} \\
Q_{12} &= \frac{\nu_{21}E_1}{1-\nu_{12}\nu_{21}} \\
Q_{22} &= \frac{E_2}{1-\nu_{12}\nu_{21}} \\
Q_{66} &= G_{12}
\end{aligned}
\quad , \tag{A.3}
$$

and ν_{21} is defined by the reciprocal relation

$$
\frac{\nu_{21}}{E_2} = \frac{\nu_{12}}{E_1} \quad . \tag{A.4}
$$

If the lamina fiber orientation is rotated by an angle θ as indicated in Fig. A-2, then the stress-strain relations in the *x-y* coordinate system are

$$
\begin{Bmatrix} \sigma_x \\ \sigma_y \\ \tau_{xy} \end{Bmatrix} = \begin{bmatrix} \overline{Q}_{11} & \overline{Q}_{12} & \overline{Q}_{16} \\ \overline{Q}_{12} & \overline{Q}_{22} & \overline{Q}_{26} \\ \overline{Q}_{16} & \overline{Q}_{26} & \overline{Q}_{66} \end{bmatrix} \begin{Bmatrix} \varepsilon_x \\ \varepsilon_y \\ \gamma_{xy} \end{Bmatrix} \quad , \tag{A.5}
$$

in which the transformed reduced stiffnesses, $\overline{Q}_{ij}$, are

$$
\begin{aligned}
\bar{Q}_{11} &= Q_{11}\cos^4\theta + 2(Q_{12}+2Q_{66})\sin^2\theta\cos^2\theta + Q_{22}\sin^4\theta \\
\bar{Q}_{12} &= (Q_{11}+Q_{22}-4Q_{66})\sin^2\theta\cos^2\theta + Q_{12}(\sin^4\theta+\cos^4\theta) \\
\bar{Q}_{22} &= Q_{11}\sin^4\theta + 2(Q_{12}+2Q_{66})\sin^2\theta\cos^2\theta + Q_{22}\cos^4\theta \\
\bar{Q}_{16} &= (Q_{11}-Q_{12}-2Q_{66})\sin\theta\cos^3\theta + (Q_{12}-Q_{22}+2Q_{66})\sin^3\theta\cos\theta \\
\bar{Q}_{26} &= (Q_{11}-Q_{12}-2Q_{66})\sin^3\theta\cos\theta + (Q_{12}-Q_{22}+2Q_{66})\sin\theta\cos^3\theta \\
\bar{Q}_{66} &= (Q_{11}+Q_{22}-2Q_{12}-2Q_{66})\sin^2\theta\cos^2\theta + Q_{66}(\sin^4\theta+\cos^4\theta)
\end{aligned}
\qquad \text{(A.6)}
$$

A.2 Multiple-Layered Configurations

A laminate is defined as two or more laminae bonded together to act as one structural element. The orientation of each lamina, θ, is defined with respect to the x-y geometric coordinate axes. An expanded view of the upper half of an eight layer $[\pm 45/0/90]_s$ laminate is shown in Fig. A-3. Each lamina in the laminate is assumed to be in a state of plane stress, and the stress-strain relations of the k^{th} lamina can be expressed as

$$
\begin{Bmatrix} \sigma_x \\ \sigma_y \\ \tau_{xy} \end{Bmatrix}_k = \begin{bmatrix} \bar{Q}_{11} & \bar{Q}_{12} & \bar{Q}_{16} \\ \bar{Q}_{12} & \bar{Q}_{22} & \bar{Q}_{26} \\ \bar{Q}_{16} & \bar{Q}_{26} & \bar{Q}_{66} \end{bmatrix}_k \begin{Bmatrix} \varepsilon_x \\ \varepsilon_y \\ \gamma_{xy} \end{Bmatrix}_k . \qquad \text{(A.7)}
$$

The stiffness of a laminate is derived from the properties of the constituent laminae by applying classical lamination theory. Classical lamination theory, commonly referred to as CLT, is based on a number of hypotheses regarding stresses and deformations. These hypotheses are:

- Each lamina is in a state of plane stress.
- A laminate is assumed to consist of perfectly bonded laminae. Therefore, displacements are continuous across lamina boundaries.

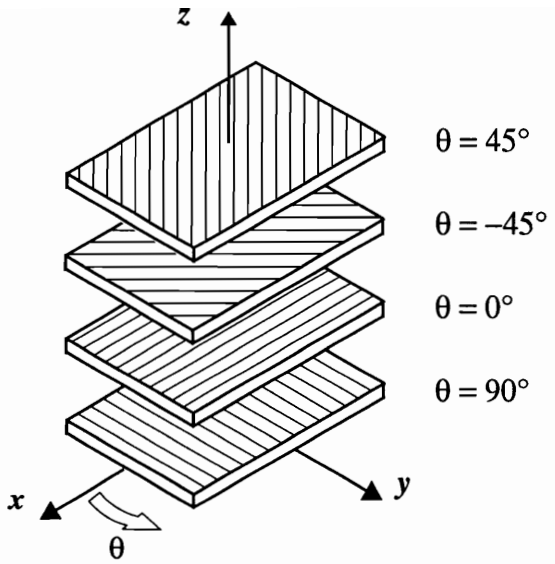

Fig. A-3 Expanded view of top half of $[\pm 45/0/90]_s$ laminate

- The Kirchhoff hypothesis is assumed to be valid. That is, for a thin plate, a line originally straight and normal to the reference surface of the plate remains straight and normal when the plate is subjected to extension and bending. Thus, the transverse shear strains γ_{xz} and γ_{yz} are equal to zero. Also, the length of the normal is presumed to be constant ($\varepsilon_z = 0$).

The implications of the Kirchhoff hypothesis on the laminate displacements u, v, and w in the x-, y-, and z-coordinate directions are demonstrated by the laminate cross section in the x-z plane shown in Fig. A-4. In the deformed cross section, the displacements in the x- and z-directions of a point on the reference surface are u_o and w_o, respectively. Point C lies on a line that in the undeformed cross section is straight and normal to the reference surface. Application of the Kirchhoff hypothesis specifies that in the deformed cross section:

- The line through point C remains straight. Thus, if this line rotates by an angle ω_y about the y-axis, then

$$u_C = u_o + z_C \omega_y \quad . \tag{A.8}$$

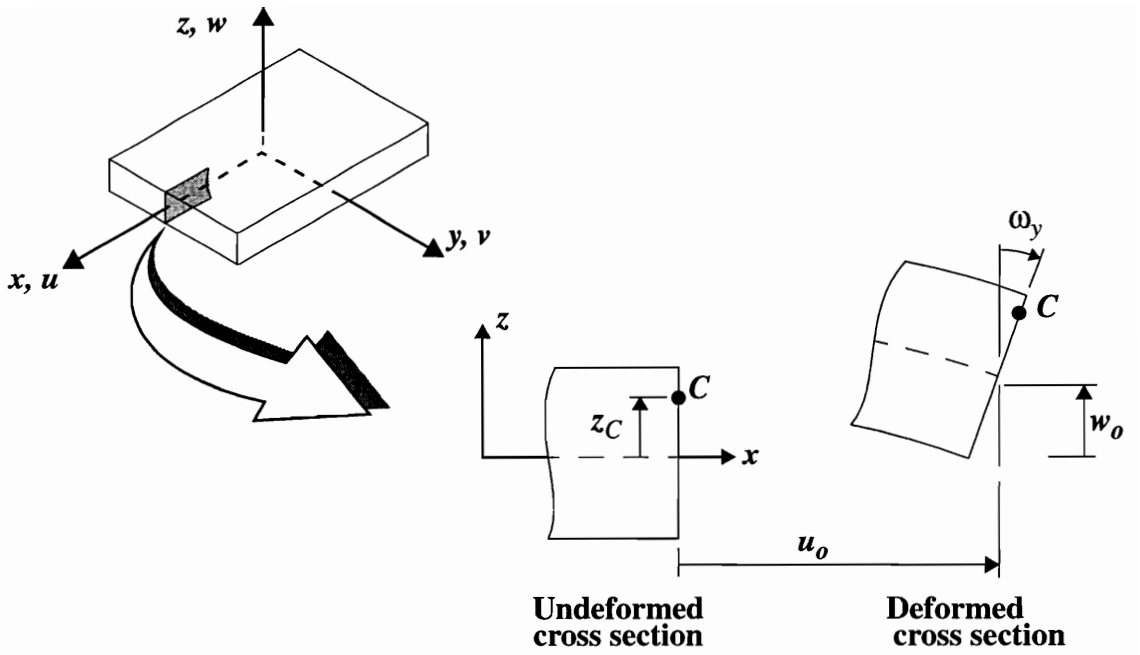

Fig. A-4 Kirchhoff hypothesis for deformation in the *x*-*z* plane

- The line through point C remains normal to the reference surface. Thus, in the deformed cross section, ω_y is the rotation of the reference surface about the *y*-axis, that is,

$$\omega_y = tan^{-1}\left(-\frac{\partial w_o}{\partial x}\right) \cong -\frac{\partial w_o}{\partial x} \quad , \tag{A.9}$$

where it is assumed that the rotation is moderate, i.e., $\omega_y < 20°$. Therefore, by Kirchhoff's hypothesis the displacement in the *x*-direction, *u*, at any point through the thickness of the laminate is

$$u(x, y, z) = u_o(x, y) - z\frac{\partial w_o}{\partial x} \quad . \tag{A.10}$$

Following the same procedure for a laminate cross section in the *y*-*z* plane, the displacement in the *y*-direction, *v*, at any point through the thickness of the laminate can be derived as

$$v(x, y, z) = v_o(x, y) - z\frac{\partial w_o}{\partial y} \quad . \tag{A.11}$$

Since the Kirchhoff hypothesis also assumes that the length of the normal is a constant, for moderate rotations, the displacement in the z-direction is uniform through the thickness of the laminate, i. e.,

$$w(x, y, z) = w_o(x, y) \quad . \tag{A.12}$$

A.3 Nonlinear Strain-Displacement Relations

For finite deformations of an elastic body, the strain-displacement relations in a Lagrangian description are, using idicial notation,

$$\varepsilon_{ij} = \frac{1}{2}\left(\frac{\partial u_i}{\partial x_j} + \frac{\partial u_j}{\partial x_i} + \frac{\partial u_k}{\partial x_i}\frac{\partial u_k}{\partial x_j}\right) \quad . \tag{A.13}$$

The ε_{ij} are components of the so-called Green's strain tensor. The Lagrangian description indicates that the spatial coordinates x_1, x_2, and x_3 (i.e., x, y, and z) refer to the initial undeformed configuration. Green's strain tensor (A.13) can be written in the form (Ref. A2)

$$\begin{aligned}
\varepsilon_x &= e_x + \frac{1}{2}\left[e_x^2 + \left(\frac{1}{2}e_{yx} + \omega_z\right)^2 + \left(\frac{1}{2}e_{zx} - \omega_y\right)^2\right] \\
\varepsilon_y &= e_y + \frac{1}{2}\left[e_y^2 + \left(\frac{1}{2}e_{xy} - \omega_z\right)^2 + \left(\frac{1}{2}e_{yz} + \omega_x\right)^2\right] \\
\varepsilon_z &= e_z + \frac{1}{2}\left[e_z^2 + \left(\frac{1}{2}e_{xz} + \omega_y\right)^2 + \left(\frac{1}{2}e_{yz} - \omega_x\right)^2\right] \\
\varepsilon_{xy} &= e_{xy} + e_x\left(\frac{1}{2}e_{xy} - \omega_z\right) + e_y\left(\frac{1}{2}e_{yx} + \omega_z\right) + \left(\frac{1}{2}e_{zx} - \omega_y\right)\left(\frac{1}{2}e_{zy} + \omega_x\right) \\
\varepsilon_{yz} &= e_{yz} + e_y\left(\frac{1}{2}e_{yz} - \omega_x\right) + e_z\left(\frac{1}{2}e_{zy} + \omega_x\right) + \left(\frac{1}{2}e_{xy} - \omega_z\right)\left(\frac{1}{2}e_{xz} + \omega_y\right) \\
\varepsilon_{zx} &= e_{zx} + e_x\left(\frac{1}{2}e_{xz} + \omega_y\right) + e_z\left(\frac{1}{2}e_{zx} - \omega_y\right) + \left(\frac{1}{2}e_{yz} - \omega_x\right)\left(\frac{1}{2}e_{xy} + \omega_z\right)
\end{aligned} \quad , \tag{A.14}$$

where ε_{ij} are nonlinear strains, e_{ij} are linear strains, and ω_i are the rotations about the i-axis. The shear components of strain in engineering, represented by ε_{xy}, ε_{yz}, and ε_{zx}, are twice larger than the corresponding shear component of the strain tensor. The linear strains and rotations are defined by

$$
\begin{aligned}
e_x &= \frac{\partial u}{\partial x} \qquad e_y = \frac{\partial v}{\partial y} \qquad e_z = \frac{\partial w}{\partial z} \\
e_{yz} &= \frac{\partial w}{\partial y} + \frac{\partial v}{\partial z} \qquad e_{zx} = \frac{\partial u}{\partial z} + \frac{\partial w}{\partial x} \\
e_{xy} &= \frac{\partial u}{\partial y} + \frac{\partial v}{\partial x} \qquad \omega_x = \frac{1}{2}\left(\frac{\partial w}{\partial y} - \frac{\partial v}{\partial z}\right) \\
\omega_y &= \frac{1}{2}\left(\frac{\partial u}{\partial z} - \frac{\partial w}{\partial x}\right) \qquad \omega_z = \frac{1}{2}\left(\frac{\partial v}{\partial x} - \frac{\partial u}{\partial y}\right)
\end{aligned}
\qquad \text{(A.15)}
$$

where u, v, and w are the displacement components in the x-, y-, and z-directions, respectively. Introduction of Eqs. (A.10), (A.11), and (A.12) into Eqs. (A.15) yields

$$
\begin{aligned}
e_x &= \frac{\partial u_o}{\partial x} - z\frac{\partial^2 w}{\partial x^2} \qquad e_y = \frac{\partial v_o}{\partial y} - z\frac{\partial^2 w}{\partial y^2} \\
e_{xy} &= \frac{\partial u_o}{\partial y} + \frac{\partial v_o}{\partial x} - 2z\frac{\partial^2 w}{\partial x \partial y} \\
e_{xy} &= \frac{\partial u_o}{\partial y} + \frac{\partial v_o}{\partial x} - 2z\frac{\partial^2 w}{\partial x \partial y} \\
\omega_x &= \frac{\partial w}{\partial y} \qquad \omega_y = -\frac{\partial w}{\partial x} \qquad \omega_z = \frac{1}{2}\left(\frac{\partial v_o}{\partial x} - \frac{\partial u_o}{\partial y}\right) \\
e_z &= 0 \qquad e_{yz} = 0 \qquad e_{zx} = 0
\end{aligned}
\qquad \text{(A.16)}
$$

where the o subscript on w has been omitted for convenience. Substitution of Eqs. (A.16) into Eqs. (A.14) yields

$$
\begin{aligned}
\varepsilon_x &= \frac{\partial u_o}{\partial x} - z\frac{\partial^2 w}{\partial x^2} + \frac{1}{2}\left[\left(\frac{\partial u_o}{\partial x} - z\frac{\partial^2 w}{\partial x^2}\right)^2 + \left(\frac{\partial v_o}{\partial x} - z\frac{\partial^2 w}{\partial x \partial y}\right)^2 + \left(\frac{\partial w}{\partial x}\right)^2\right] \\
\varepsilon_y &= \frac{\partial v_o}{\partial y} - z\frac{\partial^2 w}{\partial y^2} + \frac{1}{2}\left[\left(\frac{\partial v_o}{\partial y} - z\frac{\partial^2 w}{\partial y^2}\right)^2 + \left(\frac{\partial u_o}{\partial y} - z\frac{\partial^2 w}{\partial x \partial y}\right)^2 + \left(\frac{\partial w}{\partial y}\right)^2\right] \\
\varepsilon_z &= \frac{1}{2}\left[\left(\frac{\partial w}{\partial x}\right)^2 + \left(\frac{\partial w}{\partial y}\right)^2\right] \\
\varepsilon_{xy} &= \frac{\partial u_o}{\partial y} + \frac{\partial v_o}{\partial x} - 2z\frac{\partial^2 w}{\partial x \partial y} + \left(\frac{\partial u_o}{\partial x} - z\frac{\partial^2 w}{\partial x^2}\right)\left(\frac{\partial u_o}{\partial y} - z\frac{\partial^2 w}{\partial x \partial y}\right) \\
&\quad + \left(\frac{\partial v_o}{\partial y} - z\frac{\partial^2 w}{\partial y^2}\right)\left(\frac{\partial v_o}{\partial x} - z\frac{\partial^2 w}{\partial x \partial y}\right) + \left(\frac{\partial w}{\partial x}\right)\left(\frac{\partial w}{\partial y}\right) \\
\varepsilon_{yz} &= \left(\frac{\partial v_o}{\partial y} - z\frac{\partial^2 w}{\partial y^2}\right)\left(-\frac{\partial w}{\partial y}\right) + \left(\frac{\partial u_o}{\partial y} - z\frac{\partial^2 w}{\partial x \partial y}\right)\left(-\frac{\partial w}{\partial x}\right) \\
\varepsilon_{zx} &= \left(\frac{\partial u_o}{\partial x} - z\frac{\partial^2 w}{\partial x^2}\right)\left(-\frac{\partial w}{\partial x}\right) + \left(-\frac{\partial w}{\partial y}\right)\left(\frac{\partial v_o}{\partial x} - z\frac{\partial^2 w}{\partial x \partial y}\right) \quad .
\end{aligned}
\tag{A.17}
$$

In cases when the thickness of a plate is much smaller than the other plate dimensions, the higher-order terms containing z may be eliminated and Eqs. (A.17) may be simplified to yield

$$
\begin{aligned}
\varepsilon_x &= \frac{\partial u_o}{\partial x} - z\frac{\partial^2 w}{\partial x^2} + \frac{1}{2}\left[\left(\frac{\partial u_o}{\partial x}\right)^2 + \left(\frac{\partial v_o}{\partial x}\right)^2 + \left(\frac{\partial w}{\partial x}\right)^2\right] \\
\varepsilon_y &= \frac{\partial v_o}{\partial y} - z\frac{\partial^2 w}{\partial y^2} + \frac{1}{2}\left[\left(\frac{\partial v_o}{\partial y}\right)^2 + \left(\frac{\partial u_o}{\partial y}\right)^2 + \left(\frac{\partial w}{\partial y}\right)^2\right] \\
\varepsilon_z &= \frac{1}{2}\left[\left(\frac{\partial w}{\partial x}\right)^2 + \left(\frac{\partial w}{\partial y}\right)^2\right] \\
\gamma_{xy} &= \varepsilon_{xy} = \frac{\partial u_o}{\partial y} + \frac{\partial v_o}{\partial x} - 2z\frac{\partial^2 w}{\partial x \partial y} + \left(\frac{\partial u_o}{\partial x}\right)\left(\frac{\partial u_o}{\partial y}\right) + \left(\frac{\partial v_o}{\partial y}\right)\left(\frac{\partial v_o}{\partial x}\right) + \left(\frac{\partial w}{\partial x}\right)\left(\frac{\partial w}{\partial y}\right) \\
\gamma_{yz} &= \varepsilon_{yz} = \left(\frac{\partial v_o}{\partial y}\right)\left(-\frac{\partial w}{\partial y}\right) + \left(\frac{\partial u_o}{\partial y}\right)\left(-\frac{\partial w}{\partial x}\right) \\
\gamma_{zx} &= \varepsilon_{zx} = \left(\frac{\partial u_o}{\partial x}\right)\left(-\frac{\partial w}{\partial x}\right) + \left(\frac{\partial v_o}{\partial x}\right)\left(-\frac{\partial w}{\partial y}\right) \quad ,
\end{aligned}
\tag{A.18}
$$

where the common practice of representing the engineering shear strains by γ_{ij} has been introduced.

Eqs. (A.18) can be rewritten as

$$
\begin{aligned}
&\varepsilon_x = \varepsilon_x^o + z\kappa_x \qquad \varepsilon_y = \varepsilon_y^o + z\kappa_y \qquad \gamma_{xy} = \gamma_{xy}^o + z\kappa_{xy} \quad , \\
&\varepsilon_z = \varepsilon_z^o \qquad \gamma_{yz} = \gamma_{yz}^o \qquad \gamma_{zx} = \gamma_{zx}^o
\end{aligned}
\tag{A.19}
$$

where κ_x, κ_y and κ_{xy} are the curvatures at the reference surface ($z = 0$) given by

$$
\kappa_x = -\frac{\partial^2 w}{\partial x^2} \qquad \kappa_y = -\frac{\partial^2 w}{\partial y^2} \qquad \kappa_{xy} = -2\frac{\partial^2 w}{\partial x \partial y} \quad ,
\tag{A.20}
$$

and ε_x^o, ε_y^o, ε_z^o, γ_{xy}^o, γ_{yz}^o, and γ_{zx}^o, are reference surface strains defined by

$$
\begin{aligned}
\varepsilon_x^o &= \frac{\partial u_o}{\partial x} + \frac{1}{2}\left[\left(\frac{\partial u_o}{\partial x}\right)^2 + \left(\frac{\partial v_o}{\partial x}\right)^2 + \left(\frac{\partial w}{\partial x}\right)^2\right] \\
\varepsilon_y^o &= \frac{\partial v_o}{\partial y} + \frac{1}{2}\left[\left(\frac{\partial v_o}{\partial y}\right)^2 + \left(\frac{\partial u_o}{\partial y}\right)^2 + \left(\frac{\partial w}{\partial y}\right)^2\right] \\
\varepsilon_z^o &= \frac{1}{2}\left[\left(\frac{\partial w}{\partial x}\right)^2 + \left(\frac{\partial w}{\partial y}\right)^2\right] \\
\gamma_{xy}^o &= \frac{\partial u_o}{\partial y} + \frac{\partial v_o}{\partial x} + \left(\frac{\partial u_o}{\partial x}\right)\left(\frac{\partial u_o}{\partial y}\right) + \left(\frac{\partial v_o}{\partial y}\right)\left(\frac{\partial v_o}{\partial x}\right) + \left(\frac{\partial w}{\partial x}\right)\left(\frac{\partial w}{\partial y}\right) \\
\gamma_{yz}^o &= \left(\frac{\partial v_o}{\partial y}\right)\left(-\frac{\partial w}{\partial y}\right) + \left(\frac{\partial u_o}{\partial y}\right)\left(-\frac{\partial w}{\partial x}\right) \\
\gamma_{zx}^o &= \left(\frac{\partial u_o}{\partial x}\right)\left(-\frac{\partial w}{\partial x}\right) + \left(\frac{\partial v_o}{\partial x}\right)\left(-\frac{\partial w}{\partial y}\right) \quad .
\end{aligned}
\tag{A.21}
$$

Under the conditions of small strain and moderate rotations, Eqs. (A.21) may be further simplified to

$$
\begin{aligned}
\varepsilon_x^o &= \frac{\partial u_o}{\partial x} + \frac{1}{2}\left(\frac{\partial w}{\partial x}\right)^2 \\
\varepsilon_y^o &= \frac{\partial v_o}{\partial y} + \frac{1}{2}\left(\frac{\partial w}{\partial y}\right)^2 \\
\varepsilon_z^o &= \frac{1}{2}\left[\left(\frac{\partial w}{\partial x}\right)^2 + \left(\frac{\partial w}{\partial y}\right)^2\right] \\
\gamma_{xy}^o &= \frac{\partial u_o}{\partial y} + \frac{\partial v_o}{\partial x} + \left(\frac{\partial w}{\partial x}\right)\left(\frac{\partial w}{\partial y}\right) \\
\gamma_{yz}^o &= 0 \\
\gamma_{zx}^o &= 0 \quad .
\end{aligned}
\tag{A.22}
$$

For small strains and small rotations, Eqs. (A.22) reduce further to

$$
\varepsilon_x^o = \frac{\partial u_o}{\partial x} \qquad \varepsilon_y^o = \frac{\partial v_o}{\partial y} \qquad \gamma_{xy}^o = \frac{\partial u_o}{\partial y} + \frac{\partial v_o}{\partial x}
$$
$$
\varepsilon_z^o = 0 \qquad \gamma_{yz}^o = 0 \qquad \gamma_{zx}^o = 0 \quad .
\tag{A.23}
$$

The expressions for the reference surface strains as defined in Eqs. (A.21) through Eqs. (A.23) represent three levels of complexity and accuracy in representing nonlinear behavior. The most accurate definitions for the reference surface strains, as shown in Eqs. (A.21), are used in the STAGS finite element code (Ref. A5) for the 4-node displacement-based quadrilateral shell element (element 410, Ref. A6). The simplified definitions shown in Eqs. (A.22) correspond to von Kármán nonlinear plate theory and are the most commonly used form of nonlinear strain-displacement relations. The most simplified definitions, shown in Eqs. (A.23), are linear strain-displacement relations with no coupling between inplane and out-of-plane displacements. This form is used when considering linear elasticity only, as is the case in many texts when presenting classical lamination theory.

Independent of which definition is used for the reference surface strains, application of Kirchhoff's hypothesis does imply a linear variation of strain through the thickness of the entire laminate. The strain relations in Eqs. (A.19) can be written in matrix form as

$$\begin{Bmatrix} \varepsilon_x \\ \varepsilon_y \\ \gamma_{xy} \end{Bmatrix} = \begin{Bmatrix} \varepsilon_x^o \\ \varepsilon_y^o \\ \gamma_{xy}^o \end{Bmatrix} + z \begin{Bmatrix} \kappa_x \\ \kappa_y \\ \kappa_{xy} \end{Bmatrix} \quad . \tag{A.24}$$

By substituting Eq. (A.24) into Eq. (A.7), the stresses in the k^{th} layer of a laminated plate can be expressed in terms of the laminate reference surface strains and curvatures as

$$\begin{Bmatrix} \sigma_x \\ \sigma_y \\ \tau_{xy} \end{Bmatrix}_k = \begin{bmatrix} \overline{Q}_{11} & \overline{Q}_{12} & \overline{Q}_{16} \\ \overline{Q}_{12} & \overline{Q}_{22} & \overline{Q}_{26} \\ \overline{Q}_{16} & \overline{Q}_{26} & \overline{Q}_{66} \end{bmatrix}_k \left(\begin{Bmatrix} \varepsilon_x^o \\ \varepsilon_y^o \\ \gamma_{xy}^o \end{Bmatrix} + z \begin{Bmatrix} \kappa_x \\ \kappa_y \\ \kappa_{xy} \end{Bmatrix} \right) \quad . \tag{A.25}$$

Since $\overline{Q}_{ij}$ can be different in each layer of the laminate, the strain variation which is linear through the thickness gives a stress variation which is piecewise linear and most likely discontinuous from one layer to the next.

A.4 Laminate Stiffnesses and Compliances

As a laminate consists of two or more laminae bonded together to act as one structural element, the resultant forces and moments acting on a laminate are obtained by integrating

the stresses in each lamina through the thickness of the laminate. For a laminate composed of N laminae, or layers, with the laminate reference surface located at $z = 0$, bottom surface at $z = h_1$, and top surface at $z = h_2$, the laminate force and moment resultants are defined by

$$\begin{Bmatrix} N_x \\ N_y \\ N_{xy} \end{Bmatrix} = \int_{h_1}^{h_2} \begin{Bmatrix} \sigma_x \\ \sigma_y \\ \tau_{xy} \end{Bmatrix} dz = \sum_{k=1}^{N} \int_{z_{k-1}}^{z_k} \begin{Bmatrix} \sigma_x \\ \sigma_y \\ \tau_{xy} \end{Bmatrix}_k dz \quad , \tag{A.26}$$

$$\begin{Bmatrix} Q_x \\ Q_y \end{Bmatrix} = \int_{h_1}^{h_2} \begin{Bmatrix} \tau_{xz} \\ \tau_{yz} \end{Bmatrix} dz = \sum_{k=1}^{N} \int_{z_{k-1}}^{z_k} \begin{Bmatrix} \tau_{xz} \\ \tau_{yz} \end{Bmatrix}_k dz \quad , \tag{A.27}$$

and

$$\begin{Bmatrix} M_x \\ M_y \\ M_{xy} \end{Bmatrix} = \int_{h_1}^{h_2} \begin{Bmatrix} \sigma_x \\ \sigma_y \\ \tau_{xy} \end{Bmatrix} z dz = \sum_{k=1}^{N} \int_{z_{k-1}}^{z_k} \begin{Bmatrix} \sigma_x \\ \sigma_y \\ \tau_{xy} \end{Bmatrix}_k z dz \quad , \tag{A.28}$$

in which N_x, N_y, N_{xy} are membrane forces, Q_x, Q_y are transverse shear forces, and M_x, M_y, M_{xy} are bending and twisting moments, all per unit length (width) of the cross section of the laminate, and z_k, and z_{k-1} are the z values at the top and bottom of the k^{th} layer. The force and moment resultants are shown in Fig. A-5. Eqs. (A.26) and (A.28) can be expressed as

$$\begin{Bmatrix} N \\ M \end{Bmatrix} = \begin{bmatrix} A & B \\ B & D \end{bmatrix} \begin{Bmatrix} \varepsilon^o \\ \kappa \end{Bmatrix} \quad , \tag{A.29}$$

where

$$N = \begin{Bmatrix} N_x \\ N_y \\ N_{xy} \end{Bmatrix} \qquad M = \begin{Bmatrix} M_x \\ M_y \\ M_{xy} \end{Bmatrix} \qquad \varepsilon^o = \begin{Bmatrix} \varepsilon_x^o \\ \varepsilon_y^o \\ \gamma_{xy}^o \end{Bmatrix} \qquad \kappa = \begin{Bmatrix} \kappa_x \\ \kappa_y \\ \kappa_{xy} \end{Bmatrix}$$

$$A = \begin{bmatrix} A_{11} & A_{12} & A_{16} \\ A_{12} & A_{22} & A_{26} \\ A_{16} & A_{26} & A_{66} \end{bmatrix} \qquad B = \begin{bmatrix} B_{11} & B_{12} & B_{16} \\ B_{12} & B_{22} & B_{26} \\ B_{16} & B_{26} & B_{66} \end{bmatrix} \qquad D = \begin{bmatrix} D_{11} & D_{12} & D_{16} \\ D_{12} & D_{22} & D_{26} \\ D_{16} & D_{26} & D_{66} \end{bmatrix} \quad . \tag{A.30}$$

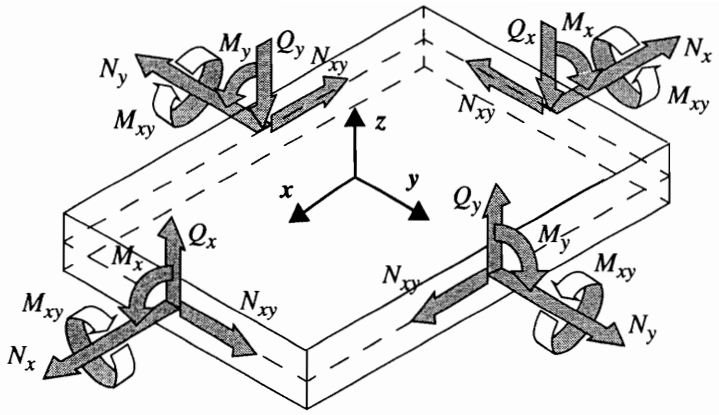

Fig. A-5 Directions of positive stress resultants and moments on a flat laminate

The elements A_{ij}, B_{ij}, D_{ij} in Eqs. (A.30) are given by

$$
\begin{aligned}
A_{ij} &= \int_{h_1}^{h_2} (\bar{Q}_{ij})_k dz = \sum_{k=1}^{N} (\bar{Q}_{ij})_k (z_k - z_{k-1}) \\
B_{ij} &= \int_{h_1}^{h_2} (\bar{Q}_{ij})_k z dz = \frac{1}{2} \sum_{k=1}^{N} (\bar{Q}_{ij})_k (z_k^2 - z_{k-1}^2) \\
D_{ij} &= \int_{h_1}^{h_2} (\bar{Q}_{ij})_k z^2 dz = \frac{1}{3} \sum_{k=1}^{N} (\bar{Q}_{ij})_k (z_k^3 - z_{k-1}^3) \quad ,
\end{aligned}
\tag{A.31}
$$

in which A_{ij} are the membrane stiffnesses, B_{ij} are the coupling stiffnesses, and D_{ij} are the bending stiffnesses.

The stiffnesses B_{ij} represent coupling between inplane extension and transverse bending. In the current work, all laminates are symmetric with respect to the laminate reference surface. Therefore, $\bar{Q}_{ij}$ is an even function of z and the coupling stiffnesses disappear (B_{ij} = 0). Thus, Eq. (A.29) simplifies to

$$
\begin{Bmatrix} N \\ M \end{Bmatrix} = \begin{bmatrix} A & 0 \\ 0 & D \end{bmatrix} \begin{Bmatrix} \varepsilon^o \\ \kappa \end{Bmatrix} \quad , \tag{A.32}
$$

or

$$\begin{Bmatrix} N_x \\ N_y \\ N_{xy} \end{Bmatrix} = \begin{bmatrix} A_{11} & A_{12} & A_{16} \\ A_{12} & A_{22} & A_{26} \\ A_{16} & A_{26} & A_{66} \end{bmatrix} \begin{Bmatrix} \varepsilon_x^o \\ \varepsilon_y^o \\ \gamma_{xy}^o \end{Bmatrix} \qquad \begin{Bmatrix} M_x \\ M_y \\ M_{xy} \end{Bmatrix} = \begin{bmatrix} D_{11} & D_{12} & D_{16} \\ D_{12} & D_{22} & D_{26} \\ D_{16} & D_{26} & D_{66} \end{bmatrix} \begin{Bmatrix} \kappa_x \\ \kappa_y \\ \kappa_{xy} \end{Bmatrix} \quad . \qquad \text{(A.33)}$$

The A_{16}, and A_{26} terms represent coupling between the inplane extension and shear strains. These terms are a simple through-the-thickness integration of $\overline{Q}_{16}$, $\overline{Q}_{26}$ for each lamina forming the laminate. For a balanced laminate, i.e., one having an equal number of laminae at +θ and -θ orientations, these coupling terms are equal to zero. The D_{16} and D_{26} terms represent coupling between the out-of-plane bending and twisting curvatures. For orthotropic laminates (lamina oriented at 0° and 90° only), these terms are equal to zero.

In many situations the applied loads are known and the resulting strains are unknown. Therefore, it is often convenient to express the reference surface strains and curvatures in terms of the force and moment resultants. Equation (A.33) can be expressed in inverted form as

$$\begin{Bmatrix} \varepsilon_x^o \\ \varepsilon_y^o \\ \gamma_{xy}^o \end{Bmatrix} = \begin{bmatrix} a_{11} & a_{12} & a_{16} \\ a_{12} & a_{22} & a_{26} \\ a_{16} & a_{26} & a_{66} \end{bmatrix} \begin{Bmatrix} N_x \\ N_y \\ N_{xy} \end{Bmatrix} \qquad \begin{Bmatrix} \kappa_x \\ \kappa_y \\ \kappa_{xy} \end{Bmatrix} = \begin{bmatrix} d_{11} & d_{12} & d_{16} \\ d_{12} & d_{22} & d_{26} \\ d_{16} & d_{26} & d_{66} \end{bmatrix} \begin{Bmatrix} M_x \\ M_y \\ M_{xy} \end{Bmatrix} \quad , \qquad \text{(A.34)}$$

where $[a] = [A]^{-1}$ and $[d] = [D]^{-1}$. The $[a]$ and $[d]$ matrices are the laminate membrane and bending compliances, respectively.

A.5 Equivalent Engineering Constants

The stiffness and compliance matrices defined in the previous section can sometimes elude physical understanding. To simplify matters, laminate stiffnesses can be expressed in terms of equivalent engineering constants. These constants are listed in Ref. A7 and can be derived from Eqs. (A.34) by considering the strains for load cases which have only one force or moment resultant applied, and all other loads are equal to zero. Equivalent engineering constants are average properties which, if applied to a homogeneous plate of the same thickness, would provide the same stiffness as the laminate.

Some of the equivalent engineering constants for inplane loading are

$$E_x^o = \frac{1}{ha_{11}} \qquad E_y^o = \frac{1}{ha_{22}} \qquad G_{xy}^o = \frac{1}{ha_{66}}$$
$$\nu_{xy}^o = \frac{-a_{12}}{a_{11}} \qquad \eta_{xy,\,x}^o = \frac{-a_{16}}{a_{11}} \quad , \tag{A.35}$$

where h is the thickness of the laminate. The constants E_x^o, E_y^o, and G_{xy}^o are moduli and reflect the stiffness of the laminate when subjected to a single inplane load, N_x, N_y, or N_{xy} respectively. The constant ν_{xy}^o is Poisson's ratio which characterizes contraction in the y-direction caused by an inplane load in the x-direction. The constant $\eta_{xy,\,x}^o$ is the coefficient of mutual influence of the second kind. It characterizes shearing in the x-y plane caused by an inplane load in the x-direction.

Analogous relations are also defined for the flexural constants. Some of the equivalent engineering constants for bending are

$$E_x^f = \frac{12}{h^3 d_{11}} \qquad E_y^f = \frac{12}{h^3 d_{22}} \qquad G_{xy}^f = \frac{12}{h^3 d_{66}}$$
$$\nu_{xy}^f = \frac{-d_{12}}{d_{11}} \qquad \eta_{xy,\,x}^f = \frac{-d_{16}}{d_{11}} \quad . \tag{A.36}$$

The constants E_x^f, E_y^f, and G_{xy}^f are moduli and reflect the stiffness of the laminate when subjected to a single bending moment, M_x, M_y, or M_{xy}, respectively. The constant ν_{xy}^f is Poisson's ratio which characterizes the curvature in the y-direction caused by a bending moment in the x-direction, M_x. The constant $\eta_{xy,\,x}^f$ is the coefficient of mutual influence of the second kind. It characterizes twisting caused by a bending moment in the x-direction, M_x.

A.6 Stiffness Computations for Built-Up Structures

The discussions above represent stiffness computations for thin laminated plates. If a structure is created by joining thin plate components, and the cross section of the structure does not warp during deformation, then it may be possible to represent the stiffness of the structure by the sum of the stiffnesses of its components. A box beam, as shown in Fig. A-6, is a common example of a built-up structure that is fabricated by joining thin plates. The box beam consists of lower and upper face sheets and two webs which close the sec-

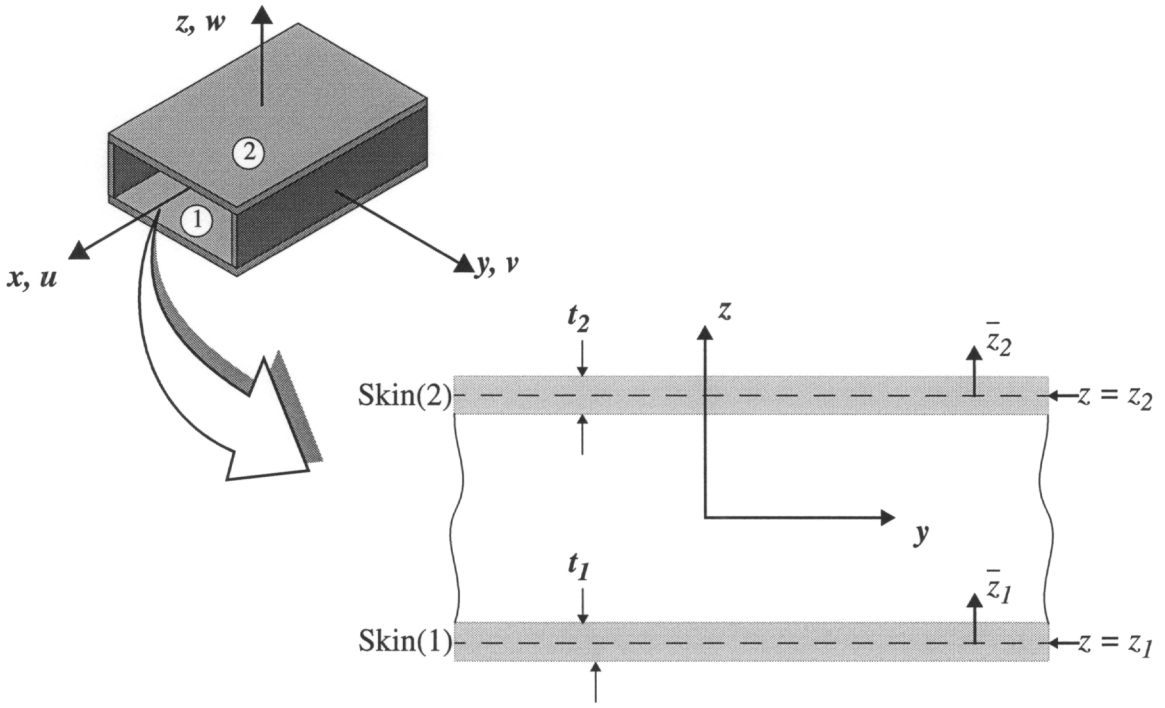

Fig. A-6 Simple box beam with lower and upper face sheets, Skin(1) and Skin(2)

tion. In Fig. A-6 the lower and upper face sheets of the box beam are labeled as Skin(1) and Skin(2), respectively, and local z-coordinates, z_1 and z_2, correspond to the through-thickness location in each face sheet. If the cross sectional area of the webs are small relative to the cross sectional area of the skins, the stiffness of the box beam is often approximated by assuming that the face sheets are the primary load carrying components, and that the web stiffness may be ignored. If these assumptions are made, then the membrane stiffness of the box beam $(A_{ij})^{\text{box}}$ can be expressed in a format consistent with that defined for a laminate in Eq. (A.31), namely,

$$
\begin{aligned}
(A_{ij})^{\text{box}} &= \left(\int_{\left(z_1 - \frac{t_1}{2}\right)}^{\left(z_2 + \frac{t_2}{2}\right)} (\overline{Q}_{ij})_k dz \right) \\
&= \left(\int_{\left(z_1 - \frac{t_1}{2}\right)}^{\left(z_1 + \frac{t_1}{2}\right)} (\overline{Q}_{ij})_k dz + \int_{\left(z_2 - \frac{t_2}{2}\right)}^{\left(z_2 + \frac{t_2}{2}\right)} (\overline{Q}_{ij})_k dz \right) .
\end{aligned}
\tag{A.37}
$$

If the z-coordinate is replaced with the local coordinate in each face sheet,

$$
\begin{aligned}
\bar{z}_1 &= z - z_1 \qquad d\bar{z}_1 = dz \\
\bar{z}_2 &= z - z_2 \qquad d\bar{z}_2 = dz
\end{aligned} \quad ,
\tag{A.38}
$$

then Eq. (A.37) can be written as

$$
\begin{aligned}
(A_{ij})^{\text{box}} &= \left(\int_{\left(-\frac{t_1}{2}\right)}^{\left(\frac{t_1}{2}\right)} (\overline{Q}_{ij})_k d\bar{z}_1 + \int_{\left(-\frac{t_2}{2}\right)}^{\left(\frac{t_2}{2}\right)} (\overline{Q}_{ij})_k d\bar{z}_2 \right) \\
&= (A_{ij})^{\text{Skin(1)}} + (A_{ij})^{\text{Skin(2)}} \quad .
\end{aligned}
\tag{A.39}
$$

Thus, when the stiffness of the webs is ignored, the membrane stiffness of the box beam is a simple summation of the membrane stiffness of each face sheet.

Similarly, the bending stiffness of the box beam $(D_{ij})^{\text{box}}$ can be expressed in a format consistent with that defined for a laminate in Eq. (A.31).

$$(D_{ij})^{\text{box}} = \left(\int_{\left(z_1 - \frac{t_1}{2}\right)}^{\left(z_2 + \frac{t_2}{2}\right)} (\overline{Q}_{ij})_k z^2 dz \right)$$

$$= \left(\int_{\left(z_1 - \frac{t_1}{2}\right)}^{\left(z_1 + \frac{t_1}{2}\right)} (\overline{Q}_{ij})_k z^2 dz + \int_{\left(z_2 - \frac{t_2}{2}\right)}^{\left(z_2 + \frac{t_2}{2}\right)} (\overline{Q}_{ij})_k z^2 dz \right) . \tag{A.40}$$

If the z-coordinate is replaced with the local coordinate in each face sheet,

$$\begin{aligned} \bar{z}_1 &= z - z_1 \qquad & d\bar{z}_1 &= dz \\ \bar{z}_2 &= z - z_2 \qquad & d\bar{z}_2 &= dz \end{aligned} , \tag{A.41}$$

then Eq. (A.40) becomes

$$(D_{ij})^{\text{box}} = \left(\int_{\left(-\frac{t_1}{2}\right)}^{\left(\frac{t_1}{2}\right)} (\overline{Q}_{ij})_k [(z_1)^2 + 2z_1\bar{z}_1 + (\bar{z}_1)^2] d\bar{z}_1 \right)$$

$$+ \left(\int_{\left(-\frac{t_2}{2}\right)}^{\left(\frac{t_2}{2}\right)} (\overline{Q}_{ij})_k [(z_2)^2 + 2z_2\bar{z}_2 + (\bar{z}_2)^2] d\bar{z}_2 \right) . \tag{A.42}$$

If the laminate membrane and bending stiffness definitions of Eq. (A.31) are applied, Eq. (A.42) can be expressed as

$$\begin{aligned} (D_{ij})^{\text{box}} = {} & (z_1)^2 (A_{ij})^{\text{Skin(1)}} + 2z_1 (B_{ij})^{\text{Skin(1)}} + (D_{ij})^{\text{Skin(1)}} \\ & + (z_2)^2 (A_{ij})^{\text{Skin(2)}} + 2z_2 (B_{ij})^{\text{Skin(2)}} + (D_{ij})^{\text{Skin(2)}} \end{aligned} . \tag{A.43}$$

If the face sheets are symmetric, then $B_{ij} = 0$ and Eq. (A.42) reduces to

$$\begin{aligned} (D_{ij})^{\text{box}} = {} & (z_1)^2 (A_{ij})^{\text{Skin(1)}} + (D_{ij})^{\text{Skin(1)}} \\ & + (z_2)^2 (A_{ij})^{\text{Skin(2)}} + (D_{ij})^{\text{Skin(2)}} \end{aligned} . \tag{A.44}$$

Thus, when the stiffness of the webs is ignored and the face sheets are symmetric, the bending stiffness of the box beam is the summation of the bending stiffness of each face sheet plus the product of the face sheet's inplane stiffness times the square of the distance of the face sheet from the box beam's neutral axis.

Consider now the relative magnitude of the terms in Eq. (A.44). The box beam shown in Fig. A-6 has face sheets that are thin compared to the web height. Therefore, $(z_1)^2 > (\bar{z}_1)^2$ and $(z_2)^2 > (\bar{z}_2)^2$. Applying these relations to Eq. (A.42) and using the resulting simplified form in Eq. (A.44), it can be concluded that the bending stiffness of the box beam $(D_{ij})^{box}$ is dominated by the terms in Eq. (A.44) associated with the membrane stiffness of the face sheets. Also, by considering that a bending load on a box beam reduces to predominately membrane loading in the face sheets, especially for thin-walled shell structures, then the fundamental conclusion to be drawn from the above discussion is that the membrane and bending stiffnesses of a box beam, and other structures formed by assembling thin-walled shells, are dominated by the membrane stiffnesses of the individual components of the structure. Thus, the membrane and bending stiffnesses of a built-up structure should be most effectively altered by tailoring the membrane stiffnesses of the thin-walled components.

References

A1. Jones, R. M., Mechanics of Composite Materials, McGraw-Hill Book Co., New York, 1975.

A2. Chia, C. Y., Nonlinear Analysis of Plates, McGraw-Hill, New York, 1980.

A3. Sensmeier, M. D., Griffin, O. H., Jr., and Johnson, E. R., "Static and Dynamic Large Deflection Response of Graphite-Epoxy Beams," NASA CR-4118, 1988.

A4. Anonymous, Product Data for Hercules Carbon Prepreg Tape AS4-3502, Number 855-2, Hercules Inc., Wilmington, DE 19894.

A5. Brogan, F. A., Rankin, C. C., and Cabiness, H. D., "STAGS Users Manual," Lockheed Palo Alto Research Laboratory, Report LMSC P032594, 1994.

A6. Rankin, C. C., and Brogan, F. A., "The Computational Structural Mechanics Testbed Structural Element Processor ES5: STAGS Shell Element," NASA CR-4358, 1991.

A7. Tsai, S. W., Theory of Composites Design, Think Composites, Dayton OH, 1992, pp. 7.1-7.8.

Vita

Richard D. Young was born on November 13, 1963 in Milledgeville, Georgia. He attended high school at Hammondsport Central School in Hammondsport, New York. He completed his undergraduate studies while participating in a 3-2 Cooperative Engineering Program, and in May of 1986 received a Bachelor of Science degree in Mechanical Engineering from Rensselaer Polytechnic Institute in Troy, New York, and a Bachelor of Science degree in Physics from the State University College at Fredonia in Fredonia, New York. He received his Master of Science degree in Engineering Mechanics from Virginia Polytechnic Institute and State University in Blacksburg, Virginia, in September of 1987, and then entered the doctoral program in Engineering Mechanics at the same university as a fellow in the NASA Graduate Student Researchers Program. After completing his course work, he spent one year in residency at the NASA Langley Research Center in Hampton, Virginia. In January of 1990, he took a leave of absence from Virginia Polytechnic Institute and State University and was employed as a structural engineer by Lockheed Engineering and Sciences Company at the Langley Program Office in Hampton, Virginia. While employed by Lockheed Engineering and Sciences Company, now called Lockheed Martin Engineering and Science Services, he supported testing and analysis of composite and metallic structures for the Structural Mechanics Branch of the NASA Langley Research Center. He fulfilled his requirements for the Ph.D. degree in Engineering Mechanics in July of 1996, and continues to be employed by Lockheed Martin.